

# AGARD

ADVISORY GROUP FOR AEROSPACE RESEARCH & DEVELOPMENT  
7 RUE ANCELLE, 92200 NEUILLY-SUR-SEINE, FRANCE

AGARD CONFERENCE PROCEEDINGS 583

## Radar Signature Analysis and Imaging of Military Targets

(l'Analyse de la signature radar et de la vidéoscopie de cibles  
militaires)

*Papers presented at the Sensor and Propagation Panel Symposium held in Ankara, Turkey,  
7-10 October 1996.*

19970429 192



**NORTH ATLANTIC TREATY ORGANIZATION**

**DISTRIBUTION STATEMENT A**

Approved for public release;  
Distribution Unlimited

Published April 1997

*Distribution and Availability on Back Cover*

# AGARD

ADVISORY GROUP FOR AEROSPACE RESEARCH & DEVELOPMENT

7 RUE ANCELLE, 92200 NEUILLY-SUR-SEINE, FRANCE

**AGARD CONFERENCE PROCEEDINGS 583**

## **Radar Signature Analysis and Imaging of Military Targets**

(l'Analyse de la signature radar et de la vidéoscopie de cibles militaires)

Papers presented at the Sensor and Propagation Panel Symposium held in Ankara, Turkey,  
7-10 October 1996.



North Atlantic Treaty Organization  
*Organisation du Traité de l'Atlantique Nord*

# The Mission of AGARD

The mission of AGARD is to bring together the leading personalities of the NATO nations in the fields of science and technology relating to aerospace for the following purposes:

- Exchanging of scientific and technical information;
- Continuously stimulating advances in the aerospace sciences relevant to strengthening the common defence posture;
- Improving the co-operation among member nations in aerospace research and development;
- Providing scientific and technical advice and assistance to the North Atlantic Military Committee in the field of aerospace research and development (with particular regard to its military application);
- Rendering scientific and technical assistance, as requested, to other NATO bodies and to member nations in connection with research and development matters in the aerospace field;
- Providing assistance to member nations for the purpose of increasing their scientific and technical potential;
- Recommending effective ways for the member nations to use their research and development capabilities for the common benefit of the NATO community.

The highest authority within AGARD is the National Delegates Board consisting of officially appointed senior representatives from each member nation. The mission of AGARD is carried out through the Panels which are composed of experts appointed by the National Delegates, the Consultant and Exchange Programme and the Aerospace Application Studies Programme. The results of AGARD work are reported to the member nations and the NATO Authorities through the AGARD series of publications, of which this is one.

Participation in AGARD activities is by invitation only and is normally limited to citizens of the NATO nations.

The content of this publication has been reproduced  
directly from material supplied by AGARD or the authors.

Published April 1997

Copyright © AGARD 1997  
All Rights Reserved

ISBN 92-836-0039-8



*Printed by Canada Communication Group  
45 Sacré-Cœur Blvd., Hull (Québec), Canada K1A 0S7*

# **Radar Signature Analysis and Imaging of Military Targets**

**(AGARD CP-583)**

## **Executive Summary**

Radar has been around for more than half a century now. During this time it has reached both widespread application and a high degree of sophistication. Still, it is far from being a mature science. Major improvements in concept, componentry and information exaction continue to make radar more capable in detecting and identifying targets. Parallel with this development, the concealment of military targets is an ever-increasing necessity and is progressing with similar strides. A review of recent developments in the analysis of radar signatures of military targets is therefore timely and appropriate.

The symposium addressed many aspects of this multi-faceted topic. Numerical target modeling holds great attraction. Methods are presented to render the problem computationally more efficient. Simulation and scaled measurements in comparison with full-size target measurements serve to build confidence in using a cost-effective combination of these techniques to determine radar cross section data. Environmental factors such as rain depolarization and surface multi-path propagation were considered, along with man-made chaff as they impact on radar. An important subject for study was the robustness of non-cooperative target identification based on target doppler characteristics, polarimetry and one- or two-dimensional imaging. The availability of large amounts of data from modern radar systems makes the automation of target detection almost mandatory. The benefits of different approaches are compared. Signature modification is a prerequisite for target survival in the sophisticated electronic warfare arena of the future. Papers ranged from low radar cross section structural designs and retrofits to active cancellation techniques.

# **L'analyse de la signature radar et la vidéoscopie des cibles militaires**

**(AGARD CP-583)**

## **Synthèse**

Le radar existe depuis maintenant plus d'un demi-siècle. Au cours de cette période, cette technique a trouvé une grande diversité d'applications et a atteint un niveau de sophistication élevé. Cependant, elle n'est pas encore parvenue à sa maturité scientifique. Les améliorations importantes dans le domaine des concepts, des composants et de la collecte de données qui continuent à être apportées, rendent les radars de plus en plus performants dans la détection et l'identification des cibles. Parallèlement à ce développement, la dissimulation des cibles militaires devient de plus en plus impérative et les progrès réalisés dans ce domaine sont également impressionnants. Par conséquent, il est opportun et approprié d'envisager une analyse des signatures des cibles militaires à l'heure actuelle.

Le symposium a examiné plusieurs aspects de cette question à facettes multiples. La modélisation numérique de la cible est un sujet très attrayant. Des méthodes sont présentées pour une approche plus poussée du problème, par l'informatique. La simulation et les mesures à l'échelle, comparées aux mesures effectuées sur les cibles en vraie grandeur servent à accroître la confiance en la mise en œuvre d'une combinaison de ces techniques visant à déterminer la surface équivalente radar. Des considérations d'environnement, telles que la dépolarisation par la pluie et la propagation par trajets multiples en surface, étaient examinées, ainsi que les conséquences pour les radars des leurres artificiels. La disponibilité de volumes considérables de données fournies par les systèmes radar modernes rend l'automatisation de la détection de la cible quasi-obligatoire. Une comparaison des avantages des différentes approches était faite. La modification de la signature est une condition préalable indispensable à la survie de la cible dans l'espace sophistiqué de la guerre électronique de demain. Les communications présentées auraient des projets structuraux à faible surface équivalente radar et remise à hauteur, jusqu'aux techniques de dissimulation interactives.

# Contents

	<b>Page</b>
<b>Executive Summary</b>	iii
<b>Synthèse</b>	iv
<b>Theme/Thème</b>	viii
<b>Preface/Préface</b>	ix
<b>Sensor and Propagation Panel</b>	xi
	<b>Reference</b>
<b>SESSION I: EM CODE DEVELOPMENT</b>	
Chairman: G. Brown	
<b>RCS Evaluations with Computational Electromagnetics</b>	1
by Ü. Gülçat, E. Usta and A.R. Aslan	
<b>An Advanced Numerical Scheme for Computational Electromagnetics</b>	2
by J.G. Gallagher, T.E. Hodgetts, C.C. Lytton, M.T. Arthur and I.D. King	
<b>Réflexivité RADAR d'une Cible Illuminée par une Onde Sphérique</b>	3
by P. Pouliguen, P. Gadenne and J.Y. Marty	
<b>Low Frequency Scattering by Targets Above a Ground Plane</b>	4
by G. Dassios and R. Kleinman	
<b>RCS Calculations with the Parabolic Wave Equation</b>	5
by M.F. Levy, P-P. Borsboom, A.A. Zaporozhets and A. Zebic-Le Hyaric	
<b>SESSION II: TARGET DETECTION AND CLASSIFICATION</b>	
Chairman: H.B. Wallace	
<b>Fast Radar Cross Section (RCS) Computation via the Fast Multipole Method</b>	6
by L. Gürel	
<b>Statistical Analysis of Propagation Parameters for Polarimetric Radar Measurements</b>	7
by V. Santalla del Rio and Y.M.M. Antar	
<b>Extended Target Simulation at a Physical Level</b>	8
by S.H.W. Simpson and P.E.R. Galloway	
<b>Algorithms which use the Phase Information to Improve the Target Resolution in Range and Doppler</b>	9*
by D. Nagel	
<b>Paper 10 withdrawn</b>	
<b>Livorno '96: The Centimetre and Millimetre Wave Radar Signature and Propagation Trial</b>	11
by NATO AC/243 (Panel 3/RSG.21)	
by H.J.M. Heemskerk	

\*Published in Classified Supplement

- A Comparison of Signature Measurements of Multiple T72M1 Tanks at 35 GHz** 12\*  
by H.B. Wallace, S.R. Stratton and R.L. Bender

**SESSION III: FREQUENCY SCALED MEASUREMENTS**

Chairman: J. Schiller

- Réponse Impulsionnelle de Cibles Militaires Tridimensionnelles** 13  
**Conception, Développement et Validation d'un Banc de Mesure**  
by M. Piette

**Paper 14 withdrawn**

- Novel HF, Radar, and IR Absorber Material** 15  
by G. Nimtz

- Experimental Evaluation of Material Parameters for RCS Prediction Codes** 16  
by J. Preißner and V. Stein

- Captive-Target Imaging at Sub-MM through CM Wavelengths** 17  
by R.A. Marr and U.H.W. Lammers

- Imaging 3D Structures from Limited-Angle Backscattered Data** 18  
by D.A. Pommett, M.A. Fiddy, R.A. Marr, U.H.W. Lammers and J.B. Morris

**SESSION IV: SIGNAL PROCESSING ALGORITHMS**

Chairman: G. Wyman

- Reconnaissance Automatique de Cibles Détectées par le Radar de Surveillance SCB2130A** 19  
by M.C. Pirlot

**Paper 20 withdrawn**

**Paper 21 withdrawn**

- Modeling of ISAR Imagery for Ships** 22  
by K. Emir and E. Topuz

- An Approach to Physical Level Chaff Simulation** 23  
by S.H.W. Simpson and P.E.R. Galloway

- SAR/ISAR Image Focussing on Moving Hard Targets** 24\*  
by P.N.R. Stoye

**SESSION V: MODELLING OF COMPLEX TARGETS**

Chairman: E. Schweicher

- Radar-Absorbing Structures for Large Military Aircraft** 24A\*  
by J. Kruse and H-P. Wentzel

- Etude de la Compatibilité des Signatures IR et Radar** 25\*  
by G. Berginc and F. Normand

- Réduction active de signature radar : principes et applications possibles** 26\*  
**(Active RCS cancellation : principes and possible applications)**  
by F. Christophe, F. Tardivel, R. Kété, E. Gimonet, E. Brochier and P. Borderies

- Nouveaux Outils d'Analyse de la S.E.R. des Cibles** 27\*  
by J.P. Marcellin, F. Tardivel and J.C. Castelli

\*Published in Classified Supplement

**Analysis of Experimental Data for NCTR Target Modelling** 28  
by M. Moruzzis, J-C. Guillerot and C. Lestrade

**The Effect of the Sea Surface on the Measured Radar Signature of Ships and Simple Targets Close to the Sea Surface** 29\*  
by F.M. Talbot, P. Beeney and J.F. Bassett

**Radar Signature Analysis of Facade Constructions on Airport Buildings and Reduction of their Reflection Characteristics** 29A\*  
by A. Frye

**SESSION VI: TARGET DISCRIMINATION (ATR)**

Chairman: M.A.G. Peters

**Comparison of the Computed and Measured RCS of the A109 Helicopter of the Belgian Army** 30\*  
by I. De Leeneer, A. Barel, E. Schweicher and V. Soubry

**Banc à Haute Résolution (BHR) pour l'analyse de cibles marines (High Resolution Bench (HRB) for the Analysis of Ship Signatures)** 31  
by C. Delhote, F. Perret and J. Isnard

**Marine Target Imaging by Airborne SAR and ISAR Techniques** 32\*  
by D. Perthuis, J.-Ph. Hardange, F. Kufner and D. Rapsilber

**NCI Mode Development and Integration for Airborne Pulsed Doppler Radars** 33\*  
by D. Nagel

**Identification of Aircraft on the Basis of 1- and 2-D-Radar Images** 34\*  
by F. Dommermuth, Kh. Rosenbach and J. Schiller

**Field Trials to Investigate Detectability of Small RCS Targets** 34A\*  
by J. Kruse, J. Kaiser, H. Traut, J. Krüger and H. Galler

**SESSION VII: TARGET DETECTION (POLARIMETRY)**

Chairman: I. Anderson

**Development and Realization of Stealth Constructions Suitable for Naval Applications Shown by the Example of a Camouflage Shell for the SERO 14** 34B\*  
by H. Gerke, J. Kruse and M. Hochmann

**Model Based Image Analysis for the Detection of High Value Surface Radar Targets** 35\*  
by K.-H. Bers, K. Jäger and K. Jurkiewicz

**MERIC - Moyen Expérimental pour la Reconnaissance et l'Identification des Cibles** 36\*  
by P. Brouard, S. Attia and R. Guern

**Millimeterwave Signatures of Tank Mock-Ups** 37\*  
by H. Essen and H. Schimpf

**Detection of Extended Targets in Millimeter Wave Radar Imagery** 38\*  
by H. Schimpf and H. Essen

**Preliminary Results of Automatic Target Detection and Classification from High Resolution SAR Imagery** 39\*  
by M.R. Nottingham and A.M. Horne

\*Published in Classified Supplement

# Theme

Airborne/spaceborne weapons systems and high value surface targets are more likely to survive in combat and to accomplish their mission, if they are of low observability to enemy sensors. Major advances have been made in airborne synthetic aperture radar (SAR). Novel techniques such as interferometry and polarimetry are under investigation. The continuously improving resolution and the capability of long range day/night operation, as well as smoke, weather and foliage penetration have made radar a primary sensor for target detection and classification. Consequently, radar cross section (RCS) reduction and signature modification play an important role in the effort to enhance the survival probability of military targets. The RCS is greatly reduced by controlled redirection or by absorption of incident energy. This impacts on the shape of these targets and affects the integration of subsystems such as armaments, engines and antennas into weapons systems. A need exists to carefully monitor the RCS of complex targets throughout their design, construction and operational phases. Driven by this need, RCS simulation and measurement have made great advances in recent years. Target imaging for the purpose of pinpointing scattering centres on complex targets has achieved a high degree of sophistication. This is in large measure due to the availability of wideband coherent measurement instrumentation and fast digital processors with large memory capacity. The signal received by a single-wavelength radar is typically the vector sum of returns from multiple scatterers on the target. It relates to the target's total RCS from a particular aspect angle. Signals received over a spacial range of aspect angles represent RCS variability and may be processed into one-, two- or three-dimensional target images. Wideband radars yield wavelength dependent total RCS data, RCS data as a function of range, or image enhancement along the range direction. Radar images provide a valuable diagnostic tool for RCS control.

The topics to be covered include:

- Modelling of complex targets;
  - EM code development
  - Computational methods
- Signature evaluation;
  - RCS measurement
  - Direct and synthetic imaging
  - Aimpoint selection
- Signal processing algorithms;
  - Image generation, enhancement and evaluation
  - Target detection and classification
- Frequency scaled measurements;
  - Model target requirements
  - Measurement validation
- Calibration procedures;
  - Standards
  - Error budgets
- Target discrimination;
  - Target/background characteristics
  - Polarimetry
- Camouflage techniques.
  - RCS reduction through shaping
  - Radar absorbing materials
  - Signature modifications

# Thème

Les chances de survie au combat et d'exécution de la mission des systèmes d'armes aéroportés/spatioportés et des cibles de surface de grande valeur sont d'autant plus grandes qu'ils ne présentent qu'une faible observabilité aux senseurs ennemis. Des avancées majeures ont été réalisées dans le domaine des radars à ouverture synthétique aéroportés (SAR). De nouvelles techniques telles que l'interférométrie et la polarimétrie sont à l'étude. L'amélioration permanente de la résolution et la possibilité d'exploitation jour/nuit à grande distance, ainsi que la pénétration de fumées, de feuillages et de conditions météorologiques dégradées font du radar le senseur de choix pour la détection et la classification. Par conséquent, la réduction de la surface équivalente radar (RCS) et la modification de la signature jouent un rôle important dans l'amélioration de la probabilité de survie des cibles militaires. La surface équivalente radar est réduite par la réorientation contrôlée de l'énergie incidente ou par son absorption. Ces techniques ont un impact considérable sur la forme de ces cibles et influent également sur l'intégration dans les systèmes d'armes de différents sous-systèmes tels que les armements, les moteurs et les antennes. Il est nécessaire de surveiller très attentivement les surfaces équivalentes des cibles complexes tout au long de leur conception, leur fabrication et durant les phases opérationnelles. Suite à l'expression de ce besoin, de grands progrès ont été réalisés en simulation et en calcul de la surface équivalente radar ces dernières années. L'application de l'imagerie de la cible à l'identification très précise des centres des cibles complexes a atteint un degré de sophistication très élevé. Ceci est dû, dans une large mesure, à la disponibilité d'instrumentation de mesure cohérente à large bande et de processeurs numériques rapides à grande capacité mémoire. Le signal reçu par un radar fonctionnant sur une seule longueur d'onde est typiquement le vecteur somme des retours de dispersions multiples sur la cible. Il se rapporte à la totalité de la surface équivalente de la cible, vue sous un angle de présentation particulier. Des signaux reçus spatialement, résultant de la variation des RCS sous tous les angles, représentent la variabilité du RCS et peuvent faire l'objet d'un traitement destiné à fournir des représentations de cibles à une, deux ou trois dimensions. Les radars à large bande fournissent des données RCS globales en fonction de la longueur d'onde, des données RCS en fonction de la distance et permettent l'amélioration d'images dans l'axe du radar. Les images radar constituent un outil de diagnostic précieux pour le contrôle du RCS. Les sujets examinés comprennent:

- La modélisation de cibles complexes;
  - l'élaboration des codes électromagnétiques
  - les méthodes de calcul
- l'évaluation de la signature radar;
  - le calcul du RCS
  - l'imagerie directe et synthétique
  - choix du point de visée
- algorithmes de traitement du signal;
  - la génération, l'amélioration et l'évaluation des images
  - la détection et la classification des images
- les mesures en fonction de la fréquence;
  - les spécifications des cibles maquettes
  - la validation de la mesure
- les procédures de calibration;
  - les normes
  - les bilans d'erreur
- la discrimination de la cible;
  - les caractéristiques de la cible/du fond
  - la polarimétrie
- les techniques de camouflage.
  - la diminution du RCS par le profilage
  - les matériaux absorbants
  - la modification de la signature radar

# Preface

## Is the analysis of radar signatures still necessary?

It is a truism to say that the qualities of a defence system are defined by its ability to detect enemy targets and to classify them, and therefore to recognize and, if possible, identify them.

If we compare the main types of sensors capable of carrying out these operations, we are forced to conclude, on the one hand, that not only is radar still in the lead insofar as concerns detection, as it has much greater range than sensors working in the visible and IR domains, but it is incomparably superior in penetrating natural and man-made atmospheric obscurants. On the other hand, radar is active, which means it can be seen, whereas visible and IR sensors are passive and therefore undetectable. At first sight, therefore, it would seem that radar and other types of sensors are equally matched.

At this stage of the argument, the non-believer will object that visible and IR sensors clearly have much greater potential for classification, given the superior spatial resolution resulting from their use of much shorter wavelengths.

Radar would seem to lose points here. In reality, things are quite different, as major advances have been made in the field of synthetic aperture radars (SAR) and new technologies, such as interferometry and polarimetry are emerging. It will be objected that stealth targets will make radars obsolete. This argument against radar is unacceptable as, on the one hand, a target can only really be said to be stealthy if it is discrete at all wavelengths, from microwaves to optical wavelengths and, on the other hand, new types of radars are emerging which are capable of revealing stealth targets; these are the ultra wide band (UWB), HF and VHF radars.

Radar can still be said to have a bright future. Much more eminent persons than my modest self have said so, loud and clear. Suffice it to quote R.W. SELDEN, Chief Scientist of the US Air Force, who declared a few years ago that interconnected radar networks had far more potential than the following types of detection:

1. Concepts based on the interruption of cosmic rays or radio and TV signals;
- 2) Acoustic or seismic sensor systems;
- 3) Electro-optic systems.

It follows that the reduction of radar cross-section (RCS) and the modification of radar signatures will continue to play an important role in the survivability of military targets. This is why, over the next four days, we shall be reviewing the state-of-the-art in the field of theoretical and experimental methods for the determination and reduction of radar signature and the processes for improving radar imaging systems.

Emile SCHWEICHER  
06 October 1996

# Préface

## L'étude de la signature radar n'est-elle pas dépassée?

C'est un truisme que d'affirmer que les qualités d'un système de défense sont ses capacités de détecter les cibles ennemies et de les classifier, donc de les connaître et si possible de les identifier.

Si l'on compare les principaux capteurs capables d'effectuer ces opérations, l'on est forcé de conclure, d'une part, que le radar jouit toujours d'un avantage en ce qui concerne la détection puisque sa portée est meilleure que celle des capteurs travaillant dans les domaines visibles et IR et qu'elle est même incomparablement meilleure au travers des obscurcissants atmosphériques naturels et artificiels. D'autre part, le radar est actif, ce qui le fait repérer alors que les capteurs visible et IR sont passifs et donc indétectables. A première vue il y a donc match nul entre le radar et les autres capteurs.

Arrivé à ce stade de raisonnement, le profane objectera que les capteurs visible et IR présentent à l'évidence de meilleures potentialités de classification à cause de leur meilleure résolution spatiale liée à leur utilisation de longueurs d'onde nettement plus faibles.

Sur ce point les radars semblent perdants. En réalité il n'en est rien, car des avancées majeures ont été réalisées dans le domaine des radars à synthèse d'ouverture (SAR) et de nouvelles technologies émergent parmi lesquelles il faut citer l'interférométrie et la polarimétrie. On objectera que les cibles furtives rendront les radars obsolètes. Cet argument contre les radars est irrecevable car, d'une part, une cible n'est réellement furtive que si elle est discrète à toutes les longueurs d'onde, depuis les micro-ondes jusqu'aux longueurs d'onde optiques et, d'autre part, de nouveaux types de radars émergent qui sont capables de déshabiller les cibles furtives; ce sont les radars HF et VHF et les radars à bande ultra large (UWB).

Le radar jouit donc encore d'un bel avenir. Des personnages bien plus importants que ma modeste personne l'affirment haut et fort. Je me contenterai de citer R.W. SELDEN, "Chief Scientist" de l'US Air Force, qui affirmait il y a quelques années que les réseaux de radars interconnectés ont un bien meilleur potentiel que les moyens de détection suivants:

- 1°) les concepts basés sur l'interruption de rayons cosmiques ou de signaux radio et TV;
- 2°) les systèmes de capteurs acoustiques ou sismiques;
- 3°) les systèmes électro-optiques.

Par conséquent, la réduction de la SER ou surface équivalent radar (RCS) et la modification de la signature radar continueront à jouer un rôle important de la probabilité de survie des cibles militaires. C'est la raison pour laquelle, pendant 4 jours, nous tenterons de faire le point sur les méthodes théoriques et expérimentales de détermination et de réduction de la signature radar ainsi que sur les procédés d'amélioration des systèmes d'imagerie radar.

Emile SCHWEICHER  
06 octobre 1996

# Sensor and Propagation Panel

**Chairman:** Mr. F. CHRISTOPHE  
Dept. Micro-Ondes  
ONERA-CERT Toulouse  
BP 4025  
2, Avenue E. Belin  
31055 Toulouse Cedex  
France

**Deputy Chairman:** Dr. P.S. CANNON  
Tactical Communications Department  
Defence Research Agency  
St Andrews Road  
Malvern, Worcs WR14 3PS  
U.K.

## SYMPOSIUM TECHNICAL PROGRAMME COMMITTEE

**Chairmen:** Dr. U. LAMMERS (United States)  
Prof. Dr. E. SCHWEICHER (Belgium)

**Members:** Dr. I. ANDERSON (United Kingdom)  
Prof. G. BROWN (United States)  
Mr. F. CHRISTOPHE (France)  
Dr. P.A. KOSSEY (United States)  
Dr. R. KLEMM (Germany)  
Dr. V. STEIN (Germany)  
Prof. A. VANDER VORST (Belgium)  
Mr. G. WYMAN (United Kingdom)

## PANEL EXECUTIVE

Lt. Col. G. DEL DUCA (Italy)

**from Europe**  
AGARD-NATO  
ATTN: SPP Executive  
7, rue Ancelle  
92200 Neuilly-sur-Seine  
France

**from North America**  
AGARD NATO/SPP  
PSC 116  
APO AE 09777

Phone: 33-1-55.61.22.68

Fax: 33-1-55.61.22.99

# RCS Evaluations with Computational Electromagnetics

Ü. Gülçat

E. Usta

A.R. Aslan

Faculty of Aeronautics and Astronautics  
İTÜ, 80626, Maslak, Istanbul, Turkey

## 1. SUMMARY

Application of a finite difference time domain method for the solution of the Maxwell's equations involving arbitrary shapes are presented. The method used is based on explicit Lax-Wendroff scheme applied to the transformed equations expressed in generalized coordinates. Only the scattered field variables are solved to evaluate the surface current and the bistatic radar cross section. The computer code developed is first calibrated with the analytical solutions and then the code is used to calculate the RCS for perfectly conducting arbitrary shapes immersed in transverse magnetic plane waves.

## 2. INTRODUCTION

The radar signature calculations play an essential role in designing aerodynamically efficient shapes having low RCS. A crude way of radar signature estimation for a complex shape may be based on combined theory of geometrical and physical optics together with the superposition of solutions with simple shapes (Ref 1). This approach, however, utilizes only the first order approximations and therefore, is rather inaccurate. More accurate way of evaluating RCS is based on the numerical solution of time-domain Maxwell's equations in calculating the electromagnetic scattering about arbitrary shapes. During past 15 years results of several studies based on time-domain solutions have appeared in open literature. These studies use finite difference (Ref 2-3), finite volume (Ref 4) and the finite element method (Ref 5) in discretization of space either in two or in three dimensions. The methods developed in Computational Fluid Dynamics for mesh generation around arbitrary shapes and the solution of hyperbolic equations

are directly applicable to the Computational Electromagnetics in solving Maxwell's equations. A coupled analysis is also possible to shape airfoils with reduced RCS while predicting the aerodynamic characteristics (Ref3).

In this study a computer code based on finite difference solution of Maxwell's equations is developed and implemented for calculating the electromagnetic scattering about arbitrary shapes. The well known Lax-Wendroff scheme is used for the solution of the equations expressed in generalized coordinates. The equations are normalized so that the CFL condition is easily imposed. The solution in time is carried up to a sufficiently large time levels to see the periodicity in the near field solution. Afterwards, the time-domain solution is transformed to the frequency domain for radar cross section evaluations. Finally, the effect of near field is mapped to the far field since the RCS is defined as the effect of the scattered field at infinity (Ref 6).

The code is calibrated with calculating the scattered field about a circular cylinder where the calculated induced surface current agrees very well with the analytical solution (Ref 7). After the calibration, the scattered field about a NACA 0012 airfoil is studied. The results obtained here compares well with the numerical solutions given in References 2-4. Finally, RCS evaluations for a generic helicopter fuselage is provided. The Navier-Stokes equations are also solved around the fuselage to predict the drag coefficient. Therefore, somewhat synergistic approach in solving a multidisciplinary problem of shaping for aerodynamic efficiency and low RCS, is implemented.

### 3. FORMULATION

The governing equations for electromagnetic scattering, the boundary conditions on the surface of the scatterer, the non-reflecting boundary conditions at the outer boundary of the finite domain, the numerical scheme and the RCS evaluation from the scattered field will be given in this section.

#### 3.1. Governing Equations

The electromagnetic fields in general are obtained as solutions to Maxwell's equations given as boundary value problems. These equations are first order and coupled partial differential equations given in terms of the intensities of electric and magnetic field vectors varying with time. Assuming a source free and lossless media the equations read (Ref 8), for a scattered field as well

$$\nabla \times \vec{E} + \mu_o \frac{\partial \vec{H}}{\partial t} = 0 \quad (1)$$

$$\nabla \times \vec{H} - \epsilon_o \frac{\partial \vec{E}}{\partial t} = 0 \quad (2)$$

where  $\vec{E}$  and  $\vec{H}$  are the scattered electric and the magnetic field intensity vectors in time domain, and  $\epsilon_o$  and the  $\mu_o$  are the permittivity and the permeability coefficients, respectively, in free space. In three dimensions equations 1 and 2 give 6 coupled differential equations. In two dimensions however the equations become three coupled partial differential equations. For the transverse magnetic (TM) mode only the  $E^z$ ,  $H^x$  and  $H^y$  components and, for the transverse electric (TE) mode, however, only the  $H^z$ ,  $E^x$  and  $E^y$  play role.

In two dimensions when Maxwell equations are normalized with respect to the speed of light  $c_o$  in free space and with respect to the characteristic length of the scatterer, in conservative form they read

$$Q_t + F_x + G_y = 0 \quad (3)$$

where subscripts indicate differentiation.

In TM mode

$$Q = \begin{bmatrix} E^z \\ H^x \\ H^y \end{bmatrix} \quad F = \begin{bmatrix} -H^y \\ 0 \\ -E^z \end{bmatrix} \quad G = \begin{bmatrix} H^x \\ E^z \\ 0 \end{bmatrix}$$

and in TE mode similarly

$$Q = \begin{bmatrix} H^z \\ E^x \\ E^y \end{bmatrix} \quad F = \begin{bmatrix} E^y \\ 0 \\ H^z \end{bmatrix} \quad G = \begin{bmatrix} -E^x \\ -H^z \\ 0 \end{bmatrix}$$

Equations 3 can be transformed into the generalized coordinates with  $\xi = \xi(x, y)$  and  $\eta = \eta(x, y)$  to give (Ref.9),

$$Q_t + F_\xi + G_\eta = 0 \quad (4)$$

and in TM mode

$$Q = \frac{1}{|J|} \begin{bmatrix} E^z \\ H^x \\ H^y \end{bmatrix} \quad F = \frac{1}{|J|} \begin{bmatrix} \xi_y H^x - \xi_x H^y \\ \xi_y E^z \\ -\xi_x E^z \end{bmatrix}$$

$$G = \frac{1}{|J|} \begin{bmatrix} \eta_y H^x - \eta_x H^y \\ \eta_y E^z \\ -\eta_x E^z \end{bmatrix}$$

in TE mode

$$Q = \frac{1}{|J|} \begin{bmatrix} H^z \\ E^x \\ E^y \end{bmatrix} \quad F = \frac{1}{|J|} \begin{bmatrix} \xi_x E^y - \xi_y E^x \\ -\xi_y H^z \\ \xi_x H^z \end{bmatrix}$$

$$G = \frac{1}{|J|} \begin{bmatrix} \eta_x E^y - \eta_y E^x \\ -\eta_y H^z \\ \eta_x H^z \end{bmatrix}$$

In terms of Jacobien fluxes  $A$  and  $B$ , the equations are cast in more convenient form to be solved numerically. Where

$$A = \frac{\partial F}{\partial Q} \quad \text{and} \quad B = \frac{\partial G}{\partial Q}$$

to give

$$A = \begin{bmatrix} 0 & \xi_y & -\xi_x \\ \xi_y & 0 & 0 \\ -\xi_x & 0 & 0 \end{bmatrix}, \quad B = \begin{bmatrix} 0 & \eta_y & -\eta_x \\ \eta_y & 0 & 0 \\ -\eta_x & 0 & 0 \end{bmatrix}$$

for TM mode and

$$A = \begin{bmatrix} 0 & -\xi_y & \xi_x \\ -\xi_y & 0 & 0 \\ \xi_x & 0 & 0 \end{bmatrix}, \quad B = \begin{bmatrix} 0 & -\eta_y & \eta_x \\ -\eta_y & 0 & 0 \\ \eta_x & 0 & 0 \end{bmatrix}$$

for TE mode.

### 3.2. Boundary Conditions

#### 3.2.1 Surface boundary conditions

The reflecting boundary conditions for perfectly conducting scatterers read as

$$\vec{n} \times (\vec{E} + \vec{E}^i) = 0 \quad (5)$$

where  $\vec{E}$  is the scattered and  $\vec{E}^i$  is the incident field on the surface and  $\vec{n}$  is the unit outward normal to the surface. For the TM mode only the  $z$  component of the  $\vec{E}$  field plays role therefore (5) reads as

$$E^z = -E^{z,i} \quad (6)$$

For the magnetic field at a perfectly conducting surface the reflecting boundary condition reads as

$$\vec{n} \cdot (\vec{H} + \vec{H}^i) = 0 \quad (7)$$

where  $\vec{H}$  is the scattered and  $\vec{H}^i$  is the incident magnetic fields on the surface. The scalar form of the (7) becomes

$$H^n = -H^{n,i} \quad (8)$$

where  $H^n$  and  $H^{n,i}$  are the normal components of the scattered and the incident magnetic fields, respectively.

Here, to be able to impose the boundary conditions on  $H^x$  and  $H^y$ , one needs to have one more equation. This equation is obtained from the tangential component of the Maxwell's equation written on the surface to give

$$\vec{t} \cdot \vec{H} = \frac{\eta_x H^x + \eta_y H^y}{\sqrt{\eta_x^2 + \eta_y^2}} \quad (9)$$

The normal component of the magnetic field in terms of  $H^x$  and  $H^y$  is

$$\vec{n} \cdot \vec{H} = \frac{\xi_x H^x + \xi_y H^y}{\sqrt{\xi_x^2 + \xi_y^2}} \quad (10)$$

Now, equations 6, 9 and 10 completes the boundary conditions on the surface.

#### 3.2.2 Non-reflecting boundary conditions

For most of the problems solved numerically, the external boundaries must end at a finite distance from the scatterer. Therefore, the boundary

conditions at the outer boundary must have non-reflective property. In this study, the absorbing boundary conditions given in Ref.10 is used. They read as

$$\psi_t + c_o \psi_n = 0 \quad (11)$$

where  $\psi$  is defined as

$$\psi = \begin{bmatrix} E^z \\ H^x \\ H^y \end{bmatrix}$$

and  $n$  represents the coordinate normal to the outer boundary.

### 3.3 Radar Cross Section

The power associated with the intensity of the scattered electric field is the indicative of the radar cross section of the scatterer. In two dimensions it is defined as

$$\sigma = \lim_{r \rightarrow \infty} 2\pi r \left| \frac{e(\theta)}{e^i} \right|^2 \quad (12)$$

where,  $e$  and  $e^i$  are the scattered and the incident electrical fields expressed in the frequency domain and  $\theta$  is the azimuthal angle. For the sake of convenience RCS is expressed in dB:  $\sigma(\text{dB}) = 10 \log_{10} \sigma$ . The magnetic field induced surface current density is given with,

$$J = \left| \frac{\vec{n} \times h^t(\theta)}{h^i(\theta)} \right| \quad (13)$$

Here,  $h^t$  and  $h^i$  are the total and the incident magnetic field intensities in frequency domain also. This implies that, one has to compute the frequency domain values for the various field variables obtained in time domain. The numerical transformation is performed easily using Fast Fourier Transform technique given in Ref.11.

The integral relation between the induced surface current and the electric field intensity in two dimensions reads as,

$$e^i(r) = k_o \eta_o \int_c J(r) H_o^2(k_o |r - r'|) dl \quad (14)$$

where  $H_o^2$  is the Hankel function of the second kind and zero order,  $k_o$  is the wave number and  $\eta_o$  is the intrinsic impedance. For a plane incident wave

$$e^i(r) = e_o \exp[jk_o r \cos(\theta - \theta^i)]$$

where  $\theta^i$  is the angle of incidence.

The far field scattered electric intensity in terms of the induced surface current on a scatterer, due to the property of the Hankel function with large arguments (Ref.12), becomes

$$e(r, \theta) \sim K \int_c J(x', y') \exp[jk_o(x' \cos \theta + y' \sin \theta)] dl' \quad (15)$$

where  $K$  is given by

$$K = \frac{k_o \eta_o}{\sqrt{8\pi k_o r}} \exp[-j(k_o r + \frac{3\pi}{4})]$$

The evaluation of the RCS, now requires the following steps to be taken,

- obtain the scattered magnetic field in time domain,
- transform the time domain data to frequency domain,
- obtain the induced surface current from the magnetic field,
- find the effect of near field on farfield using (15),
- find the RCS value using (12).

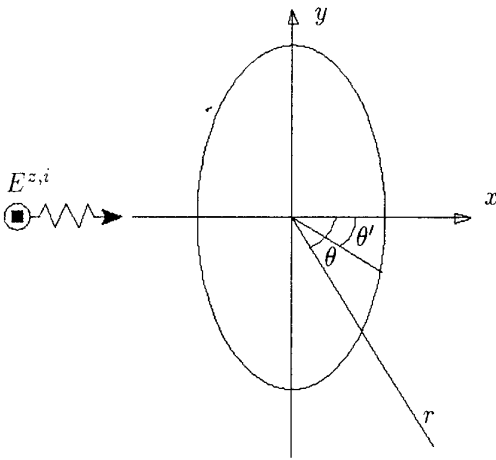


Figure 1. Geometrical definitions for the calculation of RCS and  $J$ .

#### 4. NUMERICAL FORMULATION

Lax-Wendroff scheme is applied for the numerical solution of the governing equations written for TM mode. The scheme is second order accurate both in time and in space. It is based on the Taylor series expansion of the unknown vector  $Q$  about the time coordinate  $t$ . The Taylor series expansion reads as

$$Q_{i,j}^{n+1} = Q_{i,j}^n + \Delta t Q_t + \frac{\Delta t^2}{2} Q_{tt} + O(\Delta t^3) \quad (16)$$

If the time derivatives of the right hand side of Eq.16 is expressed in terms of the space derivatives, following relations in generalized coordinates are obtained

$$Q_t = -F_\xi - G_\eta \quad (17.a)$$

$$Q_{tt} = A(F_{\xi\xi} + G_{\xi\eta}) + A_\xi(F_\xi + G_\eta) + B(F_{\xi\eta} + G_{\eta\eta}) + B_\eta(F_\xi + G_\eta) \quad (17.b)$$

Substituting 17 into 16 gives

$$Q_{ij}^{n+1} = Q_{ij}^n - \Delta t(F_\xi + G_\eta) + \frac{\Delta t^2}{2} [A(F_{\xi\xi} + G_{\xi\eta}) + A_\xi(F_\xi + G_\eta) + B(F_{\xi\eta} + G_{\eta\eta}) + B_\eta(F_\xi + G_\eta)] \quad (18)$$

If one uses the central differencing for the space derivatives in Eq. 18 the following expression for the new time level is obtained.

$$\begin{aligned} Q_{i,j}^{n+1} = & Q_{i,j}^n - \frac{\Delta t}{2} (F_{i+1,j}^n - F_{i-1,j}^n + G_{i,j+1}^n \\ & - G_{i,j-1}^n) + \frac{\Delta t^2}{2} \left[ A \left( F_{i+1,j}^n - 2F_{i,j}^n + F_{i-1,j}^n \right. \right. \\ & \left. \left. + \frac{G_{i+1,j+1}^n - G_{i+1,j-1}^n - G_{i-1,j+1}^n + G_{i-1,j-1}^n}{4} \right. \right. \\ & \left. \left. + \frac{A_{i+1,j} - A_{i-1,j}}{2} \times \right. \right. \\ & \left. \left. \left( \frac{F_{i+1,j}^n - F_{i-1,j}^n + G_{i,j+1}^n - G_{i,j-1}^n}{2} \right) \right. \right. \\ & \left. \left. + B \left( G_{i,j+1}^n - 2G_{i,j}^n + G_{i,j-1}^n \right. \right. \right. \\ & \left. \left. \left. + \frac{F_{i+1,j+1}^n - F_{i+1,j-1}^n - F_{i-1,j+1}^n + F_{i-1,j-1}^n}{4} \right) \right. \right. \\ & \left. \left. \left. + \frac{B_{i,j+1} - B_{i,j-1}}{2} \times \right. \right. \right. \\ & \left. \left. \left. \left( \frac{F_{i+1,j}^n - F_{i-1,j}^n + G_{i,j+1}^n - G_{i,j-1}^n}{2} \right) \right] \quad (19) \end{aligned}$$

#### 5. RESULTS and DISCUSSION

Using the code developed, three different objects are treated as scatterers in transverse magnetic wave in following form,

$$E^{z,i} = E_o \sin [k_o (x \cos \theta^i + y \sin \theta^i - c_o t)]$$

$$H^{x,i} = \frac{E^{z,i} \sin \theta^i}{\mu_o c_o}, \quad H^{y,i} = -\frac{E^{z,i} \cos \theta^i}{\mu_o c_o} \quad (20)$$

where  $\theta^i$  is the angle of incidence of the wave.

First, the code is calibrated with the scattering from a circular cylinder. After obtaining satisfactory results, then the radar cross section of NACA 0012 airfoil at zero angle of incidence is solved. Finally, RCS for a generic helicopter fuselage is calculated. Sametime, the drag coefficient of the fuselage is also computed to study aerodynamic shaping for the low radar signature.

### 5.1 Circular Cylinder

For the numerical study, the grid generated external to the cylinder with  $150 \times 75$  points is shown in Fig.2. A radially stretched grid is preferred for fine resolution near the surface.

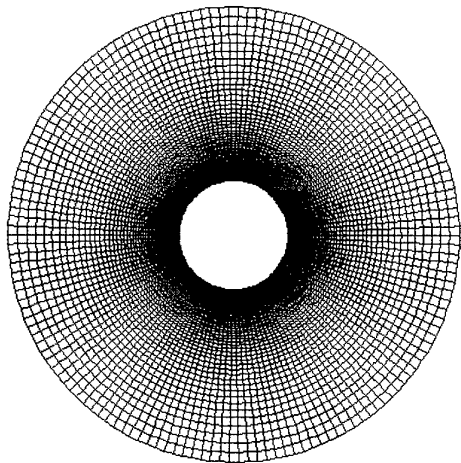


Figure 2. Grid about the circular cylinder,  $150 \times 75$  points stretched in radial direction.

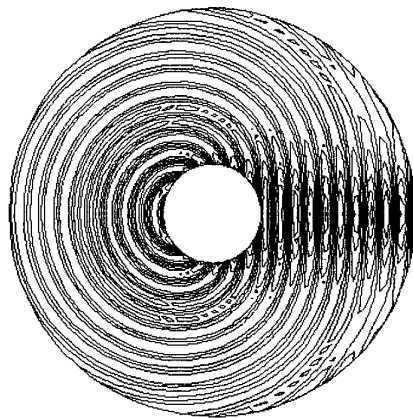


Figure 3. Scattered electric field intensity,  $E^z$ , about the circular cylinder.

The solution is carried up to the dimensionless

time level of  $t = 12\lambda$ , and shown on Fig. 3 is the scattered electric field intensity  $E^z$  at that time level with  $ka = 10$ . The time domain solution is transformed to the frequency domain using FFT. Shown on Fig. 4 is the magnitude of the normalized surface current density  $J$  on the circular cylinder. As seen from the figure, fine mesh solution agrees very well with the closed form solution. However, the solution with the

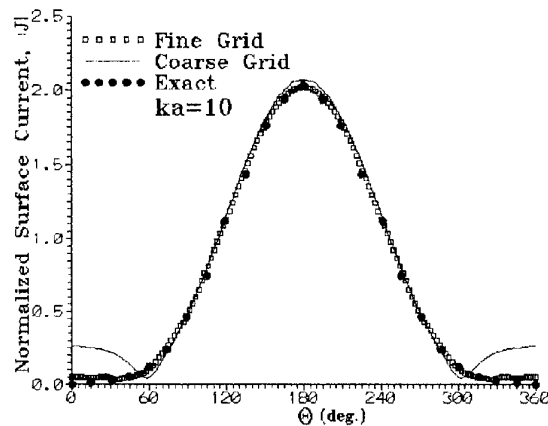
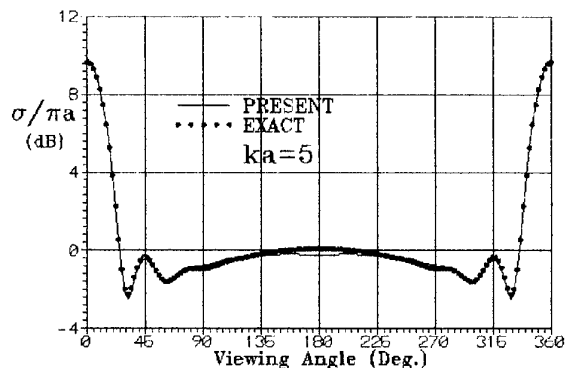
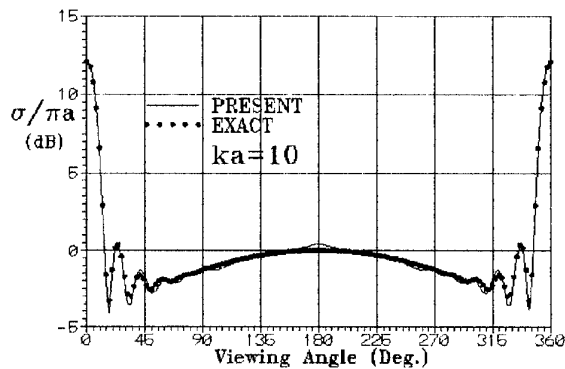


Figure 4. Magnitude of the normalized surface current density  $|J|$  on the circular cylinder.



a)



b)

Figure 5. RCS values for the circular cylinder. a)  $ka = 5$ , b)  $ka = 10$ .

uniform coarse grid deviates from the exact solution at around the aft of the body surface. Shown on Figs. 5 a and b are the RCS values for the circular cylinder for two different wave numbers,  $ka = 5$  and  $ka = 10$ , respectively. The overall agreement with the exact solution is well, whereas there is a slight discrepancy at about the frontal region for  $ka = 10$ .

**5.2 NACA 0012 Airfoil**

The electromagnetic scattering from the airfoil at zero angle of incidence is studied with a grid having 120x51 points as shown in Fig 6. The scattered electric field intensity  $E^z$  at time level  $t = 8\lambda$ ,  $\lambda$  is the dimensionless wavelength, is shown in Fig. 7.

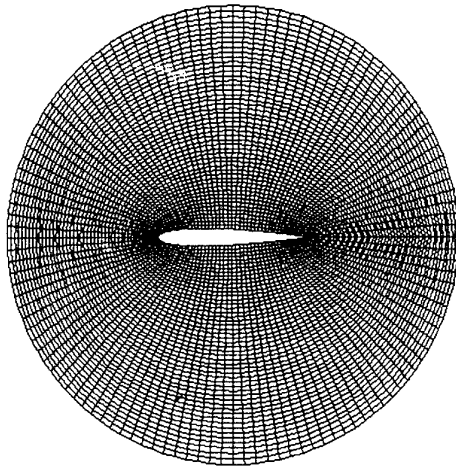


Figure 6. Grid about the NACA0012 airfoil, 120x51 points.



Figure 7. Scattered electric field intensity,  $E^z$ , about the NACA0012 airfoil.

The RCS obtained, via transforming the time domain to frequency domain, is shown in Fig.8.,

wherein the numerical results agree well with the solution given in Ref.3.

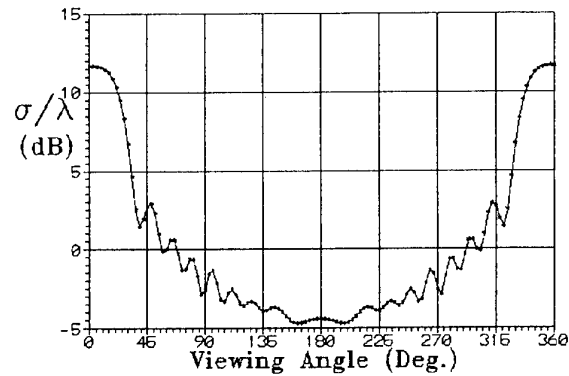


Figure 8. RCS for the NACA0012 airfoil,  $\lambda = 0.25$  chord.

**5.3 Helicopter Fuselage**

Finally, the electromagnetic scattering from an arbitrarily shaped fuselage is studied with the code developed here. At the same time, aerodynamic characteristics of the fuselage is also

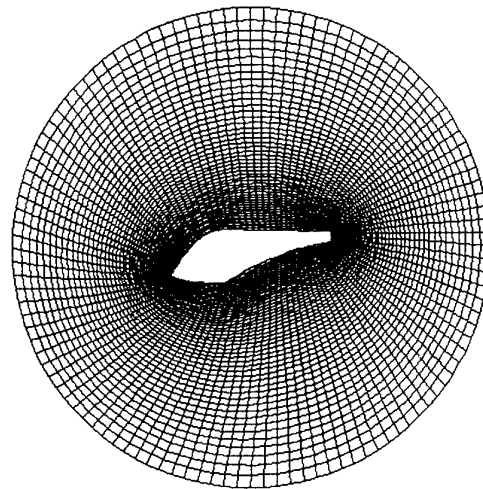


Figure 9. Grid about the generic helicopter fuselage, 112x51 points.

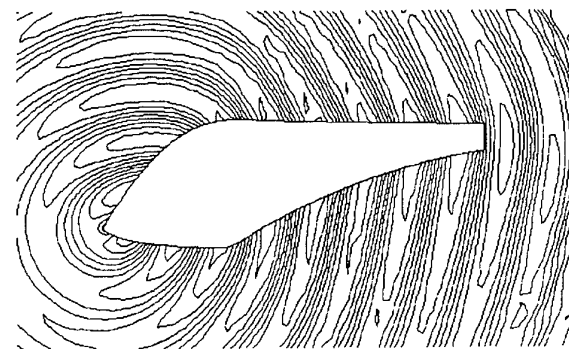


Figure 10. Scattered electric field intensity,  $E^z$ , about the helicopter fuselage.

studied to shape the body for low radar signature. The grid used in this study has 112x51 points to discretize the domain as shown in Fig. 9. Shown on Fig. 10 is the scattered electric field intensity at dimensionless time level  $t = 8\lambda$ . The corresponding radar cross section is shown in Fig. 11. To lower the RCS values, the fuselage is modified from round fronted shape to a sharp fronted shape as shown in Fig. 12. The comparison between the round and sharp fronted fuselage in terms of the RCS values, is also given in Fig. 11., where the lowering in the RCS values are in the order of 10 dB's.

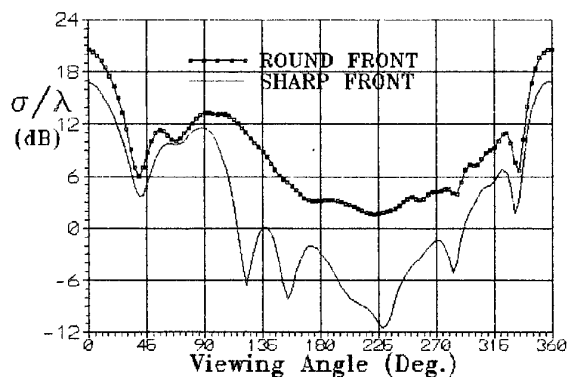


Figure 11. RCS values for the round and sharp fronted helicopter fuselage.

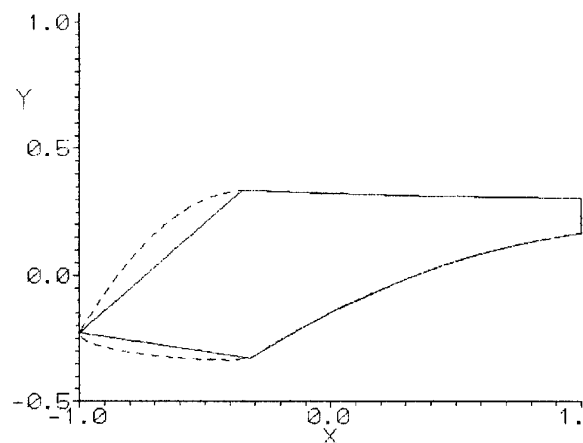


Figure 12. Geometries of the round and sharp fronted helicopter fuselage.

For comparison purposes, the electric field intensity near the sharp fronted fuselage is shown in Fig. 13. at again time level  $t = 8\lambda$ . When compared with Fig. 10., the flattening of the scattered waves because of the flat lines are apparent.

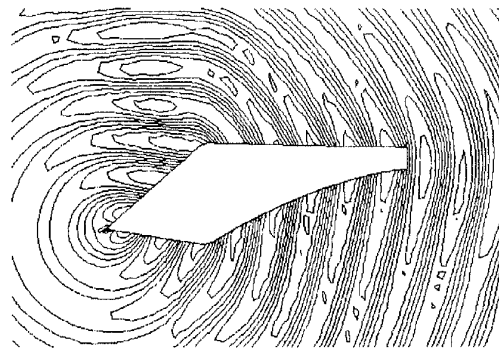


Figure 13. Scattered electric field intensity,  $E^z$ , about the sharp fronted helicopter fuselage.

For all studies the time step  $\Delta t$  is chosen in such a way that the maximum CFL number is unity.

In solving the Maxwell equations, the CPU time elapsed per time step per grid point is  $3 \times 10^{-5}$  s on the Pentium 100. The overall time consumed for calculating RCS is about 15 minutes starting from scratch.

Shown on Fig. 14 is the 3-D surface and the grid at the plane of symmetry generated for three dimensional viscous flow solution about the round fronted fuselage. The drag coefficient calculated for this round fronted fuselage geometry is  $C_d = 0.2$ , (Ref.13).

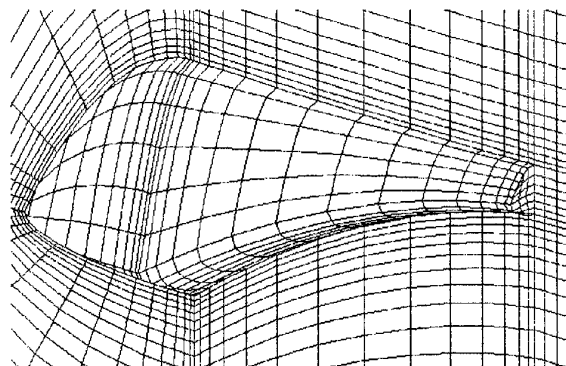


Figure 14. 3-D grid about the generic helicopter fuselage.

## 6. CONCLUSIONS

Lax-Wendroff scheme is applied to solution of Maxwell's equation for solving the electromagnetic scattering about arbitrarily shaped 2-D

objects. The solution is used to predict the radar cross section of the scatterer. The results obtained compare well with the known solutions in open literature. The code is also used in aerodynamic shaping of an helicopter fuselage for low signature.

### ACKNOWLEDGMENT

This work is partially supported by İTÜ Research Fund. The authors are greatly indebted to Prof. S. Edis for his invaluable help in getting the fund.

### REFERENCES

1. Hitzel, S.M., "Aerodynamics and Radar Signature: A Combination of Theoretical Methods", *J.Aircraft*, 25, 5, May 1988, pp.399-404.
2. Umashankar, K., and Taflove, A., "A Novel Method to Analyze Electromagnetic Scattering of Complex Objects", *IEEE Transactions of Electromagnetic Compatibility, EMC-24*, 4, November 1982, pp.397-405.
3. Vinh, H., van Dam, C.P., and Dwyer, H.A., "Airfoil Shaping for Reduced Radar Cross Section", *J.Aircraft*, 31, 4, July-Aug. 1994, pp.787-793.
4. Shankar, V., Hall, W.F., and Mohamadian, A., "A Time Domain Differential Solver for Electromagnetic Scattering Problems", *Proc. IEEE.*, 77, 5, May 1989, pp.709-721.
5. Morgan, K., Hassan, O., and Peraire, J., "The Solution of Maxwell's Equations in The Time Domain using Unstructured Grids", in "Proceedings of the 8th International Conference on Numerical Methods in Laminar and Turbulent Flows", Swansea, U.K., July 1993, pp.1382-1393.
6. Ruck, G.T., Barrick, D.E., Stuart, W.D., and Krichbaum, C.K., "Radar Cross Section Handbook, 1 and 2", New York, NY, Plenum, 1970.
7. Senior, T.B.A., and Uslenghi, P.L.E., "The Circular Cylinder", *Electromagnetic and Acoustic Scattering by Simple Shapes*, Bowmann, J.J, Senior, T.B.A., and Uslenghi, P.L.E. (Eds.), John Wiley and Sons, 1969, pp.95-128.
8. Balanis, C.A., "Advanced Engineering Electromagnetics", John Wiley and Sons, New York, 1989.
9. Hoffman, J., "Numerical Methods for Scientists and Engineers", Mc-Graw Hill, New York, 1993.
10. Mur, G., "Absorbing Boundary Conditions for the Finite-Difference Approximations of the Time Domain Electromagnetic-Field Equations", *IEEE Transactions of Electromagnetic Compatibility, EMC-23*, 4, November 1981, pp.377-382.
11. Press, W.H., Flannery, B.P., Teukolsky, S.A., and Vetterling, W.T., "Numerical Recipes: The Art of Scientific Computing", Cambridge, Cambridge University Press, 1992.
12. Hildebrand, F.B., "Advanced Calculus for Applications", New Jersey, Prentice Hall, 1962.
13. Aslan, A.R., Gülçat, Ü., and Mısırlıoğlu, A., "A PCG/E-B-E Iteration for High Order and Fast Solution of 3-D Navier-Stokes", in "Progress and Challenges in CFD Methods and Algorithms", AGARD CP 578, October 1995, Paper 19.

## DISCUSSION

**Discussor's name:** H. SCHIPPERS

**Comment/Question:**

Can you explain differences in RCS values for the round and sharp fronted helicopter fuselage when illuminated on the rear (fig. 11, viewing angle  $0^\circ$  and  $360^\circ$ )?

**Author/Presenter's reply:**

The difference comes from numerical results and may be due to the integral effect of the whole surface.

**Discussor's name:** G. BROWN

**Comment/Question:**

Please explain your use of the time coordinate in terms of the electromagnetic wavelength. Is this a scaling?

**Author/Presenter's reply:**

The time coordinate is expressed in terms of the non-dimensional wavelength which is scaled with characteristic length (radius or chord length).

## AN ADVANCED NUMERICAL SCHEME FOR COMPUTATIONAL ELECTROMAGNETICS

J.G. Gallagher  
T.E. Hodgetts  
C.C. Lytton  
M.T. Arthur  
I.D. King  
Defence Research Agency  
St. Andrew's Road  
Malvern, Worcs.  
WR14 3PS, United Kingdom

### SUMMARY

Computational electromagnetics and computational fluid dynamics have evolved as independent areas of numerical analysis, but the equations which are solved in these two areas are fundamentally similar. It therefore seems plausible that methods developed in one area should also be applicable to the other, with possible savings of time and computer resources. This paper describes a test of this idea: a general method originally developed for aerodynamic calculations by specialists at the Farnborough site of the Defence Research Agency (DRA) is now being adapted for electromagnetic calculations, with the collaboration of specialists at the DRA's Malvern site. The preliminary results are very encouraging.

### INTRODUCTION

The work described here was undertaken because of a desire to find a radically different method of solving electromagnetic scattering problems numerically. Apart from quasi-optical techniques at high frequencies, the usual methods of computational electromagnetics (CEM) for scattering bodies are all variations of the so-called "method of moments" (described below). This method has had many successful applications at DRA Malvern and elsewhere, but it also has inherent disadvantages, particularly when the scatterer is large compared to the wavelength, but not so large or so simple in shape that quasi-optical techniques can be used. This intermediate size range has been recognised as difficult ever since the method of moments came into common use in the early 1970s (see [1], e.g.), which is why a radical alternative method has been wanted.

The DRA has established a project to study whether such an alternative can be provided by adapting the methods of computational fluid dynamics (CFD) used by researchers at DRA Farnborough. We have focused our attention on one of these methods, the cell-vertex method described by Hall [2], which is being progressively modified and re-programmed by one of us (C.C.L.). Before describing the Hall-Lytton method

in detail, we give an overview of it in relation to the method of moments.

### OVERVIEW

The method of moments, as applied to scattering problems, essentially consists of formulating an integral equation which expresses the scattered field in terms of the currents induced on (or in) the scatterer by the incident field. The scatterer is then divided into "finite elements" of its surface or volume which are small in relation to the wavelength of the field; using these, the integral in the equation may be reduced reasonably accurately to a weighted sum over the unknown currents in the elements. Maxwell's equations are linear, and so are the boundary conditions on the surface of the scatterer; so the unknown currents (or parameters specifying them) are found to satisfy a set of simultaneous linear equations, given by the weighted sum's value under various conditions.

As mentioned above, this method has disadvantages when the scatterer is large compared to the wavelength. No finite element may be larger in any dimension than some modest fraction of the wavelength (typically 1/8), so the number of elements required to cover a scatterer's surface is inversely proportional to the square of the wavelength or proportional to the square of the frequency. It is usually found that every unknown current significantly affects all the simultaneous linear equations; so their matrix of coefficients is both very large (in proportion to the square of the number of finite elements, which is itself proportional to the square of the scatterer's size in wavelengths) and very time-consuming to invert or factorise (in proportion to the cube of the number of elements and so to the sixth power of the frequency). If the scatterer is penetrated by the incident field, the finite elements may have to fill its volume as well as covering its surface, and their number is even greater. Another problem is that the method of moments is essentially applied to one frequency at a time, so a scatterer's response to a broad-band radar (e.g.) can only be determined by repeating the entire calculation for many closely-spaced single frequencies. It is true

that the incident field appears only on the right-hand side of the simultaneous linear equations, so that at one frequency a scatterer can be analysed from many angular viewpoints with one matrix inversion or factorisation; but this is not always very useful, because it frequently happens that the response at or near one angular viewpoint (such as head-on) is much more important than the response at any other angle.

The Hall-Lytton method, in contrast to the finite elements of the method of moments, uses finite differences, operating directly with Maxwell's partial differential equations for the components of the electromagnetic field; these are calculated on a grid (or mesh, or array) of points in space with stepping in time. Since the method uses time-stepping rather than working with a specified frequency, it is directly suited to calculating a scatterer's response to broad-band or pulsed transmissions; and since finite-difference methods work by propagating changes from each grid point to and from its neighbours at each step, we do not have to manipulate a matrix representing the interaction of every point with every other point. The total amount of computation still depends strongly on the highest significant frequency of excitation through its effect on the spacing and step size required for stability, but the growth rate is proportional to the fourth or fifth power of the frequency instead of the sixth.

The use of finite differences directly in Maxwell's equations is not an original idea in itself; simple algorithms on Cartesian grids have been studied at least since the work by Yee [3] in 1966. However, to make the idea competitive with the method of moments, three things are necessary: (i) a good finite-difference algorithm (accurate, self-consistent and stable); (ii) a good grid (well-conformed to the scatterer's irregularities, and spaced more finely where the field components are changing rapidly); and (iii) a good outer boundary condition (to prevent spurious reflections from the outside edges or surfaces of the grid, so that a pure outgoing field is obtained). Each of these requirements (and particularly the third) has attracted much attention, and the literature is now vast, with new papers almost every month in such journals as *IEEE Transactions MTT* and *Microwave Letters*; but most publications describe their authors' *ad hoc* inventions for particular problems. In contrast, we present a universal algorithm, applicable to a whole family of partial differential equations, and already extensively tested in aerodynamic applications; our methods of generating conforming grids have been tested in the same way (although we do not discuss them in detail). Designing finite-difference algorithms and grid generators is a branch of numerical analysis, which is a complex and specialised mathematical art; the well-known book *Numerical Recipes* [4] has done

much to popularise its techniques, but also gives many illustrations of its hidden dangers. We think, therefore, that by adapting well-tested general methods rather than inventing new special ones, we have chosen the better way.

We now begin to describe what the Hall-Lytton method is.

#### ADVANCED NUMERICAL SCHEME; OUTLINE

The heart of Hall's method for CFD is an algorithm for treating an equation of the general form

$$\frac{\partial U}{\partial t} = - \left( \frac{\partial F}{\partial x} + \frac{\partial G}{\partial y} + S \right) \quad (1)$$

where  $U$ ,  $F$  and  $G$  are column vectors of dependent variables, which may have functional equations (but not other differential equations) relating them, and  $S$  is a column vector of source terms (which may vanish). (The equation is written in its original two-dimensional form from [2]; a term  $(\partial H/\partial z)$  may be added in three dimensions.) The space derivatives in this equation can be used to express a vector curl or divergence; so, since Maxwell's equations all take the form of a curl or a divergence equated to a first-order time derivative (sometimes added to a source term), they can all be put in the form (1).

This method, as remarked earlier, works directly with the fundamental first-order differential equations of electromagnetics or fluid dynamics. That is to say, we do not need to use any of the conventional transformations into higher-order equations satisfied by potential functions (in CEM) or stream functions (in CFD), nor does it matter whether such transformations would give a scalar problem (depending on only one potential or stream function) or a vector problem (depending on two or more such functions). The use of first-order equations is generally agreed to give better stability, and greater freedom from spurious solutions which finite-differencing may create. It also allows greater flexibility; separating the two principal electromagnetic polarisations is not necessary in principle, although doing so may still be convenient in practice. (In fact, we have done so for our two-dimensional tests, to reduce the number of independent variables; this point will be mentioned again later.) Moreover, the interface boundary conditions are given directly in terms of field components rather than in terms of potential functions; and this is also true of the constitutive relations which define the permeability, permittivity and conductivity of material media (which require particularly careful treatment in time-domain analysis, unless the properties of all the media are independent of the frequency).

## ADVANCED NUMERICAL SCHEME; DETAILS

We solve eqn.(1) numerically in the following way (Hall [2]); this description is given for one component in the column vectors  $U$ ,  $F$ ,  $G$  and  $S$ , but the extension to several components is immediate (likewise the extension if the additional term  $(\partial H/\partial z)$  is present).

Suppose we have calculated the values after  $n$  time steps, and we now wish to proceed to the  $(n+1)$ -th step; then, by Taylor's theorem

$$\delta U = \left( \frac{\partial U}{\partial t} \right)^{(n)} \delta t + \frac{1}{2} \left( \frac{\partial}{\partial t} \left( \frac{\partial U}{\partial t} \right) \right)^{(n)} (\delta t)^2 \quad (2a)$$

to the second order, where  $\delta U = U^{(n+1)} - U^{(n)}$  and  $\delta t = t^{(n+1)} - t^{(n)}$ . On substituting into eqn.(2a) from eqn.(1) and interchanging orders of differentiation, we get

$$\delta U = - \left[ \frac{\partial F}{\partial x} + \frac{\partial G}{\partial y} + S \right]^{(n)} \delta t - \frac{1}{2} \left[ \frac{\partial}{\partial x} \left\{ \frac{\partial F}{\partial U} \cdot \frac{\partial U}{\partial t} \right\} + \frac{\partial}{\partial y} \left\{ \frac{\partial G}{\partial U} \cdot \frac{\partial U}{\partial t} \right\} + \left\{ \frac{\partial S}{\partial U} \cdot \frac{\partial U}{\partial t} \right\} \right]^{(n)} (\delta t)^2 \quad (2b)$$

where the terms like  $(\partial F/\partial U)$  and  $(\partial U/\partial t)$  are in general square matrices and column vectors, respectively. Now,  $U$  is defined at the nodes of a grid, and the grid may also be considered to be made up of cells, each cell being defined by four nodes like  $A$ ,  $B$ ,  $C$ ,  $D$  (see the Figure page). We may calculate the functions  $F$  and  $G$  at the node corners of a cell, and then apply Gauss' theorem to the cell, giving

$$\iint \left\{ \frac{\partial F}{\partial x} + \frac{\partial G}{\partial y} \right\}^{(n)} ds = \oint \left( F \hat{n}_x + G \hat{n}_y \right)^{(n)} \cdot d\mathbf{l} \quad (3)$$

where  $\hat{n}_x$  and  $\hat{n}_y$  are unit normal vectors, and their dot product is taken with the differential vector  $d\mathbf{l}$ . The right-hand side of eqn.(3) may be evaluated using the trapezium rule; this has second-order relative error, but we are using it to calculate a first-order correction in eqn.(2b), so the absolute error is third-order. On dividing this right-hand side by the cell's area (the

integral over  $(ds)$ , for which also we use the trapezium rule), we have the value of

$$-\left\{ \frac{\partial F}{\partial x} + \frac{\partial G}{\partial y} \right\}^{(n)} \quad (4)$$

at the centroid of the cell  $ABCD$  (the point 1 in the Figure); and the first-order change in  $U$ ,  $\Delta U$ , is obtained by subtracting  $S$  from this and then multiplying the result by  $(\delta t)$ , as is obvious from eqn.(2b). However, this first-order change is referred to the wrong place — a cell's centroid, instead of a node (cell's vertex). We remove this difficulty by noting that each node is itself the centroid of four cells' centroids (thus,  $C$  is the centroid of 1, 2, 3, 4 in the Figure); so we take  $\Delta U$  at  $C$  to be the weighted mean of  $\Delta U$  at 1, 2, 3, 4, with the weightings being the areas of the cells containing each of the four points 1, 2, 3, 4. This weighting was shown by Hall [2] to give better stability when the cells vary markedly in size, which is likely to happen in our electromagnetic problems; we remarked in the "Overview" on the importance of a well-conformed and spaced grid when attempting to follow accurately the surface of an irregular scatterer.

To complete the calculation of  $\delta U$  in eqn.(2b), we need to determine the factor multiplying  $(\delta t)^2$ . We note first that in this factor  $(\partial U/\partial t)$  may be replaced by  $(\Delta U/\delta t)$ , since we require only first-order relative accuracy. It is then trivial to evaluate the second-order contributions due to  $S$  (involving  $(\partial S/\partial U)$ ). To treat the other two terms in the square brackets multiplying  $(\delta t)^2$ , we write them as

$$\left[ \frac{\partial}{\partial x} \left\{ \frac{\partial F}{\partial U} \cdot \Delta U \right\} + \frac{\partial}{\partial y} \left\{ \frac{\partial G}{\partial U} \cdot \Delta U \right\} \right]^{(n)} (\delta t)^{-1} \quad (5)$$

and we calculate the expressions in brackets at the centroids of the cells to first-order relative accuracy, which is done by taking the mean of the values at each centroid's four neighbouring nodes; then we again apply Gauss' theorem (in the form of eqn.(3)) to a dual cell like the one shown in dotted lines in the Figure — defined by four centroids instead of four nodes — to obtain the second-order part of  $\delta U$  at the node enclosed by the dual cell. When the first-order and second-order changes have thus been calculated for every node, the values of  $U$  at the nodes are updated; and the  $(n+1)$ -th time step is complete. (The choice of time step is governed by the conventional Courant-Friedrichs-Levy criterion.)

A summary of the process is included in the Figure.

## APPLICATION TO MAXWELL'S EQUATIONS

The components of the vectors  $U$ ,  $F$ ,  $G$  and  $S$  can be taken as the conventional components of the three-dimensional field vectors  $\underline{E}$ ,  $\underline{H}$ ,  $\underline{B}$  and  $\underline{D}$ . In the most general case there are eight scalar partial differential equations relating these (three from each Maxwellian curl equation and one from each divergence equation), but whenever a simplification is supplied by theoretical considerations it can be incorporated into the computer programming, because of the generality of eqn.(1). Such simplifications include the standard linear relationships between  $\underline{B}$  and  $\underline{H}$  and between  $\underline{D}$  and  $\underline{E}$  (with the current density  $\underline{J}$  included, if a conducting medium is present); these relationships require modification if the excitation covers a broad frequency band, because the parameters of a medium with conductivity or hysteresis depend on the frequency, but we shall not discuss this problem as it is common to all time-domain methods. As remarked earlier, we have also used in our numerical experiments the convenient fact that in two dimensions the eight scalar Maxwellian equations separate into two independent sets of four, one for each polarisation (at least when all media are isotropic; e.g. Jones [5]); again, there is nothing about this separation which is special to our method. There are, however, special features of the grid and its boundaries, and we outline these next.

## GRIDS AND BOUNDARY CONDITIONS

Nothing in the mathematics which has been presented so far requires the edges of any cell (or its walls, in three dimensions) to be aligned with any particular direction; on the Figure page, we can take the  $x$ -variable in eqn.(1) as horizontally-directed and the  $y$ -variable as vertically-directed, while the grid is represented as not even straight-edged, much less perpendicular. Our algorithm can therefore be used with a separate conforming grid generator, since there are no built-in assumptions about the grid except the obvious implication that it is sufficiently fine to follow all necessary detail; it need not be everywhere orthogonal, for instance. The separate generator can be one proven in aerodynamic applications, since there are no requirements fundamentally different from the electromagnetic case; in both cases we wish to cover a surface or surfaces and to divide up the volume around and between the surfaces. In both cases also, the surface-specific boundary conditions take the form of tangential and normal conditions at the surfaces, and again there is no fundamental difference; although when an element of  $U$  is to be continuous through a surface, it is convenient if the cells which actually touch the surface are orthogonal to it. Even singular points or lines do not create any fundamental distinctions, since both in aerodynamics and electromagnetics the possible singularities must satisfy

requirements of finite energy. In fact, the only important difference between the two cases is the treatment of the outer boundary of the grid, which is our next topic.

## TREATMENT OF THE OUTER BOUNDARY

The computational treatment of the outer boundary of a finite-difference grid has been an extremely fashionable subject since Berenger [6] described his "Perfectly-Matched Layer" in 1994, and we intend to contribute to the literature in due course. For the moment, we shall merely say that we are implementing the variant of Berenger's hypothetical material which was described by Sacks *et al.* [7], because the "splitting" of Maxwell's equations introduced by Berenger is an inconvenience in applying our general algorithm (eqn.(1)), and also complicates the separation of the polarisations for testing purposes (which is already complicated because these materials are anisotropic). Sacks' type of material is also more convenient for constructing an outer boundary without corners, which is more natural for use with an algorithm based on the flow patterns around aerofoils.

## PROGRESS AND PRELIMINARY RESULTS

The work described above is far from being fully implemented. In particular, our implementation of the outer-boundary layer is incomplete, so our numerical experiments have been largely confined to tests of the propagation of a sinusoidal pulse from the front to the back of simple scattering objects; these tests do not continue for enough time steps for reflections from the outer boundary to corrupt the results. In spite of this restriction, comparisons of these tests with theoretical predictions of the response to an infinite sinusoid have given very encouraging preliminary results. As a sample of our algorithm's behaviour, we present two graphs (Graph 1 and Graph 2) showing a comparison between results from two sizes of two-dimensional grid, one with half the spacing of the other, and theoretical predictions. These graphs exhibit the response of an infinite circular lossless dielectric cylinder, with relative permittivity 2.56 and relative permeability 1, to a transverse electric (TE) sinusoid whose frequency is such that the circumference of the cylinder is 5 free-space wavelengths (chosen as a resonance condition). The horizontal co-ordinate of the graphs is angle in degrees, measured around the cylinder from the line of normal incidence ( $0^\circ$ ); the vertical co-ordinates are amplitude relative to unit excitation (Graph 1) and phase in degrees (Graph 2). The two sets of grid results are plotted continuously; the predictions are plotted as individual points at intervals of  $6^\circ$  around the cylinder.

Further progress will be described at the conference.

## ACKNOWLEDGEMENTS

We gratefully acknowledge the work of Dr. C.R. Brewitt-Taylor of DRA Malvern, whose analysis and computer program [8] (based on the theory described by Stratton [9]) provided the theoretical predictions.

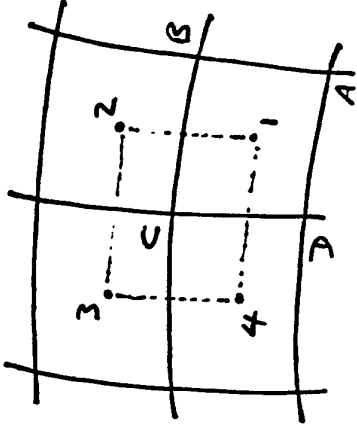
© British Crown Copyright 1996 /DERA

Published with the permission of the Controller of Her Britannic Majesty's Stationery Office.

## REFERENCES

1. Mittra, R. (ed.), "Numerical and Asymptotic Techniques in Electromagnetics", New York and Berlin, Springer-Verlag, 1975.
2. Hall, M.G., "Cell-Vertex Multigrid Schemes for Solution of the Euler Equations", Royal Aircraft Establishment Tech. Memo. AERO 2029, 1985.
3. Yee, K.S., "Numerical Solution of Initial Boundary Value Problems Involving Maxwell's Equations in Isotropic Media", IEEE Trans. Antennas and Propagation, *AP-14*, 1966, pp 302-306.
4. Press, W.H., Flannery, B.P., Teukolsky, S.A. and Vetterling, W.T., "Numerical Recipes: The Art of Scientific Computing", Cambridge and New York, Cambridge University Press, 1986 (and later editions).
5. Jones, D.S., "The Theory of Electromagnetism" (International Series of Monographs on Pure and Applied Mathematics, vol. 47), Oxford and New York, Pergamon Press, 1964.
6. Berenger, J.-P., "A Perfectly Matched Layer for the Absorption of Electromagnetic Waves", J. Comp. Physics, *114*, 1994, pp 185-200.
7. Sacks, Z.S., Kingsland, D.M., Lee, R. and Lee, J.-F., "A Perfectly Matched Anisotropic Absorber for Use as an Absorbing Boundary Condition", IEEE Trans. Antennas and Propagation, *AP-43*, 1995, pp 1460-1463.
8. Brewitt-Taylor, C.R., "Program MIESCAT: Scattering from Cylinders and Spheres", Defence Research Agency (Malvern) Radar Sensors and Techniques Divisional Memo. AD2-43/91, 1991.
9. Stratton, J.A., "Electromagnetic Theory" (International Series in Physics), New York and London, McGraw-Hill, 1941.

## MECHANICS OF CELL-VERTEX METHOD



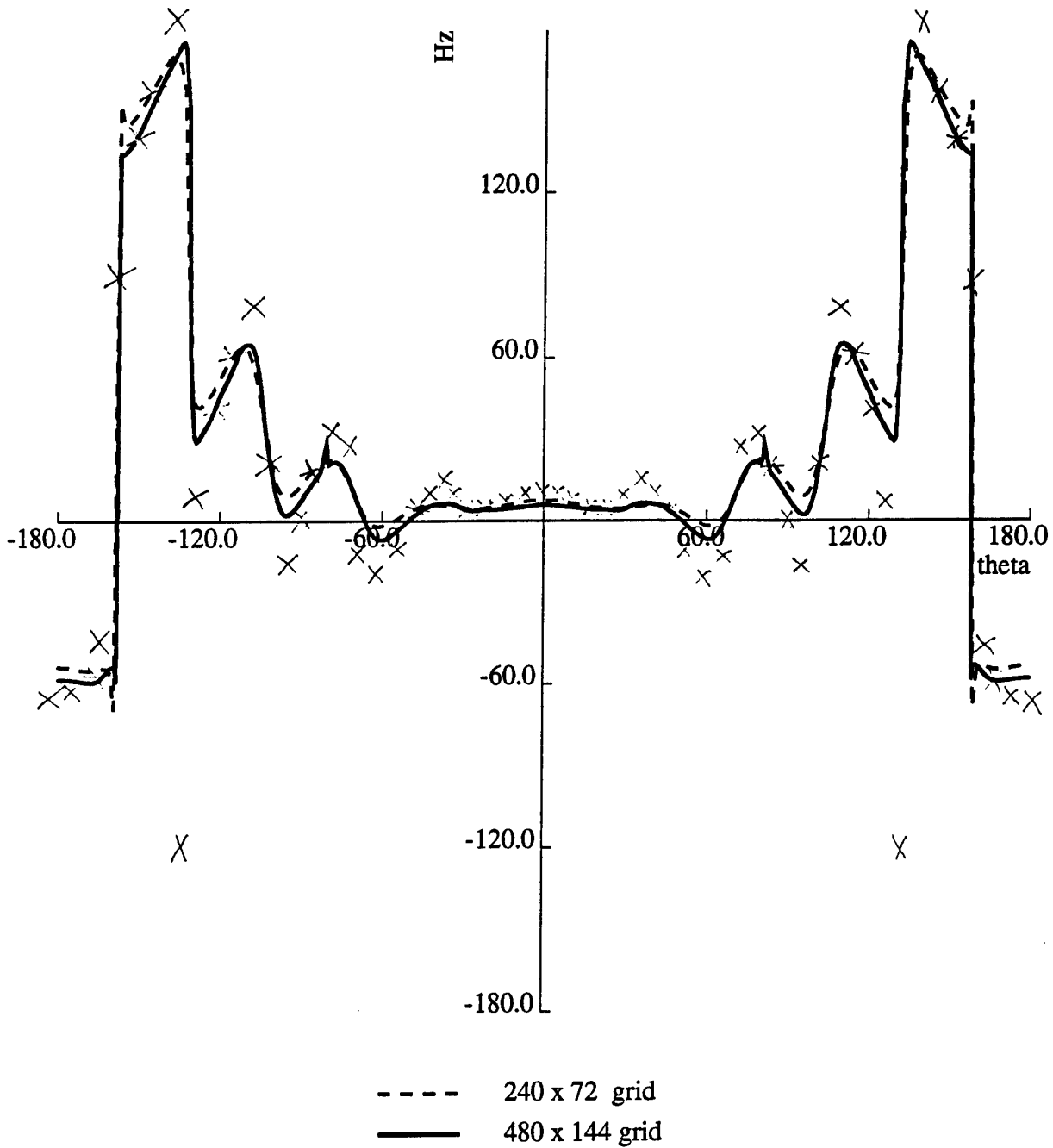
- U defined at grid nodes like A,B,C,D
  - Compute F, G at nodes, then apply Gauss' Theorem over cell ABCD:
- $$\iint \left( \frac{\partial F}{\partial x} + \frac{\partial G}{\partial y} \right) ds = \oint (F \hat{n}_x + G \hat{n}_y) \cdot d\mathbf{l}$$
- Right side can be evaluated approximately by trapezium rule
  - Left side yields approximation for first-order term  $\left( \frac{\partial F}{\partial x} + \frac{\partial G}{\partial y} \right)$  at centroid 1
  - The second-order divergence term can be written in terms of first-order flux increments known at cell centroids like 1,2,3,4. Apply Gauss' Theorem again over the dual cell 1234, of which node C is regarded as being the centroid, to get approximation for second-order term at node C



### Phase, total Hz field along cylinder surface

Circular Cylinder; TE mode;  $\mu = 1.0$ ,  $\epsilon = 2.56$ ;  $\beta = 0.0$ ,  $ka = 5$

#### Grid Refinement Comparison



Graph 2

**Discussor's name:** G. BROWN

**Comment/Question:**

Could you comment on how you will deal with sharp edges using your method?

**Author/Presenter's reply:**

You need to treat the node on the edge differently since it makes a triangular cell with the associated nodes, its neighbours. All other cells are still quadrilaterals. The application of Gauss' theorem is as valid for triangular cells as for quadrilateral cells. The change on the "edge" node is updated by several centroid nodes surrounding the "edge" node.

## Réfectivité RADAR d'une Cible Illuminée par une Onde Sphérique

P. Pouliguen - P. Gadenne - J.Y. Marty

CELAR  
BP 7419  
35174 Bruz Cedex  
France

### 1. RESUME

Cet article décrit une méthode théorique de calcul de la Surface Equivalente Radar (S.E.R.) d'une cible illuminée par une onde électromagnétique plane ou sphérique. La méthode est basée sur le formalisme intégral de STRATTON-CHU, simplifié par les hypothèses de l'Optique Physique. Développée et mise sous la forme du code de calcul SERMAIL par le CELAR, elle est utilisée en particulier pour contrôler la qualité des acquisitions dans la grande base de mesures de S.E.R. SOLANGE, dont les caractéristiques sont rappelées. Une comparaison des résultats théoriques et expérimentaux obtenus sur quelques cibles canoniques est également fournie.

### 2. INTRODUCTION

La maîtrise de signature, et de signature radar en particulier, est un domaine dans lequel l'armement s'est trouvé rapidement impliqué. En effet elle permet d'assurer une meilleure chance de succès aux missions de pénétration en territoire adverse et améliore la survie des matériels.

La maîtrise de signature radar nécessite :

- des études de réduction du niveau de SER (furtivité),
- une recherche de plus grande vraisemblance des systèmes de leurrage,
- une optimisation des systèmes de brouillage...

Les études d'efficacité des systèmes d'armes nécessitent par ailleurs le développement de moyens de simulation, numériques ou hybrides, pour lesquels la signature des matériels constitue un paramètre d'entrée.

Lors de la conception et du développement des matériels, il est donc nécessaire de disposer et mettre en œuvre des moyens capables de mesurer (bases de mesures, chambres anéchoïques, etc....) ou prédire (codes de calcul) la signature. Les résultats issus des mesures ou des calculs sont alors utilisés pour valider et améliorer les concepts retenus pour réaliser un matériel, ou pour en vérifier les performances. Ces résultats peuvent également être utilisés comme données d'entrées des simulations.

La mesure et le calcul de la SER constituent deux démarches complémentaires qui toutes deux présentent leurs mérites et faiblesses respectives.

La mesure permet d'évaluer un matériel réel, c'est à dire de prendre en compte l'ensemble des paramètres susceptibles de contribuer à sa signature.

Le calcul nécessite une description très fine de la cible. Certains paramètres, qui peuvent jouer un rôle non négligeable (fentes, brides, tolérances de fabrication, présence de matériaux divers ou d'équipements particuliers etc.....), sont difficiles à décrire ou parfois "oubliés".

Les bases de mesures sont généralement des moyens lourds dont le coût de développement et de mise en œuvre est important, surtout lorsque l'évaluation à réaliser porte sur de gros matériels (missiles, blindés, avions etc....).

Le développement et la mise en œuvre d'un code de calcul sont beaucoup moins onéreux d'autant que les machines auxquels ils font appel sont également utilisées à d'autres fins par les entreprises.

Les bases de mesures sont confrontées à un problème de précision de mesures, lié aux conditions expérimentales qui permettent rarement de réaliser les évaluations dans les conditions réelles d'emploi du matériel.

Les imprécisions concernent essentiellement le rayonnement et l'environnement.

Les problèmes de rayonnement tiennent au fait que les bases sont généralement trop courtes (quelques dizaines à quelques centaines de mètres) vis à vis de la dimension des cibles à évaluer (quelques mètres) : les conditions de planéité d'onde (critère de FRAUNHOFER) et d'homogénéité de champ ne sont pas respectées. Il peut en résulter des erreurs, qui dans certains cas peuvent être prohibitives (quelques dizaines de dB).

Ces erreurs peuvent être corrigées a posteriori mais les formules de correction ne sont pas toujours valables notamment lorsque les phénomènes physiques de rétrodiffusion sont multiples (association de réflexions, ondes rampantes et ondes guidées par exemple).

Il est également possible d'associer aux moyens de mesures des optiques de transformation de l'onde sphérique en onde plane (Compact-Ranges), mais le coût de réalisation et de possession de ces systèmes est très élevé.

Les problèmes d'environnement ont pour origine la présence de réflexions ou d'objets parasites dans le moyen de mesures.

Les réflexions parasites sont en général faibles ou quasi inexistantes dans les chambres anéchoïques. Elles sont plus difficiles à maîtriser pour les autres moyens où l'emploi d'aériens très performants constitue une démarche incontournable.

Les objets parasites concernent essentiellement l'ensemble des systèmes à mettre en œuvre pour orienter le matériel à tester (positionneurs, élingues etc....). Ici encore il existe des méthodes pour réduire la SER des positionneurs (mâts profilés) et/ou l'annuler. Mais ces méthodes ne sont qu'approximatives.

Le calcul n'est évidemment pas concerné par l'ensemble de ces défauts. Cependant, pour le calcul prédictif de la S.E.R. de matériels de grandes dimensions vis à vis de la longueur d'onde, l'emploi des méthodes dites "exactes" n'est actuellement guère envisageable car il nécessite des puissances de calcul considérables. Seules les méthodes asymptotiques hautes fréquences sont utilisables mais il en résulte une marge d'incertitude. Ces méthodes présentent cependant l'avantage de parfaitement décrire la physique des phénomènes.

Les systèmes de positionnement utilisés limitent en général le volume angulaire dans lequel la mesure d'une cible peut être réalisée. Cette contrainte n'affecte évidemment pas le calcul.

Enfin, pour terminer cette comparaison, une évidence : "la mesure nécessite la disponibilité et la présence du matériel... le calcul s'affranchit de cette contrainte".

Dans le cadre des missions qui lui sont confiées, le CELAR (Centre d'Electronique de L'Armement), établissement de la Délégation Générale pour l'Armement (DGA) situé près de RENNES en BRETAGNE, s'est beaucoup investi dans la mesure de la signature RADAR. A cette fin, il a développé et met en œuvre trois grandes bases qui permettent l'évaluation de tous types de matériels dont l'envergure n'excède pas 20 mètres et la masse 70 tonnes (missiles, blindés, avions etc....).

Parallèlement à ces moyens, le CELAR développe et dispose d'outils de modélisations prédictives. Cela lui permet d'assurer des prestations de grande qualité en utilisant précisément la complémentarité des deux démarches mesure/calcul notamment pour valider les résultats obtenus, qu'ils proviennent de la mesure ou qu'ils proviennent du calcul.

L'objet du présent article, après avoir présenté l'une des bases de mesures (SOLANGE), est de décrire un outil de modélisation (le code SERMAIL) et de fournir des résultats comparatifs obtenus sur des cibles simples compte tenu des effets de champ proche et de bistatisme.

### 3. PRESENTATION DE LA BASE SOLANGE DU CELAR

La base SOLANGE est l'un des trois moyens importants dont dispose le Centre d'Electronique de l'Armement pour réaliser des mesures de détectabilité de cibles. Cette base est plus particulièrement dédiée aux évaluations sur avions d'arme opérationnels ou gros missiles.

La base SOLANGE est constituée d'un ensemble de génie civil en béton comprenant une poutre horizontale {1} de 35 mètres de longueur reposant sur deux voiles {2} nervurés verticaux de 33 mètres de hauteur. Cette structure supportant le positionneur {3} de cibles est rigidifiée par un cylindre {4} de béton de 58 mètres de diamètre et 40 mètres de hauteur.

Au fond du cylindre, sur un mât vertical de 28 mètres de hauteur, est installée la plate-forme de mesure {5} dont l'altitude est variable. Le déplacement vertical de l'instrumentation permet ainsi de définir un angle de tir dans le plan vertical compris entre  $-10^\circ$  et  $+10^\circ$ .

Deux portes de 18 mètres de largeur et 33 mètres de hauteur chacune, entièrement tapissées de matériau absorbant, ainsi qu'un toit recouvrant la totalité de l'installation ferment entièrement la base. Le fait d'être totalement close assure à

la base SOLANGE une disponibilité tous temps ainsi qu'une grande discrétion vis à vis de l'extérieur.

Les deux grandes portes sont placées 26 mètres en arrière de la cible et leur ouverture motorisée permet de réaliser des mesures sur fond de ciel.

Le positionneur situé dans la poutre horizontale de la base est un dispositif électromécanique qui assure les fonctions de hissage et de mise en attitude de la cible face au senseur de mesure.

La fonction hissage est assurée par un treuil {8} (capacité 25 tonnes) qui déplace à la fois la cible (15 tonnes maximum) suspendue à des élingues en Kévlar et le système de mise en attitude lui-même. En situation de travail, le positionneur est verrouillé à l'intérieur de la poutre et l'aéronef est suspendu à 15 mètres du sol, à environ 53 mètres des aériens de la plate-forme de mesure {5}.

La mise en attitude angulaire de la cible est réalisée par des rotations de couronnes sur des plans horizontaux ou obliques avec les caractéristiques suivantes:

Angle	Limites	Précision
Roulis	0 à $30^\circ$	0,1°
Tangage	0 à $30^\circ$	0,1°
Lacet	360° en continu	0,01°

Les angles de roulis et de tangage sont des inclinaisons de prépositionnement de la cible qui tourne sur elle-même en continu autour d'un axe vertical (ou incliné) à une vitesse réglable entre 1 tour en 2 heures et 1 tour en 1 minute.

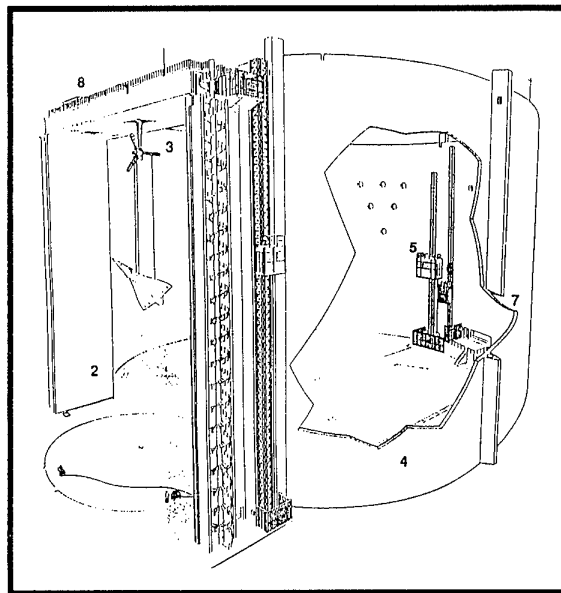


Figure 1 : Schéma écorché de la base SOLANGE (Avant qu'elle ne soit complètement fermée)

Le déclenchement des mesures est généralement asservi à l'information renvoyée par le codeur de lacet du positionneur; toutefois, lorsqu'une très grande précision est requise dans le positionnement de la cible (mesures de Surfaces Equivalentes Laser en particulier) un système d'interférométrie Laser baptisé SOFIA est mis en œuvre. Ce système permet de connaître à tout moment la position de la cible avec une précision en gisement de  $0,01^\circ$  et une précision en distance de 0,5 mm.

La base SOLANGE autorise différents types de mesures, parmi lesquelles on peut citer les :

- > Mesures de Surfaces Equivalentes Radar (SER)
- > Mesures de Surfaces Equivalentes Laser (SEL)
- > Mesures de diagrammes d'antennes sur porteurs
- > Evaluations de fusées de proximité en phase finale

Actuellement, les mesures de SER représentent la partie la plus importante de l'activité de la base. Ces mesures sont réalisées grâce à une chaîne de mesures cohérente appelée SAFARI (Système d'Analyse en Fréquence Automatique et Rapide pour Imagerie). Cette dernière a été conçue et réalisée par le CELAR; ses performances sont liées à l'utilisation de synthétiseurs à commutation rapide (rampe de 512 fréquences acquise en 3 millisecondes) et large bande permettant de travailler en synthèse directe entre 1 et 18 GHz.

Les acquisitions peuvent être réalisées en mode CW ou découpé, avec un angle de bistatisme dans le plan vertical compris entre 0° et 26° entre les antennes d'émission et de réception (sans déplacement longitudinal de celles ci).

Les quelques chiffres présentés ci-dessous synthétisent les principales caractéristiques des mesures de SER que l'on peut obtenir sur la base :

*Bande de Fréquences :* 1 à 18 GHz  
(extensions prévues entre 100 MHz et 1 GHz et vers les bandes millimétriques)

*Méthodes de mesures :* Réponses Impulsionnelles  
Diagrammes de SER  
Images bidimensionnelles ISAR

*Sensibilité standard:* Mode diagramme: -40 dBm<sup>2</sup>  
Mode imagerie: -70 dBm<sup>2</sup>

*Résolution typique des images:* 5 x 5 cm<sup>2</sup>

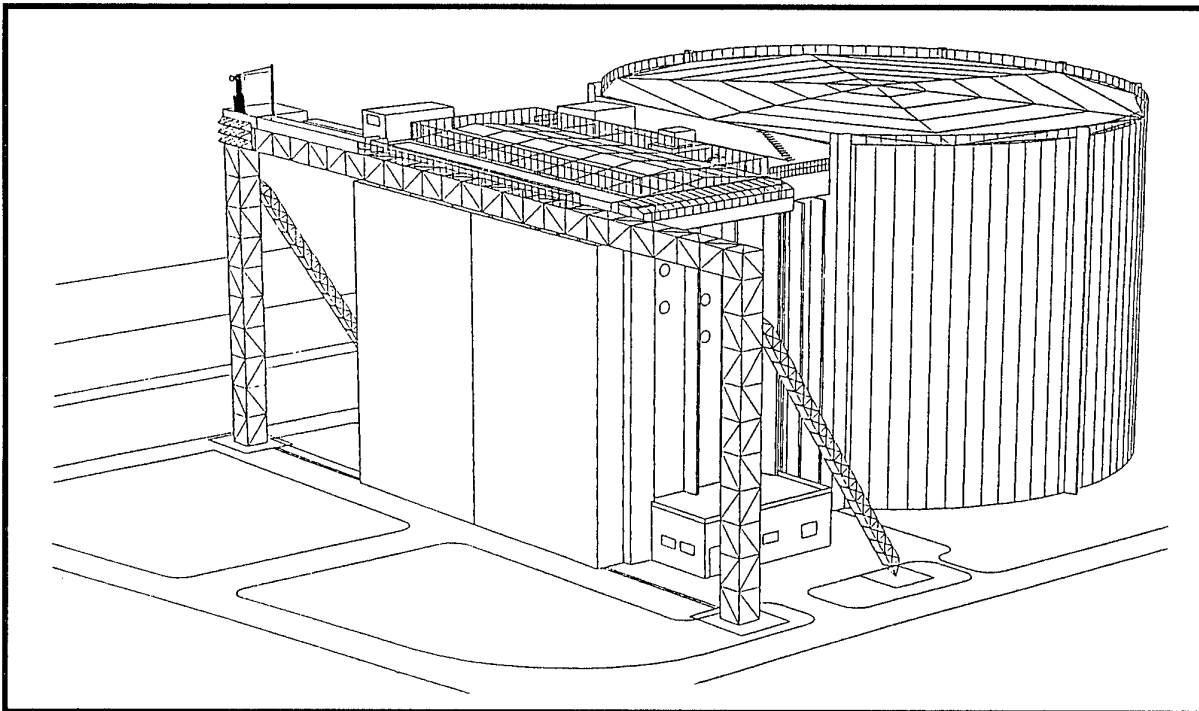


Figure 2 : Vue générale de la base SOLANGE

#### 4. LE CODE SERMAIL

Le CELAR développe un outil de calcul (SERMAIL) permettant d'évaluer la réflectivité Radar d'une cible dans les conditions représentatives des mesures en bases d'essais, c'est à dire en configurations de champs proche et lointain, monostatique et bistatique.

Dans la version actuelle de SERMAIL, les phénomènes physiques modélisés comprennent :

- les réflexions jusqu'au second ordre dont la méthode de calcul est basée sur l'intégration directe des formules intégrales de STRATTON-CHU dans lesquelles les courants surfaciques sont approximés par les courants de l'Optique Géométrique. Il s'agit donc d'une méthode entièrement fondée sur l'Optique Physique (O.P.). Le fait d'intégrer directement le formalisme de STRATTON-CHU sans approximation sur la distance permet l'évaluation du champ rayonné en zone proche.
- les diffractions du premier ordre par les arêtes, calculées selon le formalisme des courants équivalents de MITZNER.

La description géométrique de la cible s'effectue à l'aide de fichiers CAO générés par le mailleur I-DEAS. Les mailleurs sont des triangles isocèles dont la dimension des arêtes doit être égale à environ  $\lambda/3$  ( $\lambda$  étant la longueur d'onde) ; ce critère est imposé par la méthode de calcul pour une bonne restitution de la phase du champ rerayonné par la cible.

#### 4.1. Méthodes d'étude théoriques

##### 4.1.1. Equations intégrales des champs

La figure 3 présente la configuration générale de la diffraction par un obstacle de surface  $\Sigma$  ( $\Sigma=S+S_0$ ) dont le centre O, choisi arbitrairement comme origine des phases, est situé à la distance E d'un émetteur localisé au point Q et à la distance R d'un récepteur placé au point d'observation P. L'élément de surface  $ds$  de normale  $\hat{n}$ , appartenant à la surface illuminée S de l'objet, reçoit un champ incident  $(\vec{E}_i; \vec{H}_i)$  de direction  $\hat{e}$  et rayonne un champ  $(\vec{E}_R; \vec{H}_R)$  dans la direction  $\hat{r}$ . La surface  $S_0$  représente la zone d'ombre de l'objet.

Une solution exacte de ce problème a été formulée par STRATTON et CHU [1], sous forme d'équations intégrales, en appliquant l'analogie vectoriel du théorème de GREEN aux équations de MAXWELL. En considérant une dépendance temporelle en  $e^{-j\omega t}$ , les équations intégrales de STRATTON et CHU s'écrivent en fonction du champ total  $(\vec{E}; \vec{H})$  sur la surface  $\Sigma$  de l'obstacle :

$$\vec{E}_R(P) = \frac{1}{4\pi} \iint_{\Sigma} \left\{ j\omega\mu(\hat{n}\wedge\vec{H})\phi + (\hat{n}\wedge\vec{E})\wedge\nabla'\phi + (\hat{n}\cdot\vec{E})\nabla'\phi \right\} d\Sigma \quad (1)$$

$$\vec{H}_R(P) = \frac{1}{4\pi} \iint_{\Sigma} \left\{ -j\omega\epsilon(\hat{n}\wedge\vec{E})\phi + (\hat{n}\wedge\vec{H})\wedge\nabla'\phi + (\hat{n}\cdot\vec{H})\nabla'\phi \right\} d\Sigma \quad (2)$$

avec :

$$\vec{E} = \vec{E}_i + \vec{E}_R \quad \text{et} \quad \vec{H} = \vec{H}_i + \vec{H}_R$$

Dans ces expressions  $\mu$  et  $\epsilon$  désignent respectivement la perméabilité (H/m) et la permittivité (F/m) du milieu de propagation.

$\nabla'\phi$  désigne le gradient de  $\phi$  par rapport à la variable P' sur la surface S.

$$\phi \text{ est la fonction de GREEN : } \phi = \frac{e^{jk|\vec{r}'|}}{|\vec{r}'|} \quad \text{et} \quad |\vec{r}'| = |\vec{R} - \vec{R}'|$$

##### 4.1.2. L'Optique Physique

Les équations intégrales (1) (2) n'ont généralement pas de solution analytique. L'Optique Physique (O.P.) facilite leur résolution à l'aide de trois hypothèses simplificatrices :

1) *Les dimensions de la cible sont très supérieures à la longueur d'onde (hypothèse de haute fréquence).* Les courants décroissent alors très rapidement dans la zone d'ombre et on les considère nuls sur la surface  $S_0$  non directement illuminée par l'onde incidente.

2) *Les rayons de courbure de la surface directement illuminée sont très supérieurs à la longueur d'onde.* Dans ce cas, tout se passe comme s'il y avait localement un phénomène de réflexion sur un plan tangent à la surface (lois de SNELL-DESCARTES) ; ce qui permet d'exprimer les courants surfaciques équivalents (ou le champ total en surface) en fonction du champ incident et ainsi de transformer les équations intégrales en intégrales définies. Cette hypothèse est très restrictive car la notion de plan tangent est incompatible avec celle de discontinuité de surface ; la solution de l'O.P. ne s'applique donc qu'à une classe limitée d'obstacles. La notion de discontinuité étant exclue, la plupart des phénomènes sensibles à la polarisation ne peuvent être traités par la méthode. Toutefois, en bistatique l'O.P. restitue une information polarimétrique.

3) *La cible est suffisamment éloignée du point d'observation P pour que les fronts d'onde soient sphériques.* Cette condition de sphéricité [2] des ondes s'exprime par la relation :

$$R > 0,62 \sqrt{\frac{D^3}{\lambda}} \quad (3)$$

où : R est la distance d'observation

D est la plus grande dimension de la cible

$\lambda$  est la longueur d'onde.

Cette condition, qui permet de considérer les champs électrique et magnétique localement orthogonaux, est peu contraignante dans le cadre des applications Radar. Elle délimite la zone de champ proche radiatif, quelquefois appelée zone de FRESNEL [2] [3].

##### 4.1.3. Les Courants Equivalents

La Méthode des Courants Equivalents (M.C.E.) est basée sur le calcul d'intégrales linéiques de rayonnement. La source du champ diffracté par une discontinuité d'arête en un point quelconque de l'espace est attribuée à des courants équivalents "fictifs", électriques et magnétiques, circulant le long de l'arête. Ces courants sont calculés en supposant l'arête localement rectiligne autour de chaque point du contour considéré. Il s'agit de l'analogie de l'approximation du plan tangent de l'Optique Physique.

Le champ diffracté par une discontinuité d'arête de contour C, en zones proche et lointaine s'exprime, en termes de courants filaires électriques  $I_e$  et magnétiques  $I_m$  le long de C [6]:

$$\vec{E}_d = -jk \int_C \left[ Z I_e \hat{r} \wedge (\hat{r} \wedge \hat{t}) + I_m (\hat{r} \wedge \hat{t}) \right] \phi dt \quad (4)$$

Dans cette expression  $\hat{r}$  et  $\hat{t}$  désignent respectivement la direction de diffraction et la tangente locale à l'arête.

MITZNER [5] et MICHAELI [6] sont les premiers à avoir proposé une théorie rigoureuse de la M.C.E. La proposition de MICHAELI peut être considérée comme une extension de la Théorie Géométrique de la Diffraction (T.G.D) de KELLER et celle de MITZNER comme une extension de la Théorie Physique de la Diffraction (T.P.D.) d'UFIMTSEV.

## 4.2. Les phénomènes modélisés dans SERMAIL

### 4.2.1. Les réflexions simples et doubles

Considérons deux surfaces  $S_i$  et  $S_j$ , exposées à la configuration Radar bistatique indiquée par la figure 4, respectivement inscrites dans un référentiel  $(\hat{n}_i, \hat{v}_i, \hat{w}_i)$  où  $\hat{n}_i$  et  $(\hat{v}_i, \hat{w}_i)$  représentent respectivement la normale et le plan de la surface  $i$ . Le système Radar est caractérisé par son émetteur  $Q$  et son récepteur  $P$  respectivement situés aux distances  $E_i$  et  $R_i$  du centre de  $i$  et  $e_i$  et  $r_i$  d'un élément de surface  $ds_i$ . Deux éléments de surface  $ds_i$  et  $ds_j$  sont distants de  $d_{ij} = d_{ji}$ .

En considérant les hypothèses de l'O.P., les champs électrique et magnétique réfléchis au premier ordre  $(\vec{E}_r(P); \vec{H}_r(P))$  et au second ordre  $(\vec{E}_{rr}(P); \vec{H}_{rr}(P))$ , en zones proche et lointaine, s'expriment après quelques développements sur (1) et (2) par les relations :

$$\begin{pmatrix} \vec{E}_r(P) \\ \vec{E}_{rr}(P) \end{pmatrix} = \frac{j}{4\pi\omega\epsilon} \iint_S \{(-1 + jkr + k^2r^2) \vec{J}_{op}^{(1,2)} + (k^2r^2 + jkr) \vec{M}_{op}^{(1,2)} \wedge \hat{r} + (3 - j3kr - k^2r^2) \left\{ \hat{r} \cdot \vec{J}_{op}^{(1,2)} \right\} \hat{r} \} \frac{\phi}{r^2} ds \quad (5a)$$

$$\begin{pmatrix} \vec{H}_r(P) \\ \vec{H}_{rr}(P) \end{pmatrix} = \frac{j}{4\pi\omega\mu} \iint_S \{(-1 + jkr + k^2r^2) \vec{M}_{op}^{(1,2)} - (k^2r^2 + jkr) Z \vec{J}_{op}^{(1,2)} \wedge \hat{r} + (3 - j3kr - k^2r^2) \left\{ \hat{r} \cdot \vec{M}_{op}^{(1,2)} \right\} \hat{r} \} \frac{\phi}{r^2} ds \quad (5b)$$

où  $S = S_i + S_j$  et où  $Z$  et  $k$  désignent respectivement l'impédance et le nombre d'onde dans le milieu de propagation :

$$Z = \sqrt{\frac{\mu}{\epsilon}} \quad (\Omega) \quad \text{et} \quad k = \omega\sqrt{\mu\epsilon}$$

Les courants de l'Optique Physique s'écrivent sur la surface  $S_i$  de l'obstacle :

- Pour une réflexion du premier ordre :
- sur un corps parfaitement conducteur :

$$\begin{aligned} \vec{J}_{op}^{(1)}(S_i) &= 2\hat{n}(S_i) \wedge \vec{H}_i^Q(S_i) \\ \vec{M}_{op}^{(1)}(S_i) &= 0 \end{aligned} \quad (6)$$

- sur un corps diélectrique :

$$\begin{aligned} \vec{J}_{op}^{(1)}(S_i) &= \hat{n}(S_i) \wedge [\vec{H}_i^Q(S_i) + \vec{H}_r^Q(S_i)] \\ \vec{M}_{op}^{(1)}(S_i) &= [\vec{E}_i^Q(S_i) + \vec{E}_r^Q(S_i)] \wedge \hat{n}(S_i) \end{aligned} \quad (7)$$

où  $(\vec{E}_i^Q(S_i); \vec{H}_i^Q(S_i))$  et  $(\vec{E}_r^Q(S_i); \vec{H}_r^Q(S_i))$  sont respectivement les champs électriques et magnétiques, en provenance de l'émetteur  $Q$ , incidents et réfléchis sur le plan tangent à la surface  $S_i$ .

L'approximation du plan tangent permet d'écrire les composantes de  $(\vec{E}_i^Q(S_i); \vec{H}_i^Q(S_i))$ , parallèles et normales au plan de réflexion, en fonction des composantes de  $(\vec{E}_r^Q(S_i); \vec{H}_r^Q(S_i))$ , parallèles et normales au plan d'incidence, sous la forme :

$$\vec{E}_r^Q(S_i) = \begin{bmatrix} E_{r//}^Q(S_i) \\ E_{r\perp}^Q(S_i) \end{bmatrix} = \begin{bmatrix} E_{i//}^Q(S_i) \\ E_{i\perp}^Q(S_i) \end{bmatrix} \cdot \begin{bmatrix} R_E^// & 0 \\ 0 & R_E^\perp \end{bmatrix} \quad (8a)$$

$$\vec{H}_r^Q(S_i) = \begin{bmatrix} H_{r//}^Q(S_i) \\ H_{r\perp}^Q(S_i) \end{bmatrix} = \begin{bmatrix} H_{i//}^Q(S_i) \\ H_{i\perp}^Q(S_i) \end{bmatrix} \cdot \begin{bmatrix} R_H^// & 0 \\ 0 & R_H^\perp \end{bmatrix} \quad (8b)$$

où  $(R_E^//; R_E^\perp)$  et  $(R_H^//; R_H^\perp)$  sont respectivement les coefficients de réflexion électriques et magnétiques de FRESNEL [8].

- Pour une réflexion du second ordre :
- sur un corps parfaitement conducteur :

$$\begin{aligned} \vec{J}_{op}^{(2)}(S_i) &= 2\hat{n}(S_i) \wedge \vec{H}_i^{S_j}(S_i) \\ \vec{M}_{op}^{(2)}(S_i) &= 0 \end{aligned} \quad (9)$$

- sur un corps diélectrique :

$$\begin{aligned} \vec{J}_{op}^{(2)}(S_i) &= \hat{n}(S_i) \wedge [\vec{H}_i^{S_j}(S_i) + \vec{H}_r^{S_j}(S_i)] \\ \vec{M}_{op}^{(2)}(S_i) &= [\vec{E}_i^{S_j}(S_i) + \vec{E}_r^{S_j}(S_i)] \wedge \hat{n}(S_i) \end{aligned} \quad (10)$$

$(\vec{E}_i^{S_j}(S_i); \vec{H}_i^{S_j}(S_i))$  est le champ électromagnétique proche bistatique rayonné par  $S_j$  sur  $S_i$ , calculé à l'aide des expressions (5a) et (5b).

$(\vec{E}_r^{S_j}(S_i); \vec{H}_r^{S_j}(S_i))$  est le champ électromagnétique réfléchi sur le plan tangent à la surface  $S_i$ , après une première réflexion sur  $S_j$ .

L'approximation du plan tangent permet d'écrire les composantes de  $(\vec{E}_r^{S_j}(S_i); \vec{H}_r^{S_j}(S_i))$ , parallèles et normales au plan de réflexion, en fonction des composantes de  $(\vec{E}_i^{S_j}(S_i); \vec{H}_i^{S_j}(S_i))$ , parallèles et normales au plan d'incidence, sous la forme :

$$\vec{E}_r^{S_j}(S_i) = \begin{bmatrix} E_{r//}^{S_j}(S_i) \\ E_{r\perp}^{S_j}(S_i) \end{bmatrix} = \begin{bmatrix} E_{i//}^{S_j}(S_i) \\ E_{i\perp}^{S_j}(S_i) \end{bmatrix} \cdot \begin{bmatrix} R_E^// & 0 \\ 0 & R_E^\perp \end{bmatrix} \quad (11a)$$

$$\vec{H}_r^{S_j}(S_i) = \begin{bmatrix} H_{r//}^{S_j}(S_i) \\ H_{r\perp}^{S_j}(S_i) \end{bmatrix} = \begin{bmatrix} H_{i//}^{S_j}(S_i) \\ H_{i\perp}^{S_j}(S_i) \end{bmatrix} \cdot \begin{bmatrix} R_H^// & 0 \\ 0 & R_H^\perp \end{bmatrix} \quad (11b)$$

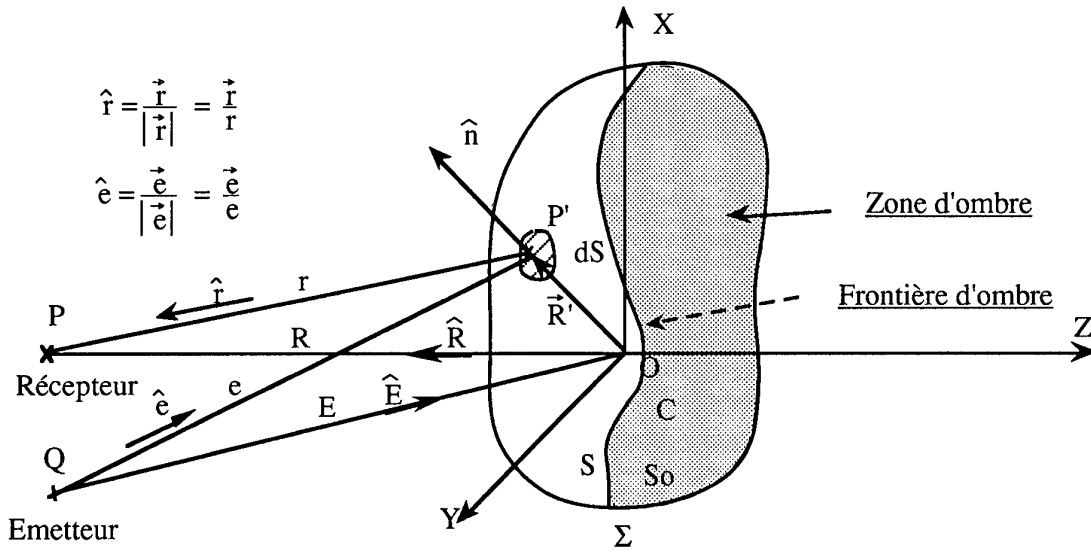


Figure 3 : Géométrie générale du problème de la diffraction

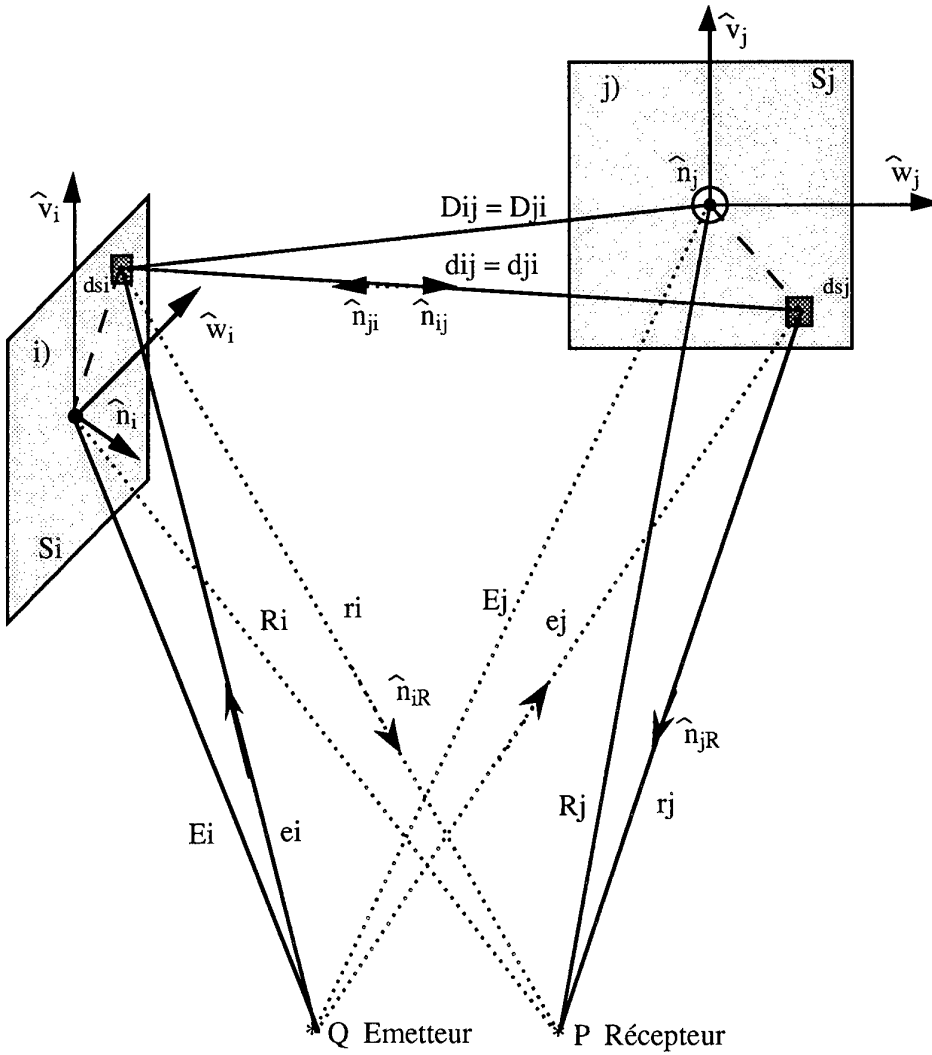


Figure 4 : Réflexions simples et doubles

Le principe du calcul des réflexions doubles consiste à calculer toutes les interactions entre les surfaces  $S_i$  et  $S_j$ .

Les champs électrique et magnétique doublement réfléchis ( $\vec{E}_{rr}(P)$ ;  $\vec{H}_{rr}(P)$ ) sont donc obtenus par itération sur les expressions (5a) et (5b).

#### Application à un conducteur parfait

Pour une cible métallique, en limitant l'étude au seul champ magnétique et en écrivant le champ incident à la surface de la cible sous la forme :

$$\vec{H}_i(P) = H_i(Q) \frac{e^{jk_e}}{e} \hat{h}_i$$

où  $H_i(Q)$  représente l'amplitude du champ incident au point d'émission  $Q$ , après quelques développements on montre que le champ réfléchi au premier ordre peut s'exprimer sous la forme :

$$\vec{H}_r(P) = \frac{H_i(Q)}{2\pi} \iint_S \left( -jk + \frac{1}{r} \right) \left[ (\hat{r} \cdot \hat{n}) \hat{h}_i - (\hat{r} \cdot \hat{h}_i) \hat{n} \right] \cdot \frac{e^{jk(e+r)}}{e \cdot r} ds \quad (12)$$

On montre également que le champ rayonné au second ordre par la surface  $j$ , après couplage avec la surface  $i$ , s'exprime par la relation :

$$\vec{H}_{rrij}(P) = \frac{H_i(Q)}{(2\pi)^2} \iint_{S_i} \iint_{S_j} \left( jk - \frac{1}{r_j} \right) \left( jk - \frac{1}{d_{ij}} \right) \cdot \hat{p}_j R \frac{\exp(jk(e_i + d_{ij} + r_j))}{e_i \cdot d_{ij} \cdot r_j} ds_j ds_i \quad (13)$$

avec :

$$\begin{aligned} \hat{p}_j R &= (\hat{n}_j R \cdot \hat{n}_j) \cdot \hat{p}_{ij} - (\hat{n}_j R \cdot \hat{p}_{ij}) \cdot \hat{n}_j \\ \hat{p}_{ij} &= (\hat{n}_{ij} \cdot \hat{n}_i) \cdot \hat{h}_i - (\hat{n}_{ij} \cdot \hat{h}_i) \cdot \hat{n}_i \end{aligned}$$

De la même façon, le champ rayonné par la surface  $i$ , après couplage avec la surface  $j$ , s'écrit :

$$\vec{H}_{rriji}(P) = \frac{H_i(Q)}{(2\pi)^2} \iint_{S_j} \iint_{S_i} \left( jk - \frac{1}{r_i} \right) \left( jk - \frac{1}{d_{ji}} \right) \cdot \hat{p}_i R \frac{\exp(jk(e_j + d_{ji} + r_i))}{e_j \cdot d_{ji} \cdot r_i} ds_i ds_j \quad (14)$$

avec :

$$\begin{aligned} \hat{p}_i R &= (\hat{n}_i R \cdot \hat{n}_i) \cdot \hat{p}_{ji} - (\hat{n}_i R \cdot \hat{p}_{ji}) \cdot \hat{n}_i \\ \hat{p}_{ji} &= (\hat{n}_{ji} \cdot \hat{n}_j) \cdot \hat{h}_j - (\hat{n}_{ji} \cdot \hat{h}_j) \cdot \hat{n}_j \end{aligned}$$

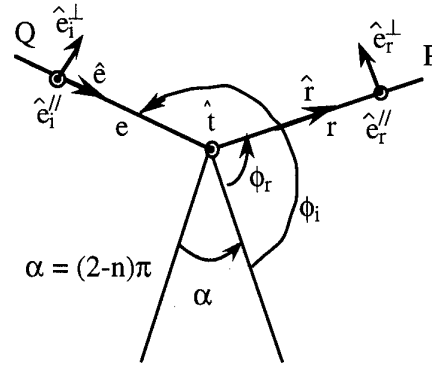
Le champ magnétique doublement réfléchi par les surfaces  $S_i$  et  $S_j$  s'exprime donc :

$$\vec{H}_{rr}(P) = \vec{H}_{rrij}(P) + \vec{H}_{rriji}(P) \quad (15)$$

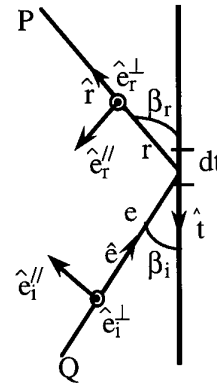
#### 4.2.2. Les diffractions simples par les arêtes

Dans SERMAIL, les diffractions simples par les arêtes métalliques sont traitées selon le formalisme des courants équivalents proposé par MITZNER.

La figure 5 montre un dièdre, d'angle interne  $\alpha = (2-n)\pi$ , dont la tangente locale à l'arête est représentée par  $\hat{t}$ , illuminé par une onde électromagnétique selon une incidence  $\hat{e}$ .



Plan normal à l'arête



Plan parallèle à l'arête

Figure 5 : Diffraction par l'arête d'un dièdre

En utilisant l'expression de KNOTT [7] du formalisme de MITZNER, on écrit le champ diffracté en  $P$  par une arête de contour  $C$ , sous la forme :

$$\vec{E}_d = 2E_i(Q) \int_C \frac{e^{jk(e+r)}}{e \cdot r} \begin{bmatrix} (D_m - D_m^{op}) \cos \gamma \hat{e}_r^\perp \\ -(D_e - D_e^{op}) \frac{\sin \beta}{\sin \beta'} \sin \gamma \hat{e}_r^\parallel \\ -(D_{em} \sin \beta' - D_{em}^{op}) \frac{\sin \beta}{\sin \beta'} \cos \gamma \hat{e}_r^\parallel \end{bmatrix} dt \quad (16)$$

avec :

les vecteurs normaux et parallèles au plan de diffraction :

$$\hat{e}_r^\perp = \frac{\hat{t} \wedge \hat{r}}{|\hat{t} \wedge \hat{r}|} \quad \text{et} \quad \hat{e}_r^\parallel = \hat{r} \wedge \hat{e}_r^\perp$$

les vecteurs normaux et parallèles au plan d'incidence :

$$\hat{e}_i^\perp = \frac{\hat{t} \wedge \hat{e}}{|\hat{t} \wedge \hat{e}|} \quad \text{et} \quad \hat{e}_i^\parallel = \hat{e} \wedge \hat{e}_i^\perp$$

L'angle  $\gamma$  est l'angle entre le vecteur polarisation  $\hat{p}$  du champ électrique incident sur l'arête et la normale au plan d'incidence :

$$\gamma = \arccos \left( \frac{\hat{e}_i^\perp \cdot \hat{p}}{|\hat{p}|} \right) \quad \text{avec} \quad \hat{p} = \frac{\vec{E}_i}{|\vec{E}_i|}$$

Les coefficients de diffraction  $D_m$ ,  $D_e$  et  $D_{em}$  sont identiques à ceux de MICHAELI.  $D_m^{OP}$ ,  $D_e^{OP}$  et  $D_{em}^{OP}$  correspondent aux termes de l'Optique Physique. Tous ces coefficients sont donnés dans [6] et [7].

Ce formalisme des courants équivalents améliore les résultats de la Théorie Géométrique de la Diffraction sur trois points fondamentaux :

1. Les champs diffractés restent bornés sur les caustiques.
2. La direction de diffraction des ondes n'est plus confinée sur une génératrice du cône de KELLER.
3. Les singularités des coefficients de diffractions  $D_e$ ,  $D_m$  et  $D_{em}$ , dans les régions de transition des frontières d'ombre et de réflexion, sont compensées par les singularités apparaissant dans les coefficients de l'Optique Physique  $D_e^{OP}$ ,  $D_m^{OP}$  et  $D_{em}^{OP}$ .

#### 4.3. Notion de S.E.R. en champ proche

Dans SERMAIL, les champs électrique et magnétique totaux rerayonnés par un obstacle s'expriment donc par la sommation cohérente des champs réfléchis, doublement réfléchis et diffractés :

$$\vec{H}_T(P) = \vec{H}_R(P) + \vec{H}_{\pi}(P) + \vec{H}_d(P) \quad (17a)$$

$$\vec{E}_T(P) = \vec{E}_R(P) + \vec{E}_{\pi}(P) + \vec{E}_d(P) \quad (17b)$$

La Surface Equivalente Radar (S.E.R.) d'une cible est définie par la relation :

$$\sigma = 4\pi R^2 \frac{P_r}{p_i} \quad (18)$$

où  $p_r$  est la densité superficielle de puissance rayonnée par la cible, reçue par le Radar, et où  $p_i$  est la densité superficielle de puissance incidente à la surface de la cible.

L'application du théorème de POYNTING permet d'écrire la S.E.R. sous la forme :

$$\sigma = 4\pi R^2 \frac{|\vec{E}_T(P) \wedge \vec{H}_T^*(P)|}{|\vec{E}_i(S) \wedge \vec{H}_i^*(S)|} \quad (19)$$

où  $(\vec{E}_i(S); \vec{H}_i(S))$  représente le champ électromagnétique incident sur la surface  $S$  de la cible et où l'exposant \* indique la quantité complexe conjuguée.

Lorsque les distances respectives  $E$  et  $R$  (cf figure 3) entre le centre de phase de la cible, l'émetteur et le récepteur, deviennent très grandes, l'expression (19) tend vers la formule classique de la S.E.R. :

$$\sigma \approx \lim_{R \rightarrow \infty} 4\pi R^2 \frac{|\vec{E}_T(P)|^2}{|\vec{E}_i(S)|^2} \approx \lim_{R \rightarrow \infty} 4\pi R^2 \frac{|\vec{H}_T(P)|^2}{|\vec{H}_i(S)|^2} \quad (20)$$

Le diagramme de S.E.R. de la cible est alors indépendant des distances  $E$  et  $R$ .

Pour rendre comparable le calcul de la puissance rerayonnée par une cible en zone proche avec la S.E.R., grandeur généralement obtenue en région lointaine, nous avons défini une expression appelée "S.E.R. champ proche", valable sous l'hypothèse de sphéricité des ondes "condition (3)" (ondes localement planes ou TEM) incidente et rayonnée par la cible, sous la forme :

$$\sigma \approx 4\pi E^2 R^2 \frac{|\vec{H}_T(P)|^2}{|\vec{H}_i(Q)|^2} \approx 4\pi E^2 R^2 \frac{|\vec{E}_T(P)|^2}{|\vec{E}_i(Q)|^2} \quad (21)$$

Pour prendre en compte les différences de trajet entre la source et les différents points de la surface  $S$  de la cible, cette formulation considère l'existence d'un champ électromagnétique incident "fictif"  $(\vec{E}_i(Q); \vec{H}_i(Q))$  au point d'émission  $Q$ . A grande distance, l'expression (21) tend asymptotiquement vers l'expression (20).

## 5. ANALYSE DES RESULTATS ET VALIDATIONS EXPERIMENTALES

Dans ce paragraphe, des exemples d'application du code SERMAIL sur un disque, un dièdre et un cylindre, en conditions de champ proche sont présentés. Les S.E.R. théoriques du dièdre et du cylindre sont comparées aux résultats expérimentaux obtenus dans SOLANGE.

### 5.1. Le disque

La figure 6 représente une vue de dessus d'un disque métallique de diamètre  $D=1m$ , d'épaisseur supposée nulle, dont le centre de phase  $O$  est situé à une distance  $d$  du système Radar. Le disque est illuminé par une onde électromagnétique sphérique centrée sur le centre de phase  $O$ . Il est en rotation d'angle  $\theta$  par rapport au plan normal à l'axe Radar.

La S.E.R. du disque est calculée en mode "holographique", c'est à dire sur une bande angulaire  $\Delta\theta$  et sur une bande de fréquences  $\Delta F$ .

La figure 7 présente deux hologrammes calculés respectivement à 500 mètres (champ lointain) et 10 mètres (champ proche) sur un domaine fréquentiel de 1 GHz à 25 GHz avec un pas de 100 MHz et sur un domaine angulaire de  $-5^\circ$  à  $+5^\circ$  avec un pas de  $0,1^\circ$ . La figure 8 fournit des coupes aux gisements fixes  $0^\circ$  et  $4^\circ$  ainsi qu'aux fréquences fixes 12 GHz et 18 GHz, en champs proche (traits fins) et lointain (traits gras).

L'hologramme champ lointain confirme les résultats classiques du diagramme de S.E.R. d'une plaque. On retrouve bien un lobe principal dont l'amplitude augmente et dont la largeur décroît en fonction de la fréquence, accompagné de lobes secondaires dont l'amplitude diminue avec le gisement.

En champ proche, on constate un affaissement et un élargissement du lobe principal qui fusionne avec les lobes secondaires sur quelques degrés. Pour les gisements proches de zéro degré on observe une succession de maxima et de minima, en fonction de la fréquence, confirmant le phénomène d'arches périodiques montré par la coupe de l'hologramme au gisement nul (figure 8). La figure 8 montre également de fortes dégradations du diagramme de S.E.R. autour du spéculaire et notamment la quasi annulation de l'énergie au gisement  $0^\circ$  à 12 GHz.

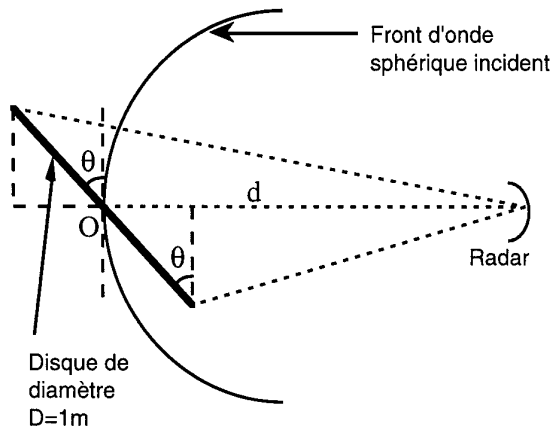


Figure 6 : Illumination sphérique du disque (vue de dessus)

### 5.2. Le dièdre

La cible étudiée est un dièdre métallique d'angle intérieur  $90^\circ$ , composé de 2 plaques carrées d'épaisseurs supposées nulles et de côté 49 cm. Sa S.E.R. est calculée à une distance "antennes - cible" égale à 15,50 m en polarisations parallèles horizontales (HH), conformément à la figure 9, pour 3 fréquences respectivement égales à 4 GHz, 6 GHz et 8 GHz. Dans ces conditions, à 8 GHz la zone de FRAUNHOFER de la cible débute à environ 50 m.

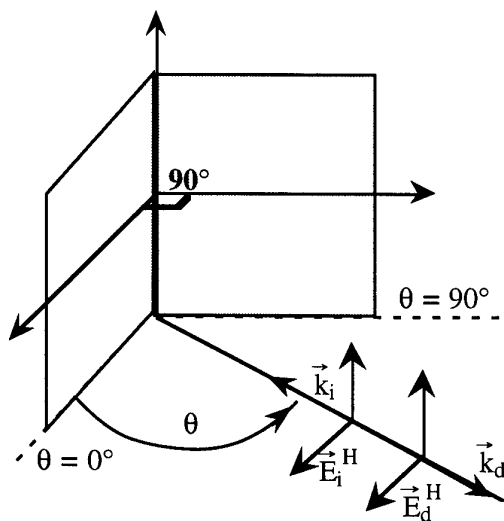


Figure 9 : Diffraction par un dièdre d'angle interne  $90^\circ$

Les résultats sont fournis sur la figure 10. Les diagrammes supérieurs gauche et droite correspondent respectivement aux calculs effectués à 4 GHz et 6 GHz, celui du bas correspond au calcul effectué à 8 GHz. Les diagrammes de S.E.R. théoriques (traits gras) et expérimentales (traits fins) se recoupent très bien au niveau des réflexions simples et doubles.

Quelques écarts apparaissent principalement pour les basses fréquences et les premiers lobes suivant les réflexions simples. Ils peuvent être causés par l'épaisseur des panneaux constituant le dièdre mesuré, non prise en compte dans le calcul. Les effets de champ proche sont peu marqués sur ces résultats.

### 5.3. Le cylindre

La figure 12 montre la superposition des diagrammes de S.E.R. d'un cylindre métallique à base circulaire de longueur 2,60m et de diamètre 0,40m, respectivement mesurée dans la base SOLANGE et calculée à l'aide du code SERMAIL, à 14 GHz, pour la configuration "champ proche bistatique" (cf. figure 11) suivante :

- axe du cylindre parallèle au plan horizontal et en rotation sur  $\pm 5^\circ$  autour de  $90^\circ$  (spéculaire sur la génératrice)
- distance "antenne émission - cible" : 54,64m
- distance "antenne réception - cible" : 24,82m
- angle entre la direction d'émission du Radar et le plan horizontal :  $12^\circ$
- angle entre la direction de réception du Radar et le plan horizontal :  $-28^\circ$ .

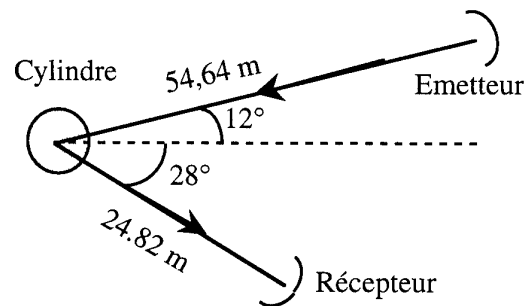


Figure 11 : Configuration bistatique champ proche pour le cylindre

Le bistatisme dans le plan vertical est de  $40^\circ$ , du fait du déplacement longitudinal de l'antenne de réception au sol.

La courbe en traits gras correspond à la mesure et la courbe en traits fins fournit la S.E.R. théorique obtenue à l'aide du code SERMAIL. On constate un bon accord entre ces deux résultats avec des écarts d'environ 0,4 dB sur les maxima. L'atténuation des lobes secondaires sur les mesures peut s'expliquer par l'état d'usure des bords du cylindre qui sont émoussés. A titre indicatif, une troisième courbe, en pointillés, indique la S.E.R. monostatique du même cylindre, calculée en conditions de champ lointain.

## CONCLUSION

Cette étude présente une méthode théorique de calcul de la S.E.R. monostatique et bistatique d'une cible Radar illuminée par une onde électromagnétique plane ou sphérique, c'est à dire en conditions expérimentales de mesures en laboratoire (chambre anéchoïque, ...).

La méthode est basée sur le formalisme intégral de STRATTON-CHU simplifié par les hypothèses de l'Optique Physique et sur le concept des Courants Equivalents proposé par MITZNER. Elle s'applique essentiellement aux réflexions simples et doubles ainsi qu'aux diffractions simples.

Des phénomènes remarquables sont mis en évidence en zone proche, comme par exemple le comportement périodique "en forme d'arches" de la S.E.R. axiale du disque en fonction de la fréquence. Les effets du champ proche sur les réflexions doubles sont également étudiés pour le cas du dièdre métallique et des recouvrements significatifs sont obtenus avec les mesures.

Enfin, la méthode de calcul proposée est validée par comparaison avec la S.E.R. d'un cylindre métallique de grandes dimensions mesurée en champ proche bistatique dans la base de mesures de S.E.R. SOLANGE du CELAR.

## BIBLIOGRAPHIE

- [1] J. A. STRATTON, "Electromagnetic Theory", McGraw - Hill Book Company, Inc., New York (1941).
- [2] C. A. BALANIS, "Antenna Theory Analysis and Design", Harper & Row Publishers, New-York (1982).
- [3] W.L. STUTZMAN, G.A. THIELE, "Antenna theory and design", Wiley & Sons, New-York (1981).
- [4] R. F. HARRINGTON, "Time - harmonic electromagnetic fields", McGraw - Hill Book Company, Inc., New York, (1961).
- [5] K.M. MITZNER, "Incremental length diffraction coefficients", Aircraft Division Northrop Corp., Tech. Rep. No. AFAL-TR-73-296, (1974).
- [6] A. MICHAELI, "Equivalent edge currents for arbitrary aspects of observation", IEEE Trans. Antennas Propagation, Vol. AP-23, no. 3, pp. 252-258 (March 1984).
- [7] E.F. KNOTT, "The relationship between Mitzner's IDLC and Michaeli's Equivalent Currents", IEEE Trans. Antennas Propagation, Vol. AP-33, no. 1, pp. 112-114 (January 1985).
- [8] G.T. RUCK, D.E. BARRICK, W.D. STUART and C.K. KRICHBAUM, "Radar Cross Section Handbook", Plenum Press, New York, (1970).

Figure 7 : S.E.R. d'un disque de diametre 1m

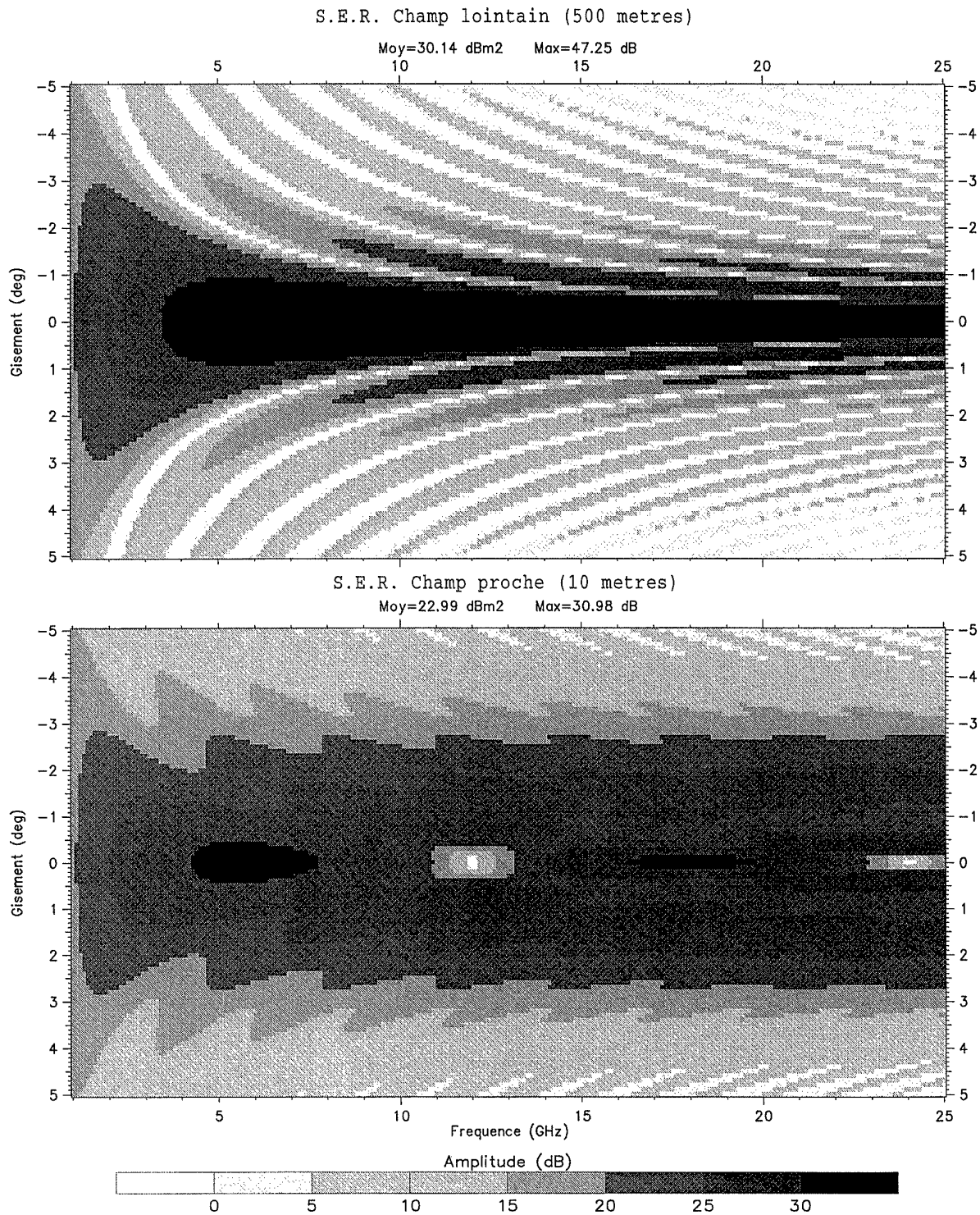


Figure 8 : S.E.R. d'un disque de diametre 1m

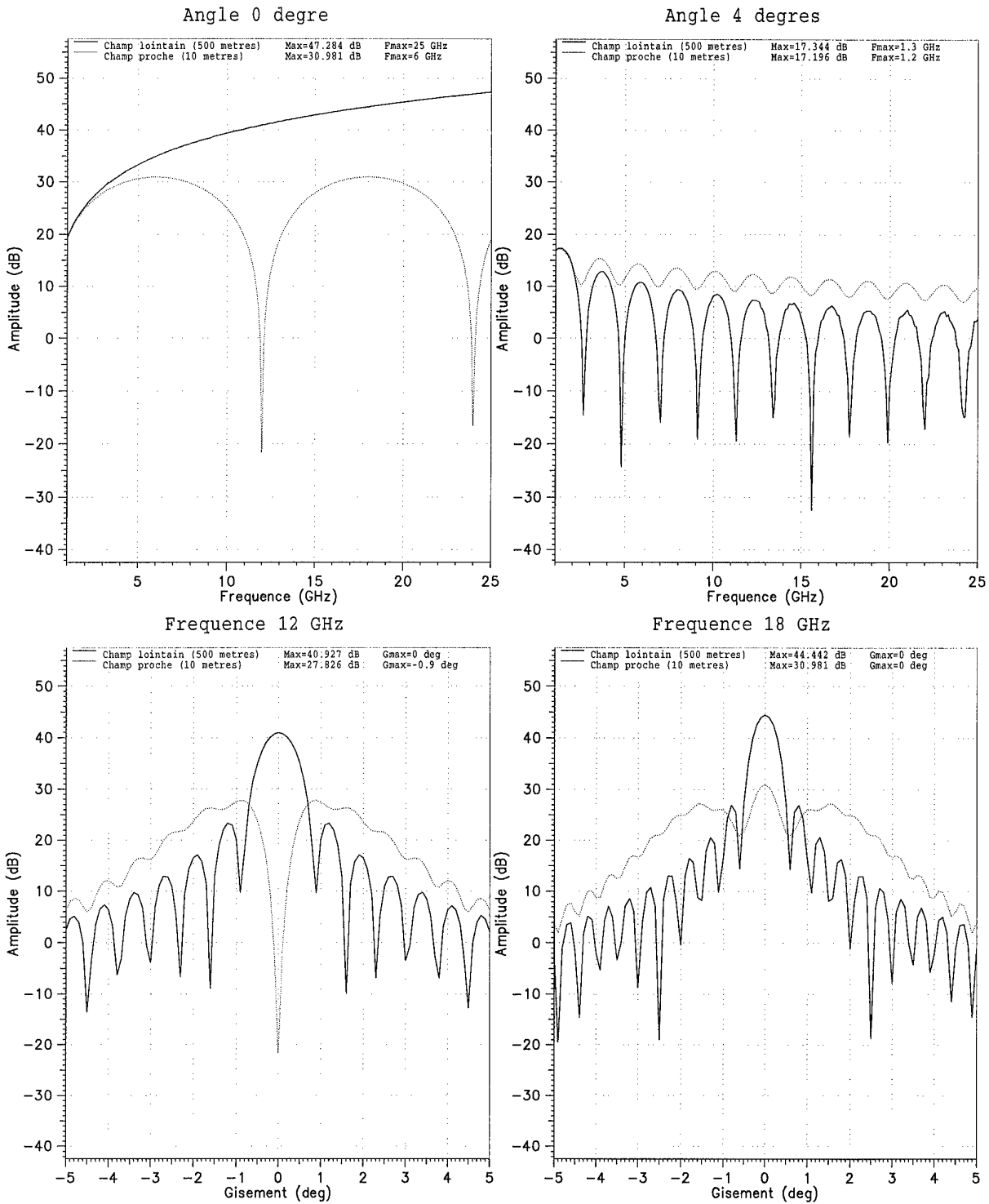


Figure 10 : S.E.R. d'un diedre de 49cm x 49cm a 15,5 m - Polarisation HH

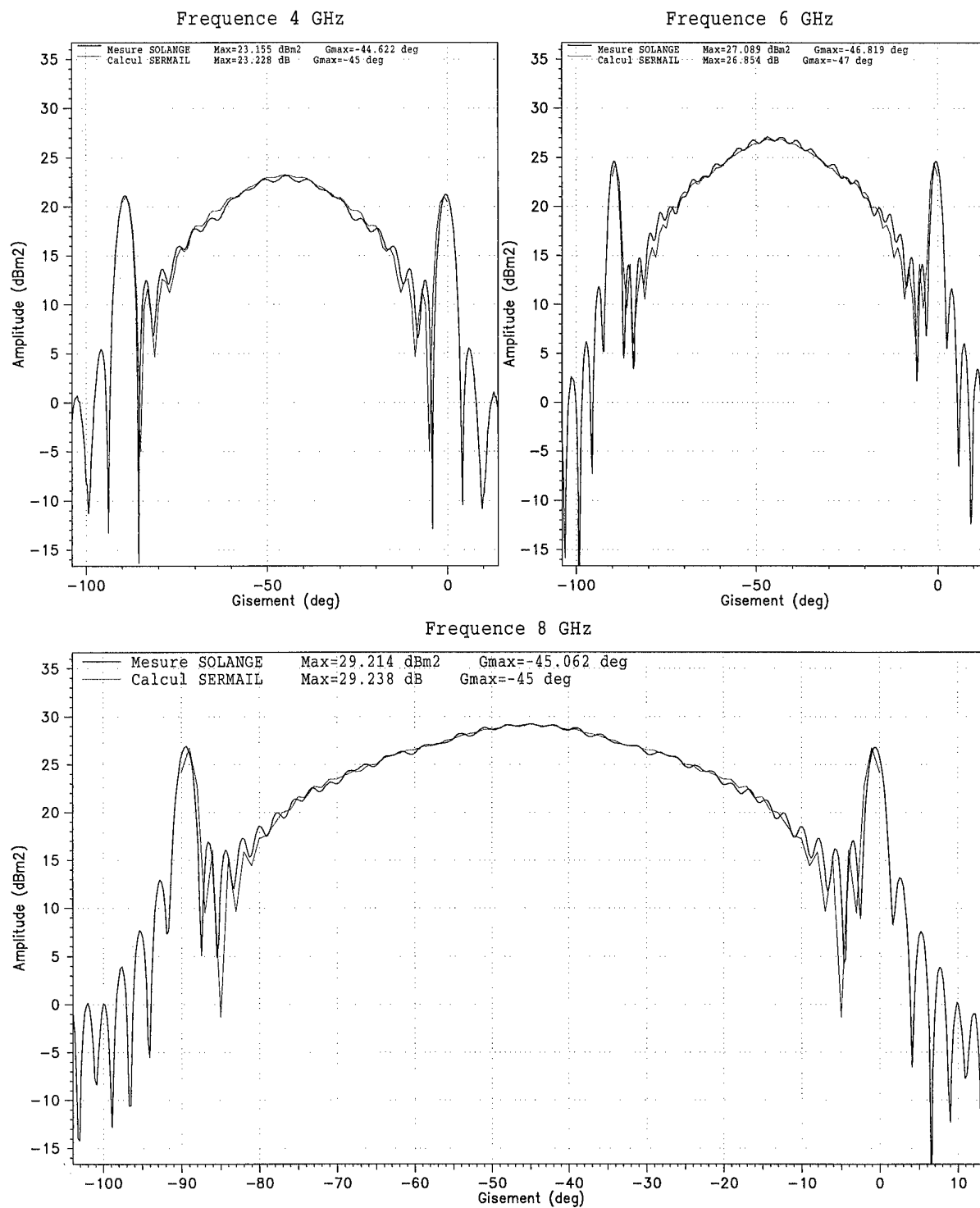
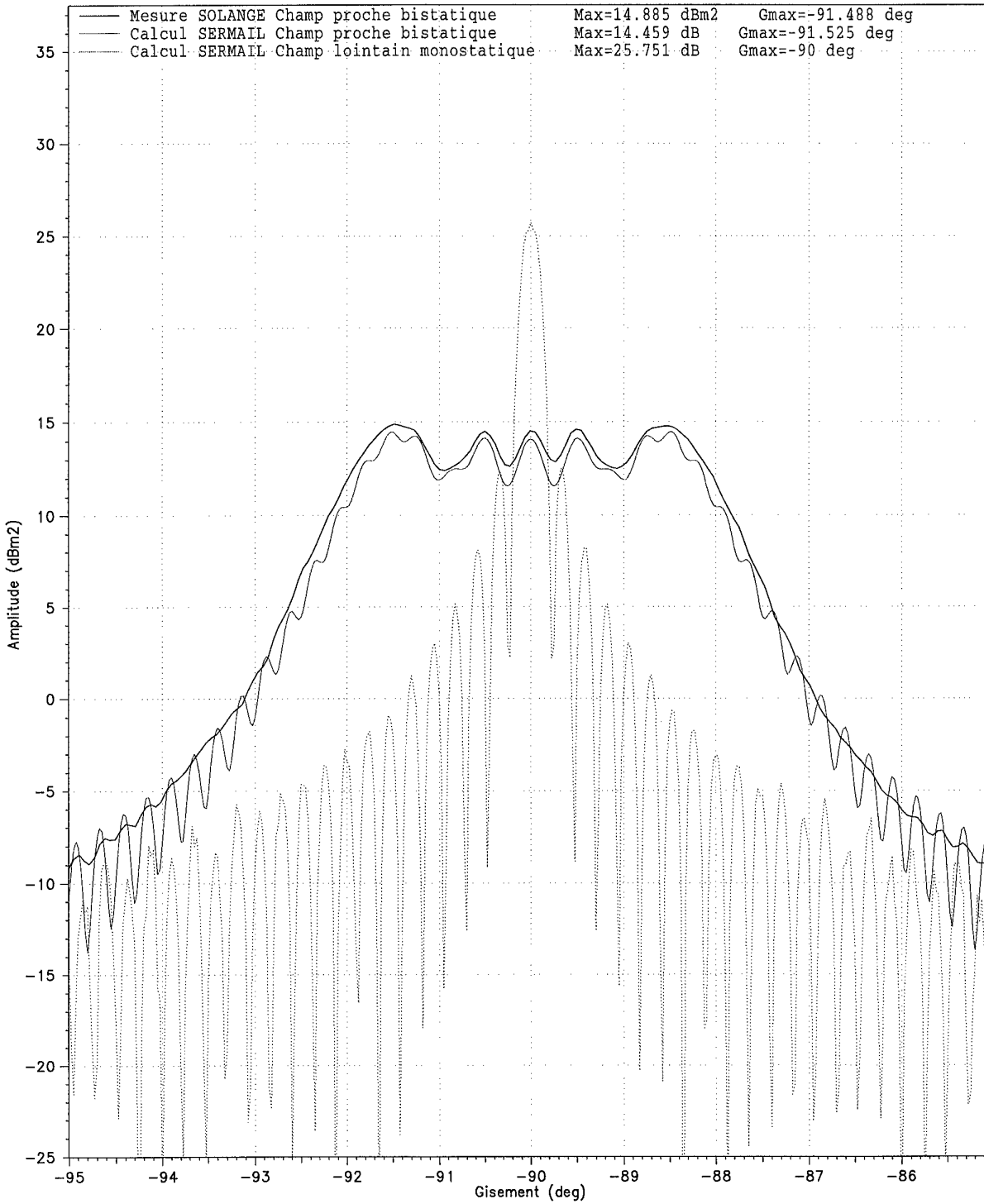


Figure 12 : S.E.R. bistatique champ proche d'un cylindre

Dimensions cylindre (diametre 0,40m - longueur 2,60m) - Frequence 14 GHz



## DISCUSSION

**Discussor's name:** E. SCHWEICHER

**Comment/Question:**

Quel est le critère de flèche que vous utilisez, en d'autres termes quelle est la distance maximale que vous admettez entre chaque élément planaire et la surface réelle courbe que vous modélisez par des éléments planaires?

*Translation:*

*What is the camber criterion which you use, in other words, what is the maximum distance which you allow between each planar element and the effective curved surface which you model by means of these elements?*

**Author/Presenter's reply:**

Le critère de flèche que nous utilisons est égal à  $\lambda/16$ , où  $\lambda$  représente la longueur d'onde.

*Translation:*

*The camber criterion which we use is equal to  $\lambda/16$ , where  $\lambda$  represents the wavelength.*

**Discussor's name:** A. BICCI

**Comment/Question:**

Is the current integration for obtaining near field data based on facet elements? Are these facets considered flat?

**Author/Presenter's reply:**

The integration is based on flat facet elements.

**Discussor's name:** G. BROWN

**Comment/Question:**

Do you see a need to go to three or more multiple bounces and do you plan to do this?

**Author/Presenter's reply:**

Je pense en effet qu'il est nécessaire d'intégrer dans ce code de calcul des interactions d'ordre supérieures. Cela est d'ailleurs prévu dans les prochaines extensions de code.

*Translation:*

*Yes indeed, I think it is necessary to incorporate higher order interactions into this code. In fact, this is already planned for future code extensions.*

**Discussor's name:** U. LAMMERS

**Comment/Question:**

Is your technique of measuring the RCS of large targets in the near field equivalent to that where you would have to use a large collimating reflector (compact range) to simulate far field conditions?

**Author/Presenter's reply:**

Notre technique de correction des mesures "champ proche - champ lointain" permet de corriger les phénomènes du 1<sup>er</sup> ordre (réflexions et diffractions simples). Des comparaisons croisées avec des bases de mesures équipées de réflecteurs (compact range) l'ont prouvé.

*Translation:*

*Our "near field - far field" correction technique enables correction of 1st order phenomena (simple reflections and diffractions). Cross comparisons with measurement bases equipped with compact range reflectors have proved it.*

# LOW FREQUENCY SCATTERING BY TARGETS ABOVE A GROUND PLANE

**George Dassios**

Department of Chemical Engineering  
University of Patras & ICE/HT-FORTH  
P.O. Box 1414, GR 26500 Patras  
Greece

and

**Ralph Kleinman**

Center for the Mathematics of Waves  
Department of Mathematical Sciences  
University of Delaware  
Newark, DE 19716  
U.S.A.

## SUMMARY

Low frequency scattering by isolated targets in free space has been well studied and there exists a general theory as well as explicit results for special target shapes. In the present paper we develop a comparable theory for low frequency scattering of targets above a flat plane. The presence of the ground plane has a considerable effect on the radar cross section of the scatterer and this effect is highly dependent on the boundary condition used to model the ground.

To gain an understanding of how the target-ground interaction affects the low frequency radar cross section a number of different models are treated. Attention is directed to scalar scattering by small three dimensional objects on which either Dirichlet or Neumann boundary conditions are imposed. The object is located above a ground plane on which again either Dirichlet or Neumann conditions are imposed, resulting in four different combined boundary value problems. The incident wave originates in the half space containing the object. The full low frequency expansion of the scattered field is obtained in terms of solutions of a sequence of potential problems. The first non-trivial term is found explicitly for a spherical target and compared with the corresponding result when the ground plane is absent. These results provide some essential benchmarks in inducing a reasonable extrapolation from the free space target signature of a general object to its signature in the presence of a ground plane.

## LIST OF SYMBOLS

$\mathbf{r}$	=	Field point position vector
$\mathbf{r}'$	=	Integration point position vector
$R$	=	Distance between $\mathbf{r}$ and $\mathbf{r}'$
$S$	=	Scattering surface in upper half space
$S_i$	=	Image of scatterer in lower half space
$S_0$	=	Ground plane - $z = 0$
$V^-$	=	Interior of $S$
$V^+$	=	Exterior of $S$ above ground plane
$V_i^-$	=	Image of $V^-$ in ground plane
$V_i^+$	=	Image of $V^+$ in ground plane
$u^{inc}$	=	Incident field
$u_0^\pm$	=	Total field with no scatterer
$u^T$	=	Total field
$u_n^T$	=	Low frequency expansion coefficients
$g$	=	Scattering amplitude or far field coefficient
$D$	=	Superscript denoting Dirichlet boundary condition
$N$	=	Superscript denoting Neumann boundary condition
$\hat{\mathbf{k}}$	=	Direction of incident plane wave
$\hat{\mathbf{n}}$	=	Outward unit normal

## INTRODUCTION

In many tactical applications of radar and sonar scattering, the physical situation is more realistically modelled with the inclusion of infinite plane rather than assuming that the target is immersed in free space. It is well known that the presence of a ground plane significantly affects the scattering behavior of a target. Moreover it has long been recognized that the scattering problem involving a scattering configuration of target above a ground plane may be replaced by an

equivalent problem of scattering by the target and its image in the ground plane. ([see e.g. [1]]) This allows for the reduction of the scattering problem to integral equations over finite boundaries rather than the boundary of the target and the infinite ground plane. However until now there has been no thorough low frequency analysis of this scattering configuration. Low frequency analysis is useful in that it reduces a scattering problem to a sequence potential problems which are easier to solve. Furthermore, even the lowest order terms carry information that is useful in target discrimination. this process has been exploited for scattering of targets in free space, e.g. [2], but not for targets above a ground plane.

In this paper, we derive the integral equations and representations governing this scattering configuration for a number of different boundary conditions. These integral representations are then used to derive a full low frequency formalism for scattering by an arbitrarily shaped target above a ground plane. The lowest order terms in these low frequency expansions are discussed in detail and some explicit results for spherical targets are given.

#### NOTATION AND PROBLEM FORMULATION

Let  $\mathbf{r} = (x, y, z)$  denote a point in three space ( $\mathbb{R}^3$ ) and  $\mathbf{r}_i = (x, y, -z)$  denote its image in the plane,  $z = 0$ . See Figure 1. Assume that a known incident wave  $u^{\text{inc}}(\mathbf{r})$  impinges on a target consisting of a simply connected bounded region  $V^-$  in  $\mathbb{R}^3$  with boundary  $S = \partial V^-$  which lies above the plane  $z = 0$  denoted by  $S_0$ . Denote by  $V^+$  the portion of  $\mathbb{R}^3$  exterior to  $V^-$  and above  $S_0$ , and denote by  $V_i^+$  and  $V_i^-$  the images of  $V^+$  and  $V^-$  in  $S_0$ .

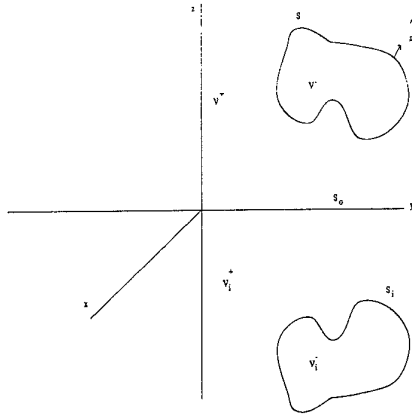


Figure 1:

We consider the following scattering problems: For a known incident field  $u^{\text{inc}}(\mathbf{r})$  find  $u^s(\mathbf{r})$  in  $V^+$  such that

$$(\nabla^2 + k^2) u^s(\mathbf{r}) = 0 \quad \text{in } V^+, \quad (1)$$

$$\lim_{r \rightarrow \infty} \frac{\partial u^s}{\partial r} - iku^s = 0, \quad \mathbf{r} \in V^+, \quad r = |\mathbf{r}|, \quad (2)$$

and  $u^s(\mathbf{r})$  satisfies one of the following sets of boundary conditions:

$$D, D: \quad u^s(\mathbf{r}) = -u_0^-(\mathbf{r}) \quad \mathbf{r} \in S \quad (3a)$$

$$u^s(\mathbf{r}) = 0 \quad \mathbf{r} \in S_0 \quad (3b)$$

$$N, N: \quad \frac{\partial u^s(\mathbf{r})}{\partial n} = -\frac{\partial u_0^+(\mathbf{r})}{\partial n} \quad \mathbf{r} \in S \quad (4a)$$

$$\frac{\partial u^s(\mathbf{r})}{\partial n} = 0 \quad \mathbf{r} \in S_0 \quad (4b)$$

$$D, N: \quad u^s(\mathbf{r}) = -u_0^+(\mathbf{r}) \quad \mathbf{r} \in S \quad (5a)$$

$$\frac{\partial u^s(\mathbf{r})}{\partial n} = 0 \quad \mathbf{r} \in S_0 \quad (5b)$$

$$N, D: \quad \frac{\partial u^s(\mathbf{r})}{\partial n} = -\frac{\partial u_0^-(\mathbf{r})}{\partial n}, \quad \mathbf{r} \in S \quad (6a)$$

$$u^s(\mathbf{r}) = 0, \quad \mathbf{r} \in S_0 \quad (6b)$$

where

$$u_0^+(\mathbf{r}) = u^{\text{inc}}(\mathbf{r}) + u^{\text{inc}}(\mathbf{r}_i) \quad (7a)$$

$$u_0^-(\mathbf{r}) = u^{\text{inc}}(\mathbf{r}) - u^{\text{inc}}(\mathbf{r}_i) \quad (7b)$$

The functions  $u_0^+$  and  $u_0^-$  solve the scattering problem for Neumann and Dirichlet conditions on  $S_0$  respectively in the absence of a scatterer,  $S \cup V^-$ .

#### INTEGRAL EQUATIONS AND REPRESENTATIONS

The integral representations which form the basis for the low frequency expansion are obtained from a standard application of Green's theorem. If  $u^s(\mathbf{r})$  satisfies the Helmholtz equation (1) and the radiation condition (2) in  $V^+$  then

$$\alpha(\mathbf{r}) u^s(\mathbf{r}) = \frac{1}{4\pi} \int_{S \cup S_0} \left\{ u^s(\mathbf{r}') \frac{\partial}{\partial n'} \frac{e^{ikR}}{R} - \frac{e^{ikR}}{R} \frac{\partial}{\partial n'} u^s(\mathbf{r}') \right\} ds' \quad (8)$$

where

$$R = |\mathbf{r} - \mathbf{r}'| = \sqrt{(x - x')^2 + (y - y')^2 + (z - z')^2}, \quad (9)$$

$$\alpha(\mathbf{r}) = \begin{cases} 1, & \mathbf{r} \in V^+ \\ 1/2, & \mathbf{r} \in S_0 \cup S \\ 0, & z < 0 \text{ and } \mathbf{r} \in V^-, \end{cases} \quad (10)$$

and the normal  $\hat{\mathbf{n}}'$  is directed into  $V^+$  so that on  $S_0$ ,  $\frac{\partial}{\partial n'} = \frac{\partial}{\partial z'}$ . Replacing  $z$  by  $-z$  (or  $\mathbf{r}$  by  $\mathbf{r}_i$ ) in (8) yields

$$\alpha(\mathbf{r}_i) u^s(\mathbf{r}_i) =$$

$$\frac{1}{4\pi} \int_{S \cup S_0} \left\{ u^s(\mathbf{r}') \frac{\partial}{\partial n'} \frac{e^{ikR_i}}{R_i} - \frac{e^{ikR_i}}{R_i} \frac{\partial}{\partial n'} u^s(\mathbf{r}') \right\} ds' \quad (11)$$

where

$$R_i = |\mathbf{r}_i - \mathbf{r}'| = \sqrt{(x-x')^2 + (y-y')^2 + (z+z_i)^2} \quad (12)$$

and

$$\begin{aligned} \alpha(\mathbf{r}_i) &= 1, & \mathbf{r}_i \in V^+ \text{ (or } \mathbf{r} \in V_i^+) \\ &= \frac{1}{2}, & \mathbf{r}_i \in S_0 \cup S \text{ (or } \mathbf{r} \in S_0 \cup S_i) \\ &= 0, & z > 0 \text{ and } \mathbf{r}_i \in V^- \text{ (or } \mathbf{r} \in V_i^-) \end{aligned} \quad (13)$$

Moreover if  $u_0(\mathbf{r})$  satisfies the Helmholtz equation in  $V^-$  (which is the case for  $u_0^+$  and  $u_0^-$ ) then

$$\begin{aligned} (\beta(\mathbf{r}) - 1) u_0(\mathbf{r}) &= \\ \frac{1}{4\pi} \int_S \left\{ u_0(\mathbf{r}') \frac{\partial}{\partial n'} \frac{e^{ikR}}{R} - \frac{e^{ikR}}{R} \frac{\partial u_0(\mathbf{r}')}{\partial n'} \right\} ds' \end{aligned} \quad (14)$$

where

$$\begin{aligned} \beta(\mathbf{r}) &= 1, & \mathbf{r} \in V^+ \cup S_0 \text{ and } z < 0 \\ &= \frac{1}{2}, & \mathbf{r} \in S \\ &= 0, & \mathbf{r} \in V^- \end{aligned} \quad (15)$$

and

$$\begin{aligned} (\beta(\mathbf{r}_i) - 1) u_0(\mathbf{r}_i) &= \\ \frac{1}{4\pi} \int_S \left\{ u_0(\mathbf{r}') \frac{\partial}{\partial n'} \frac{e^{ikR_i}}{R_i} - \frac{e^{ikR_i}}{R_i} \frac{du_0(\mathbf{r}')}{\partial n'} \right\} ds' \end{aligned} \quad (16)$$

where

$$\begin{aligned} \beta(\mathbf{r}_i) &= 1, & \mathbf{r}_i \in V^+ \cup S_0 \text{ (or } \mathbf{r} \in V_i^+ \cup S_0) \text{ and } z > 0 \\ &= \frac{1}{2}, & \mathbf{r}_i \in S \text{ (or } \mathbf{r} \in S_i) \\ &= 0, & \mathbf{r}_i \in V^- \text{ (or } \mathbf{r} \in V_i^-). \end{aligned} \quad (17)$$

Equations (8), (11), (14) and (16) are the basic relations which are used in each of the boundary value problems described above.

*D, D:* For the boundary conditions given by (3a,b) we choose  $u_0$  to be  $u_0^-$  in (14) and (16), consider the combination (8)-(11) + (14)-(16), incorporate the boundary conditions (3a,b) and define

$$u^T(\mathbf{r}) = u_0^-(\mathbf{r}) + u^s(\mathbf{r}) \quad (18)$$

to obtain

$$\begin{aligned} u_0^-(\mathbf{r}) - \frac{1}{4\pi} \int_S \frac{\partial}{\partial n'} u^T(\mathbf{r}') \left[ \frac{e^{ikR}}{R} - \frac{e^{ikR_i}}{R_i} \right] ds' &= \\ u_0^T(\mathbf{r}), & \mathbf{r} \in V^+ \\ 0, & \mathbf{r} \in S. \end{aligned} \quad (19)$$

*N, N:* For the boundary conditions (4a,b) we choose  $u_0(\mathbf{r}) = u_0^+(\mathbf{r})$  in (14) and (16), define

$$u^T(\mathbf{r}) = u_0^+(\mathbf{r}) + u^s(\mathbf{r}) \quad (20)$$

and consider the combination (8) + (11) + (14) + (16) to obtain

$$\begin{aligned} u_0^+(\mathbf{r}) + \frac{1}{4\pi} \int_S u^T(\mathbf{r}') \frac{\partial}{\partial n'} \left[ \frac{e^{ikR}}{R} + \frac{e^{ikR_i}}{R_i} \right] ds' &= \\ u^T(\mathbf{r}), & \mathbf{r} \in V^+ \\ \frac{1}{2} u^T(\mathbf{r}), & \mathbf{r} \in S. \end{aligned} \quad (21)$$

We remark that in addition to the boundary conditions, the facts that

$$\left[ \frac{e^{ikR}}{R} - \frac{e^{ikR_i}}{R_i} \right] = 0 \quad \text{on } S_0$$

and

$$\frac{\partial}{\partial n'} \left[ \frac{e^{ikR}}{R} + \frac{e^{ikR_i}}{R_i} \right] = 0 \quad \text{on } S_0$$

were used in deriving (19) and (21) respectively.

*D, N:* In similar fashion for the boundary conditions (5a,b) choose  $u_0(\mathbf{r}) = u_0^+(\mathbf{r})$  in (14) and (16), define

$$u^T(\mathbf{r}) = u_0^+(\mathbf{r}) + u^s(\mathbf{r}) \quad (22)$$

and consider the combination (8) + (11) + (14) + (16) to obtain

$$\begin{aligned} u_0^+(\mathbf{r}) - \frac{1}{4\pi} \int_S \frac{\partial u^T(\mathbf{r}')}{\partial n'} \left[ \frac{e^{ikR}}{R} + \frac{e^{ikR_i}}{R_i} \right] ds' &= \\ u^T(\mathbf{r}), & \mathbf{r} \in V^+ \\ 0, & \mathbf{r} \in S. \end{aligned} \quad (23)$$

*N, D:* Finally, for the boundary conditions (6a,b) we take  $u_0(\mathbf{r}) = u_0^-(\mathbf{r})$  in (14) and (16), define

$$u^T(\mathbf{r}) = u_0^-(\mathbf{r}) + u^s(\mathbf{r}) \quad (24)$$

and take the combination (8)-(11) + (14)-(16) to obtain

$$\begin{aligned} u_0^-(\mathbf{r}) + \frac{1}{4\pi} \int_S u^T(\mathbf{r}') \frac{\partial}{\partial n'} \left[ \frac{e^{ikR}}{R} - \frac{e^{ikR_i}}{R_i} \right] ds' &= \\ u^T(\mathbf{r}), & \mathbf{r} \in V^+ \\ \frac{1}{2} u^T(\mathbf{r}), & \mathbf{r} \in S. \end{aligned} \quad (25)$$

The relations (19), (21), (23) and (25) are the basic integral representations and equations for the four different boundary value problems under consideration. Observe that (19) and (23) contain integral equations of the first kind on  $S$  for the unknown quantity  $\frac{\partial u^T}{\partial n}$

on  $S$  while (21) and (25) are integral equations of the second kind for the unknown quantity  $u^T$  on  $S$ . Second kind equations can be obtained for the problems where Dirichlet conditions are imposed on  $S$  by differentiating the representations contained in (19) and (23).

### LOW FREQUENCY EXPANSIONS

To obtain low frequency expansions we assume that

$$u^T(\mathbf{r}) = \sum_{n=0}^{\infty} \frac{(ik)^n}{n!} u_n^T(\mathbf{r}) \quad (26a)$$

$$u_0^{\pm}(\mathbf{r}) = \sum_{n=0}^{\infty} \frac{(ik)^n}{n!} u_{0n}^{\pm}(\mathbf{r}) \quad (26b)$$

where the low frequency coefficients,  $u_n^T(\mathbf{r})$  and  $u_{0n}^{\pm}(\mathbf{r})$  are independent of  $k$  and while  $u_n^T(\mathbf{r})$  are as yet unknown,  $u_{0n}^{\pm}(\mathbf{r})$  are known if  $u^{\text{inc}}(\mathbf{r})$  is known from equation (7a,b). If  $u^{\text{inc}}(\mathbf{r})$  is a plane wave propagating in the direction  $\hat{\mathbf{k}}$  ( $\hat{\mathbf{r}}$  denotes the unit vector) then

$$u_{0n}^{\pm} = (\hat{\mathbf{k}} \cdot \mathbf{r})^n \pm (\hat{\mathbf{k}} \cdot \mathbf{r}_i)^n. \quad (27)$$

Substituting (26a,b) into (19), (21), (23) and (25), expanding  $\frac{e^{ikR}}{R}$  and  $\frac{e^{ikR_i}}{R_i}$  in powers of  $k$ , employing the Cauchy theorem for reordering products of series and equating like powers of  $ik$  we obtain, for  $\mathbf{r} \in V^+$

$$D, D: u_n^T(\mathbf{r}) = u_{0n}^-(\mathbf{r}) - \frac{1}{4\pi} \sum_{m=0}^n \binom{n}{m} \int_S (R^{m-1} - R_i^{m-1}) \frac{\partial u_{n-m}^T(\mathbf{r}')}{\partial n'} ds' \quad (28)$$

$$N, N: u_n^T(\mathbf{r}) = u_{0n}^+(\mathbf{r}) + \frac{1}{4\pi} \sum_{m=0}^n \binom{n}{m} \int_S \frac{\partial}{\partial n'} (R^{m-1} + R_i^{m-1}) u_{n-m}^T(\mathbf{r}') ds' \quad (29)$$

$$D, N: u_n^T(\mathbf{r}) = u_{0n}^+(\mathbf{r}) - \frac{1}{4\pi} \sum_{m=0}^n \binom{n}{m} \int_S (R^{m-1} + R_i^{m-1}) \frac{\partial u_{n-m}^T(\mathbf{r}')}{\partial n'} ds' \quad (30)$$

$$N, D: u_n^T(\mathbf{r}) = u_{0n}^-(\mathbf{r}) + \frac{1}{4\pi} \sum_{m=0}^n \binom{n}{m} \int_S \frac{\partial}{\partial n'} (R^{m-1} - R_i^{m-1}) u_{n-m}^T(\mathbf{r}') ds'. \quad (31)$$

These equations express the  $n^{\text{th}}$  coefficient in terms of all the preceding coefficients as well as the  $n^{\text{th}}$  coefficient itself. The advantage of this representation lies in the fact that the term involving  $u_n^T$  in the right hand sides of (28)–(31) is recognizable as a regular potential function (solution of Laplace's equation which decays as  $r \rightarrow \infty$ ). Hence equations (28)–(31) may be rewritten as

$$D, D: u_n^T(\mathbf{r}) = F_n^{D,D}(\mathbf{r}) + \phi_n^{D,D}(\mathbf{r}) \quad (32a)$$

$$N, N: u_n^T(\mathbf{r}) = F_n^{N,N}(\mathbf{r}) + \phi_n^{N,N}(\mathbf{r}) \quad (32b)$$

$$D, N: u_n^T(\mathbf{r}) = F_n^{D,N}(\mathbf{r}) + \phi_n^{D,N}(\mathbf{r}) \quad (32c)$$

$$N, D: u_n^T(\mathbf{r}) = F_n^{N,D}(\mathbf{r}) + \phi_n^{N,D}(\mathbf{r}) \quad (32d)$$

where

$$F_n^{D,D}(\mathbf{r}) = u_{0n}^-(\mathbf{r}) - \frac{1}{4\pi} \sum_{m=1}^n \binom{n}{m} \int_S (R^{m-1} - R_i^{m-1}) \frac{\partial u_{n-m}^T(\mathbf{r}')}{\partial n'} ds' \quad (33a)$$

$$F_n^{N,N}(\mathbf{r}) = u_{0n}^+(\mathbf{r}) + \frac{1}{4\pi} \sum_{m=1}^n \binom{n}{m} \int_S \frac{\partial}{\partial n'} (R^{m-1} + R_i^{m-1}) u_{n-m}^T(\mathbf{r}') ds' \quad (33b)$$

$$F_n^{D,N}(\mathbf{r}) = u_{0n}^+(\mathbf{r}) - \frac{1}{4\pi} \sum_{m=1}^n \binom{n}{m} \int_S (R^{m-1} + R_i^{m-1}) \frac{\partial u_{n-m}^T(\mathbf{r}')}{\partial n'} ds' \quad (33c)$$

$$F_n^{N,D}(\mathbf{r}) = u_{0n}^-(\mathbf{r}) + \frac{1}{4\pi} \sum_{m=1}^n \binom{n}{m} \int_S \frac{\partial}{\partial n'} (R^{m-1} - R_i^{m-1}) u_{n-m}^T(\mathbf{r}') ds' \quad (33d)$$

(the sums are identically zero for  $n = 0$ ) and

$$\phi_n^{D,D}(\mathbf{r}) = -\frac{1}{4\pi} \int_S \left( \frac{1}{R} - \frac{1}{R_i} \right) \frac{\partial u_n^T(\mathbf{r}')}{\partial n'} ds' \quad (34a)$$

$$\phi_n^{N,N}(\mathbf{r}) = \frac{1}{4\pi} \int_S \frac{\partial}{\partial n'} \left( \frac{1}{R} - \frac{1}{R_i} \right) u_n^T(\mathbf{r}') ds' \quad (34b)$$

$$\phi_n^{D,N}(\mathbf{r}) = -\frac{1}{4\pi} \int_S \left( \frac{1}{R} + \frac{1}{R_i} \right) \frac{\partial u_n^T(\mathbf{r}')}{\partial n'} ds' \quad (34c)$$

$$\phi_n^{N,D}(\mathbf{r}) = \frac{1}{4\pi} \int_S \frac{\partial}{\partial n'} \left( \frac{1}{R} - \frac{1}{R_i} \right) u_n^T(\mathbf{r}') ds' \quad (34d)$$

In this form it is seen that if  $u_m^T$  are known for  $m = 0, 1, \dots, n-1$  then the problem of finding  $u_n^T$  is reduced to the following boundary value problems for  $\phi_n$ :

$$\begin{aligned} D, D: \quad \nabla^2 \phi_n^{D,D}(\mathbf{r}) &= 0, \quad \mathbf{r} \in V^+; \\ \phi_n^{D,D}(\mathbf{r}) &= O\left(\frac{1}{r^2}\right) \text{ as } r \rightarrow \infty; \\ \phi_n^{D,D}(\mathbf{r}) &= -F_n^{D,D}(\mathbf{r}), \quad \mathbf{r} \in S; \\ \phi_n^{D,D}(\mathbf{r}) &= 0, \quad z = 0 \end{aligned} \quad (35)$$

$$\begin{aligned} N, N: \quad \nabla^2 \phi_n^{N,N}(\mathbf{r}) &= 0, \quad \mathbf{r} \in V^+; \\ \phi_n^{N,N}(\mathbf{r}) &= O\left(\frac{1}{r^2}\right) \text{ as } r \rightarrow \infty; \\ \frac{\partial \phi_n^{N,N}(\mathbf{r})}{\partial n} &= -\frac{\partial F_n^{N,N}(\mathbf{r})}{\partial n}, \quad \mathbf{r} \in S; \\ \frac{\partial \phi_n^{N,N}}{\partial n} &= 0, \quad z = 0 \end{aligned} \quad (36)$$

$$\begin{aligned}
D, N: \quad \nabla^2 \phi_n^{D,N}(\mathbf{r}) &= 0, \quad \mathbf{r} \in V^+; \\
\phi_n^{D,N}(\mathbf{r}) &= O\left(\frac{1}{r}\right) \text{ as } r \rightarrow \infty; \\
\phi_n^{D,N}(\mathbf{r}) &= -F_n^{D,N}(\mathbf{r}), \quad \mathbf{r} \in S; \\
\frac{\partial \phi_n^{D,N}(\mathbf{r})}{\partial n} &= 0, \quad z = 0
\end{aligned} \tag{37}$$

$$\begin{aligned}
N, D: \quad \nabla^2 \phi_n^{N,D}(\mathbf{r}) &= 0, \quad \mathbf{r} \in V^+; \\
\phi_n^{N,D}(\mathbf{r}) &= O\left(\frac{1}{r^2}\right) \text{ as } r \rightarrow \infty; \\
\frac{\partial \phi_n^{N,D}(\mathbf{r})}{\partial n} &= -\frac{\partial F_n^{D,D}(\mathbf{r})}{\partial n}, \quad \mathbf{r} \in S; \\
\phi_n^{N,D}(\mathbf{r}) &= 0, \quad z = 0.
\end{aligned} \tag{38}$$

The growth as  $r \rightarrow \infty$  is determined from the asymptotic forms of (34a-d) and we remark that only  $\phi_n^{D,N}$  decays as  $\frac{1}{r}$ , the other potentials all decay as  $\frac{1}{r^2}$ . Thus the problem of determining the coefficients  $u_n^T$  is reduced to a succession of potential problems wherein only the boundary data on  $S$  changes with  $n$ .

### THE FAR FIELD

The quantity of most concern in target discrimination problems is the far field coefficient or scattering amplitude from which scattering cross sections may be determined. This quantity,  $g$ , is defined through the asymptotic relation

$$u^s(\mathbf{r}) = \frac{e^{ikr}}{ikr} g + O\left(\frac{1}{r^2}\right). \tag{39}$$

The differential scattering cross section is given in terms of  $g$  by

$$\sigma(\hat{x}) = \frac{4\pi}{k^2} |g|^2. \tag{40}$$

Explicit low frequency expressions for  $g$  may be obtained by taking the asymptotic forms of the integrands in (19), (21), (23) and (25)

$$\frac{e^{ikR}}{R} \pm \frac{e^{ikR_i}}{R} = \frac{e^{ikr}}{r} \left( e^{-ik\hat{\mathbf{r}}\cdot\mathbf{r}'} \pm e^{-ik\hat{\mathbf{r}}_i\cdot\mathbf{r}'} \right) \tag{41}$$

to find that

$$g^{D,D} = -\frac{ik}{4\pi} \int_S (e^{-ik\hat{\mathbf{r}}\cdot\mathbf{r}'} - e^{-ik\hat{\mathbf{r}}_i\cdot\mathbf{r}'} ) \frac{\partial u^T(\mathbf{r}')}{\partial n'} ds' \tag{42a}$$

$$g^{N,N} = \frac{ik}{4\pi} \int_S \frac{\partial}{\partial n'} (e^{-ik\hat{\mathbf{r}}\cdot\mathbf{r}'} + e^{-ik\hat{\mathbf{r}}_i\cdot\mathbf{r}'} ) u^T(\mathbf{r}') ds' \tag{42b}$$

$$g^{D,N} = -\frac{ik}{4\pi} \int_S (e^{-ik\hat{\mathbf{r}}\cdot\mathbf{r}'} + e^{-ik\hat{\mathbf{r}}_i\cdot\mathbf{r}'} ) \frac{\partial}{\partial n'} u^T(\mathbf{r}') ds' \tag{42c}$$

$$g^{N,D} = \frac{ik}{4\pi} \int_S \frac{\partial}{\partial n'} (e^{-ik\hat{\mathbf{r}}\cdot\mathbf{r}'} - e^{-ik\hat{\mathbf{r}}_i\cdot\mathbf{r}'} ) u^T(\mathbf{r}') ds'. \tag{42d}$$

The power series expansions of the exponentials in (42a-d) together with the low frequency expansions

(26a) and (32a-d) enable us to obtain low frequency expansions of the scattering amplitudes as follows

$$g^{D,D} = -\frac{1}{4\pi} \sum_{n=1}^{\infty} \frac{(ik)^{n+1}}{n!} \sum_{m=1}^n \binom{n}{m} (-1)^m \int_S [(\hat{\mathbf{r}}\cdot\mathbf{r}')^m - (\hat{\mathbf{r}}_i\cdot\mathbf{r}')^m] \frac{\partial}{\partial n'} (F_{n-m}^{D,D}(\mathbf{r}') + \phi_{n-m}^{D,D}(\mathbf{r}')) ds' \tag{43a}$$

$$g^{N,N} = \frac{1}{4\pi} \sum_{n=1}^{\infty} \frac{(ik)^{n+1}}{n!} \sum_{m=1}^n \binom{n}{m} (-1)^m \int_S \frac{\partial}{\partial n'} [(\hat{\mathbf{r}}\cdot\mathbf{r}')^m + (\hat{\mathbf{r}}_i\cdot\mathbf{r}')^m] (F_{n-m}^{N,N}(\mathbf{r}') + \phi_{n-m}^{N,N}(\mathbf{r}')) ds' \tag{43b}$$

$$g^{D,N} = -\frac{1}{4\pi} \sum_{n=0}^{\infty} \frac{(ik)^{n+1}}{n!} \sum_{m=1}^n \binom{n}{m} (-1)^m \int_S [(\hat{\mathbf{r}}\cdot\mathbf{r}')^m + (\hat{\mathbf{r}}_i\cdot\mathbf{r}')^m] \frac{\partial}{\partial n'} (F_{n-m}^{D,N}(\mathbf{r}') + \phi_{n-m}^{D,N}(\mathbf{r}')) ds' \tag{43c}$$

$$g^{N,D} = \frac{1}{4\pi} \sum_{n=1}^{\infty} \frac{(ik)^{n+1}}{n!} \sum_{m=1}^n \binom{n}{m} (-1)^m \int_S \frac{\partial}{\partial n'} [(\hat{\mathbf{r}}\cdot\mathbf{r}')^m - (\hat{\mathbf{r}}_i\cdot\mathbf{r}')^m] (F_{n-m}^{N,D}(\mathbf{r}') + \phi_{n-m}^{N,D}(\mathbf{r}')) ds' \tag{43d}$$

### LOWEST ORDER TERMS - PLANE WAVE INCIDENCE

When the incident field is a plane wave the low frequency expansion coefficients are given by equation (27). The first few are

$$\begin{aligned}
u_{00}^-(\mathbf{r}) &= 0 & u_{01}^-(\mathbf{r}) &= 2z k_z \\
u_{00}^+(\mathbf{r}) &= 2 & u_{01}^+(\mathbf{r}) &= 2x k_x + ry k_y
\end{aligned} \tag{44}$$

where  $k_x, k_y$  and  $k_z$  are the rectangular components of the unit incident direction vector  $\hat{\mathbf{k}}$ . Introducing these coefficients into (33a-d) we find that

$$F_0^{D,D}(\mathbf{r}) = F_0^{N,D}(\mathbf{r}) = 0, \tag{45a}$$

$$F_0^{N,N}(\mathbf{r}) = F_0^{D,N}(\mathbf{r}) = 2, \tag{45b}$$

$$F_1^{D,D}(\mathbf{r}) = F_1^{N,D}(\mathbf{r}) = 2z k_z, \tag{46a}$$

$$F_1^{N,N}(\mathbf{r}) = 2x k_x + 2y k_y, \tag{46b}$$

$$F_1^{D,N}(\mathbf{r}) = 2x k_x + 2y k_y - \frac{1}{4\pi} \int_S \frac{\partial}{\partial n'} \phi_0^{D,N}(\mathbf{r}') ds'. \tag{46c}$$

Having found the lowest order  $F$ 's we may now formulate the lowest order boundary value problems. From (35) we see that  $\phi_0^{D,D}(\mathbf{r}) = 0$  since it solves a (well-posed) homogeneous boundary value problem. Similarly  $\phi_0^{N,N}(\mathbf{r}) = 0$  and  $\phi_0^{N,D}(\mathbf{r}) = 0$ . The first nontrivial boundary value problems to be solved are

$$\begin{aligned}
D, D: \quad \nabla^2 \phi_1^{D,D}(\mathbf{r}) &= 0, \mathbf{r} \in V^+; \\
\phi_1^{D,D}(\mathbf{r}) &= O\left(\frac{1}{r^2}\right) \text{ as } r \rightarrow \infty; \\
\phi_1^{D,D}(\mathbf{r}) &= -2z k_z, \mathbf{r} \in S; \\
\phi_1^{D,D}(\mathbf{r}) &= 0, z = 0
\end{aligned} \tag{47}$$

$$\begin{aligned}
N, N: \quad \nabla^2 \phi_1^{N,N}(\mathbf{r}) &= 0, \mathbf{r} \in V^+; \\
\phi_1^{N,N}(\mathbf{r}) &= O\left(\frac{1}{r^2}\right) \text{ as } r \rightarrow \infty; \\
\frac{\partial \phi_1^{N,N}}{\partial n} &= -2n_x k_x - 2n_y k_y, \mathbf{r} \in S; \\
\frac{\partial \phi_1^{N,N}}{\partial n} &= 0, z = 0
\end{aligned} \tag{48}$$

$$\begin{aligned}
D, N: \quad \nabla^2 \phi_0^{D,N}(\mathbf{r}) &= 0, \mathbf{r} \in V^+, \\
\phi_0^{D,N}(\mathbf{r}) &= O\left(\frac{1}{r}\right) \text{ as } r \rightarrow \infty; \\
\phi_1^{D,N}(\mathbf{r}) &= -2, \mathbf{r} \in S; \\
\frac{\partial \phi_0^{D,N}}{\partial n} &= 0, z = 0
\end{aligned} \tag{49}$$

$$\begin{aligned}
N, D: \quad \nabla^2 \phi_1^{N,D}(\mathbf{r}) &= 0, \mathbf{r} \in V^+, \\
\phi_1^{N,D}(\mathbf{r}) &= O\left(\frac{1}{r^2}\right) \text{ as } r \rightarrow \infty; \\
\frac{\partial \phi_1^{N,D}}{\partial n} &= -2n_z k_z, \mathbf{r} \in S; \\
\phi_1^{N,D}(\mathbf{r}) &= 0, z = 0
\end{aligned} \tag{50}$$

These boundary value problems are awkward in that they involve the infinite boundary  $z = 0$ . However consideration of this boundary may be eliminated by considering the boundary value problems for  $S \cup S_i$  which arise by continuing  $\phi_1^{D,D}(\mathbf{r})$  and  $\phi_1^{N,D}(\hat{\mathbf{r}})$  into  $V_i^+$  as odd functions of  $z$  and continuing  $\phi_1^{N,N}(\mathbf{r})$  and  $\phi_0^{D,N}(\mathbf{r})$  as even functions of  $z$ . The corresponding boundary value problems for  $S$  and its image are

$$\begin{aligned}
D, D: \quad \nabla^2 \psi_1^{D,D}(\mathbf{r}) &= 0, \mathbf{r} \in V^+ \cup V_i^+ \cup S_0 \\
\psi_1^{D,D}(\mathbf{r}) &= O\left(\frac{1}{r^2}\right) \text{ as } r \rightarrow \infty
\end{aligned} \tag{51}$$

$$\begin{aligned}
N, N: \quad \nabla^2 \psi_1^{N,N}(\mathbf{r}) &= 0, \mathbf{r} \in V^+ \cup V_i^+ \cup S_0 \\
\psi_1^{N,N}(\mathbf{r}) &= O\left(\frac{1}{r^2}\right) \text{ as } r \rightarrow \infty \\
\frac{\partial \psi_1^{N,N}}{\partial n}(\mathbf{r}) &= -2n_x k_x - 2n_y k_y, \\
\mathbf{r} &\in S \cup S_i
\end{aligned} \tag{52}$$

$$\begin{aligned}
D, N: \quad \nabla^2 \psi_0^{D,N}(\mathbf{r}) &= 0, \mathbf{r} \in V^+ \cup V_i^+ \cup S_0 \\
\psi_0^{D,N}(\mathbf{r}) &= O\left(\frac{1}{r}\right) \text{ as } r \rightarrow \infty \\
\psi_0^{D,N}(\mathbf{r}) &= -2, \mathbf{r} \in S \cup S_i
\end{aligned} \tag{53}$$

$$\begin{aligned}
N, D: \quad \nabla^2 \psi_1^{N,D}(\mathbf{r}) &= 0, \mathbf{r} \in V^+ \cup V_i^+ \cup S_0 \\
\psi_1^{N,D}(\mathbf{r}) &= O\left(\frac{1}{r^2}\right) \text{ as } r \rightarrow \infty \\
\frac{\partial \psi_1^{N,D}}{\partial n} &= -2n_z k_z, \mathbf{r} \in S \cup S_i
\end{aligned} \tag{54}$$

The restrictions of the functions  $\psi$  to  $V^+$  are the corresponding functions  $\phi$ .

Using this fact together with (45) and (46) in the expressions for the scattering amplitudes, (43a-d), we find

$$g^{D,D} = \frac{(ik)^3}{2\pi} \hat{r}_z \int_S z' \frac{\partial}{\partial n'} (2z' k_z + \psi_1^{D,D}(\mathbf{r}')) ds' + O(k^4) \tag{55a}$$

$$g^{N,N} = -\frac{(ik)^3}{4\pi} \int_S \frac{\partial}{\partial n'} (2\hat{r}_x x' + 2\hat{r}_y y') (2x' k_x + 2y' k_y + \psi_1^{N,N}(\mathbf{r}')) ds' + O(k^4) \tag{55b}$$

$$g^{D,N} = -\frac{(ik)}{2\pi} \int_S \frac{\partial}{\partial n'} \psi_0^{D,N}(\mathbf{r}') ds' + O(k^2) \tag{55c}$$

$$g^{N,D} = -\frac{(ik)^3}{2\pi} \hat{r}_z \int_S n_z (2z' k_z + \psi_1^{N,D}(\mathbf{r}')) ds' + O(k^4) \tag{55d}$$

where  $(\hat{r}_x, \hat{r}_y, \hat{r}_z)$  are the rectangular components of the unit vector  $\hat{\mathbf{r}}$ . Since it may be shown that

$$\int_S z' \frac{\partial z'}{\partial n'} ds' = |V^-| \tag{56}$$

and

$$\int_S \frac{\partial}{\partial n'} (\hat{r}_x x' + \hat{r}_y y') (x' k_x + y' k_y) ds' = (\hat{r}_x k_x + \hat{r}_y k_y) |V^-| \tag{57}$$

where  $|V^-|$  is the volume of the region  $V^-$  we may rewrite some of these expressions as

$$g^{D,D} = \frac{(ik)^3}{2\pi} (2k_z \hat{r}_z |V^-| + \hat{r}_z \int_S \frac{\partial \psi_1^{D,D}}{\partial n'}(\mathbf{r}') ds') + O(k^4) \tag{58a}$$

$$g^{N,N} = -\frac{(ik)^3}{2\pi} \{2(\hat{r}_x k_x + \hat{r}_y k_y) |V^-| + \int_S \frac{\partial}{\partial n'} (\hat{r}_x x' + \hat{r}_y y') \psi_1^{N,N}(\mathbf{r}') ds'\} + O(k^4) \tag{58b}$$

$$g^{N,D} = -\frac{(ik)^3}{2\pi} \hat{r}_z \{2k_z |V^-| + \int_S n_z \psi_1^{N,D}(\mathbf{r}') ds'\} + O(k^4) \tag{58c}$$

Expressions (58a-c) clearly indicate that in addition to the expected volume dependence of the lowest order term in the scattering amplitude, there is an additional term which carries other geometric information about the scatterer. An alternate form for these expressions which more clearly illustrate the effect of the ground plane is

$$g^{D,D} = \frac{(ik)^3}{4\pi} \left\{ \int_S \hat{\mathbf{r}} \cdot \mathbf{r}' \frac{\partial}{\partial n'} (2z' k_z + \psi_1^{D,D}(\mathbf{r}')) ds' \right. \tag{59a}$$

$$\begin{aligned}
& - \int_{S_i} \hat{\mathbf{r}} \cdot \mathbf{r}' \frac{\partial}{\partial n'} (2z'k_z + \psi_1^{D,D}(\mathbf{r}')) ds' \Big\} + O(k^4) \\
g^{N,N} = & - \frac{(ik)^3}{4\pi} \left\{ \int_S \frac{\partial}{\partial n'} ((\hat{\mathbf{r}} \cdot \mathbf{r}') (2x'k_x + 2y'k_y \right. \\
& \left. + \psi_1^{N,N}(\mathbf{r}')) ds' \right. \\
& \left. + \int_{S_i} \frac{\partial}{\partial n'} (\hat{\mathbf{r}} \cdot \mathbf{r}') (2x'k_x + 2y'k_y + \psi_1^{N,N}(\mathbf{r}')) ds' \right\} \\
& + O(k^4) \quad (59b) \\
g^{D,N} = & - \frac{(ik)}{4\pi} \left\{ \int_S \frac{\partial}{\partial n'} \psi_0^{D,N}(\mathbf{r}') ds' + \right. \\
& \left. \int_{S_i} \frac{\partial}{\partial n'} \psi_0^{D,N}(\mathbf{r}') ds' \right\} + O(k^2) \quad (59c) \\
g^{N,D} = & - \frac{(ik)^3}{4\pi} \left\{ \int_S \hat{\mathbf{r}} \cdot \hat{\mathbf{n}}(\mathbf{r}') (2z'k_z + \psi_1^{N,D}(\mathbf{r}')) ds' \right. \\
& \left. - \int_{S_i} \hat{\mathbf{r}} \cdot \hat{\mathbf{n}}(\mathbf{r}') (2z'k_z + \psi_1^{N,D}(\mathbf{r}')) ds' \right\} + O(k^4) \\
& (59d)
\end{aligned}$$

These expressions illustrate exactly how the presence of the ground plane and the boundary condition on it affect the low frequency scattering amplitude. It is particularly noteworthy that for the Dirichlet boundary condition in  $S$  and a Neumann condition on  $S_0$ ,  $g^{D,N}$  is  $O(k)$  just as for the Dirichlet condition on  $S$  in the absence of a ground plane [e.g. 2], whereas a Dirichlet condition on the ground plane changes the low frequency behavior drastically, so that it has the same  $k$  dependence as for the case of the Neumann condition on  $S$  in the absence of the ground plane.

#### An example.

Of course, in order to complete the determination of the low frequency scattering amplitude, one must determine the solutions of the boundary value problems (51)–(54). Thus it is not possible for an arbitrary boundary  $S$  by other than numerical methods. But it is possible in the case of a sphere and we conclude with this example.

We introduce bispherical coordinates [e.g. 3]

$$x = \frac{a \sin \theta \cos \phi}{\cosh \eta - \cos \theta}, \quad -\infty < \eta < +\infty \quad (60a)$$

$$y = \frac{a \sin \theta \sin \phi}{\cosh \eta - \cos \theta}, \quad 0 \leq \theta \leq \pi \quad (60b)$$

$$z = \frac{a \sinh \eta}{\cosh \eta - \cos \theta}, \quad 0 \leq \theta < 2\pi, a > 0 \quad (60c)$$

In these coordinates  $\eta = 0$  is the plane  $z = 0$  and  $\eta = \eta_0$  is the sphere,

$$x^2 + y^2 + (z - a \coth \eta_0)^2 = \frac{a^2}{\sinh^2 \eta_0} \quad (61)$$

with center at  $a \coth \eta_0$  and radius  $\frac{a}{\sinh \eta_0}$  while  $\eta = -\eta_0$  is the image sphere in the plane  $z = 0$ . Separation of variables provides the general solution of Laplace's equation in these coordinates as

$$\begin{aligned}
\phi = & \sqrt{\cosh \eta - \cos \theta} \sum_{n=0}^{\infty} [a_n e^{(n+1/2)\eta} + b_n e^{-(n+1/2)\eta}] \\
& \sum_{m=0}^n P_n^m(\cos \theta) [c_m \cos m\phi + d_m \sin m\phi]. \quad (62)
\end{aligned}$$

Then the problem of determining  $\phi_0^{D,N}$  becomes that of determining  $a_n, b_n, c_m, d_m$  so that the expression given above is equal to  $-2$  when  $\eta = \eta_0$  and equal to zero when  $\eta = 0$ . Using the expansion [4]

$$\frac{1}{\sqrt{\cosh \eta - \cos \theta}} = \sqrt{2} \sum_{n=0}^{\infty} e^{-(n+1/2)|\eta|} P_n(\cos \theta) \quad (63)$$

we have

$$\begin{aligned}
& \sum_{n=0}^{\infty} (a_n e^{(n+1/2)\eta_0} + b_n e^{-(n+1/2)\eta_0}) \\
& \sum_{m=0}^n P_n^m(\cos \theta) [c_m \cos m\phi + d_m \sin m\phi] \\
& = -2\sqrt{2} \sum_{n=0}^{\infty} e^{-(n+1/2)\eta_0} P_n(\cos \theta) \quad (64)
\end{aligned}$$

and

$$\sum_{n=0}^{\infty} (a_n + b_n) \sum_{m=0}^n P_n^m(\cos \theta) (c_m \cos m\phi + d_m \sin m\phi) = 0 \quad (65)$$

from which we conclude that

$$\begin{aligned}
b_n & = -a_n \\
c_m & = d_m = 0, \quad m \geq 1 \\
c_0 & = 1
\end{aligned}$$

and

$$a_n = -\sqrt{2} \frac{e^{-(n+1/2)\eta_0}}{\sinh(n+1/2)\eta_0} \quad (66)$$

so that

$$\begin{aligned}
\phi_0^{D,N} = & -2\sqrt{2} \sqrt{\cosh \eta - \cos \theta} \sum_{n=0}^{\infty} \frac{\sinh(n+1/2)\eta}{\sinh(n+1/2)\eta_0} \\
& e^{-(n+1/2)\eta_0} P_n(\cos \theta). \quad (67)
\end{aligned}$$

To determine  $\phi_1^{D,D}$  we must find the coefficients in (62) so that  $\phi_1^{D,D} = 0$  on  $\eta = 0$  and on  $\eta = \eta_0$  is equal to

$-2zk_z = -2k_z \frac{a \sinh \eta_0}{\cosh y_0 - \cos \theta}$ . As in the previous case the homogeneous Dirichlet condition on  $\eta = 0$  implies that  $b_n = -a_n$  and the absence of a  $\phi$  dependence in the data implies that  $c_m = d_m = 0$ ,  $m \geq 1$  and  $c_0 = 1$ . Then the problem becomes that of determining  $a_n$  so that

$$\begin{aligned} 2\sqrt{\cosh \eta_0 - \cos \theta} \sum_{n=0}^{\infty} a_n \sinh(n+1/2) \eta_0 P_n(\cos \theta) \\ = -\frac{2k_z a \sinh \eta_0}{\cosh \eta_0 - \cos \theta} \end{aligned} \quad (68)$$

or

$$\begin{aligned} \sum_{n=0}^{\infty} a_n \sinh(n+1/2) \eta_0 P_n(\cos \theta) &= -\frac{k_z a \sinh y_0}{(\cosh \eta_0 - \cos \theta)^{3/2}} \\ &= 2k_z a \frac{d}{d\eta_0} \frac{1}{\cosh \eta_0 - \cos \theta} \end{aligned} \quad (69)$$

Again employing the expansion (63) we may rewrite (69) as

$$\begin{aligned} \sum_{n=0}^{\infty} a_n \sinh(n+1/2) \eta_0 P_n(\cos \theta) &= -2\sqrt{2} k_z a \sum_{n=0}^{\infty} \\ &(n+1/2) e^{-(n+1/2)\eta_0} P_n(\cos \theta) \end{aligned} \quad (70)$$

from which we see that

$$a_n = -2\sqrt{2} k_z a (n+1/2) \frac{e^{-(n+1/2)\eta_0}}{\sinh(n+1/2) \eta_0} \quad (71)$$

Therefore

$$\begin{aligned} \phi_1^{D,D} &= -4\sqrt{2} k_z a \sqrt{\cosh \eta - \cos \theta} \sum_{n=0}^{\infty} (n+1/2) \\ &\frac{\sinh(n+1/2) \eta}{\sinh(n+1/2) \eta_0} e^{-(n+1/2)\eta_0} P_n(\cos \theta) \end{aligned} \quad (72)$$

Comparison of (67) and (72) shows the considerable effect of the ground plane on the low frequency field for the same object above the plane.

#### ACKNOWLEDGMENT

This work was supported under AGARD SPP Support Project G-84 and AFOSR Grant No. F49620-96-1-0039.

#### REFERENCES

1. Lindell, I. *Methods for Electromagnetic Field Analysis*, Oxford Science Publications, Clarendon Press, Oxford, 1992.
2. Kleinman, R. E. and Senior, T. B. A., Low Frequency Scattering, in *Low and High Frequency Asymptotics*, V. K. Varadan and V. V. Varadan, eds., North Holland, Amsterdam, 1986, 1-70.
3. Moon, P. and Spencer, D. E., *Field Theory Handbook*, Springer-Verlag, Berlin, 1961.
4. Morse, P. and Feshbach, H., *Methods of Theoretical Physics*, Vol II, McGraw Hill, New York, 1953, p. 1299.

**Discussor's name:** G.S. BROWN

**Comment/Question:**

Did you compare your solution to the classical image approach?

**Author/Presenter's reply:**

Yes, in fact that is precisely how we obtained the solution. But it should be mentioned that image theory would not be available for more complicated conditions on the ground plane, unless one employed the complex image theory developed by I. Lindell and colleagues, which is considerably more complicated.

**Discussor's name:** M.F. LEVY

**Comment/Question:**

Do you have any plans for numerical implementation of your low-frequency theory?

**Author/Presenter's reply:**

Both Professor Dassios and I are mathematicians who are being drawn closer and closer to computational electromagnetics. But we have no immediate plans to implement this low frequency theory numerically. We would be happy to collaborate with people interested in such implementation and may do so with interested students.

**Discussor's name:** J.H. RICHTER

**Comment/Question:**

In geometries where interactions of the target with surrounding surfaces become important, clutter from such surfaces may be a more serious operational problem than cross-section changes caused by interactions with the surface.

**Author/Presenter's reply:**

I agree that clutter is a serious problem that must be addressed. However, even if the effects of clutter can be filtered out with various signal processing methods (and I think it can), the alteration of the cross-section due to interaction with the ground should be taken into account.

## RCS CALCULATIONS WITH THE PARABOLIC WAVE EQUATION

M.F. Levy, P-P. Borsboom, A.A. Zaporozhets and A. Zebic-Le Hyaric

Rutherford Appleton Laboratory

Chilton, Didcot

Oxfordshire OX11 0QX

U.K.

### 1. SUMMARY

Parabolic equation (PE) techniques have been used for some time to solve various types of wave propagation problems. They provide an efficient solution for long-range forward propagation radar and sonar predictions [1,10,12,13,14]. More recently, they have been applied to scattering problems, and in particular to RCS calculations [9,16]. Our aim in this paper is to summarise the PE techniques currently available for RCS work and to give a few typical examples in two and three dimensions.

### 2. PE BASICS

The basic idea of parabolic equation methods is to factor the wave equation into two terms representing respectively the forward and backward propagating energy.

Starting with the scalar wave equation in cartesian coordinates, we introduce the reduced function associated with a field component,

$$u(x, y, z) = \exp(-ikx)\psi(x, y, z)$$

The  $x$ -direction is the paraxial direction: in a ray picture, forward propagation corresponds to rays propagating with increasing  $x$ , and backward propagation to rays propagating with decreasing  $x$ .

The scalar wave equation in terms of  $u$  is then factored as

$$\left\{ \frac{\partial}{\partial x} + ik(1-Q) \right\} \left\{ \frac{\partial}{\partial x} + ik(1+Q) \right\} u = 0 \quad (1)$$

where  $k$  is a reference wave number and the pseudo-differential operator  $Q$  is defined by

$$Q = \sqrt{\frac{1}{k^2} \frac{\partial^2}{\partial y^2} + \frac{1}{k^2} \frac{\partial^2}{\partial z^2} + n^2(x, y, z)}$$

where  $n$  is the refractive index of the medium.

The two terms correspond respectively to forward and back propagating waves. The factorisation is formally exact in a range-independent medium for energy propagating in a cone of directions with non-zero  $x$ -coordinates, and only approximate for a range-dependent medium, since the partial  $x$ -derivative does not then commute with the operator  $Q$ .

The main difficulties are that the square-root operator  $Q$  can only be defined in a paraxial cone, and that rational approximations to it become less accurate as the cone gets wider. However the factorisation has the great advantage that both terms are pseudo-differential equations of first order in  $x$  (hence the "parabolic" terminology), which can be solved by marching techniques.

For example in a range-independent medium the forward parabolic equation has the formal solution

$$u(x + \Delta x, y, z) = e^{ik\Delta x(-1+Q)} u(x, y, z) \quad (2)$$

Hence the forward propagating field is obtained at a given range from the field at a previous range, and appropriate boundary conditions. The computational gain is substantial compared to the elliptic wave equation, which must be solved simultaneously at all points of the integration domain.

Fig. 1 illustrates forward integration of the PE.

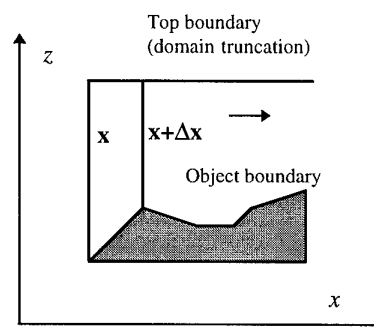


Fig. 1. Forward integration with the PE

The simplest approximation of Eq. 2 is obtained by using first order Taylor expansions of the square-root and the exponential. This yields the Standard Parabolic Equation (SPE)

$$\frac{\partial u}{\partial x} = \frac{i}{2k} \left( \frac{\partial^2 u}{\partial y^2} + \frac{\partial^2 u}{\partial z^2} \right) + \frac{ik}{2} (n^2 - 1) u \quad (3)$$

The SPE is extremely useful for solving long-range radiowave propagation problems where the paraxial cone of interest is usually narrow (of the orders of 1 or 2 degrees). We shall see in sections 3 and 4 that more sophisticated methods are available for solving large angle scattering problems.

In order to treat backward propagation, scattering objects are treated as a sequence of reflecting facets. Starting with the field set to zero on a transverse plane beyond the scatterer, the solution is marched back, adding the new facet sources at each step, as indicated in Fig. 2.

In what follows, we concentrate on the case where  $n=1$ , which is central to RCS problems. An important place is given to two-dimensional problems, depending only on the variables  $x$  and  $z$ .

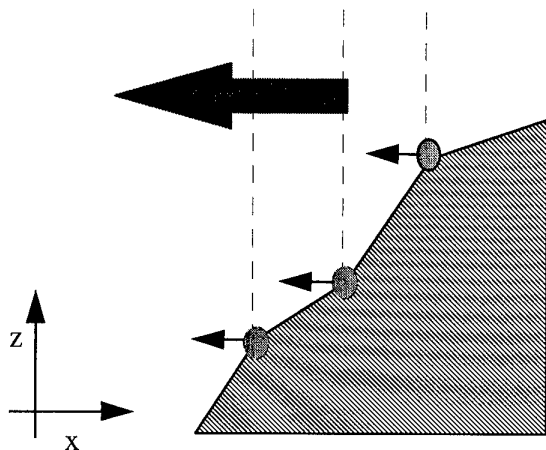


Figure 2. Backward propagation with the PE

### 3. 2D WIDE ANGLE PES

The SPE works well enough for small propagation angles but in order to model diffraction and scattering accurately, a larger angular spectrum must be taken into account. This is achieved by approximating more accurately the exponential operator introduced in Eq. 2: either as a rational function (Claerbout PE, valid up to about 40 degrees) [6] or as a Padé series (split-step Padé technique, valid for arbitrary angles) [8,21].

#### 3.1 Claerbout method

The Claerbout approximation is obtained by approximating the exponential operator in Eq. 2 as a rational function. We put  $Q = \sqrt{1+Z}$ , where  $Z = \frac{1}{k^2} \frac{\partial^2}{\partial z^2}$ , and use the Padé (1,1) approximation

$$e^{ik\Delta x(-1+\sqrt{1+Z})} \cong \frac{1+bZ}{1+aZ} \quad (4)$$

where  $a=0.25$  and  $b=0.75$ . These values are obtained by first applying a Taylor expansion to the exponential operator and then multiplying both sides of the resulting equation with  $(1+aZ)$ . By equating the powers of  $Z$  on both sides we obtain  $a$  and  $b$ . Note that by putting  $a=0$ ,  $b=0.5$  we obtain the SPE.

An estimate of the maximum angle of propagation for various PEs has been discussed by Lee and McDaniel [13]. For the Claerbout PE this maximum angle is roughly 40 degrees compared with 15-20 degrees for the SPE.

By applying the Claerbout approximation we have gained another 20 degrees in angular range. However, this improved accuracy comes at the cost of an increased sensitivity to numerical errors in both the initial field and the boundary conditions on scatterers [20]. Furthermore, the angles encountered when treating diffraction and scattering from objects with edges and corners or by small objects easily exceed this upper boundary of 40 degrees. A more accurate and numerically more stable method was therefore desirable and was found in the split-step Padé technique which is treated in the next section.

#### 3.2 Split-step Padé method

The split-step Padé (SSP) solution, which is valid for very wide propagation angles, has been introduced by M.D. Collins [8]. A Padé approximation is applied to the exponential operator in the form

$$e^{ik\Delta x(-1+\sqrt{1+Z})} \cong 1 + \sum_{j=1}^N \frac{a_j Z}{1+b_j Z} \quad (5)$$

where the  $2N$  complex coefficients  $(a_j, b_j)$  have to be determined.

We use the method described in [8], where  $2N-1$  constraints are used to enforce equality of the first terms of the Taylor expansions of both sides, and the remaining constraint is that the negative real axis is mapped to the upper half of the complex plane. This last constraint forces the energy associated with the evanescent spectrum to decay with range, which ensures stability of the method. The coefficients are computed with a Newton algorithm as in [8]. As the number  $N$  of terms increases, so does the angular cone of validity. With  $N=8$ , propagation angles of up to 70 degrees can be modelled [21]. The method is very stable, and allows the use of large range steps.

The Padé approximation yields the split-step Padé solution:

$$u(x+\Delta x, z) = u(x, z) + \sum_{j=1}^N q_j(x+\Delta x, z) \quad (6)$$

where the  $N$  auxiliary functions  $q_j$  are defined by

$$q_j(x+\Delta x, z) = a_j(1+b_j Z)^{-1} Z u(x, z), \quad j=1, 2, \dots, N \quad (7)$$

This equation is solved at the advanced range by solving for each  $q_j$ . One advantage of this method is that it lends itself quite well to parallel computing, as the  $q_j$ 's can be solved for independently at each step.

The resulting matrices are tridiagonal and the system can conveniently be solved using a Gaussian elimination method [21].

#### 4. 3D PEs

##### 4.1 Axial symmetry

Three-dimensional problems simplify if there is axial symmetry with respect to the  $x$ -axis. Written in cylindrical coordinates  $(r, \theta, x)$ , the SPE becomes

$$\frac{1}{r^2} \frac{\partial^2 u}{\partial \theta^2} + \frac{\partial^2 u}{\partial r^2} + \frac{1}{r} \frac{\partial u}{\partial r} + 2ik \frac{\partial u}{\partial x} = 0 \quad (8)$$

For the axially symmetric case, this simplifies to

$$\frac{\partial^2 u}{\partial r^2} + \frac{1}{r} \frac{\partial u}{\partial r} + 2ik \frac{\partial u}{\partial x} = 0 \quad (9)$$

The numerical solution is obtained with a Crank-Nicolson scheme. The apparent singularity at  $r=0$  is resolved by using the fact that the radial derivative must vanish on the axis of symmetry.

##### 4.2 General case: Padé methods

We rewrite the 3-dimensional PE as

$$\frac{\partial u}{\partial x} + ik(1 - \sqrt{1+Y+Z})u = 0 \quad (10)$$

where the operators  $Y$ ,  $Z$  are given by

$$Y = \frac{1}{k^2} \frac{\partial^2}{\partial y^2}, \quad Z = \frac{1}{k^2} \frac{\partial^2}{\partial z^2}$$

The formal solution is given by

$$u(x + \Delta x, y, z) = \exp(ik\Delta x(-1 + \sqrt{1+Y+Z}))u(x, y, z) \quad (11)$$

If we neglect coupling between  $Y$  and  $Z$ , the RHS of Eq. 11 factors into two terms, one involving only  $Y$  and one involving only  $Z$ . This treatment speeds up the computations considerably, but is limited to certain types of scatterers, for which boundary conditions decouple in  $y$  and  $z$  [20].

We now apply a Taylor expansion to the square-root operator. In order to treat the case of wide-angle propagation along the  $y$ -axis and narrow angle propagation along the  $z$ -axis, we use the Taylor expansion of third order in  $y$  and first order in  $z$ . Eq. 11 becomes

$$u(x + \Delta x, y, z) = e^{ik\Delta x \left( \frac{Y}{2} - \frac{Y^2}{8} + \frac{Y^3}{16} \right)} e^{ik\Delta x \frac{Z}{2}} u(x, y, z) \quad (12)$$

We now apply Padé (S,T) approximations (i.e. a rational function where S and T are the powers of the denominator and the numerator, see [19] for example) to

the  $Y$  and  $Z$  exponential terms separately. Good results are obtained for scattering problems with a combination of Padé (1,1) and Padé (2,1) schemes [20]. Both schemes are unconditionally stable. The Padé (1,1) scheme does not reduce oscillations that might be introduced by discontinuities in the field, for example at an object's edges, but is very flexible for incorporation of boundary conditions. The Padé (2,1) scheme suppresses oscillations, but is less amenable to boundary modelling. We have used the Padé (1,1) scheme for propagation along the scatterer, followed by the Padé (2,1) scheme once the field leaves the scatterer.

#### 5. DOMAIN TRUNCATION

Because the PE is solved with a marching method, the integration domain only needs to be truncated in the directions transverse to the paraxial direction ( $z$ -axis for 2D problems,  $y$ - $z$  plane for 3D problems). Several methods are available.

##### 5.1 Absorbing layers

This is the simplest way of truncating the integration domain. It consists of adding an absorbing layer around the domain of interest. This is easy to implement, but can be computationally expensive: at large scattering angles the absorbing layer can be two orders of magnitude larger than the domain of interest in order to avoid spurious reflections.

##### 5.2 Non-local boundary conditions

These provide clean truncation of the integration domain by matching the fields inside and outside the domain. This is done by expressing the outgoing solution outside the domain as a function of the solution on the boundary.

In two dimensions, non-local boundary conditions (NLBCs) are of the form

$$u(x, z_b) = \int_0^x \frac{\partial u}{\partial x}(x-t, z_b) w(t) dt + I(x) \quad (13)$$

where  $w$  is a singular kernel matched to the medium outside the domain and to the PE in use,  $z_b$  is the height of the horizontal boundary of interest, and  $I(x)$  represents incoming energy. Appropriate kernels are available for constant and linear media, and for the various versions of the PE (SPE, Claerbout, split-step Padé) [11,15,21].

Because NLBCs take into account the global properties of the solution, they are perfectly transparent at all angles of incidence. The NLBC formulation in the paraxial framework does not conflict with the marching of the solution, since it only involves values of the field before the range of interest.

In three dimensions, it is convenient to use cylindrical coordinates as in section 4.1. The non-local boundary

condition is applied along a tube centered on the  $x$ -axis [17].

NLBCs provide a very powerful truncation method which is applicable in particular to obliquely incident plane waves [21].

### 5.3 Perfectly Matched Layer

The Bérenger perfectly matched layers (PML) [2,3], originally designed to solve the full Maxwell's equations, can be adapted for the parabolic equation framework [7]. A PML medium is introduced outside the domain of interest, with the property that all outgoing waves are fully transmitted at the interface without generating any reflections.

Consider first a 2-dimensional example. The standard PE in a 2D PML medium for a matched interface at  $z=0$  is

$$\frac{1}{1-i\eta(z)} \frac{\partial}{\partial z} \left( \frac{1}{1-i\eta(z)} \frac{\partial u}{\partial z} \right) + 2ik \frac{\partial u}{\partial x} = 0 \quad (14)$$

where

$$\begin{cases} \eta(z) = 0, & z \leq 0 \\ \eta(z) > 0, & z > 0 \end{cases}$$

It can be shown that the solution of Eq.14 coincides with the usual PE solution in the half-plane below the interface, and has the form of a damped wave above the interface. For example an upward propagating plane wave with unit amplitude and angle  $\alpha$  between the  $x$ -axis and the direction of propagation, the PML solution has the form:

$$\exp\left(-ik\left(\frac{x}{2}\sin^2\alpha + z\sin\alpha\right) - kz\eta(z)\sin\alpha\right).$$

The PE for the PML can also be viewed as the generalization of the PE to a space where coordinate  $z$  has been mapped to complex coordinate  $\tilde{z}$  [18], given

$$\text{by } \tilde{z} = z - i \int_0^z \eta(s) ds.$$

In an infinite PML medium, the choice of the damping function  $\eta$  is arbitrary. In practice, the PML medium must be implemented with finite thickness, and some care must be taken in the choice of  $\eta$  in order to avoid spurious reflections at the top of the layer. A very thin PML is usually adequate (typically of the order of 10 grid points). In cases where two-sided truncation is required (top and bottom of the domain), it should be noted that this version of the PML is only applicable for either a point source inside the domain or an incident plane wave propagating in the  $x$ -direction.

We followed the recommendations in [3], where the damping function is a geometrical progression of the form  $\eta(z) = \eta_0 (g^{1/\Delta z})^z$ , where  $\Delta z$  is the distance

between grid points. In the numerical examples below, we have used  $\eta_0 = 10^{-9}$ ,  $g = 4$  and a thickness of 16 grid points. These parameters were obtained from a set of trial runs and seem adequate for the examples treated here. However for more general cases, for example involving long-range propagation, further investigation of optimal damping profiles is required.

For 3-dimensional problems the PML-layers are placed around the computational domain. For an rectangular domain (see Fig. 3) the top and bottom layers are generated by the transformation of the  $z$ -coordinate, the left and right layers by the transformation of the  $y$ -coordinate.

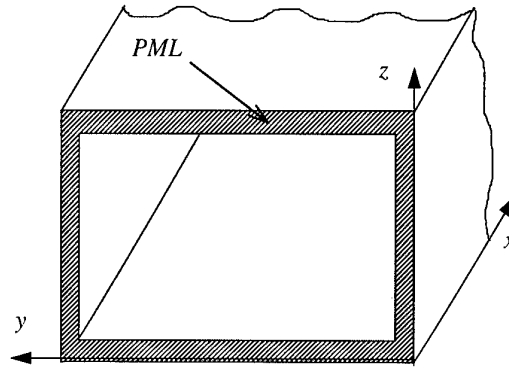


Fig. 3. PML in 3 dimensions

For a cylindrical domain (propagation along the axis of the cylinder) the layer is generated by the transformation of the radial  $r$ -coordinate.

## 6. BOUNDARY CONDITIONS ON SCATTERERS

### 6.1 2D problems

Scattering is modelled by treating the object as a series of vertical sections. The field is propagated from section to section using the PE whilst applying boundary conditions appropriate for a perfect electric conductor with or without a dielectric coating.

In case of a perfectly conducting obstacle either the field is set to zero on the boundary (TM polarization) or the normal derivative of the field is set to zero on the obstacle (TE polarization). For a coated scatterer, we apply a surface impedance mixed boundary condition:

$$\frac{\partial u}{\partial n}(x, z) = ik\delta(x, z) \quad (15)$$

where  $\frac{\partial}{\partial n}$  is the normal derivative and  $\delta$  is the normalized surface impedance, which depends on the slope of the boundary and the field polarization.

All three types of boundary conditions have been implemented and incorporated in the finite difference scheme we use to solve the PE. The normal derivative in Eq. 15 is expressed in terms of derivatives in height and

range. The SPE is used to replace the numerically difficult derivative in range by the second order derivative in height.

The backscattered field is obtained by treating the object as a sequence of point-apertures. On each contact point, the geometrical optical reflected field is added to the backward propagating field. The reflected field is obtained from the incident field by multiplication with the polarization dependent Fresnel reflection coefficient.

## 6.2 3D problems

The vector nature of the boundary conditions for general 3D electromagnetic scattering problems makes them untractable for the scalar PE method. However electromagnetic boundary conditions become scalar for certain scatterer geometries in the perfectly conducting case [20]. This is the case in particular for normal incidence on a block-shaped obstacle. Appropriate conditions (field or normal field derivative equal to zero) are applied on each facet, depending on polarization of the incident field.

Acoustic problems are easier to solve: the acoustically soft case (acoustic pressure is zero on the scatterer) is straightforward to implement for objects or arbitrary shapes.

The acoustically hard case (normal derivative of the acoustic pressure is zero on the scatterer) can be implemented without difficulty for the axially symmetric PE, but not for the Padé methods of section 4.2 since the boundary condition does not split into  $y$  and  $z$  parts.

## 6.3 Rough objects

Rough surfaces can be treated in a deterministic way with the PE method, by representing the rough surface explicitly as a composite of facets, as shown in Fig. 4 below. Here we use a set of rectangular plates, shifted along the normal to the surface with a Gaussian distribution of zero mean. The boundary conditions are applied to each plate, neglecting the side areas.

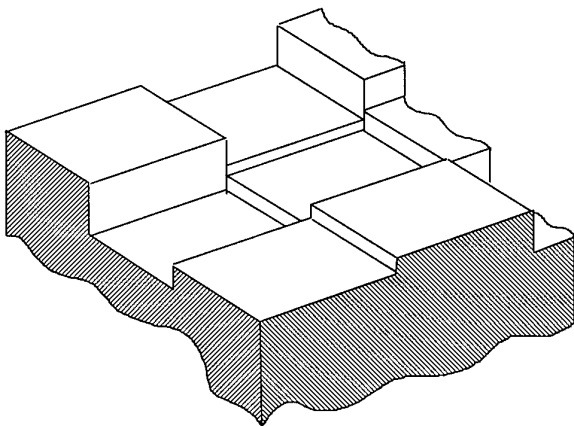


Fig. 4. Representation of rough surface for PE scattering

## 7. NEAR-FIELD/FAR-FIELD

The two-way PE solution gives the field at all points of the computational domain. The RCS is obtained from these near-field results by solving the PE in vacuum explicitly.

In the 2-dimensional case, the solution after leaving the obstacle is given by

$$u(x, z) = \frac{ik}{2} e^{-ik(x-x_0)} \int_{-\infty}^{\infty} u(x_0, z') \frac{x-x_0}{\rho(z')} H_1^{(1)}(k\rho(z')) dz' \quad (16)$$

where  $x_0$  is any range beyond the obstacle and  $\rho(z') = \sqrt{(x-x_0)^2 + (z-z')^2}$ .

The PE field  $u$  is related to the incident field  $u_i$  and the scattered field  $u_s$  by  $u = u_s + u_i$  in the forward direction and  $u = u_s$  in the backward direction. Letting  $(x, z)$  go to infinity along the direction  $\theta$  in Eq. 16, we get the RCS  $\sigma(\theta)$  for an incident plane wave of unit amplitude:

$$\sigma(\theta) = k \cos^2 \theta \left| \int_{-\infty}^{\infty} u_s(x_0, z') e^{-ikz' \sin \theta} dz' \right|^2 \quad (17)$$

For the 3D case, the RCS formula is

$$\sigma(\theta, \varphi) = (k^2 \cos^2 \theta / \pi). \quad (18)$$

$$\left| \iint u_s(x_0, y', z') e^{-ik \sin \theta (y' \cos \varphi + z' \sin \varphi)} dy' dz' \right|^2$$

Equations 17 and 18 show that  $\sigma$  is closely related to the angular spectrum of the near field.

The range extent of the PE integration domain may be kept to a minimum, since the RCS may be obtained from the near field on any transverse plane. Numerical computations require a single one or two-dimensional FFT.

## 8. 2D EXAMPLES

### 8.1 Cylinder

We treat the case of a horizontally polarised wave incident from the left on a perfectly conducting circular cylinder of radius  $a$  with  $ka=10$  and  $\lambda=1m$ .

Fig. 5 shows contours of the real part of the scattered field obtained with the split-step Padé (SSP) method used with 8 terms. Note the accurate representation of wide-angle scatter, and the perfect truncation with a non-local boundary condition specially adapted for the SSP [21]. Integration time for this case is of the order of a minute on a 100 MHz Pentium PC.

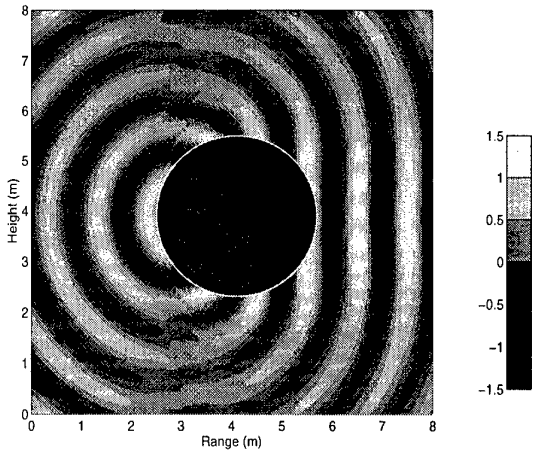


Fig. 5. Real part of scattered field

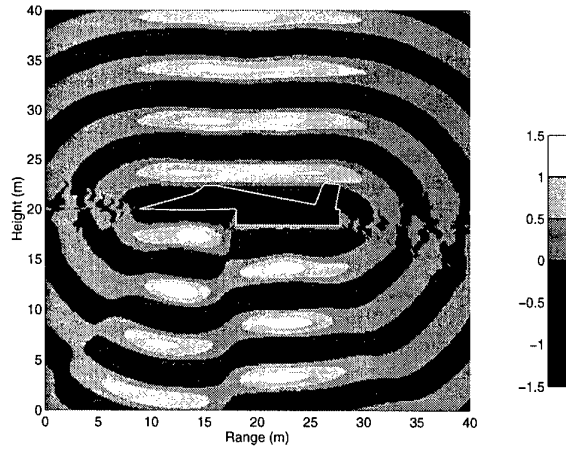


Fig. 7. Contours of scattered field,  $\lambda=5.236\text{m}$

Fig. 6 shows the corresponding RCS results, together with the analytical solution based on a Hankel expansion (see for example [16]). Excellent agreement is obtained.

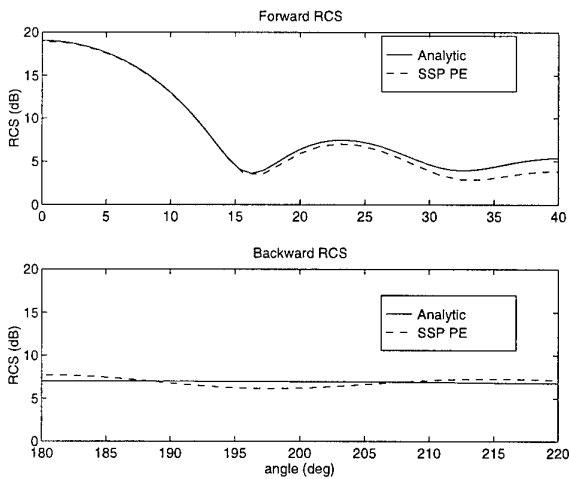


Figure 6. RCS of cylinder

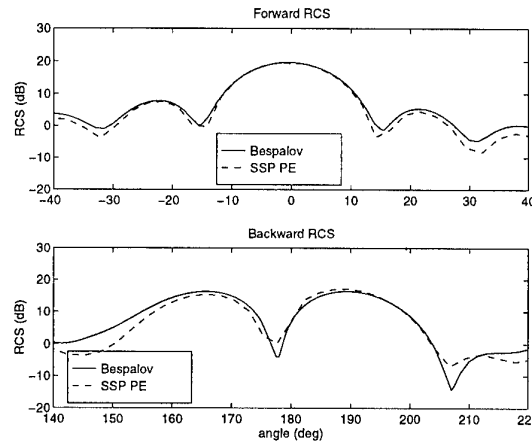


Fig. 8. RCS of aircraft for PE and FE methods,  $\lambda=5.2\text{m}$

Fig. 9 shows the PE computed RCS for a wavelength of 0.1m, corresponding to a frequency of 3 GHz. Finite-element methods would become too expensive for this frequency, whereas the PE computation time is still of the order of a minute.

### 8.2 Aircraft

Here, a horizontally polarised plane wave is incident from below on a stylised aircraft shape. The maximum dimensions of the aircraft are 19m in range and 4.2m in height. Fig. 7 shows contours of the scattered field computed with the 8 term SSP for a wavelength of 5.236 m, corresponding to a frequency of 57.2 MHz. The distortions due to the paraxial approximation are visible in scattering directions close to the horizontal.

This case has also been treated with a finite element method [4]. Fig. 8 shows RCS results for the PE and finite-element methods.

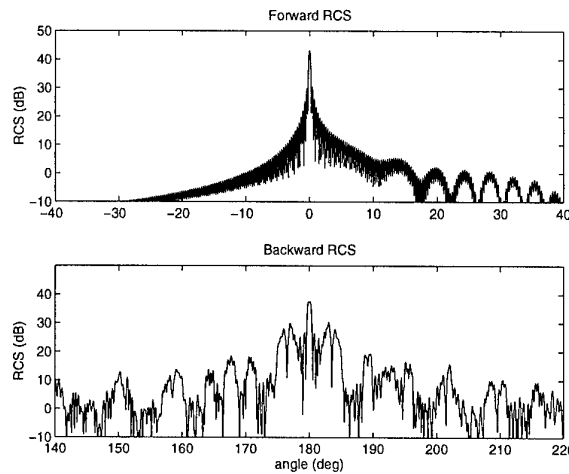


Fig. 9. RCS of aircraft,  $\lambda=0.1\text{m}$

## 9. 3D EXAMPLES

### 9.1 Acoustical scattering by a sphere

We treat the case of a plane wave incident on an acoustically soft sphere of radius 0.5m, for a reference wavelength of 0.1m. Fig. 10 shows the field amplitude contours computed with the axial symmetry PE method.

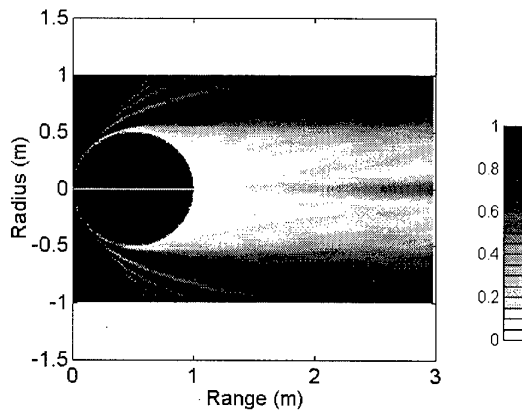


Fig. 10. Amplitude of forward scattered field,  $\lambda=0.1\text{m}$

The results are in excellent agreement with those obtained with the combination Padé (1,1)-Padé (2,1) method. This is illustrated in Fig. 11, showing the field amplitude 2m behind the sphere (3m from the origin) as a function of height, computed with the two methods. The continuous line shows the combination Padé results, and the dashed line the axial symmetry PE results.

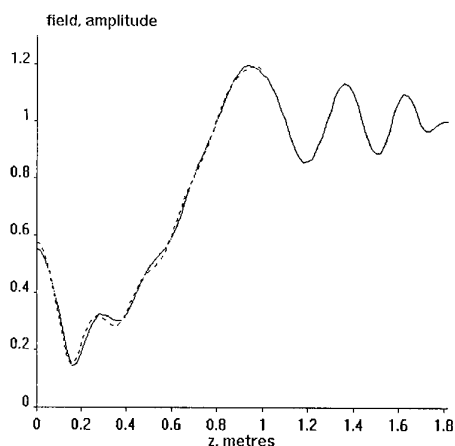


Fig. 11. Comparison of Padé and axial PE for the sphere

Fig. 12 shows the field computed with the combination Padé model in a transverse plane 20 wavelengths from the sphere. The flattening in the  $z$ -direction is due to the use of a narrow-angle PE in that direction. The near-field is used to compute the forward bistatic RCS shown in Fig. 13. The continuous line shows the PE result, while the dashed line shows the theoretical result for comparison [5]. Agreement is excellent up to 20 degrees or so. For larger angles the PE values fall off much

faster than the theoretical solution, a consequence of using a narrow-angle PE model in the  $z$ -direction.

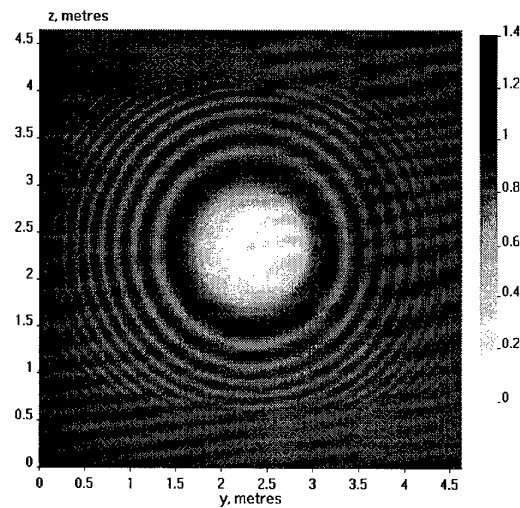


Fig. 12. Sphere near-field computed with Padé method

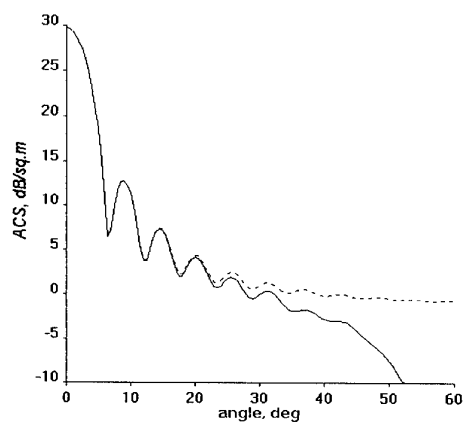


Fig. 13. Forward scatter cross-section of sphere

### 9.2 Acoustical scattering by an ogive

Fig. 14 shows field amplitude contours obtained with the axial symmetry PE method for an acoustically soft ogive. The wavelength is 0.1m.

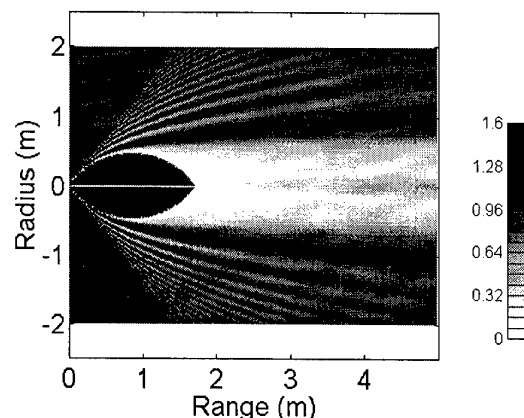


Fig. 14. Amplitude of forward scattered field,  $\lambda=0.1\text{m}$

### 9.3 EM scattering by a cube

The case of a plane wave normally incident on a perfectly conducting cube can be treated with the 3D Padé method.

The cube in the example shown here has 1m sides, and the incident wave is vertically polarised, with a wavelength of 0.1m. We have computed the scattered field for a smooth perfectly conducting cube and for a rough cube. The rough surface has been modelled as a composite of 10cm by 10cm plates of 1.5 cm variance.

Figs. 15 and 16 show the amplitude of the forward scattered field as it just leaves the smooth (respectively rough) cube. Here the PML method has been used to truncate the domain, with excellent results at all propagation angles. The perturbations due to the rough surface are clearly visible. However they become negligible very quickly, and have no effect on the forward RCS.

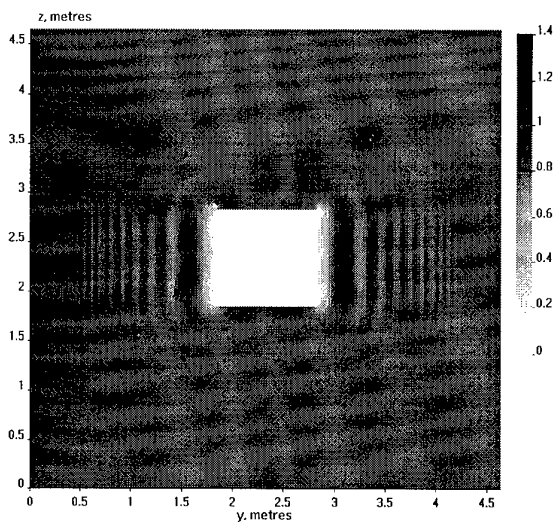


Fig. 15. Field scattered by a smooth cube

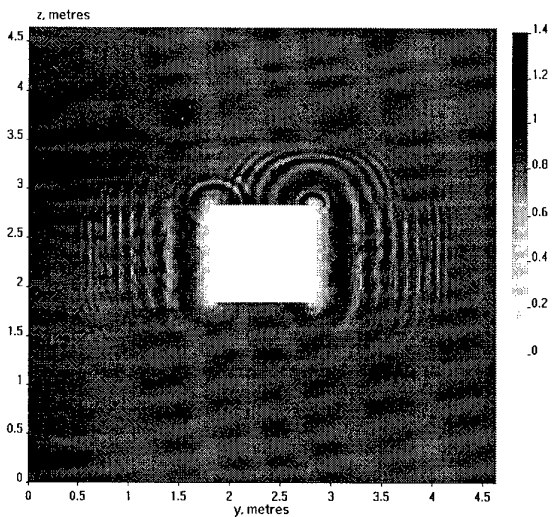


Fig. 16. Field scattered by a rough cube

Fig. 17 shows the amplitude of the backscattered field against height for  $y = 0$ , 10 m from the cube. As expected, the backscattered energy in the specular direction is greatly diminished by surface roughness, and the scattering pattern becomes asymmetric for the rough case. It should be noted that Figs. 16 and 17 correspond to just one realization of the rough surface.

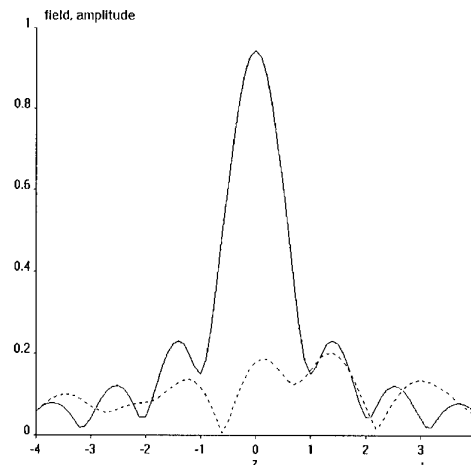


Fig. 17. Backscattered field 10 m from the cube,  $y = 0$ .  
Solid line - ideal, dotted line - rough.

## 10. CONCLUSIONS

We have described currently available parabolic equation techniques for RCS computations. The methods can be applied to scatterers ranging from a size of the order of a wavelength to several hundreds of wavelengths. The resulting algorithms provide robust and fast solutions for 2D electromagnetic scattering problems, and for 3D acoustic and electromagnetic scattering problems where boundary conditions split between the two transverse directions. More general 3D cases will require the development of a vector version of the PE.

## 11. ACKNOWLEDGMENTS

This work has been carried out with the support of the Engineering and Physical Sciences Research Council, the Radiocommunications Agency of the Department of Trade and Industry under the National Radio Propagation Programme, and the European Union under the Human Capital and Mobility scheme. The third author is currently on secondment from the University of Southampton.

We are grateful to Dr. A. Bepalov for supplying RCS results for the numerical comparisons.

## 12. REFERENCES

- [1] A. E. Barrios, "A terrain parabolic equation model for propagation in the troposphere", *IEEE Trans.*

- Antennas Propagat.*, Vol. 40, No. 12, pp. 90-98, 1994.
- [2] J.-P. Bérenger, "A perfectly matched layer for the absorption of electromagnetic waves", *J. Comp. Phys.*, Vol. 114, No 2, pp. 185-200, 1994.
- [3] J.-P. Bérenger, "Perfectly matched layer for the FDTD solution of wave-structure interaction problems", *IEEE Trans. Antennas Propagat.*, Vol. 44, No 1, pp. 110-117, 1996.
- [4] A. Béspalov, "Application of fictitious domain methods to the solution of Helmholtz equation in unbounded domain", INRIA Report No 1797, 1992.
- [5] J.J. Bowman, T.B.A. Senior and P.L.E. Uslenghi, "Electromagnetic and acoustic scattering by simple shapes", North-Holland, 1969.
- [6] J. Claerbout, "Fundamentals of Geophysical Data Processing: With Applications to Petroleum Prospecting", McGraw-Hill, 1976.
- [7] F. Collino, "Perfectly Matched Layer for the paraxial equation", *J. Comp. Phys.*, to appear.
- [8] M.D. Collins, "A Split-Step Padé solution for the Parabolic equation Method", *J. Acoust. Soc. Am.* Vol. 94, No. 4, pp. 1736-1742, 1993.
- [9] M.D. Collins, and R.B. Evans, "A two-way parabolic equation for acoustic backscattering in the ocean", *J. Acoust. Soc. Am.*, Vol. 91, pp. 1357-1368, 1992.
- [10] K.H. Craig and M.F. Levy, "Parabolic equation modelling of the effects of multipath and ducting on radar systems", *IEE Proc.-F*, Vol. 138, No. 2, pp. 153-162, 1991.
- [11] R.A. Dalrymple and P.A. Martin, Perfect boundary conditions for parabolic water-wave models, *Proc. R. Soc. London A*, vol. 437, pp. 41-54, 1992.
- [12] J.R. Kuttler and G.D. Dockery, "Theoretical description of the PE/Fourier split-step method of representing electromagnetic propagation in the troposphere", *Radio Sci.*, Vol. 26, pp. 381-303, 1991.
- [13] D. Lee and S.T. McDaniel, "Ocean acoustic propagation by finite difference methods", *Int. J. Comp. Math. Appl.*, Vol 14, No 5, pp. 305-423, 1987.
- [14] D. Lee and A. Pierce, "Parabolic equation development in recent decade", *J. Comput. Acous.*, Vol. 3, No. 2, pp. 95-173, 1995.
- [15] M.F. Levy, "Transparent boundary conditions for parabolic equation solutions of radiowave propagation problems", *IEEE Trans. Antennas Propagat.*, to appear.
- [16] M.F. Levy and P-P. Borsboom, "Radar cross-section computations using the parabolic equation method", *Electron. Lett.*, 32, pp. 1234-1236, 1996
- [17] A.V. Popov, "Accurate modeling of transparent boundaries in quasi-optics", *Radio Sci.*, to appear.
- [18] C.M. Rappaport, "Perfectly matched absorbing boundary conditions based on anisotropic lossy mapping of space", *IEEE Microwave and Guided Wave Letters*, Vol. 3, No. 3, pp. 90-92, 1995.
- [19] G.D. Smith, "Numerical solution of partial differential equations", Clarendon Press, 1985.
- [20] A.A. Zaporozhets and M.F. Levy, "Modelling of radiowave propagation in urban environment with parabolic equation method", *Electron. Lett.*, Vol. 32, No 17, pp. 1615-1616, 1996.
- [21] A. Zebic-Le Hyaric, "Non-Local Boundary Conditions for wide angles electromagnetics wave propagation problems", submitted for publication.

**Discussor's name:** I. ANDERSON

**Comment/Question:**

Can your method deal with multiple scattering/reflections on the scattering body?

**Author/presenter's reply:**

The PE method can deal with multiple scattering, but this can require several back and forth passes, depending on the geometry of the scatterer.

**Discussor's name:** R. KLEINMAN

**Comment/Question:**

Has there been any work, either qualitative or quantitative, on error analysis in using the parabolic approximation?

**Author/presenter's reply:**

Error analysis for the PE is of course related to the numerical scheme used to approximate the pseudo-differential operator  $Q$ . Partial results have been obtained in the underwater acoustics community, but further work is required, particularly for large scattering angles.

**Discussor's name:** C.D. SILLENCE

**Comment/Question:**

Does the fact that the RCS of many low RCS shapes, even in 2-D, is dominated by mechanisms involving wave propagation at 90 degrees to the incident direction, imply that the PE method cannot be applied to such targets?

**Author/presenter's reply:**

The paraxial approximation limits the study to a cone of directions lying within a  $180^\circ$  half-plane. Although it may be possible to use such a cone to include both the incident direction and  $90^\circ$  scatter from that direction, a global PE model cannot correctly model the full  $360^\circ$  circle.

**Discussor's name:** H. SCHIPPERS

**Comment/Question:**

- Can you comment on the requirements for the computational grid? Is the grid size related to the wavelength?
- Is there numerical analysis available for the spatial discretisation errors of the PDE?

**Author/Presenter's reply:**

- Our current computational grid is related to the wavelength, using  $L/20$  grid spacing. This has been dictated by resolution criteria for comparison with finite element methods, rather than by PE requirements. Further work is required to determine optimal grid-spacing.
- Numerical error analysis has been carried out for underwater acoustics application. The error depends largely on the propagation angles to be modelled and on the approximation of the pseudo-differential operator  $Q$ .

**Discussor's name:** F. CHRISTOPHE

**Comment/Question:**

J'ai été impressionné par la qualité du résultat présentant le champ diffracté par une forme d'avion incluant l'effet du conduit d'air. Mais la diffraction par le conduit d'air ne doit-elle pas obligatoirement être calculée en 3D pour être représentative?

*Translation:*

*I was impressed by the quality of the result presenting the diffracted field by an aircraft shape, including the effect of the air duct. But doesn't the air duct diffraction have to be modelled in 3D to be representative?*

**Author/Presenter's reply:**

It is of course true that the 2D example presented here does not give a realistic picture of air duct effects. This case was chosen mainly because exact controllability method results were available for comparison.

# Fast Radar Cross Section (RCS) Computation via the Fast Multipole Method

Levent Gürel

Dept. of Electrical and Electronics Engineering  
Bilkent University  
TR-0653 Bilkent, Ankara, Turkey  
lgurel@ee.bilkent.edu.tr

## 1. SUMMARY

The fast multipole method (FMM) is used for the fast radar cross section (RCS) computation of large canonical two-dimensional geometries in both homogeneous and layered media. Numerical solution of electromagnetic scattering problems are invaluable in many real-life applications. However, real-life problems translate into very large numerical problems and when accurate solutions are desired, the size of the problem that can be solved using traditional techniques is limited by the given computational resources. The FMM overcomes this difficulty with its reduced computational complexity and memory requirement. Thus, larger problems can be solved using the same computational resources and without sacrificing the accuracy of the solution. The FMM employed here uses diagonalized translation operators for the two-dimensional Helmholtz equation.

It is shown that the FMM requires  $O(N^{1.5})$  operations per iteration as opposed to the matrix-vector multiplication being an  $O(N^2)$  operation per iteration and the direct solution having  $O(N^3)$  computational complexity. In addition to the estimates of computational complexities and memory requirements of these methods, their actual performances are also compared and discussed. Solutions of several large two-dimensional canonical conductor geometries are used in these comparisons, where the excitation is a TM-polarized incident plane wave. Through these comparisons, it is demonstrated that accurate RCS computations of large geometries are possible using the FMM.

## 2. INTRODUCTION

Numerical simulation and analysis of the electromagnetic scattering phenomena are used in several engineering applications to gain important information about a system *before* it is built, thus saving time and other resources. For instance, simulations of electromagnetic scattering from stealth vehicles are by far faster and cheaper than first manufacturing these vehicles and then performing scattering measurements on them.

During a design process, it is desirable, and in some cases necessary, to numerically simulate and analyze several different geometries. Furthermore, each one

of these geometries may generate extremely large numerical problems when translated into the language of computational electromagnetics. For these reasons, it is imperative to develop efficient and fast algorithms for computational electromagnetics.

Maxwell's equations and the electromagnetic wave equation derived therefrom can be solved using either partial-differential-equation (PDE) or integral-equation (IE) techniques. The most popular PDE solvers of the computational electromagnetics are the finite element method (FEM) and the finite-difference time-domain (FDTD) method. PDE solvers generally require that the problem space be finite, although several extensions have been devised in the form of absorbing boundary conditions (ABCs) and hybrid methods to be able to use the PDE solvers in problems that are defined in unbounded media. On the other hand, IE techniques, such as the method of moments (MoM), fast multipole method (FMM) and recursive T-matrix algorithms (RTMAs), have the radiation condition built into their formulations and, therefore, can easily simulate scattering and radiation in unbounded media.

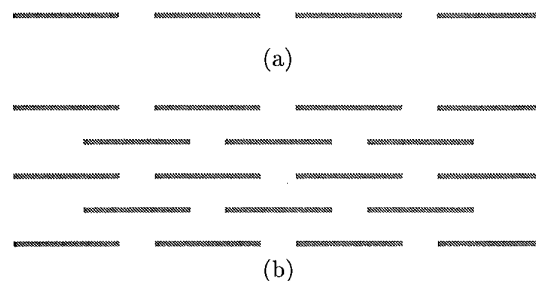


Fig. 1. (a) One-dimensional and (b) two-dimensional clustering of strips.

In this work, electromagnetic scattering from two-dimensional canonical conducting strip geometries in homogeneous and layered media will be analyzed. As examples of canonical geometries, Figs. 1(a) and 1(b) display the one-dimensional and two-dimensional clustering of conducting strips in a homogeneous medium.

Canonical problems are important since they display the performances of the solution techniques on the class of geometries they are representing, with-

out having to apply the solution technique under test to each member geometry of the class. Arbitrary geometries can be viewed as special cases of the more general canonical configurations. For instance, if a computational technique can handle the case of touching strips as in Fig. 2(a) and tilted strips as in Fig. 2(b), then it can be argued that the same technique can handle arbitrary geometries made up of touching tilted strips as in Fig. 2(c). Canonical problems will be used to compare the efficiencies and the accuracies of various solution algorithms.

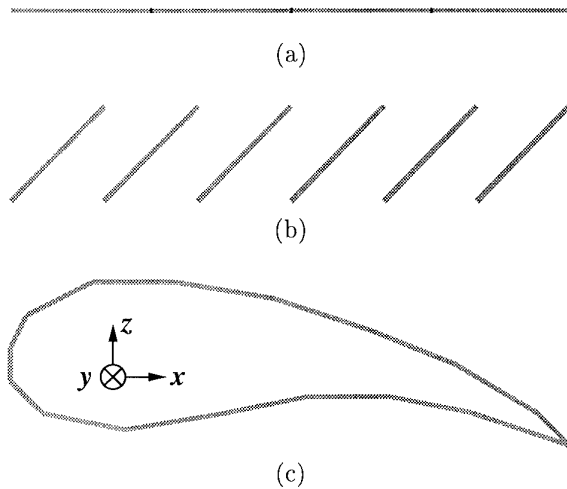


Fig. 2. (a) Touching strips forming a larger strip. (b) Canonical configuration of tilted strips. (c) A more complicated two-dimensional geometry composed of touching tilted strips.

The canonical problems illustrated in Figs. 1(a), 1(b), and 2(b) are also important on their own account since they or a slight modification thereof can be considered as finite-size frequency-selective surfaces (FSS).

The class of problems that are of interest in this work can usually be formulated using integral equations (IE) and solved by matrix solvers after converting the integral equations to matrix equations, e.g., via the method of moments (MoM). The matrix solvers can be either direct solvers, e.g., Gaussian elimination, or iterative solvers, e.g., conjugate gradient (CG) method.

A problem comprising  $N$  unknowns requires  $O(N^3)$  operations with a direct solver and  $O(N^2)$  operations per iteration with an iterative solver. If the number of iterations of the iterative solvers grows as  $O(N)$ , then the overall computational complexity of the iterative solvers becomes  $O(N^3)$ , same as the direct solvers. Both direct and iterative solvers require  $O(N^2)$  memory locations for a problem of size  $N$ .

Despite all of the advantages of IE solutions, their  $O(N^3)$  computational complexity and  $O(N^2)$  mem-

ory requirement exhaust computational resources before the relatively larger and more interesting problems can be solved. A general solution scheme with reduced computational complexity and memory requirement is essential for problems comprising very large numbers of unknowns.

The number of unknowns can indeed become very large for real-life applications. Assume that a 15 m long conducting cylinder with a radius of 3 m models the fuselage of an aircraft. If this geometry is discretized using square patches, whose sides are 0.1 wavelength, and two unknowns are defined on each patch to model the two orthogonal components of the surface current, then the number of unknowns exceeds 300,000 at 1 GHz. If the frequency is increased to 20 GHz, then the number of unknowns increases by 400 times to exceed 125,000,000! There is a clear need for algorithms with reduced computational complexities and reduced memory requirements in order to be able to solve this kind of large problems.

As a partial solution to the computational-complexity and the memory-requirement problems referred to above, two recursive T-matrix algorithms (RTMAs) were developed earlier. [1-5] The RTMAs are recursive algorithms, however, they can be considered as direct solvers for IEs since they share some of the nice properties of the direct solvers, such as generating solutions that are valid for multiple excitations, i.e., right-hand sides. In the arena of iterative solvers, the FMM has recently been developed. [6-10] In this work, the FMM is applied to the solution of electromagnetic scattering problems involving two-dimensional canonical conducting strip geometries. Both the induced current densities and the RCS of these structures are computed using FMM.

The efficiency and the accuracy of the FMM are demonstrated through comparisons with two reference solutions. First, a direct solution technique employing Gaussian elimination is used to solve the resulting matrix equation. Then, the same matrix equation is solved by using an iterative scheme, namely, the conjugate gradient squared (CGS) method, in which every iteration involves two matrix-vector multiplications.

### 3. INTEGRAL-EQUATION FORMULATION

Consider, for simplicity, that an  $E_y$ -polarized plane wave is incident on the two-dimensional geometries of Figs. 1 and 2. Since the tangential component of the total electric field must vanish on the conductors, we have

$$E_y^I(\rho) + E_y^S(\rho) = 0, \quad \rho \in S, \quad (1)$$

where  $S$  denotes the combined surface of all the conducting strips in the problem. The scattered field is

given by

$$E_y^S(\rho) = -\frac{k\eta}{4} \int_S d\rho' H_0^{(1)}(k|\rho - \rho'|) J_y(\rho'), \quad (2)$$

where  $J_y(\rho)$  is the induced current density on the strips. This current density can be expanded using  $N$  basis functions  $b_n(\rho)$  and  $N$  unknown coefficients  $a_n$ , i.e.,

$$J_y(\rho) = \sum_{n=1}^N b_n(\rho) a_n. \quad (3)$$

Combining Eqs. (1)–(3), we obtain

$$\frac{k\eta}{4} \sum_{n=1}^N \int_S d\rho' H_0^{(1)}(k|\rho - \rho'|) b_n(\rho') a_n = E_y^I(\rho), \quad \rho \in S. \quad (4)$$

Equation (4) is a representation of the boundary condition that needs to be satisfied on the conductor surfaces. In order to impose the boundary condition everywhere on the strips, testing functions  $t_m(\rho)$  can be defined on the strips and inner products of these testing functions with both sides of Eq. (4) can be constructed to obtain

$$\begin{aligned} \frac{k\eta}{4} \sum_{n=1}^N \int_S d\rho t_m(\rho) \int_S d\rho' H_0^{(1)}(k|\rho - \rho'|) b_n(\rho') a_n \\ = \int_S d\rho t_m(\rho) E_y^I(\rho), \quad m = 1, 2, \dots, N. \end{aligned} \quad (5)$$

The above can be expressed as a matrix equation

$$\bar{\mathbf{Z}}_{N \times N} \cdot \mathbf{a}_{N \times 1} = \mathbf{e}_{N \times 1}, \quad (6)$$

where

$$Z_{mn} = \frac{k\eta}{4} \int_S d\rho t_m(\rho) \int_S d\rho' H_0^{(1)}(k|\rho - \rho'|) b_n(\rho') \quad (7)$$

and

$$e_m = \int_S d\rho t_m(\rho) E_y^I(\rho). \quad (8)$$

The  $N \times N$  linear system of equations in Eq. (6) can be solved using a direct or an iterative method. The solutions through direct inversion, i.e.,

$$\mathbf{a} = \bar{\mathbf{Z}}^{-1} \cdot \mathbf{e}, \quad (9)$$

and through direct factorization of the matrix  $\bar{\mathbf{Z}}$  require  $O(N^3)$  operations. Iterative solutions are based on the minimization of a residual error vector

$$\mathbf{r}^{(i)} = \mathbf{e} - \bar{\mathbf{Z}} \cdot \mathbf{a}^{(i)} \quad (10)$$

through several iterations, where  $\mathbf{a}^{(i)}$  represents the  $i$ th guess to the solution. Thus, the iterative solutions employ one or more matrix-vector multiplications per iteration, each of which requires  $O(N^2)$

operations. The FMM works in such an iterative scheme and replaces the matrix-vector multiplication  $\bar{\mathbf{Z}} \cdot \mathbf{a}^{(i)}$  with a more intelligent algorithm that requires less than  $O(N^2)$  operations per iteration.

#### 4. MULTIPOLE EXPANSIONS AND ADDITION THEOREMS

Cylindrical and spherical harmonic wave functions are solutions of the wave equation in two dimensions and three dimensions, respectively. Thus, any solution of the wave equation  $\phi(\mathbf{r})$ , can be expanded in terms of a vector of outgoing wave functions  $\psi(\mathbf{r})$  as

$$\phi(\mathbf{r}) = \psi^t(\mathbf{r}) \cdot \mathbf{f}, \quad (11)$$

provided that  $\mathbf{r}$  is outside the smallest sphere (circle) containing the sources. If  $\mathbf{r}$  is inside the largest sphere (circle) that extends out to the sources, then  $\phi(\mathbf{r})$  can be expanded in terms of the regular part of  $\psi(\mathbf{r})$  as

$$\phi(\mathbf{r}) = \Re g \psi^t(\mathbf{r}) \cdot \mathbf{e}. \quad (12)$$

The multipole expansions given in the above are valid for both two-dimensional and three-dimensional wave functions if we interpret  $\mathbf{r}$  as

$$\mathbf{r} = \hat{x}x + \hat{y}y + \hat{z}z \quad \text{in three-dimensional space,} \quad (13)$$

$$\mathbf{r} = \rho = \hat{x}x + \hat{z}z \quad \text{in two-dimensional space.} \quad (14)$$

The vectors  $\psi(\mathbf{r})$  and  $\Re g \psi(\mathbf{r})$  of the cylindrical harmonic wave functions in the two-dimensional space are explicitly given by

$$\begin{array}{c} \psi(\mathbf{r}) \\ \downarrow \\ \vdots \\ H_{-2}^{(1)}(k\rho) e^{-i2\phi} \\ H_{-1}^{(1)}(k\rho) e^{-i\phi} \\ H_0^{(1)}(k\rho) \\ H_1^{(1)}(k\rho) e^{i\phi} \\ H_2^{(1)}(k\rho) e^{i2\phi} \\ \vdots \end{array}, \quad \begin{array}{c} \Re g \psi(\mathbf{r}) \\ \downarrow \\ \vdots \\ J_{-2}(k\rho) e^{-i2\phi} \\ J_{-1}(k\rho) e^{-i\phi} \\ J_0(k\rho) \\ J_1(k\rho) e^{i\phi} \\ J_2(k\rho) e^{i2\phi} \\ \vdots \end{array}. \quad (15)$$

We define a global coordinate system in which a coordinate vector is represented by  $\mathbf{r}$ . Furthermore, assuming that there are  $N$  scatterers (or  $N$  subscatterers) in the geometry, a local coordinate system for each of the  $N$  scatterers is defined. Figure 3 shows only two of the  $N$  scatterers, namely, the  $i$ th and the  $j$ th ones. Also shown in Fig. 3 is the global coordinate system.

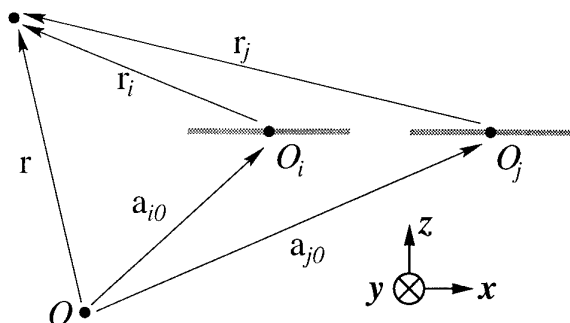


Fig. 3. Global coordinate system and two of the  $N$  local coordinate systems.

A coordinate vector associated with the  $i$ th scatterer is represented by  $\mathbf{r}_i$ . This vector can also be written in terms of  $\mathbf{r}$  and  $\mathbf{r}_j$  as

$$\begin{aligned}\mathbf{r}_i &= \mathbf{r} + \mathbf{a}_{0i} \\ &= \mathbf{r}_j + \mathbf{a}_{ji},\end{aligned}\quad (16)$$

where  $\mathbf{a}_{0i}$  and  $\mathbf{a}_{ji}$  are translation vectors from the  $i$ th local coordinate system to the global and the  $j$ th local coordinate systems, respectively.

Translational addition theorems [11–13] for the cylindrical and spherical wave functions will be used to shift the origin from one scatterer to another. The translation vector from the  $j$ th scatterer to the  $i$ th scatterer is denoted by  $\mathbf{a}_{ij}$ . We will use  $\bar{\alpha}_{ij}$  and  $\bar{\beta}_{ij}$  matrices as the translation matrices that express the expansion of the wave functions in the  $j$ th coordinate system in terms of the  $i$ th coordinate system. In other words, if  $\psi(\mathbf{r}_i)$  and  $\Re g\psi(\mathbf{r}_i)$  are the column vectors containing the cylindrical (or spherical) wave functions and their regular parts, respectively, then the translation relations are as follows (for  $\mathbf{r}_j = \mathbf{r}_i + \mathbf{a}_{ij}$ ):

$$\psi^t(\mathbf{r}_j) = \Re g\psi^t(\mathbf{r}_i) \cdot \bar{\alpha}_{ij} \quad \text{if } |\mathbf{r}_i| < |\mathbf{a}_{ij}|, \quad (17)$$

$$= \psi^t(\mathbf{r}_i) \cdot \bar{\beta}_{ij} \quad \text{if } |\mathbf{r}_i| > |\mathbf{a}_{ij}|, \quad (18)$$

$$\Re g\psi^t(\mathbf{r}_j) = \Re g\psi^t(\mathbf{r}_i) \cdot \bar{\beta}_{ij}. \quad (19)$$

Furthermore, the following relations exist among the  $\bar{\alpha}_{ij}$  and  $\bar{\beta}_{ij}$  matrices (for  $\mathbf{a}_{ij} = \mathbf{a}_{ik} + \mathbf{a}_{kj}$ ):

$$\bar{\alpha}_{ij} = \bar{\beta}_{ik} \cdot \bar{\alpha}_{kj} \quad \text{if } |\mathbf{a}_{ik}| < |\mathbf{a}_{kj}|, \quad (20)$$

$$= \bar{\alpha}_{ik} \cdot \bar{\beta}_{kj} \quad \text{if } |\mathbf{a}_{ik}| > |\mathbf{a}_{kj}|, \quad (21)$$

$$\bar{\beta}_{ij} = \bar{\beta}_{ik} \cdot \bar{\beta}_{kj}. \quad (22)$$

In two dimensions, the addition theorems (17)–(19) for cylindrical harmonic wave functions are explicitly

given by

$$H_m^{(1)}(k\rho_j) e^{im\phi_j} = \begin{cases} \sum_{n=-P/2}^{P/2} J_n(k\rho_i) e^{in\phi_i} H_{m-n}^{(1)}(ka_{ij}) e^{i(m-n)\psi_{ij}} & \text{if } \rho_i < a_{ij}, \\ \sum_{n=-P/2}^{P/2} H_n^{(1)}(k\rho_i) e^{in\phi_i} J_{m-n}(ka_{ij}) e^{i(m-n)\psi_{ij}} & \text{if } \rho_i > a_{ij}, \end{cases} \quad (23)$$

$$J_m(k\rho_j) e^{im\phi_j} = \sum_{n=-P/2}^{P/2} J_n(k\rho_i) e^{in\phi_i} J_{m-n}(ka_{ij}) e^{i(m-n)\psi_{ij}}. \quad (24)$$

Comparing Eqs. (24) and (25) to Eqs. (21)–(23), the elements of the  $\bar{\alpha}_{ij}$  and  $\bar{\beta}_{ij}$  matrices are found as

$$[\bar{\alpha}_{ij}]_{nm} = H_{m-n}^{(1)}(ka_{ij}) e^{i(m-n)\psi_{ij}}, \quad (25)$$

$$[\bar{\beta}_{ij}]_{nm} = J_{m-n}(ka_{ij}) e^{i(m-n)\psi_{ij}}. \quad (26)$$

Note that the summations in the addition theorems, which are infinitely long in principle, are truncated to keep approximately  $P$  terms.

## 5. FAST MULTIPOLE METHOD

The FMM is a relatively new method that is devised for the fast solution of integral equations in general and partial differential equations (PDEs) converted into integral equations. The FMM is a fast algorithm to compute the fields due to an arbitrary source distribution at a set of predetermined points in space. By formulating the solution of an integral equation in an iterative scheme, where one or more such field calculations are performed at each iteration, it becomes possible to reduce the complexity of the solution compared to traditional techniques. [6–8]

An integral equation may be converted to an  $N \times N$  matrix equation by applying a discretization method, e.g., method of moments. The resulting linear system of equations may be solved using a direct method, e.g., Gaussian elimination, at the expense of  $O(N^3)$  operations or an iterative technique, e.g., conjugate gradients, that requires one or more matrix-vector multiplications of complexity  $O(N^2)$  at each iteration. The direct matrix-vector multiplication(s) at each iteration may be replaced by the FMM, which has a complexity lower than  $O(N^2)$ . Both computational and memory-requirement complexities of the various FMM implementations are between  $O(N)$  and  $O(N^{3/2})$ , depending on the physical problem to be solved and the specific variant of the FMM used. The FMM achieves this performance by grouping all

the unknowns into clusters formed on the basis of physical (geometrical) proximity and by manipulating the fields of clusters instead of the fields of individual unknowns. In this context, the terms unknowns, subscatterers, substrips, and basis functions are used analogously and interchangeably. This is because a scatterer (strip) can be decomposed into several smaller subscatterers (substrips). A subscatterer can be made just as big to define a basis function on it and each basis function is associated with an unknown coefficient. Alternatively, large and complicated geometries can be thought of as being constructed from smaller pieces, where each small piece is associated with an unknown.

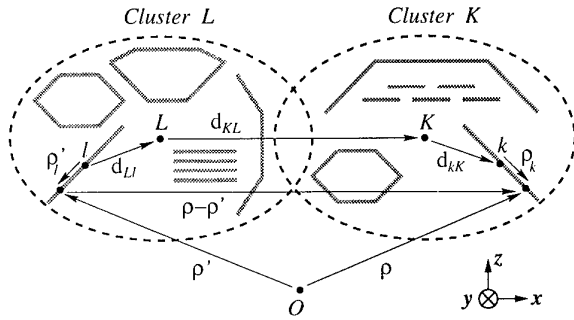


Fig. 4. Two of the many possible clusters in a representative geometry.

The  $N$  unknowns in the problem are clustered in such a way that a total of  $M$  clusters are formed and the number of unknowns in the  $L$ th cluster is  $n(L)$ . Thus,

$$N = \sum_{L=1}^M n(L). \quad (27)$$

Although the number of unknowns in each cluster can be different, as the problem size  $N$  gets larger, each cluster's population tends to be  $N/M$ . Figure 4 depicts two of the many possible clusters in a representative geometry. The two clusters are labelled as  $K$  and  $L$  and the vectors  $\rho_K$  and  $\rho_L$  point to the centers of these clusters. Also shown in Fig. 4 are the  $k$ th unknown (subscatterer) in the  $K$ th cluster and the  $l$ th unknown (substrip) in the  $L$ th cluster.

Central to the success of the FMM is the use of the addition theorems (see the previous section) to translate the fields from one cluster to another. Referring to Fig. 4, the field at point  $\rho$  due to a line source at point  $\rho'$  is defined as the Green's function and given by

$$G(\rho, \rho') = -\frac{\omega\mu}{4} H_0^{(1)}(k|\rho - \rho'|), \quad (28)$$

where

$$\rho - \rho' = \rho_k + \mathbf{d}_{kK} + \mathbf{d}_{KL} + \mathbf{d}_{Ll} - \rho'_l \quad (29)$$

Note that the vector  $\rho_k$  represents the observation point and is defined in the local coordinates of the  $k$ th substrip in the  $K$ th cluster. Similarly, the vector  $\rho'_l$  represents the source point and is defined in the local coordinates of the  $l$ th substrip in the  $L$ th cluster. Then, we have

$$H_0^{(1)}(k|\rho - \rho'|) = H_0^{(1)}[k|(\rho_k + \mathbf{d}_{kK}) + \mathbf{d}_{KL} + (\mathbf{d}_{Ll} - \rho'_l)|], \quad (30)$$

where the vector  $\mathbf{d}_{kK}$  points from the center of the  $K$ th cluster to the reference point of the  $k$ th substrip in that cluster. Similarly,  $\mathbf{d}_{Ll}$  points from the reference point of the  $l$ th substrip in the  $L$ th cluster to the center of the same cluster. In order to simplify the derivation, two new vectors will be defined as

$$\rho_{kK} = \rho_k + \mathbf{d}_{kK}, \quad (31)$$

$$\rho'_{Ll} = \mathbf{d}_{Ll} - \rho'_l. \quad (32)$$

Using the addition theorems twice, we have

$$H_0^{(1)}(k|\rho - \rho'|) = \Re g \psi^t(\rho_{kK}) \cdot \widehat{\alpha}_{KL} \cdot \Re g \psi(\rho'_{Ll}), \quad (33)$$

where

$$\left[ \Re g \psi(\rho_{kK}) \right]_m = J_m(k\rho_{kK}) e^{im\phi_{kK}} \quad (34)$$

and

$$\left[ \widehat{\alpha}_{KL} \right]_{mn} = (-1)^{m+n} H_{m+n}^{(1)}(kd_{KL}) e^{-i(m+n)\phi_{KL}}. \quad (35)$$

The regular wave functions in the above can be replaced by their integral representations

$$J_m(k\rho_{kK}) e^{im\phi_{kK}} = \frac{1}{2\pi} \int_0^{2\pi} d\phi e^{ik\rho_{kK} \cos(\phi - \phi_{kK}) + im(\phi - \frac{\pi}{2})} \quad (36)$$

and

$$J_m(k\rho'_{Ll}) e^{im\phi'_{Ll}} = \frac{1}{2\pi} \int_0^{2\pi} d\phi' e^{ik\rho'_{Ll} \cos(\phi' - \phi'_{Ll}) + im(\phi' - \frac{\pi}{2})} \quad (37)$$

Substituting first (36) and (37) in (34), and then (34) and (35) in (33), replacing  $m + n$  with  $p$ , and using the identity

$$\sum_{m=-\infty}^{\infty} e^{im(\phi - \phi')} = 2\pi\delta(\phi - \phi'), \quad (38)$$

we obtain

$$H_0^{(1)}(k|\rho - \rho'|) = \frac{1}{2\pi} \int_0^{2\pi} d\phi e^{ik\rho_{kK} \cos(\phi - \phi_{kK})} \widetilde{\alpha}_{KL}(\mathbf{k}) e^{ik\rho'_{Ll} \cos(\phi - \phi'_{Ll})}, \quad (39)$$

where

$$\tilde{\alpha}_{KL}(\mathbf{k}) = \sum_{p=-P}^P H_p^{(1)}(kd_{KL}) e^{ip(\phi - \phi_{KL} + \frac{\pi}{2})}. \quad (40)$$

Note that the infinite summation over  $p$  is truncated. If we define the wavevector  $\mathbf{k}$  as

$$\mathbf{k} = k(\hat{x} \cos \phi + \hat{z} \sin \phi) \quad (41)$$

and use the definitions of  $\rho_{kK}$  and  $\rho'_{Ll}$  as given in (31) and (32), then Eq. (39) can be rewritten as

$$H_0^{(1)}(k|\rho - \rho'|) = \frac{1}{2\pi} \int_0^{2\pi} d\phi e^{i\mathbf{k} \cdot (\rho_k + \mathbf{d}_{kK})} \tilde{\alpha}_{KL}(\mathbf{k}) e^{i\mathbf{k} \cdot (\mathbf{d}_{Ll} - \rho'_i)} \quad (42)$$

As depicted in Eq. (10), iterative solution techniques employ one or more matrix-vector multiplications per iteration. In electromagnetic problems, these matrix-vector multiplications can be expressed as

$$\mathbf{y} = \bar{\mathbf{Z}} \cdot \mathbf{x}, \quad (43)$$

where the matrix  $\bar{\mathbf{Z}}$  results from the discretization of an electromagnetic problem as in Eq. (7) and the vector  $\mathbf{x}$  is an arbitrary coefficient vector. Using the clustering concept, the above can be rewritten more explicitly as

$$y_{Kk} = \sum_{L=1}^M \sum_{l=1}^{n(L)} Z_{Kk, Ll} x_{Ll}, \quad K = 1, 2, \dots, M, \quad k = 1, 2, \dots, n(K). \quad (44)$$

Let  $\mathcal{F}(K)$  denote the set of all clusters that are in the far-field region of cluster  $K$ . Then, the summation in (44) can be split into far-field and near-field parts as

$$y_{Kk} = \underbrace{\sum_{L \in \mathcal{F}(K)} \sum_{l=1}^{n(L)} Z_{Kk, Ll} x_{Ll}}_{\text{Far Field (FF)}} + \underbrace{\sum_{L \notin \mathcal{F}(K)} \sum_{l=1}^{n(L)} Z_{Kk, Ll} x_{Ll}}_{\text{Near Field (NF)}} \quad (45)$$

In the above, the summation in the near-field part is performed as the multiplication of a sparse matrix with the coefficient vector. On the other hand, the far-field part can be rewritten using Eq. (7) as

$$\begin{aligned} y_{Kk}^{(FF)} &= \sum_{L \in \mathcal{F}(K)} \sum_{l=1}^{n(L)} Z_{Kk, Ll} x_{Ll} \quad (46) \\ &= \frac{k\eta}{4} \sum_{L \in \mathcal{F}(K)} \sum_{l=1}^{n(L)} \int_S d\rho t_{Kk}(\rho) \\ &\quad \int_S d\rho' H_0^{(1)}(k|\rho - \rho'|) b_{Ll}(\rho') x_{Ll}. \quad (47) \end{aligned}$$

Substituting (42) in the above, we obtain

$$y_{Kk}^{(FF)} = \frac{k\eta}{8\pi} \sum_{L \in \mathcal{F}(K)} \sum_{l=1}^{n(L)} \int_S d\rho_k t_{Kk}(\rho_k) \int_S d\rho'_i b_{Ll}(\rho'_i) \int_0^{2\pi} d\phi e^{i\mathbf{k} \cdot (\rho_k + \mathbf{d}_{kK})} \tilde{\alpha}_{KL}(\mathbf{k}) e^{i\mathbf{k} \cdot (\mathbf{d}_{Ll} - \rho'_i)} x_{Ll}, \quad (48)$$

which can be rearranged to read

$$\begin{aligned} y_{Kk}^{(FF)} &= \frac{k\eta}{8\pi} \int_0^{2\pi} d\phi \left( \int_S d\rho_k t_{Kk}(\rho_k) e^{i\mathbf{k} \cdot \rho_k} \right) \\ &\quad e^{i\mathbf{k} \cdot \mathbf{d}_{kK}} \sum_{L \in \mathcal{F}(K)} \tilde{\alpha}_{KL}(\mathbf{k}) \sum_{l=1}^{n(L)} e^{i\mathbf{k} \cdot \mathbf{d}_{Ll}} \\ &\quad \left( \int_S d\rho'_i b_{Ll}(\rho'_i) e^{-i\mathbf{k} \cdot \rho'_i} \right) x_{Ll}. \quad (49) \end{aligned}$$

If  $B_{Ll}(\mathbf{k})$  and  $T_{Kk}(\mathbf{k})$  are defined as the Fourier transforms of  $b_{Ll}(\rho)$  and  $t_{Kk}(\rho)$ , respectively, then the above can be rewritten as

$$y_{Kk}^{(FF)} = \frac{k\eta}{8\pi} \int_0^{2\pi} d\phi T_{Kk}^*(\mathbf{k}) e^{i\mathbf{k} \cdot \mathbf{d}_{kK}} \sum_{L \in \mathcal{F}(K)} \tilde{\alpha}_{KL}(\mathbf{k}) \sum_{l=1}^{n(L)} e^{i\mathbf{k} \cdot \mathbf{d}_{Ll}} B_{Ll}(\mathbf{k}) x_{Ll}. \quad (50)$$

It has been shown that the computational complexity of the FMM as presented in the above is  $O(NM) + O(N^2/M)$ . [6-8] This complexity is minimized by choosing  $M \propto \sqrt{N}$ , so that the computational complexity of the FMM becomes  $O(N^{3/2})$ . The memory requirement of the FMM is also  $O(N^{3/2})$ .

## 6. COMPUTATIONAL RESULTS FOR HOMOGENEOUS-MEDIA PROBLEMS

In this section, in order to demonstrate the accuracy and the efficiency of the FMM, we will present some sample RCS results. The term RCS will be used for the relevant bistatic scattering coefficient, which is  $\sigma_{yy}(\phi)$  in the case of TM scattering from two-dimensional geometries. This bistatic scattering coefficient is defined as

$$\sigma_{yy}(\phi) = 2\pi\rho \left| \frac{E_y^S(\rho \rightarrow \infty, \phi)}{E_y^I} \right|^2 \quad \text{for } \mathbf{E}^I = \hat{y} E_y^I. \quad (51)$$

The RCS results of this section are obtained for a TM (to  $y$ ) plane-wave illumination. This TM plane wave is incident at  $45^\circ$  as measured from the  $x$  axis.

The RCS results presented in this section are obtained using three different schemes: direct solution with Gaussian elimination, iterative solution with ordinary matrix-vector multiplication, and iterative solution with the FMM. The numerical results obtained using these three different schemes agree with

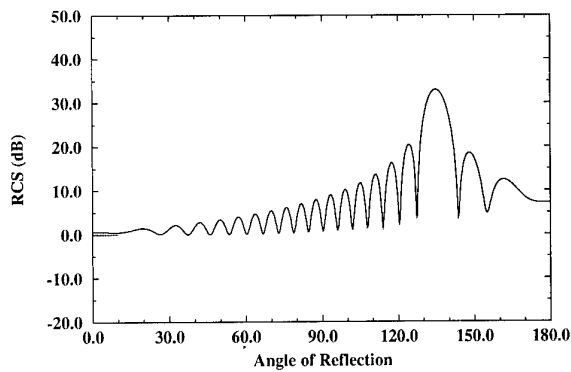


Fig. 5. RCS of a single  $10\text{-}\lambda$  strip.

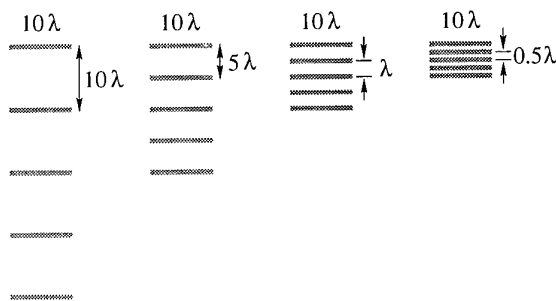


Fig. 6. Five  $10\text{-}\lambda$  strips that are vertically separated by  $10\lambda$ ,  $5\lambda$ ,  $\lambda$ ,  $0.5\lambda$ , and  $0.1\lambda$  (not shown).

each other for several digits and, therefore, are indistinguishable on the RCS plots, thus testifying to the accuracy of the FMM.

Figure 5 shows the RCS of a single  $10\text{-}\lambda$  strip. Illustrated in Fig. 6 are different configurations of vertically spaced five  $10\text{-}\lambda$  strips. Figure 7 shows the RCS of five  $10\text{-}\lambda$  strips that are separated by  $10\lambda$  in the vertical direction. In this case, the largest dimension of the geometry is  $40\lambda$  and the RCS of this structure (Fig. 7) is dramatically different than that of a single  $10\text{-}\lambda$  strip (Fig. 5). Similarly, Fig. 8 shows the RCS of five  $10\text{-}\lambda$  strips that are separated by  $5\lambda$ . Once again, in this case, the vertical dimension of the geometry, which is  $20\lambda$ , is much larger than the horizontal dimension, which is  $10\lambda$ . Figures 9, 10, and 11, on the other hand, show the RCS of structures whose vertical dimensions are  $4\lambda$ ,  $2\lambda$ , and  $0.4\lambda$ , respectively. Therefore, these RCS results bear some resemblance to the RCS of a single  $10\text{-}\lambda$  strip, especially in the neighborhood of the specular reflection direction, which is  $135^\circ$ . Particularly, the RCS of five  $10\text{-}\lambda$  strips that are separated by  $0.1\lambda$  (Fig. 11) is almost the same as the RCS of a single strip (Fig. 5), except near the grazing directions.

In order to stretch the test for the accuracy and the efficiency of the FMM, we have applied the FMM

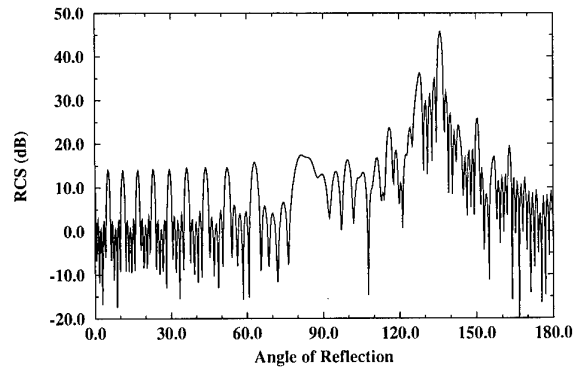


Fig. 7. RCS of five  $10\text{-}\lambda$  strips that are vertically separated by  $10\lambda$ .

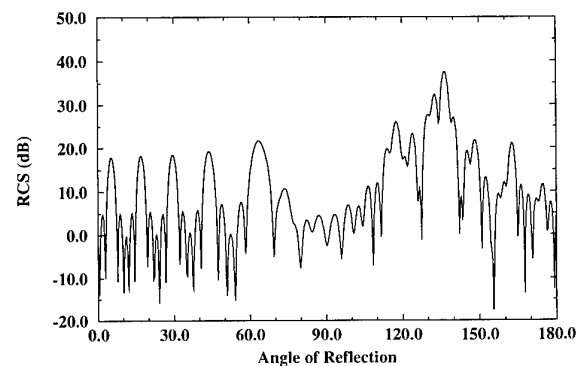


Fig. 8. RCS of five  $10\text{-}\lambda$  strips that are vertically separated by  $5\lambda$ .

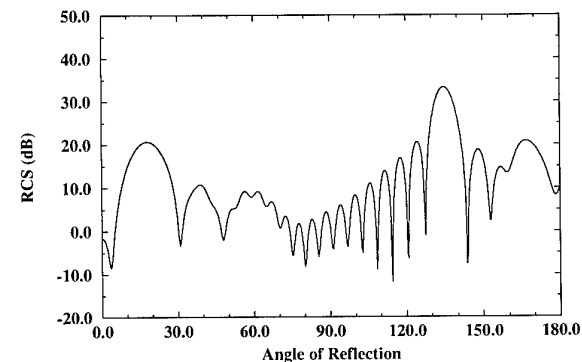


Fig. 9. RCS of five  $10\text{-}\lambda$  strips that are vertically separated by  $1\lambda$ .

to RCS computation of larger problems. Figure 12 illustrates five geometries that are made up of one to five  $100\text{-}\lambda$  touching strips. Figures 13–17 show the RCS of these geometries. These RCS results are also obtained using the reference solution techniques as explained earlier in this section. It is seen that the FMM results agree with the reference solutions for several digits.

Figure 18 depicts the comparison between the com-

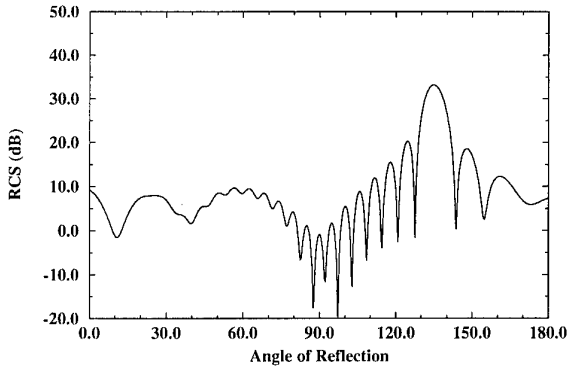


Fig. 10. RCS of five  $10\text{-}\lambda$  strips that are vertically separated by  $0.5\lambda$ .

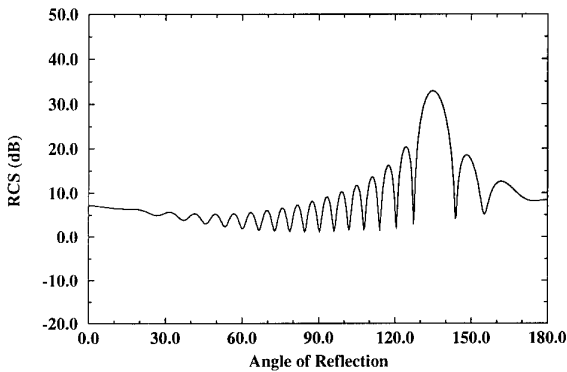


Fig. 11. RCS of five  $10\text{-}\lambda$  strips that are vertically separated by  $0.1\lambda$ .

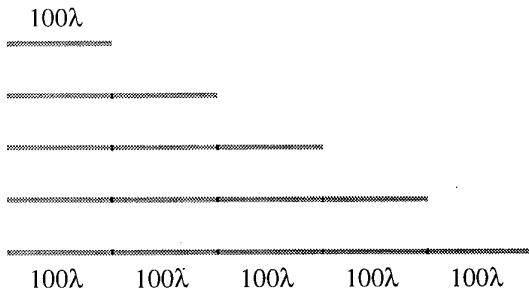


Fig. 12. Geometries of one to five touching  $100\text{-}\lambda$  wide strips.

puter times required by the FMM and the ordinary matrix-vector multiplication (MVM) for each iteration of the iterative method, which is the conjugate gradient squared (CGS) method in this case. Both the horizontal and the vertical axes of Fig. 18 are scaled logarithmically. Thus, the slope of the curve that is plotted with respect to these axes is equal to the order of computational complexity of these methods. Clearly, the FMM curve has a smaller slope than the that of the MVM curve. This is in agreement with the predictions of  $O(N^2)$  and  $O(N^{3/2})$

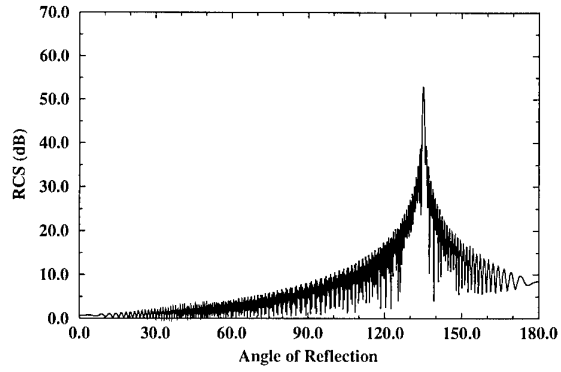


Fig. 13. RCS of a single  $100\text{-}\lambda$  wide strip.

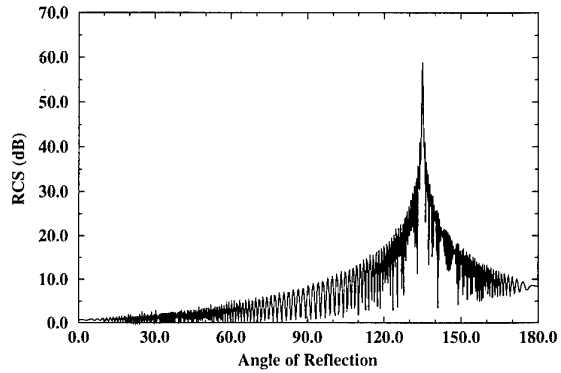


Fig. 14. RCS of two touching  $100\text{-}\lambda$  wide strips.

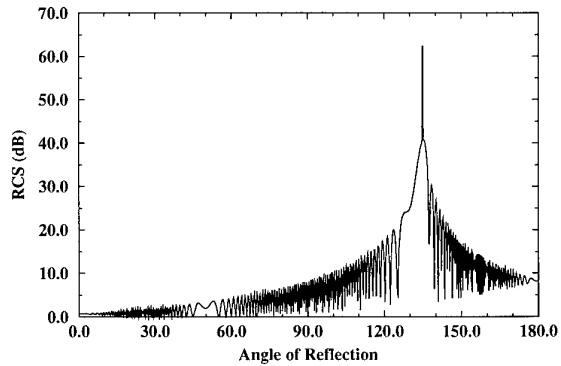


Fig. 15. RCS of three touching  $100\text{-}\lambda$  wide strips.

computational complexity for the MVM and FMM, respectively.

Figure 19 shows the comparison among the memory requirements of the CGS employing the FMM, CGS employing the ordinary matrix-vector multiplication, and the direct solution. It is seen that the slope of the FMM curve is smaller than both the MVM and the direct-solution curves. This is in agreement with the predictions of  $O(N^{3/2})$  memory requirement for the FMM and  $O(N^2)$  memory requirements for the MVM and the direct solution.

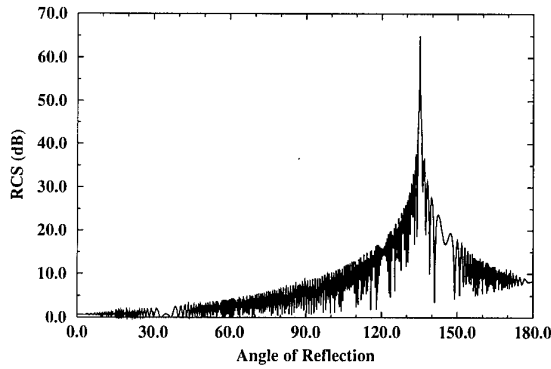


Fig. 16. RCS of four touching 100-λ wide strips.

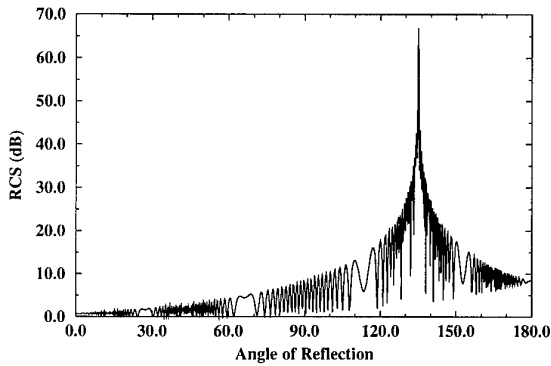


Fig. 17. RCS of five touching 100-λ wide strips.

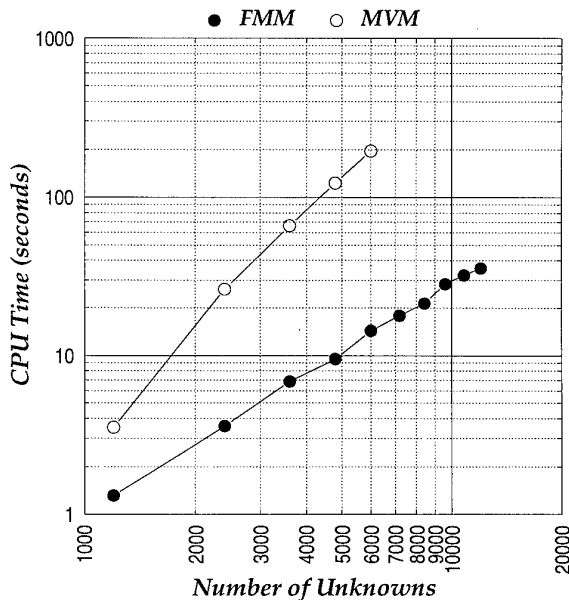


Fig. 18. Comparison of the solution times per iteration required by the FMM and the ordinary matrix-vector multiplication.

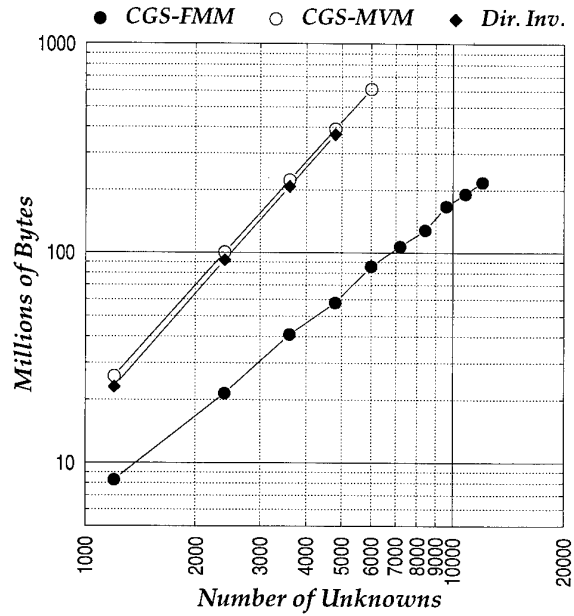


Fig. 19. Comparison of the memory requirements of the CGS employing the FMM, CGS employing the ordinary matrix-vector multiplication, and the direct solution.

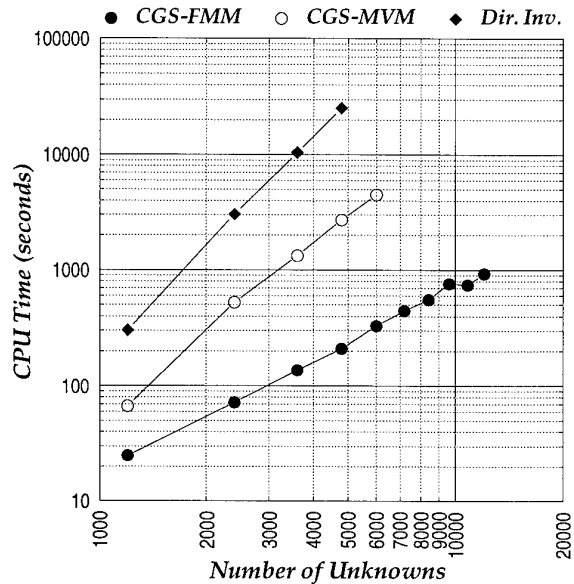


Fig. 20. Comparison of the total solution times required by the CGS employing the FMM, CGS employing the ordinary matrix-vector multiplication, and the direct solution. Filling time is not included.

Finally, Fig. 20 shows the comparison among total solution times taken by these three solution techniques. Matrix filling times are not included for any of the three methods. The FMM has the smallest slope, thus the lowest computational complexity, among the three solution techniques.

## 7. LAYERED-MEDIA PROBLEMS

Numerical solution of electromagnetic radiation and scattering problems involving layered media have gained popularity due to the need to computationally analyze various important geometries, e.g., absorber coatings to reduce RCS and structures placed on or in material substrates, such as microwave integrated circuits (MICs), printed circuit boards (PCBs), and the vast class of microstrip-like structures. Numerical analysis and simulation of these structures are needed for both functional considerations and electromagnetic-compatibility (EMC) issues.

The formulation of layered-media problems have traditionally been carried out in the spectral domain due to the availability of the Green's functions in closed forms [14,15]. Recently, a series of techniques have been developed to obtain closed-form Green's functions (CFGFs) for layered media in the spatial domain [16,17]. The use of the CFGFs in a method-of-moments (MoM) formulation replaces the numerical computation of the improper integrals in the spectral domain with numerical integrations over finite regions in the spatial domain. Furthermore, the spatial-domain integrals can be evaluated analytically in some cases [18]. Thus, this approach reduces the matrix-filling time by several orders of magnitude compared to the spectral-domain formulation. However, it does not reduce the computational complexity of the matrix-filling time and the memory requirement, which are both  $O(N^2)$ . Most importantly, despite the great savings in the matrix-filling time, the solution of the  $N \times N$  dense matrix equation remains, which requires  $O(N^3)$  operations in a direct scheme or  $O(N^2)$  operations per iteration in an iterative scheme.

By obtaining a closed-form expression for the spatial-domain Green's function for an arbitrarily layered medium and by interpreting each term of the expression as a discrete complex image, the FMM can be applied to the solution of layered-media problems. Thus, a fast solution technique for the layered-media problems can be obtained and the applicability of the FMM can be extended from homogeneous-medium problems to layered-medium problems.

## 8. FMM FOR LAYERED-MEDIA PROBLEMS

The  $y$ -directed electric field at point  $\rho = \hat{x}x + \hat{z}z$  due to a  $y$ -directed line source with unit amplitude located at point  $\rho' = \hat{x}x' + \hat{z}z'$  is given by

$$G(\rho, \rho') = -\frac{\omega\mu}{4\pi} \int_{-\infty}^{\infty} dk_x e^{ik_x(x-x')} \frac{1}{k_z} \left[ e^{ik_z|z-z'|} + \tilde{R}^{TE} e^{ik_z(z+z')} \right], \quad (52)$$

where  $\tilde{R}^{TE}$  is the generalized reflection coefficient defined at the  $z = 0$  plane due to an arbitrarily layered

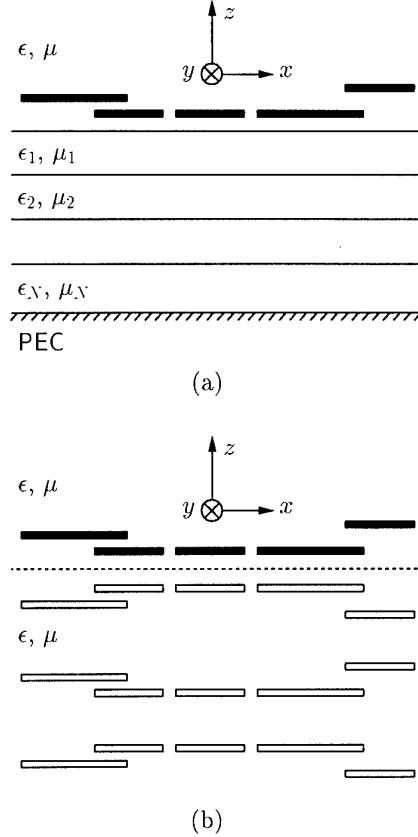


Fig. 21. (a) Original problem in a layered medium. (b) Equivalent problem with DCIs in a homogeneous medium.

substrate below this plane.

Using a robust technique by Aksun [18], Eq. (52) can be converted to a closed-form expression given by

$$G(\rho, \rho') = -\frac{\omega\mu}{4} \left[ H_0^{(1)}(k|\rho - \rho'|) + \sum_{n=1}^{N_I} a_n H_0^{(1)}(k|\rho - \rho'_n) \right], \quad (53)$$

where  $|\rho - \rho'_n| = \sqrt{(x - x')^2 + (z + z' + i\alpha_n)^2}$  and  $a_n$  and  $\alpha_n$  are complex constants for  $n = 1, 2, \dots, N_I$ .

The FMM is based on the expansion of the Green's function using the addition theorems and no such expansions exist for the layered-media Green's functions given in Eqs. (52) and (53). However, we can still employ the FMM in the solution of a layered-medium problem if we interpret Eq. (53) as the linear superposition of the field due to a source at  $\rho'$  and the fields due to  $N_I$  discrete complex images (DCIs) located at  $\rho'_n = \hat{x}x' + \hat{z}(-z' - i\alpha_n)$ . The DCIs are located at complex coordinates and, therefore, we need to use addition theorems for wave functions with complex arguments.

With the DCI interpretation, an equivalent prob-

lem is set up in a homogeneous medium. In this equivalent problem, which is illustrated in Fig. 21(b),  $N_I$  image sources in a homogeneous medium are defined corresponding to each original source in the layered-medium problem [Fig. 21(a)]. Thus, if  $N$  testing functions are defined on the original conductors,  $N(N_I + 1)$  basis functions are defined on the original conductors and their images.

The computation of the fields of  $N(N_I + 1)$  basis functions on the  $N$  testing functions is carried out using the FMM and repeated several times in an iterative scheme. Since  $N_I$  is a constant, this specific implementation of the FMM for layered-media problems has  $O(N^{3/2})$  computational complexity per iteration and  $O(N^{3/2})$  memory requirement as its homogeneous-medium counterpart.

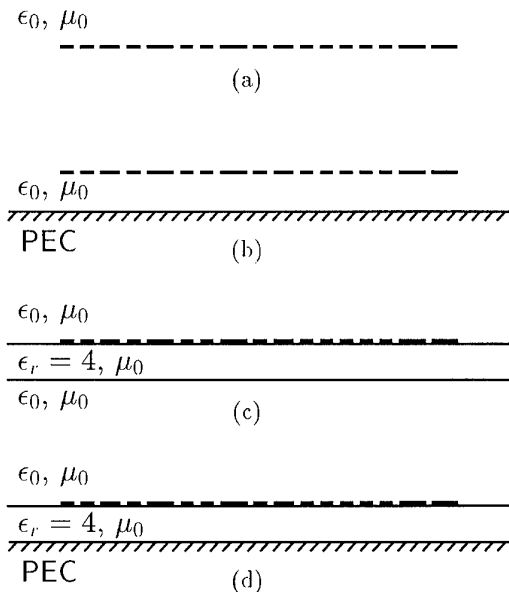


Fig. 22. Examples of layered structures.

## 9. COMPUTATIONAL RESULTS FOR LAYERED-MEDIA PROBLEMS

In order to demonstrate the accuracy and the efficiency of the layered-media implementation of the FMM presented in this letter, a series of structures (as illustrated in Fig. 22), to which the method can be applied, have been designed. Common to all these structures is an irregular, finite and planar array of strips, which has an overall extent of  $1.5\lambda_0$ . Plane waves, whose electric fields are polarized in the  $y$  direction and have unit amplitudes, are incident on the structures at  $45^\circ$  as measured from the positive  $x$  axis. Electromagnetic scattering problems for all four structures are solved using three different schemes: direct solution with Gaussian elimination, iterative solution with ordinary matrix-vector multiplication, and iterative solution with layered-medium

implementation of the FMM. The numerical results obtained using these three different schemes agree with each other for several digits and, therefore, are indistinguishable on the plots presented in Fig. 23.

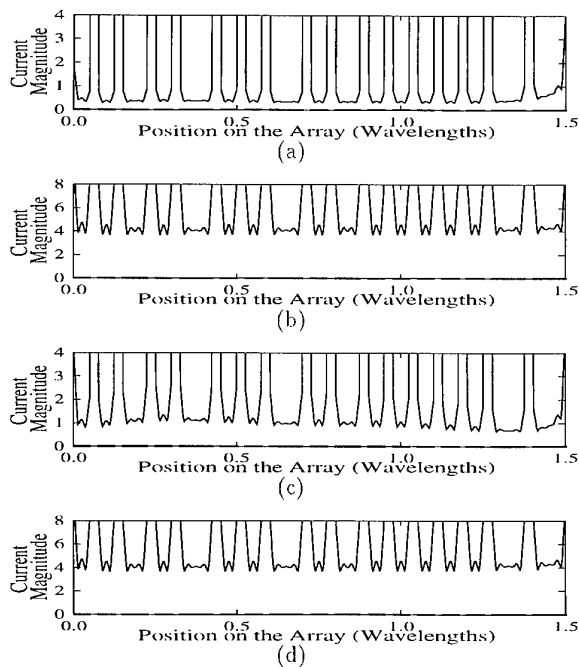


Fig. 23. Current distributions on the array corresponding to the example structures of Fig. 22.

The magnitude of the current distribution obtained on the array when the array is in free space [Fig. 22(a)] is shown in Fig. 23(a). An infinitely large conducting plane placed  $\lambda_0/100$  away from the array [Fig. 22(b)] causes the magnitude of the current distribution to increase as seen in Fig. 23(b). When the array is placed on a  $\lambda_0/100$  dielectric slab with  $\epsilon_r = 4$  as in Fig. 22(c), the magnitude of the current distribution, shown in Fig. 23(c), is seen to be modified and increased, but not as much as that of the conducting-plane case. If the dielectric slab is backed by a conducting plane as depicted in Fig. 22(d), the current magnitude becomes higher as seen in Fig. 23(d). Indeed, Fig. 23(d) can be compared to Fig. 23(b) to conclude that the conducting plane is more dominant than the relatively thin dielectric slab in determining the current distribution. However, by comparing Figs. 23(a) and (c), it is easy to see that the dielectric slab has a significant effect on the current distribution in the absence of the conducting plane.

The discretization of the conducting array shown in Fig. 22(a) results in 105 basis and testing functions. This array is duplicated many times in the layered geometry of Fig. 22(d) to obtain problems that are ten times as large. Separating the solution and filling times, we have compared the solution times of the FMM and the traditional solution techniques. Figure 24(a) compares the solution time of the FMM

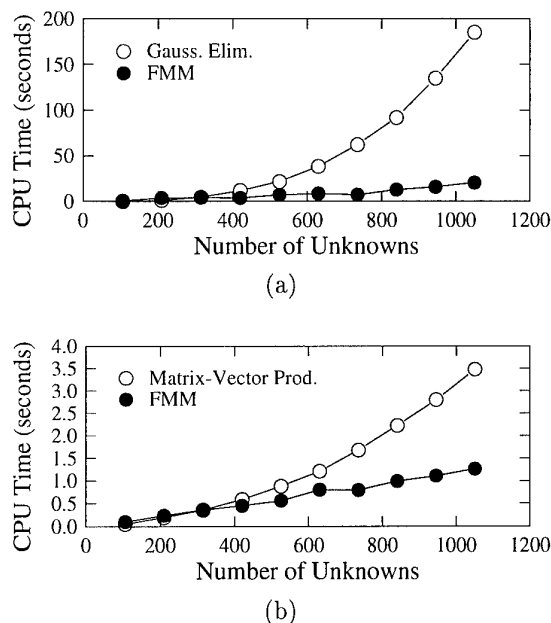


Fig. 24. (a) Comparison of the solution times of the layered-medium implementation of the FMM and the Gaussian elimination. (b) Comparison of the per-iteration solution times of the layered-medium implementation of the FMM and the ordinary matrix-vector multiplication.

to the Gaussian elimination and Fig. 24(b) compares the CPU time required during a single iteration of the FMM to the ordinary matrix-vector multiplication, respectively. As for the filling time, since only a sparse matrix of the near-field interactions is filled in the FMM as opposed to filling an  $N \times N$  dense matrix in the direct solution, filling time of the FMM is always lower.

## 10. CONCLUSIONS

The FMM is applied to the fast RCS computation of large canonical two-dimensional geometries. An integral equation based on the two-dimensional scalar Helmholtz equation is solved to compute the RCS of sample geometries of conducting strips in both homogeneous and layered media in order to demonstrate the accuracy and the efficiency of the FMM. The FMM is shown to have reduced computational complexity and memory requirement.

## REFERENCES

1. L. Gürel and W. C. Chew, "Scattering solution of three-dimensional array of patches using the recursive T-matrix algorithms," *IEEE Microwave and Guided Wave Lett.*, vol. 2, pp. 182-184, May 1992.
2. L. Gürel and W. C. Chew, "Recursive T-matrix algorithms with reduced complexities for scattering from three-dimensional patch geometries," *IEEE Trans. Antennas Propagat.*, vol. AP-41, pp. 91-99, Jan. 1993.

3. L. Gürel and W. C. Chew, "A recursive T-matrix algorithm for strips and patches," *Radio Sci.*, vol. 27, pp. 387-401, May-June 1992.
4. W. C. Chew, L. Gürel, Y. M. Wang, G. Otto, R. Wagner, and Q. H. Liu, "A generalized recursive algorithm for wave-scattering solutions in two dimensions," *IEEE Trans. Microwave Theory Tech.*, vol. MTT-40, pp. 716-723, April 1992.
5. W. C. Chew, Y. M. Wang, and L. Gürel, "Recursive algorithm for wave-scattering solutions using windowed addition theorems," *J. of Electromagn. Waves Appl.*, vol. 6, no. 11, pp. 1537-1560, Nov. 1992.
6. V. Rokhlin, "Rapid solution of integral equations of scattering theory in two dimensions," *J. Comput. Phys.*, vol. 86, pp. 414-439, Feb. 1990.
7. R. Coifman, V. Rokhlin, and S. Wandzura, "The fast multipole method for the wave equation: a pedestrian prescription," *IEEE Antennas and Propagation Magazine*, vol. 35, no. 3, pp. 7-12, June 1993.
8. C. C. Lu and W. C. Chew, "Fast algorithm for solving hybrid integral equations," *Proc. IEE*, vol. 140, Part H, pp. 455-460, Dec. 1993.
9. R. L. Wagner and W. C. Chew, "A ray-propagation fast multipole algorithm," *Microwave Opt. Tech. Lett.*, vol. 7, no. 10, pp. 435-438, July 1994.
10. C. C. Lu and W. C. Chew, "A multilevel algorithm for solving boundary integral equation of scattering," *Microwave Opt. Tech. Lett.*, vol. 7, no. 10, pp. 466-470, July 1994.
11. B. Friedman and J. Russek, "Addition theorems for spherical waves," *Quart. Appl. Math.*, vol. 12, no. 1, pp. 13-23, 1954.
12. M. Danos and L. C. Maximon, "Multipole matrix elements of the translation operator," *J. Math. Phys.*, vol. 6, pp. 766-778, May 1965.
13. W. C. Chew, "Recurrence relations for three-dimensional scalar addition theorem," *J. Electromagnetic Waves and Applications*, vol. 6, no. 2, pp. 133-142, 1992.
14. T. Itoh, "Spectral domain immittance approach for dispersion characteristics of generalized transmission lines," *IEEE Trans. Microwave Theory Tech.*, vol. MTT-28, pp. 733-736, July 1980.
15. W. C. Chew and L. Gürel, "Reflection and transmission operators for strips or disks embedded in homogeneous and layered media," *IEEE Trans. Microwave Theory Tech.*, vol. MTT-36, pp. 1488-1497, Nov. 1988.
16. Y. L. Chow, J. J. Yang, D. F. Fang, and G. E. Howard, "A closed-form spatial Green's function for the thick microstrip substrate," *IEEE Trans. Microwave Theory Tech.*, vol. MTT-39, pp. 588-592, Mar. 1991.
17. M. I. Aksun, "A robust approach for the derivation of closed-form Green's functions," *IEEE Trans. Microwave Theory Tech.*, in press.
18. L. Alatan, M. I. Aksun, K. Mahadevan, and T. Birand, "Analytical evaluation of the MoM matrix elements," *IEEE Trans. Microwave Theory Tech.*, in press.

## ACKNOWLEDGEMENTS

This work was supported in part by NATO's Scientific Affairs Division in the framework of the Science for Stability Programme and in part by the Scientific and Technical Research Council of Turkey (TUBITAK) under contract EEEAG-163.

**Discussor's name:** G. BROWN

**Comment/Question:**

You said that there are no approximations in the FMM, but how do you a priori determine what the clustering should be?

**Author/presenter's reply:**

Clustering is performed in a standard manner.

For any arbitrary geometry, the subscatterers (unknowns) are grouped together based on physical proximity. This is not an a priori information. That helps the solution.

On the other hand, there are approximations in the FMM. However, these approximations can be arbitrarily improved by choosing the parameters of the FMM to obtain as many correct digits as the user desires.

**Discussor's name:** C. D. SILENCE

How many years before FMM can be applied to full aircraft geometries at 10 GHz?

**Comment/Question:**

This depends on the support given to the project. It may take 2-5 years to accomplish this starting, from the beginning. On the other hand, this period may be shorter for a well-funded project. Scattering from large aircraft at high frequencies might have already been accomplished in confidential projects funded by defense organizations.

**Discussor's name:** M. K LEVY

**Comment/Question:**

Do you use automatic clustering algorithms which can deal with arbitrary target shapes?

**Author/Presenter's reply:**

Yes. The problem of clustering can be reduced to an optimization problem. There are several existing statistical algorithms for the solution of this optimization problem. Some of these algorithms are sub-optimal heuristic algorithms and, thus, are very efficient.

**Discussor's name:** J. G. GALLAGHER

**Comment/Question:**

I did not get a strong feeling for the accuracy of this technique and would like to have a comparison with other computational methods. For example, for strip grating problems a Floquet mode analysis of MoM results could be used to obtain a comparison.

**Author/Presenter's reply:**

All of the RCS results presented in this talk are obtained using three different solution techniques: (1) FMM, (2) MoM with direct solution, and (3) MoM with iterative solution.

All three solutions agree for several digits for all of the sample problems presented in my talk. Thus, the necessary comparisons are made to demonstrate the accuracy of the FMM.

# Statistical Analysis of Propagation Parameters for Polarimetric Radar Measurements

V. Santalla del Rio, Y.M.M. Antar\*

Dpt. Tecnologias de las comunicaciones. Universidad de Vigo. 36200 Vigo, Spain.

\*Dpt. of Electrical and Computing Engineering.

Royal Military College of Canada. Kingston, Ontario Canada K7K 5L0.

## 1 Abstract

Analysis of the polarimetric scattering matrix or the covariance matrix has become an important tool in remote sensing applications. Propagation to and back from the target is affected by the medium. Rain media usually present some anisotropy that causes depolarization of the wave and can greatly affect either the scattering matrix or the covariance matrix obtained. Depolarization effects through propagation should then be corrected for. These effects can be determined and accounted for if the characteristic polarizations of the medium (those that propagate without changing their polarizations) and their respective propagation constants are known.

In examining the backscattering properties of rain media it is found that they present reflection symmetry. This is an important property that leads to linear and orthogonal characteristic polarizations. Measurement of the covariance matrix in the polarization base defined by the characteristic polarizations allows extraction of propagation parameters from the copolar power and copolar correlation terms. Different algorithms can be designed for its extraction. In order to be able to compare them, statistical analysis of polarization covariance matrix is performed. This analysis considers also the correlation effects between successive data samples. From

the statistics of the polarization covariance matrix statistics of propagation parameters can be directly derived.

## 2 Introduction

In polarimetric radar operation and target detection against clutter, e.g. atmospheric clutter, propagation effects are important factors that could affect the target detection and identification process. Besides attenuation, propagation media often present some anisotropy so that a cross-polarized component will be generated through propagation except for two transmitted polarizations, so called characteristic polarizations of the media, which will propagate without changing polarization but with different propagation constants. The way to describe the effects of the medium on the propagation will be to specify the two characteristic polarizations and the differential attenuation and differential phase shift between them. Different authors have addressed the problem of separating scattering properties of targets from propagation effects, [1], [2], [3], [4] in polarimetric radar measurements. For this purpose, different algorithms have been designed. Analysis and comparison between them will require statistical characterization of the data.

indicate that reflection symmetry as defined in [8] exists with respect to the plane defined by the line of sight and the direction of the mean canting angle. The basic idea contained in this property is that any contribution at the radar input from a point P on the target has its corresponding contribution from its symmetric point P' with respect to a plane of symmetry that contains the line of sight of the radar. This interesting property is a consequence of the assumption of symmetrical distribution of canting angles, considered in the theoretical model used here and most others, [9], [10]. Analysis of real polarimetric data acquired with the polarization diversity radar that was in operation at the National Research Council of Canada, at Ottawa [11], has confirmed that property [12]. This property will have important consequences that will be analyzed in next section.

#### 4 Characteristic Polarizations and Propagation Parameters

In obtaining the polarization covariance matrix for rain, propagation through the media has not been considered, but rain media, composed of particles with shapes different from spherical and with a preferred orientation, behave as anisotropic media. Thus wave polarization undergoes a transformation through propagation; though there always exist two polarizations, the characteristic polarizations, that propagate through the medium without suffering depolarization. These polarizations are, generally, not linear neither orthogonal. However, in the case of meteorological targets, and as a consequence of reflection symmetry the characteristic polarizations are linear and orthogonal, coinciding with the symmetry axis of the media [12]. Considering the depolarization introduced by the medium, the measured scattering matrix if linear polarizations parallel and

orthogonal to the plane of symmetry are transmitted can be written as

$$P^t(\alpha\beta) \begin{bmatrix} S_{\alpha\alpha} & S_{\alpha\beta} \\ S_{\alpha\beta} & S_{\beta\beta} \end{bmatrix} P(\alpha\beta) \quad (8)$$

where  $P(\alpha\beta)$  is the matrix that accounts for propagation effects at the specified linear polarization base

$$P(\alpha\beta) = \frac{e^{-\gamma R}}{R} \begin{bmatrix} e^{-\Delta\gamma R/2} & 0 \\ 0 & e^{\Delta\gamma R/2} \end{bmatrix} \quad (9)$$

where:

$$\gamma = (\gamma_1 + \gamma_2)/2$$

$$\Delta\gamma = \gamma_2 - \gamma_1$$

and  $\gamma_1$  and  $\gamma_2$  are the propagation constants corresponding to the characteristic polarizations.

Now, to account for propagation effects on the covariance matrix correlations are performed using the measured scattering matrix elements as expressed in eq. (8), so the measured covariance matrix result

$$P_c(\alpha\beta) C_{\alpha\beta} P_c^{t*}(\alpha\beta) \quad (10)$$

where the propagation matrix  $P_c$  now has the simplified expression:

$$P_c(\alpha\beta) = \frac{e^{-2\gamma R}}{R^2} \begin{bmatrix} e^{-\Delta\gamma R} & 0 & 0 \\ 0 & 1 & 0 \\ 0 & 0 & e^{\Delta\gamma R} \end{bmatrix} \quad (11)$$

and  $C_{\alpha\beta}$  is given in eq. (6). Then the covariance matrix has the following form:

$$A \begin{bmatrix} |S_{\alpha\alpha}|^2 e^{-2Re(\Delta\gamma R)} & 0 & \overline{S_{\beta\beta} S_{\alpha\alpha}^*} e^{-2jIm(\Delta\gamma R)} \\ 0 & 2|S_{\alpha\beta}|^2 & 0 \\ \overline{S_{\alpha\alpha} S_{\beta\beta}^*} e^{2jIm(\Delta\gamma R)} & 0 & |S_{\beta\beta}|^2 e^{2Re(\Delta\gamma R)} \end{bmatrix} \quad (12)$$

where

$$A = \frac{e^{-4Re(\gamma)R}}{R^4} \quad (13)$$

Therefore, if the medium can be considered homogeneous, at least for some range gates, along the radio path, comparison of covariance matrices for consecutive range

indicate that reflection symmetry as defined in [8] exists with respect to the plane defined by the line of sight and the direction of the mean canting angle. The basic idea contained in this property is that any contribution at the radar input from a point P on the target has its corresponding contribution from its symmetric point P' with respect to a plane of symmetry that contains the line of sight of the radar. This interesting property is a consequence of the assumption of symmetrical distribution of canting angles, considered in the theoretical model used here and most others, [9], [10]. Analysis of real polarimetric data acquired with the polarization diversity radar that was in operation at the National Research Council of Canada, at Ottawa [11], has confirmed that property [12]. This property will have important consequences that will be analyzed in next section.

#### 4 Characteristic Polarizations and Propagation Parameters

In obtaining the polarization covariance matrix for rain, propagation through the media has not been considered, but rain media, composed of particles with shapes different from spherical and with a preferred orientation, behave as anisotropic media. Thus wave polarization undergoes a transformation through propagation; though there always exist two polarizations, the characteristic polarizations, that propagate through the medium without suffering depolarization. These polarizations are, generally, not linear neither orthogonal. However, in the case of meteorological targets, and as a consequence of reflection symmetry the characteristic polarizations are linear and orthogonal, coinciding with the symmetry axis of the media [12]. Considering the depolarization introduced by the medium, the measured scattering matrix if linear polarizations parallel and

orthogonal to the plane of symmetry are transmitted can be written as

$$P^t(\alpha\beta) \begin{bmatrix} S_{\alpha\alpha} & S_{\alpha\beta} \\ S_{\alpha\beta} & S_{\beta\beta} \end{bmatrix} P(\alpha\beta) \quad (8)$$

where  $P(\alpha\beta)$  is the matrix that accounts for propagation effects at the specified linear polarization base

$$P(\alpha\beta) = \frac{e^{-\gamma R}}{R} \begin{bmatrix} e^{-\Delta\gamma R/2} & 0 \\ 0 & e^{\Delta\gamma R/2} \end{bmatrix} \quad (9)$$

where:

$$\gamma = (\gamma_1 + \gamma_2)/2$$

$$\Delta\gamma = \gamma_2 - \gamma_1$$

and  $\gamma_1$  and  $\gamma_2$  are the propagation constants corresponding to the characteristic polarizations.

Now, to account for propagation effects on the covariance matrix correlations are performed using the measured scattering matrix elements as expressed in eq. (8). so the measured covariance matrix result

$$P_c(\alpha\beta) C_{\alpha\beta} P_c^{t*}(\alpha\beta) \quad (10)$$

where the propagation matrix  $P_c$  now has the simplified expression:

$$P_c(\alpha\beta) = \frac{e^{-2\gamma R}}{R^2} \begin{bmatrix} e^{-\Delta\gamma R} & 0 & 0 \\ 0 & 1 & 0 \\ 0 & 0 & e^{\Delta\gamma R} \end{bmatrix} \quad (11)$$

and  $C_{\alpha\beta}$  is given in eq. (6). Then the covariance matrix has the following form:

$$A \begin{bmatrix} \overline{|S_{\alpha\alpha}|^2} e^{-2Re(\Delta\gamma R)} & 0 & \overline{S_{\beta\beta} S_{\alpha\alpha}^*} e^{-2jIm(\Delta\gamma R)} \\ 0 & 2\overline{|S_{\alpha\beta}|^2} & 0 \\ \overline{S_{\alpha\alpha} S_{\beta\beta}^*} e^{2jIm(\Delta\gamma R)} & 0 & \overline{|S_{\beta\beta}|^2} e^{2Re(\Delta\gamma R)} \end{bmatrix} \quad (12)$$

where

$$A = \frac{e^{-4Re(\gamma)R}}{R^4} \quad (13)$$

Therefore, if the medium can be considered homogeneous, at least for some range gates, along the radio path, comparison of covariance matrices for consecutive range

gates will allow determination of both parameters, differential attenuation and differential phase shift. In particular the differential phase shift can be extracted from the correlation between copolar powers obtained with the characteristic polarizations of the media

$$Im(\Delta\gamma R) = \frac{1}{2} \mathcal{L}(\overline{S_{\alpha\alpha} S_{\beta\beta}^*} e^{-2jIm(\Delta\gamma R)}) - \mathcal{L}(\overline{S_{\alpha\alpha} S_{\beta\beta}^*} e^{-4jIm(\Delta\gamma R)}) \quad (14)$$

and differential attenuation can be extracted from each one of the copolar powers measured at same polarizations,

$$Re(\Delta\gamma R) = \frac{1}{2} \ln \frac{\overline{|S_{\alpha\alpha}|^2} e^{-2Re(\Delta\gamma R)}}{\overline{|S_{\alpha\alpha}|^2} e^{-4Re(\Delta\gamma R)}} \quad (15)$$

## 5 Statistics of Propagation Parameters

As we have seen, estimation of propagation parameters requires previous estimation of the covariance matrix. Then, the statistics of propagation parameters will be obtained from the statistics of the elements of the sample covariance matrix, that has been considered for most authors as the covariance matrix estimator since, in the case of uncorrelated samples of the elements of the scattering matrix, it provides the maximum likelihood estimator of the covariance matrix.

The sample covariance matrix elements are obtained by direct promediation of the products of the elements of the measured scattering matrix. This matrix is usually determined by direct measurement scheme; this requires polarization diversity in reception and transmission and the capability of amplitude and relative phase measurements in each of the polarizations configurations. If a general polarization base ( $A, B$ ) is considered, polarization  $A$  is transmitted first and the orthogonal wave components of the radar return with respect to polarization  $A$  and its orthogonal counterpart  $B$

are received simultaneously. At this time instant  $t$  the scattering matrix elements  $S_{AA}$  and  $S_{BA}$ , i.e., the first column of the matrix  $S$ , are determined. After a small time delay  $T$ , which is required to switch the transmitter polarization, polarization  $B$  is transmitted and the orthogonally polarized components  $A$  and  $B$  of the backscattered waves are again simultaneously received and recorded, yielding the scattering coefficients  $S_{AB}$  and  $S_{BB}$ , i.e., the second column of  $S$  at the time instant  $t + T$ . Employing a constant pulse repetition frequency  $PRF = 1/T$  for the transmitter polarization switching, a time series of scattering matrix elements may be recorded. The time series corresponding to each element of the scattering matrix is considered a polarimetric channel that can be statistically modeled as a complex Gaussian stationary and ergodic stochastic process [13], [14]. Samples of each channel are temporally correlated; the normalized autocorrelation is given by [13]

$$\rho(nT) = e^{-\frac{8\pi^2 \sigma_v^2 T^2 n^2}{\lambda^2}} e^{j\frac{4\pi \bar{v} n T}{\lambda}} \quad (16)$$

where  $nT$  is the time lag, a multiple of the pulse repetition period,  $\lambda$  the wavelength,  $\bar{v}$  the mean radial velocity of the hydrometeors and  $\sigma_v$  the spread of the corresponding Gaussian Doppler spectrum, proportional to the Fourier transform of  $\rho(nT)$ .

To derive the probability density functions of the elements of the sample covariance matrix let  $S_i = [s_1^i, \dots, s_n^i]^t$ ,  $i = 1, 2, 3$  be a  $n$ -dimensional vector that represents  $n$  samples of one of the three polarimetric channels defined in the monostatic case. Since we are interested in obtaining the distribution of the elements of the sample covariance matrix, we are interested in the distribution of the generic product  $S_i^t S_j^*$ . Let  $S = [S_1 \ S_2 \ S_3]^t$  a  $3n$ -dimensional vector that contains the information of the three polarimetric channels. Since it was assumed each polarimetric channel follows

a complex Gaussian stationary process, and the correlations between samples at the same time are given by eq. (16), the probability density function of  $\mathbf{S}$  is given by:

$$p(\mathbf{S}) = \frac{1}{\pi^{3n}|C_S|} \exp\{-\mathbf{S}^{t*} C_S^{-1} \mathbf{S}\} \quad (17)$$

where,

$$C_S = C \otimes \Upsilon \quad (18)$$

$C$  represents the covariance matrix,  $\otimes$  indicates Kronecker product and

$$\Upsilon = \begin{bmatrix} 1 & \rho_1 & \cdots & \rho_n \\ \rho_1^* & 1 & \cdots & \rho_{n-1} \\ \vdots & \vdots & \ddots & \vdots \\ \rho_n^* & \rho_{n-1}^* & \cdots & 1 \end{bmatrix}$$

is the normalized autocorrelation matrix.

By proper integration of eq. (17) distributions of the generic product  $\mathbf{S}_i^t \mathbf{S}_j^* = \sum_k s_k^i s_k^{j*}$  will be obtained.

Let  $Q_n$  be the  $n \times n$  unitary matrix such that  $Q_n^{t*} \Upsilon Q_n = \Lambda_n$ , where  $\Lambda_n$  is a  $n \times n$  diagonal matrix whose elements are the eigenvalues  $\lambda_1, \lambda_2, \dots, \lambda_n$  of  $\Upsilon$ . If we apply the unitary linear transformation defined by  $Q_n$  to vectors  $\mathbf{S}_i$   $i = 1, 2, 3$  the generic product  $\mathbf{S}_i^t \mathbf{S}_j^*$  will not be altered.

$$\begin{aligned} \mathbf{S}'_i &= Q_n \mathbf{S}_i \\ \mathbf{S}'_j &= Q_n \mathbf{S}_j \\ \mathbf{S}_i^t \mathbf{S}_j^* &= \mathbf{S}_i^t Q_n^t Q_n \mathbf{S}_j^* = \mathbf{S}_i^t \mathbf{S}_j^* \end{aligned} \quad (19)$$

Now, in order to get the distributions we are interested in we apply the following unitary linear transformation, defined by the matrix  $Q_{3n}$ , to the vector  $\mathbf{S}$ ,

$$Q_{3n} = \begin{bmatrix} Q_n & 0_n & 0_n \\ 0_n & Q_n & 0_n \\ 0_n & 0_n & Q_n \end{bmatrix} \quad (20)$$

where  $0_n$  is the  $n \times n$  zero matrix. Thus,

$$\mathbf{S}' = Q_{3n} \mathbf{S} \quad (21)$$

$$C_\Lambda = Q_{3n}^{t*} C_S Q_{3n} = C \otimes \Lambda_n$$

and

$$p(\mathbf{S}') = \frac{1}{\pi^{3n}|C_\Lambda|} \exp\{-\mathbf{S}'^{t*} C_\Lambda \mathbf{S}'\} \quad (22)$$

To get the statistics of the propagation parameters we are interested in obtaining the statistics of the copolar power terms (either  $|\overline{S_{\alpha\alpha}}|^2$  or  $|\overline{S_{\beta\beta}}|^2$ ) and of the phase of the copolar correlation term  $(\overline{S_{\alpha\alpha} S_{\beta\beta}^*})$ .

## 5.1 Statistics of copolar power

The probability density function of the copolar power estimator  $Y$  can be obtained by integrating of eq. (22). The result gives

$$p(Y) = \sum_{k=1}^n \frac{n C_k}{\sigma \lambda_k} \exp\left\{-\frac{ny}{\sigma \lambda_k}\right\} \quad (23)$$

where

$$C_k = \left\{ \prod_{j=1, j \neq k}^n (1 - \lambda_k^{-1} \lambda_j) \right\}^{-1} \quad (24)$$

and  $\sigma = |\overline{S_{\alpha\alpha}}|^2$  or  $\sigma = |\overline{S_{\beta\beta}}|^2$ . Using the moment theorem [15] the moments of this variable are calculated

$$E[Y] = \sigma$$

$$E[Y^2] = \frac{\sigma^2}{n^2} \sum_{k=1}^n \lambda_k^2 + \sigma^2 \quad (25)$$

$$var[Y] = \frac{\sigma^2}{n^2} \sum_{k=1}^n \lambda_k^2$$

It is also of interest (see eq. (15)) to obtain the moments of the variable  $Z = \ln Y$ . Performing the variable change and integrating, the first two order moments were calculated:

$$\begin{aligned} E[Z] &= -C - \ln n + \sum_{k=1}^n C_k \ln(\sigma \lambda_k) \\ E[Z^2] &= \frac{\pi^2}{6} + C^2 + \sum_{k=1}^n C_k \ln^2(\sigma \lambda_k) + \ln^2 n \\ &\quad - 2C \sum_{k=1}^n C_k \ln(\sigma \lambda_k) - 2 \ln n (E[Z] + \ln n) \\ var[Z] &= E[Z^2] - E[Z]^2 \end{aligned} \quad (26)$$

where  $C = 0.577215$  is Euler's constant.

The graphics show the mean and variance of  $Z$  for  $\sigma = 1$  as functions of the number of integrated pulses and the temporal correlation between samples.

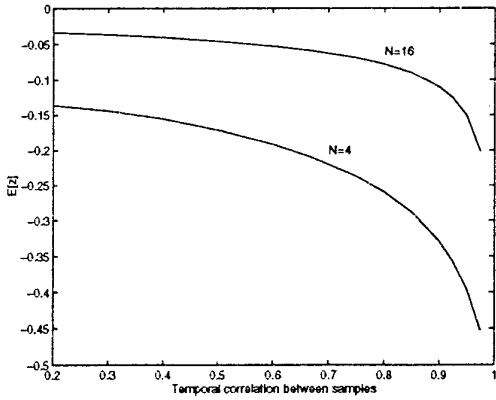


Figure 1: Mean of  $Z$

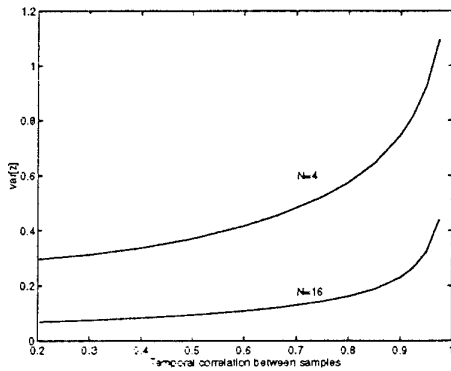


Figure 2: Variance of  $Z$

### 5.2 Statistics of copolar correlation phase

Unfortunately, it has not been possible to find closed-form expressions for the probability density function of the copolar correlation phase. However, the mean and variance can be calculated from

$$E[\Phi] = \int \arctg\left(\frac{Z^I}{Z^R}\right) p(Z^R, Z^I) dZ^R dZ^I \quad (27)$$

$$E[\Phi^2] = \int \arctg^2\left(\frac{Z^I}{Z^R}\right) p(Z^R, Z^I) dZ^R dZ^I$$

where  $Z^R$  and  $Z^I$  are the real and imaginary part of the integrated copolar corre-

lation term and  $p(Z^R, Z^I)$  its joint probability density function, which can be calculated as the Fourier transform of

$$\Phi(U^R, U^I) = \prod_{k=1}^n \left\{ 1 + \frac{\lambda_k^2}{4} \sigma_\alpha \sigma_\beta (1-k^2) (U^{R2} + U^{I2}) - j \lambda_k \sqrt{\sigma_\alpha \sigma_\beta} k (U^R \cos \phi + U^I \sin \phi) \right\}^{-1} \quad (28)$$

where the copolar correlation  $\overline{S_{\alpha\alpha} S_{\beta\beta}^*}$  has been expressed as

$$\overline{S_{\alpha\alpha} S_{\beta\beta}^*} = \sigma_\alpha \sigma_\beta k e^{j\phi}$$

with

$$\sigma_\alpha = \overline{|S_{\alpha\alpha}|^2}$$

$$\sigma_\beta = \overline{|S_{\beta\beta}|^2}$$

$$k = \overline{|S_{\alpha\alpha} S_{\beta\beta}^*|} / (\sigma_\alpha \sigma_\beta)$$

$$\phi = \angle \overline{S_{\alpha\alpha} S_{\beta\beta}^*}$$

The graphics show the mean and variance of the phase as functions of the number of integrated pulses and the correlation between successive samples for  $k = 0.6$  and  $\phi = \pi/6$  rad. Analysis of the mean and variance of the phase as functions of  $k$  indicate that as  $k$  increases, both, the bias of the mean and the variance decrease.

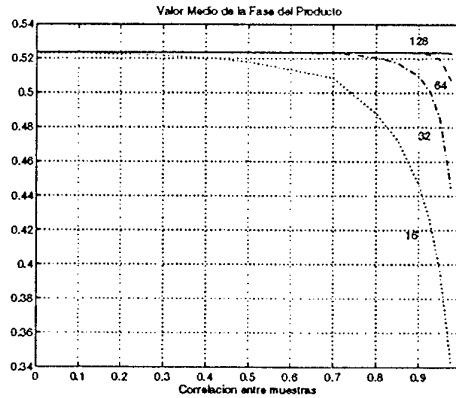


Figure 3: Mean of  $\Phi$  for  $k = 0.6$ ,  $\phi = 30$  deg.

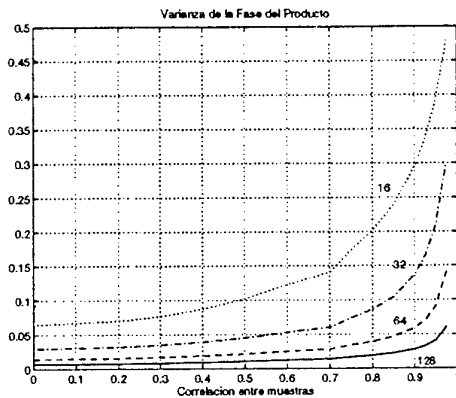


Figure 4: Variance of  $\Phi$  for  $k = 0.6$ ,  $\phi = 30$  deg.

### 5.3 Mean and Variance of Differential Attenuation and Differential Phase Shift

Once the statistics of variable  $Z$  and  $\Phi$  have been calculated the mean and variance of the differential attenuation and the differential phase shift can be obtained. If the basic algorithm of eq. (15) and (14) is considered

$$E[\text{Re}(\Delta\gamma R)] = \frac{1}{2}(E[Z(R)] - E[Z(2R)])$$

$$E[\text{Re}^2(\Delta\gamma R)] = \frac{1}{4}(E[Z(R)^2] + E[Z(2R)^2]) \quad (28)$$

$$E[\text{Im}(\Delta\gamma R)] = \frac{1}{2}(E[\Phi(R)] - E[\Phi(2R)])$$

$$E[\text{Im}^2(\Delta\gamma R)] = \frac{1}{4}(E[\Phi(R)^2] + E[\Phi(2R)^2])$$

where  $Z(R)$ ,  $\Phi(R)$  ( $Z(2R)$ ,  $\Phi(2R)$ ) indicate those variables were obtained from a range gate at a distance  $R$  ( $2R$ ).

The resulting mean and variance were calculated assuming independence between variables from different range gates. Mean and variance of the propagation parameters estimators obtained through other algorithms can be obtained based on statistics of variables  $Z$  and  $\Phi$ . In doing that it is assumed there exists independence between variables obtained at different

range gates and it should be taking into account that the stochastic process defined by those variables at different ranges are not stationary.

## 6 Conclusions

A review of characterization of backscattering properties from meteorological targets was done with the purpose of illustrating the reflection symmetry property that these particular media present and its important consequence in the characteristic polarizations, that become linear and orthogonal. Extraction of propagation parameters from measurement of the polarization covariance matrix was then shown.

In order to get the statistics of the propagation parameters the statistics of the polarization covariance matrix were obtained, considering the decorrelation that exist between successive data samples. First two order moments of the parameters of interest, differential attenuation and differential phase shift, were analysed as functions of the decorrelation between successive samples and the number of integrated pulses. Calculation of the statistics of the differential attenuation requires computation of the coefficients of the partial fraction expansion corresponding to the Laplace transform of the probability density function of the copolar power. Numerically this is an ill-posed problem when the roots of the original polynomial are close. This is the case for large number of integrated pulses and low correlation between samples. Numerical methods are investigated to solve this problem. The different algorithms for extraction of propagation parameters that have already been proposed in the literature can now be compared on the basis of the statistics found here.

## References

- [1] G. McCormick and A. Hendry, "Principles for the radar determination of

- the polarization properties of precipitation," *Radio Science*, vol. 10, pp. 421-434, 1975.
- [2] J. Hubbert, V. Chandrasekar, and V. Bringi, "Processing and interpretation of coherent dual-polarized radar measurements," *Journal of Atmosf. and Ocean. Technology*, vol. 10, pp. 155-164, 1993.
- [3] D. Bebbington, R. McGuinness, and A. Holt, "Correction of propagation effects in s-band circular polarisation diversity radars," *IEE Proc. Part H*, vol. 134, pp. 431-437, 1987.
- [4] V. Ziegler, E. Luneburg, and A. Scotch, "Weather radar polarimetry: path integrated differential phase shift optimum polarization and the elliptical ef-basis," *Journal of Electromagnetic Waves and Applications*, vol. 9, pp. 309-325, 1995.
- [5] V. Santalla, A. Pino, and Y. Antar, "Polarimetric radar covariance matrix algorithms and applications to partially polarized waves," in *IGARSS95*, (Firenze, Italy), 1995.
- [6] A. Hendry, Y. Antar, and G. McCormick, "On the relationships between the degree of preferred orientation in precipitation and dual polarization radar echo characteristics," *Radio Science*, vol. 22, pp. 37-50, 1987.
- [7] Y. Antar and A. Hendry, "Correlations techniques in two-channel linearly polarized radar systems," *Electromagnetics*, vol. 7, pp. 17-27, 1987.
- [8] S. Nghiem, S. Yueh, R. Kwok, and F. Li, "Symmetry properties in polarimetric remote sensing," *Radio Science*, vol. 27, pp. 693-711, 1992.
- [9] T. Oguchi, "Electromagnetic wave propagation and scattering in rain and other hydrometeors," *Proc. IEEE*, vol. 71, pp. 1029-1077, 1983.
- [10] J. Vivekanandan, W. Adams, and V. Bringi, "Rigorous approach to polarimetric radar modeling of hydrometeor orientation distribution," *Journal of Applied Meteorology*, vol. 30, pp. 1053-1063, 1991.
- [11] Y. Antar, A. Hendry, and G. McCormick, "Circular polarization for remote sensing of precipitation: Polarization diversity work at the national research council of Canada," *Antennas and Propagation Magazine*, vol. 34, pp. 7-16, 1992.
- [12] V. Santalla, *Caracterizacion, analisis y aplicaciones de medidas radar polarimetricas*. Tesis doctoral. Universidad de Vigo, 1996.
- [13] K. Tragl, "Doppler correction for scattering matrix measurements of random targets," *Eur. Trans. on Telecom.*, vol. 2, pp. 43-49, 1991.
- [14] F. Ulaby and M. Dobson, *Handbook of radar scattering statistics for terrain*. Norwood, MA: Artech House, 1 ed., 1989.
- [15] A. Papoulis, *Probability, Random Variables and Stochastic Processes*. New York: McGraw-Hill, 1984.

**Discussor's name:** U. LAMMERS

**Comment/Question:**

Can you give us some practical numbers as to how much depolarization there might be per kilometer and as a function of rain rate?

**Author/Presenter's reply:**

It depends on the frequency but for a rain rate around 50 mm/h<sup>2</sup>, differential attenuation is of the order of 0.25 dB/km and differential phase shift around 1.5 degrees/km.

## Extended Target Simulation at a Physical Level

**SHW Simpson, PER Galloway**  
 Roke Manor Research Ltd.  
 Roke Manor, Old Salisbury Lane  
 Romsey, Hampshire SO5/6DB, UK

### Abstract

This paper describes an approach to the simulation of radar signatures from large complex targets. The issue addressed is that given a subject radar target in the form of a geometrical design, is it possible to recognise redundancy in the electromagnetic radiation source which this target represents when illuminated by a radar? This is a key issue since the task of directly evaluating the signature is often so compute intensive as to prohibit its use in a simulator.

The paper describes the results of some research into this using super-resolution inverse synthetic aperture radar methods. An example of generic ship geometry is used to illustrate the achievable performance, but it is stressed that the underlying message is in the importance of signal processing for reduced redundancy in simulation, rather than the specific nature of the example used.

### Physical Level Simulation - The Impact of Modern Computers

The latest generation of workstations has brought what used to be considered as supercomputer processing power within the reach of virtually every research laboratory. These, coupled with software communications harnesses can bring collections of machines together to work in concert, thus realising a very useful class of parallel computer [4] [7].

Such considerations have led to the possibility of simulating real world effects at a much more basic physical level than has previously been possible.

In the current context, the impact of this is that radar signatures from large complex targets like ships can be calculated from their CAD file descriptions using computational electromagnetic codes to evaluate the radar cross-section (RCS) or other radar signature.

### Signal Processing for Reduced Redundancy - Benefits in Simulation

Whilst computation of a ship signature from a large and detailed CAD file is feasible, the execution time for the task is typically a few days on a small collection of workstations. This time is far too long to contemplate

executing the task within the event loop of a simulator.

At the other extreme, all the required signatures could be pre-calculated and stored within a data base to be accessed as required within the simulator event loop. Whilst this gets around the execution rate problem, it requires a massive unwieldy database.

Neither of these approaches are really feasible in a simulator environment that requires to respond rapidly to a call for a high resolution or complex polarisation signature. What is really required is a simpler model of the target which still retains the signature of the complex geometrical shape. This leads to the question of how much redundancy can be identified and removed from the signature calculation process?

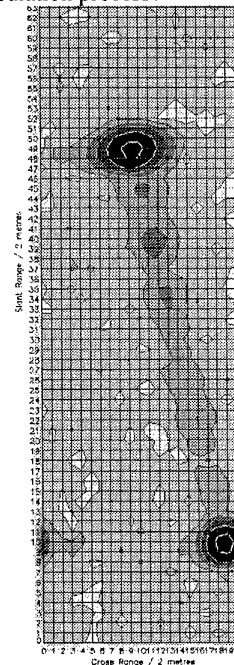


**Figure 1. 80m Rectangular Plate ISAR Image**

That redundancy does exist can be seen by studying the simple example shown in Figure 1. This shows a microwave image of a long thin conducting strip (80 metres). The procedure used to produce the image is Inverse synthetic aperture radar (ISAR) [1]. This

basically involves gathering 2D frequency domain data which is subjected to a Fourier transform to yield the image. A Kaiser-Bessel [2] window has been used and 70 dB dynamic range is shown on a two metre square grid. This image clearly illustrates that the strip can be represented by a point scatterer at each end of the strip. The frequency domain data input into the ISAR process has been produced using the EPSILON RCS prediction code [3] [4] using only an optical boundary condition. This eliminates an equivalent edge current as the explanation for the image. The true reason is that the diffraction pattern of a flat strip is practically indistinguishable from that for a pair of point sources of the correct separation over a small aspect range.

In this example the surface integration of the electromagnetic boundary condition, or the equivalent boundary integral, can be reduced to a sum of two points. This represents an enormous computational saving and suggests a general procedure for eliminating, or reducing, the redundancy in the signature calculation from complex shapes. The proviso being that an equivalent collection of point scatterers can be identified. Unfortunately, if this procedure is tried on a complex target the identification of the equivalent set of scatterers becomes marred by the interference of point spreading functions representing closely spaced sources. The procedure then breaks down, making it impossible to accurately reconstruct the signature from the image.

What is needed to solve the simulation problem is a signal processing procedure which is free of the point spreading function.

## The Impact of Super Resolution Processing

Basic Fourier processing provides a nominal resolution of:

$$\text{Resolution} = (\text{Speed of light} / 2 * \text{Bandwidth}) [1]$$

over the entire image plane. In this case the image is the object convolved with a point spreading function. Super resolution, in this context, is a class of signal processing algorithms that provides greater resolution by representing the image as a set of weighted impulses. The authors have experimented with both the *music* [5] and the *imp* [6] algorithm and both can yield good performance under suitable conditions. The price paid for this is that only a limited number of impulse sources can be identified and there is a greater associated processing load than a simple Fourier transform.

The improvement afforded over Fourier processing can

be so great as to make the procedure discussed above feasible on complex targets. This opens up vast possibilities for physically accurate simulation of radar signatures with about five orders of magnitude improvement in execution rate. The resultant execution rates are so much improved that "in-loop calculation" from the super resolution model is possible.

The alternative signal processing routes originating from a common data source are shown in Figure 2.

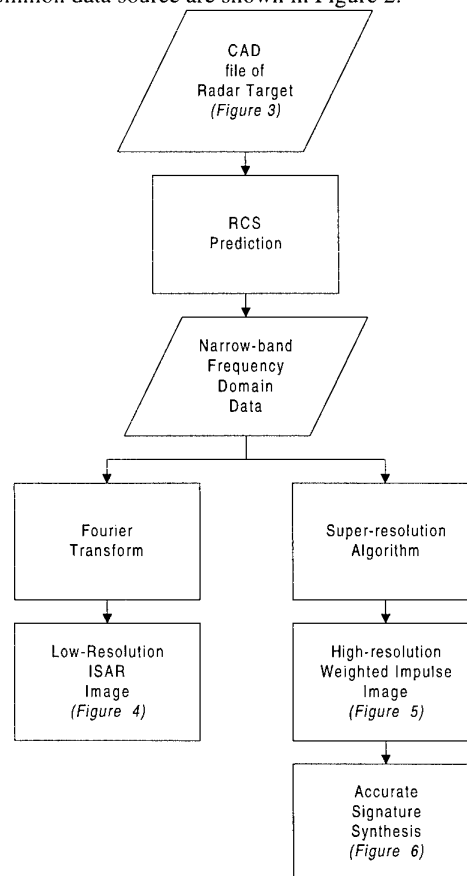


Figure 2. Alternative Signal Processing Routes

## An Illustrated Example

The example considered here is that of a generic ship. This model is of Corvette size (approximately 800 tons), about eighty metres length overall, but does not represent any physical ship in existence. The simplified CAD geometry of this model is shown in Figure 3.

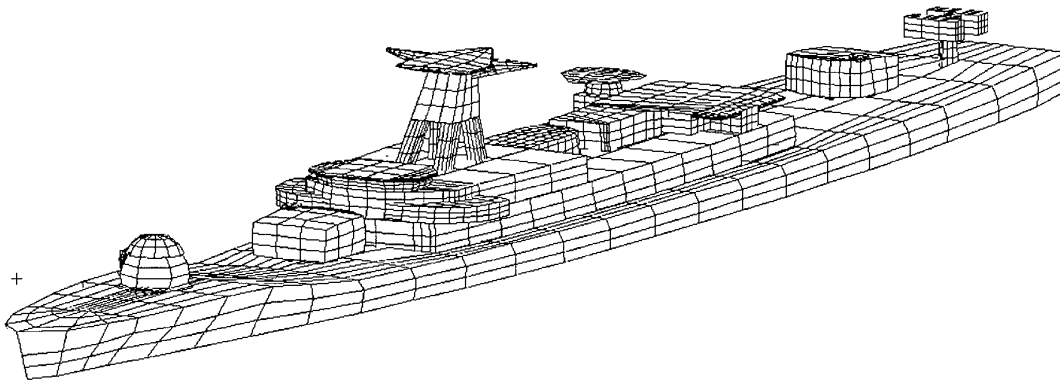


Figure 3. Generic Ship CAD Model

A typical simulation requirement is to reproduce the radar signature of the ship from any position on the horizon for a specified band of frequencies in vertical, horizontal or circular polarisation.

*(Arguably, the best way to provide this is from measured signatures. However, although frequently proposed, the required measured data is virtually impossible to obtain due to incompleteness.)*

The need for frequency diversity strictly requires the image to be calculated for each independent frequency. However, once the super resolution weighted impulse model has been evaluated for one frequency, it is remarkably reusable at other frequencies as the changed electrical path length between the points captures most of the effect of changing the frequency.

The need for polarisation diversity is best catered for by associating a 2D complex scattering matrix with each point.

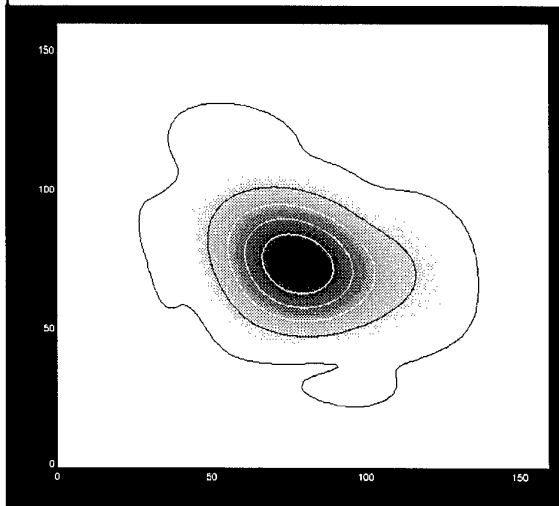


Figure 4. Low Resolution ISAR Image

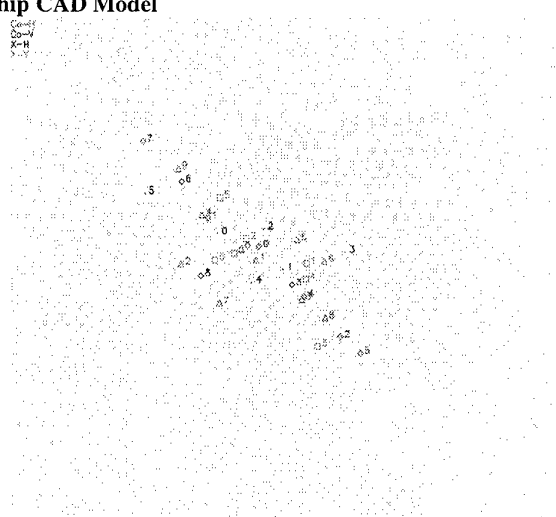


Figure 5. High Resolution Weighted Impulse Image

This has been found to be the only real difficulty, as two orthogonal polarisation images must be combined to achieve this. There is inevitably some mis-match between the images and a procedure must be worked out for dealing with this.

In Figures 4 and 5 a comparison is made between an ISAR image, produced to 16 metre resolution, and the corresponding super resolution weighted impulse image. It is clear from this extreme example that there is little hope of reproducing the bulk RCS or range profile from the ISAR image. The super-resolution image, on the other hand is capable of quite outstanding performance, as is illustrated by the overlaid signature in Figure 6. This shows the EPSILON computed signature overlaid on the re-synthesized signature derived from the weighted impulse scattering model. This technique is capable of generating high resolution signatures up to the bandwidth of the original ISAR data. If better resolution is required then higher resolution frequency domain data must be used to build the weighted impulse model.

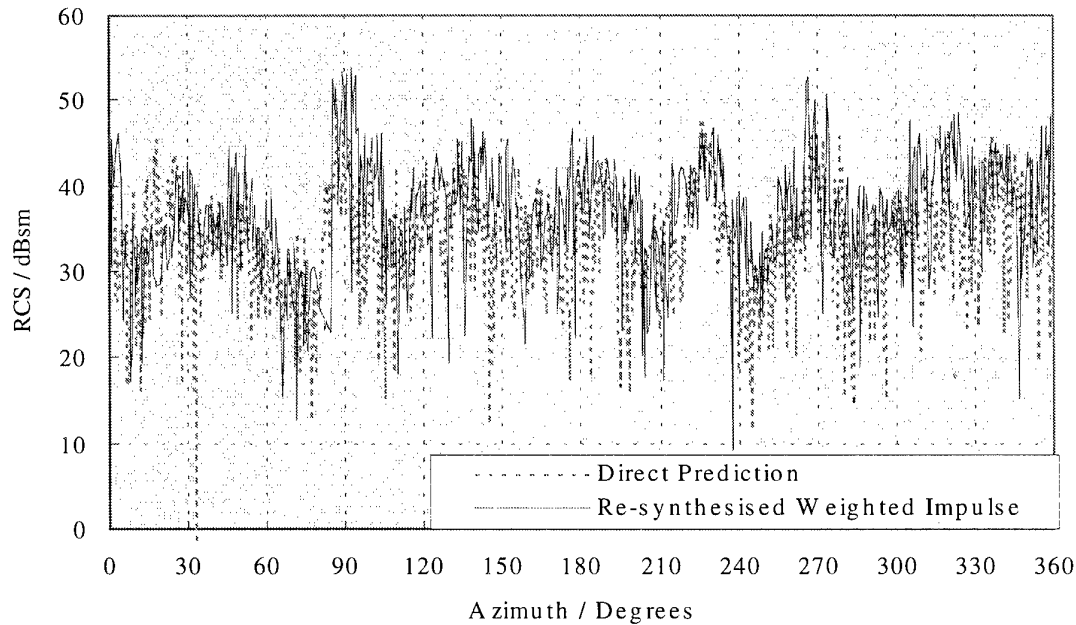


Figure 6. Overlaid RCS signatures: Direct Prediction and Super-resolution generated.

## Conclusions

A weighted impulse scattering model for the rapid simulation of complex target signatures has been shown to be derivable from ISAR data by utilising super resolution techniques. The radar signature of the complex target has been simplified to about 30 scattering points in each aspect range. This removal of redundancy allows the incorporation of sophisticated signature models into simulation systems without the need for storing a massive pre-calculated database.

The form of the weighted impulse model could be a convenient starting point for non cooperative target recognition investigations. The compactness of the data will lead to obvious advantages in recognition time and data base size.

## References

- [1] Wehner D.R. 'High Resolution Radar', Second Edition, Artech House Pub.1995. ISBN 0-89006-727-9
- [2] Harris F. J. 'On the Use of Windows for Harmonic Analysis with the Discrete Fourier Transform', Proc. IEEE Vol 66. No.1 Jan 1978.
- [3] Harman M, Simpson S., 'EPSILON - A Radar Cross Section Modeling package', Proc. UKSCS 1990.
- [4] Galloway P., Simpson S, 'Parallelisation of Radar Cross Section (RCS) Prediction for Electrically Large Targets', Proc. European Simulation Multiconference 1991.
- [5] Brandwood D. H, 'Noise space projection: MUSIC without eigenvectors', Proc IEE 134 Pt H,303-309 1987.
- [6] Mather J. L., 'The Incremental Multi-Parameter algorithm', Proc 24th Asilomar Conf. 368-372 1990.
- [7] Galloway P., 'The Operation and Control of large Parallel Simulations on a Network of Sun Workstations using CSToolsTM' ,Proc. European Simulation Symposium 1992
- [8] Boerner WM et al, 'Basic Monostatic Polarimetric Broadband Target Scattering Analysis Required for High Resolution Polarimetric Radar Target Downrange/Crossrange Imaging of Airborne Scatterers' , Seminar on Vector Inverse Methods in Radar Target Clutter Imaging, Superlec Gif-sur-Yvette, IEEE September 1986.

## Acknowledgments

The Authors wish to acknowledge the expert assistance of Mr. DH Brandwood of Roke Manor Research in the implementation of the super-resolution algorithms. This work has been carried out for the Defence Evaluation and Research Agency, an agency of the UK Ministry of Defence, and is supported by HMG.

**Discussor's name:** P. BEENEY

Please advise the rationale used to decide whether a scatterer is "significant" in the model.

**Author/Presenter's reply:**

Two strategies are being investigated:

- 1) A fixed amplitude limit, the "top" of the amplitude range being set from the greatest magnitude scatterer present (for this polarisation), e.g. take all scatterers within a 20dB range down from the largest magnitude scatterer present at this polarisation and aspect.
- 2) A fixed number of scatterers, e.g. the first 30 scatterers, in order of magnitude, for this polarisation.

(The selected strategy is implemented for each viewing aspect).

**Discussor's name:** F. SAKARYA

**Comment/Question:**

This work is about using high resolution algorithms such as MUSIC for deriving complex target signatures. However, most high resolution algorithms require too much computation and memory, even for several sources. Considering the high memory and computation requirements for MUSIC, how practical is it to use it for a large object such as a ship, or an aircraft?

Comment: There are algorithms, though, which do not have so much memory - computation requirement and are more robust, and they could be considered for such an application.

I wonder if the idea behind the derivation of ESPRIT could be applied to this problem?

**Author/presenter's reply:**

I may not have made it sufficiently clear in my presentation that it is the re-synthesis of the target signature, based on a few tens of points instead of perhaps several hundred thousand which makes the real time signature synthesis or recognition at a particular aspect possible for a complex target in a few milliseconds. The identification of these few tens of points from the hundreds of thousands in the original target data using the super resolution technique is indeed a huge computational problem in its own right and requires considerable processing and storage resource for each aspect. This computational problem, although huge, may be thought of as an "offline" or "pre-processing" stage to derive a very compact data-base, from which the principal contributors at a particular aspect can be obtained at "real time" access rates for signature re-synthesis, even for large targets such as ships and aircraft.

**Discussor's name:** J. L. VALERO

**Comment/Question:**

What is the influence of noise in the super resolution method?

**Author/Presenter's reply:**

The objective of using super resolution processing on measured or synthesised complex target data is to obtain a number of principal scatterers at each discrete viewing aspect, omitting lesser contributors. (There are two strategies for selecting principal scatterers. Please see my answer to Mr. P. Beene's question for these details). Since "noise" would generally be at a level below the principal scatterers' amplitude, this does not present a problem provided the scatterer selection is conducted with care. Very stealthy targets will probably have their principal scatterers' amplitudes much closer to the noise floor level, and this may present discrimination problems between the scatterers and "noise" when this class of target is processed with this method. However, such very stealthy targets are electrically small, whereas this technique is more applicable to larger targets, such as ships, which are inherently electrically large and possess principal scattering areas despite signature reduction considerations in their design. Thus, this method is of more application in dealing with electrically large targets with defined scatterers than those where scatterer discrimination from noise is much less apparent.

**Discussor's name:** A. BICCI

**Comment/Question:**

1. How are RCS diagrams over a large angle sector obtained from low resolution radar images?
2. Have you any discontinuity problem when passing from one sector to another?

**Author/Presenter's reply:**

1. A large number of radar images are computed on different angular sectors - at close angular increments. (Typically  $1^\circ$  or  $0.1^\circ$ ). (The chosen angular increment should anticipate the finest angular resolution needed when the signature is re-synthesised).
2. There are no problems in practice when dealing with very large targets such as a ship, due to the very high scintillation. Angular sectors should be chosen to be small enough to satisfy sampling to avoid sudden transitions and avoiding the need for interpolation - see reply to previous question, final sentence.

## Livorno'96: The Centimetre and Millimetre Wave Radar Signature and Propagation Trial by NATO AC/243(Panel 3/RSG.21)

**H.J.M. Heemsker**

chairman NATO AC/243(Panel3/RSG.21)  
TNO-Physics and Electronics Laboratory  
PO Box 96864, 2509 JG the Hague,  
the Netherlands

### 1. SUMMARY

Within NATO AC/243 Panel3 the Research Study Group (RSG.21) is performing co-operative research on maritime radar signatures and propagation at centimetre and millimetre waves. The member nations of RSG.21 have performed a measurement trial in May 1996 in Livorno Italy. The objectives of this trial were to compare national radar signature data collection and analysis methods in order to propose a common NATO method, to investigate the environmental effects on the measured radar signature of targets, to investigate the dependence of the radar signature on radar parameters, on geometrical parameters and on target parameters, and to compare RCS computation models inclusive a comparison of computed RCS with measured RCS.

The RCS measurements have been made at frequencies from 3 to 94 GHz by high resolution radars from all member nations. The targets were an auxiliary ship and a frigate. In order to investigate the environmental effects radar measurements have been made on a corner reflector on a small boat, while also meteorological parameters, refractivity profiles and sea states have been measured during the trial.

In this paper a review will be given of the Livorno'96 trial, including details on the objectives, the instrumentation and a first impression on the results.

### 2. BACKGROUND

Within NATO AC/243 Panel 3 the Research Study Group (RSG.21) is performing co-operative research on maritime radar signatures and propagation at centimetre and millimetre waves. This research is based upon the results of the experimental studies on target signatures and propagation effects in a maritime environment that has been performed by the former AC/243 (Panel3/RSG.8) and is a further detailed investigation to improve the survivability of naval targets in a hardkill-softkill environment.

The main military benefit of the investigations on maritime radar target /background signatures and related propagation effects is the improved survivability of naval vessels against radar guided missile attack by

applying signature reduction and control techniques and optimised signal processing schemes for self defence radar sensors.

The RSG will stimulate appropriate experts in other NATO groups to use the results of the RSG.21 research as an input for the simulation of survivability of ships against radar guided missile attack. This will be performed in close collaboration with AC/141 (IEG.1/SWG.4) on Electronic Warfare and will ultimately lead to an evaluation of the improved survivability of the STANAVFORLANT squadron in a hardkill-softkill environment.

The objectives in general are to examine the technical aspects of naval target signatures and related propagation effects in order to improve the ship survivability. This will be done by

- defining concepts and procedures for ship signature prediction and modelling inclusive validation of the models by measurements,
- understanding and describing the physical properties of multipath, propagation and ducting to improve the performance of fire control radars against sea skimming missiles, to analyse conditions of anomalous radar fading, to support tactical decisions and to quantify the effects on target signatures,
- performing experimental high resolution polarimetric investigations of ship, decoy and background signatures including the impact imposed by the propagation medium,
- developing concepts for signature reduction and control,
- developing concepts of aimpoint selection and homing for anti-ship missile seeker applications, and
- organising workshops on selected topics.

At present the member nations of RSG.21 are Denmark, France, Germany, Italy, Netherlands, Norway, United Kingdom and United States.

### 3. LIVORNO'96

The RSG.21 started the preparing activities for the Livorno'96 measurement campaign by end 1994. The measurements have been performed in a two weeks time period from 6-17 May 1996 and were hosted by Mariteleradar in Livorno Italy. A total of ten laboratories/institutes from all member nations have participated to the trial (table 1).

Institute		nation
Forschungsgesellschaft fur Angewandte Naturwissenschaften	FGAN-FHP	Ge
Danish Defence Research Establishment	DDRE	Dk
Norwegian Defence Research Establishment	NDRE	
Defence Research Agency Funtington	DRA	UK
TNO Physics and Electronics Laboratory	TNO-FEL	NL
Wehrtechnische Dienststelle 71	WTD71	Ge
Mariteleradar		It
DGA/CTSN/LSA	CTSN	Fr
DGA/CELAR	CELAR	Fr
NRaD	NRaD	USA

Table 1. Participants to Livorno'96.

#### 3.1 Objectives

The objectives of this trial were:

- to compare national radar signature data-collection and analysis methods,
- to determine the influence of environmental effects on the results of ship signature measurements,
- to compare boundary layer and mixed layer meteorological models that are used to determine the vertical refractivity profile,
- to compare propagation models that assess environmental effects on the amplitude and angle of arrival of radar returns,
- to describe the dependence of radar signature on radar and target parameters, and
- to compare radar signature numerical prediction codes inclusive a validation with experimental results.

#### 3.2 Methods

The plans of the RSG.21 for the Livorno'96 measurement campaign are rather ambitious. In order to manage the whole four tasks have been defined. Each task describes the activities that are required to meet the respective objectives. A short description of the tasks is given here.

##### Task 1: Radar signature data collection and analysis methods

In general each nation and possibly each institute uses its own methods to obtain the radar signature of targets. The deployed radars have different wave-forms to obtain low or high resolution data, different data processing algorithms and data presentation. Radars are calibrated by various ways. All this

makes it hard to compare and/or exchange results obtained by nations in one or more (common) trials. Therefore the RSG will make a comparison of national methods to infer the radar signature of a target, in this case a ship, by full scale measurements. The comparison should lead to a common NATO method/procedure in order to facilitate the exchange of data.

##### Task 2: Environmental effects on radar signature

By definition the radar cross section (RCS) of a target is independent on the environment. In practice however this is never the case. An exception may be when measuring a high flying object by a ground or air based up-looking radar. For maritime and land targets the measured apparent radar signature always includes environmental effects. For a ship this will include propagation effects in marine boundary and mixed layer and sea surface effects. In general this will result in different apparent radar signatures for one and the same ship, obtained by the same radar, but under different circumstances and/or at different locations.

The RSG intends to investigate methods to determine the environmental effects on the ship radar signature measurements. Special emphasis will be placed on comparison of propagation model results to measured signatures. The propagation models will also be reviewed in terms of their underlying physics and comparisons of their pros and cons will be made.

##### Task 3: Radar signature description

The radar cross section of an object depends on

- radar parameters like frequency, polarisation, illumination, and processing,
- geometrical parameters like elevation, azimuth, (incidence angle), and
- object parameters like shape, material.

In order to achieve a better understanding of the dependence of the RCS on these parameters simultaneous measurements should be made with radars operating in different frequency bands, with different polarisations and range and/or cross-range resolutions for various aspect angles on targets with different shapes and materials.

Since this was not realisable in practice the RSG has agreed to use in principle one polarisation, three resolutions, 360° aspect angle range and two ships with different shapes without radar absorbing material.

##### Task 4: Radar signature comparison

In order to obtain a better understanding of and insight into the RCS of objects without performing a lot of time consuming and costly measurements, computational models have been developed by

various institutes/organisations. These models may use various methods to approximately solve Maxwell's equations in case of a scattering object. In general the RCS prediction methods can be categorised according to four levels of mathematical sophistication:

- superposition of global solutions of basic shapes like cylinders and flat plates,
- high frequency methods like geometrical optics (GO), physical optics (PO), extended with various diffraction theories,
- boundary integral equations like method of moments, and
- Maxwell equation methods based on application of finite difference or finite elements.

This kind of models is used to obtain information on the to be expected RCS of ships, aircraft etc. already in the design stage.

For large objects like frigates only physical optics possibly extended with diffraction theory is at present capable of predicting the RCS at frequencies of interest i.e. X-band, Ku-band and higher.

Since all member nations of the RSG have at least one model available a comparison of these models will be made using predefined objects. In our case this includes a T-shape and the participating ships. Also comparisons will be made between predictions and measurements.

### 3.3 Instrumentation

A total of 10 radars (figure 1) have been installed next to each other on a platform close to the water front at Mariteleradar, Livorno Italy, operating as much simultaneously as possible at frequencies covering 2-94 GHz (see table 2).

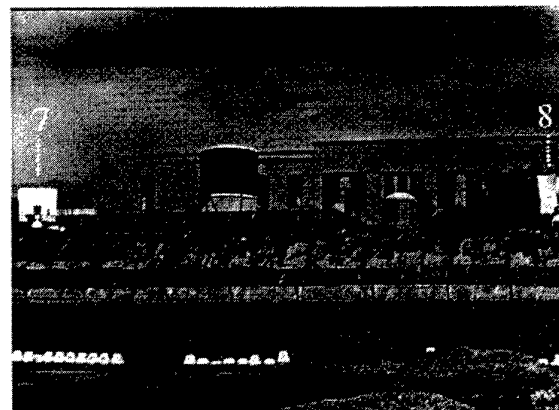
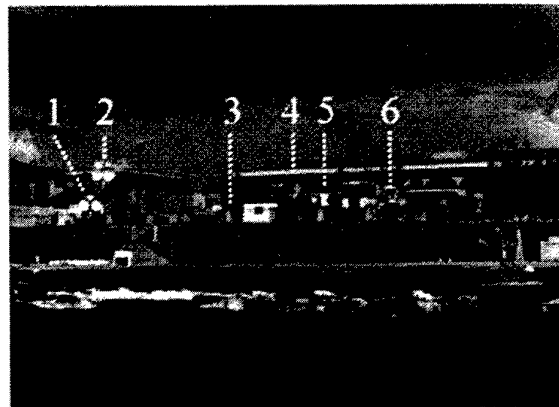
All radars have been calibrated according to national procedures prior to the trial. Calibration targets have been corner reflectors, flat plates and a sphere.

Since the RCS depends amongst others on the incidence angle of the impinging electro-magnetic field DRA, CTSN, DDRE and Mariteleradar have installed motion recorders on board the ships that measured almost continuously the ships roll, yaw and pitch. Also GPS recordings have been made.

The RCS measurements have been made with three prescribed range resolutions: full illumination, 20 m and 1 m in order to study the effects of resolution on the RCS. The group decided that horizontal polarisation on transmit and receive had to be used by all radars. Other polarisations were allowed if these could be measured 'simultaneously'.

Radar	institute	frequency range (GHz)	type	height (m)
RCS-Marine	WTD71	8-18	pulse, polarimetric	8.7
MRS	DDRE	8-18	CW polarimetric	9.6
MPR	DRA	2.9-3.1 8-18 35	pulse HH or VV	7.4 7.4 8.4
NORA	TNO-FEL	9.4, 16	pulse HH or VV	6.9
CORA	TNO-FEL	8-12	FM/pulse HH or VV	6.9
MMS300	Mariteleradar	2-18	pulse polarimetric	12.5 13.7
BHR	CTSN	8-18	FM/pulse polarimetric	6.9
CORA-35	FGAN-FHP	34.6-35.4	pulse polarimetric	7.6
CORA-94	FGAN-FHP	93.92-94.32	pulse polarimetric	7.6
MRS	NDRE	2-18	CW polarimetric	9.2

Table 2. Participating radars



1= DRA                      4= WTD71                      7= DDRE  
2= Mariteleradar        5=FGAN-FHP                8= NDRE  
3= CTSN                    6=TNO-FEL

Figure 1. Location of radars at Mariteleradar

The radars were divided into groups. All radars within a group operated simultaneously. Frequencies have been selected, such that no interference was expected. An example is given in table 3.

set 1		
nation	radar	centre frequency (GHz)
Denmark	MRS	4.7
France	BHR	9.7, 16.2
Germany	RCS Marine	10.0, 15.6
Italy	MMS-300	2-18
Netherlands	NORA-X	9.4
Netherlands	CORA	10.25
Norway	MRS	15.9
UK	MPR	34.6
Germany	CORA-35	35.0
Germany	CORA-94	94.0

set 2		
nation	radar	centre frequency (GHz)
Denmark	MRS	10.0
Netherlands	NORA-Ku	16.5
Netherlands	CORA	10.25
Norway	MRS	9.7
UK	MPR	9.25, 15.75

Table 3. Example frequency selection radars

Environmental data has been obtained from

- a meteorological buoy moored close to the measurement area,
- a weather station located at the test site close to the water front,
- weather stations near the radars,
- a hand-held weather station on the small boat,
- rocket sondes, launched from the test site,
- a waverider buoy,
- radio sondes, about 5 times per day, and
- an aircraft from Meteo-France with a refractometer.

The meteorological buoy was moored at 4.8 km from the test site in a west-south-west direction 4.5 km from the nearest land and contained instruments to measure

- air temperature,
  - air pressure,
  - relative humidity,
  - solar flux,
  - wind speed and direction,
- at 3.4 m above the sea surface. A seventh sensor measured the sea water temperature at a depth of 30 cm. This information will be used to determine the characterisation of the marine boundary layer (MBL), and enables an assessment of vertical variations in the refractivity using specific software models.

The weather station close to the water front measured

- air temperature,
- air pressure
- relative humidity,
- wind speed and direction.

The same parameters were measured by the hand-held weather station and the other stations.

Rocket sondes were launched from the test site to an altitude of maximum 800 m at a range of a few km's, from where the sonde descended on a small parachute to the sea surface. Rocket sonde and radio sondes measured air temperature, humidity and air pressure. The data was transmitted to the shore via a radio link. Both rocket and radio sondes gave information on the vertical refractivity profile.

#### 4. RADAR SIGNATURE MEASUREMENTS

Since so many radars had to operate simultaneously an interference test has been made prior to the trial, showing no mutual influence by the radars.

At the start of each day a time check was planned before beginning the measurements.

It was planned to perform radar signature measurements on various targets:

- the auxiliary ship Bradano from the Italian Navy,
- the frigate Granatiere from the Italian Navy,
- a small boat from the Italian Navy with a corner reflector from CTSN,
- a sphere, provided by Mariteleradar and DRA
- a Luneberg lens from France.

The choice of the Bradano and the Granatiere allows a study on the influence of the shape of the ship on the radar cross section (RCS).

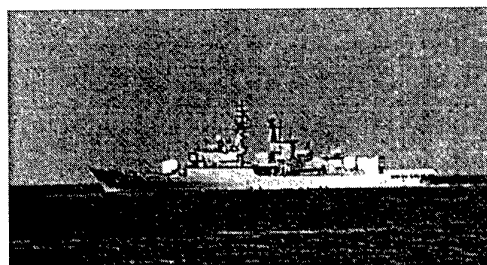


Figure 2. Italian frigate Granatiere

The RCS measurements on the Bradano and Granatiere (figure 2) have been made where the ships sailed circular runs in a clockwise (CW) or a counter-clockwise (CCW) direction at a range of about 6 km, with a circle diameter of 1000 m. A few runs have been made at ranges of 5000 and 9000 m to study the influence of the cross-range illumination of the ship. The average run time was about 10-12 minutes.

On the last day of the trial a series of four successive measurements have been made on Granatiere and Bradano to enable a direct comparison of signature results obtained under equal atmospheric and sea conditions.

Besides the circle runs four straight runs have been made enabling ISAR (Inverted synthetic aperture radar) measurements with high resolution for four aspect angles. The target ship was the Granatiere.

In order to allow a direct comparison of the results of the various radars and to allow a radar calibration a calibrated sphere and a Luneberg lens have been used.

The sphere (diameter 36.5 cm) had an RCS of  $-9.6 \text{ dBm}^2$  in the optical region and was suspended to a tethered balloon at about 200 m altitude and positioned at a range of 1 km, so that there was no influence of multipath.

Since the sphere measurements could only be made under 'no-wind' conditions only four runs have been made. Still this allowed each radar to perform one or more measurements with various parameter settings.

Measurements on the towed Luneberg lens were only allowed to be made during a one hour timeslot from 09:00-10:00. The Mondays, Wednesdays and Fridays were selected for this goal.

The Luneberg lens ( $23.6 \text{ dBm}^2$  at 8.4 GHz) was suspended to a helicopter (figure 3). Before starting the actual run the helicopter flew a straight track starting from near the radars towards the starting point of the run (at about 10 km) in order to facilitate a firm track of the lens. The run itself started at about 10 km and an altitude of 350 m for the lens. The helicopter flew a descending path towards the radar down to an altitude of about 100 m with a speed of 60 kts.

On the small boat a large radar corner reflector, provided by CTSN, has been installed at 3 m above the sea surface (figure 4). The RCS of this corner was  $26.4 \text{ dBm}^2$  at 10 GHz, which is more than 20 dB above the RCS of the small boat and well above the clutter level. While sailing a straight outgoing run the apparent radar signature of the corner has been measured.

Corner reflector measurements were limited to a time period of 4 hours per day. They have been made on 7 days during the trial mainly in the morning. An example of a preliminary result from the corner measurements is given in figure 5. The data will be used for investigating the environmental effects.



Figure 3. Luneberg lens suspended to helicopter



Figure 4. Radar corner reflector on small boat.

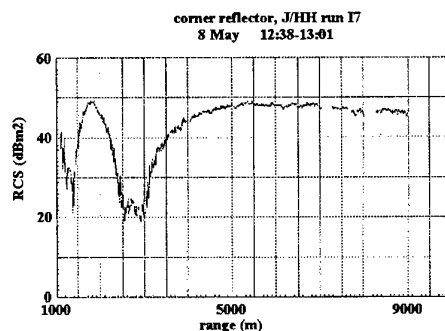


Figure 5. Measured apparent RCS of cornerreflector (TNO-FEL)

Table 4 gives an overview of the planned and realised run with the two ships, the corner reflector and the Luneberg lens.

target	range resolution	planned runs	realised runs
Bradano	full	12	14
Bradano	20 m	4	5
Bradano	1 m	10	10
Granatiere	full	10	10
Granatiere	20 m	6	8
Granatiere	1 m	10	10
corner	full	7	7
corner	20 m	9	8
corner	1 m	8	8
lens	full	8	8
lens	20 m	8	8

Table 4. Overview of planned and realised runs

Two times a day US rocket sondes have been launched by NRaD in the period 6-15 May, except for 13 and 14 May where only one was launched.

From the pressure data the height can be computed. Combining this with the air temperature and relative humidity data the vertical reflectivity profile can be computed. A preliminary result is given in figure 6 as an example.

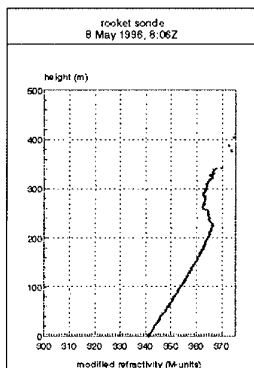


Figure 6. Modified refractivity obtained from rocket sonde data. (NRaD)

In order to characterise the propagation medium into the marine troposphere radio sondes were launched by CTSN. Each day four to six soundings were made, giving profiles of air temperature and humidity up to more than 2000 m height.

Flights with the aircraft from Meteo France gave information on the horizontal homogeneity of the propagation medium. These flights were made twice a day, one in the morning and one in the afternoon except during two days where only one flight could be made. Flights were made at various altitudes. The aircraft was equipped with a refractometer.

## 5. ANALYSIS

The analysis of the data has started now and includes analysis of nationally obtained data and a common analysis. A review of the activities is given below:

- verification measurements:
  - sphere and Luneberg lens results
- ship signature measurements:
  - measured RCS and ISAR images of Granatiere and Bradano,
  - computation of ship RCS for the radar parameters used during the trial,
  - comparison of measured and computed RCS of the ships
- environmental effects:
  - measured results of corner reflector,
  - measured meteorological parameters, refractivity profiles, sea surface parameters, identification/comparison of mixed and boundary layer models,
  - computations of refractivity profile, path losses,
  - computation of environmental effects on apparent RCS corner,
  - comparison of measurements and computations
- analysis of environmental effects on apparent RCS of the ships.

All these activities include a comparison between nationally obtained results.

Besides, a comparison of national radar signature data collection methods will be made that should result in a recommendation for a common NATO RCS measurement method.

Finally a NATO report will be written.

## 6. CONCLUDING REMARKS

The co-operative radar signature, propagation and environmental measurements are successfully conducted and produced a lot of valuable data.

Livorno'96 is a unique trial because:

- so many nations have worked co-operatively in a trial with so many radars with which many simultaneous measurements have been made over all frequency bands with various range resolutions,
- a complete set of meteorological and environmental data has been collected to characterise the propagation medium during the trial,
- direct measurements of the effects of the propagation medium on the apparent RCS of a corner has been made, and
- the collected data enable the validation of computational radar signature, marine boundary layer and propagation models.

## 7. ACKNOWLEDGEMENT

Many people have worked hard together in preparing and conducting the measurements. Due to their efforts the measurements became a success and resulted in a huge amount of valuable data with which the RSG.21 can start the analysis.

Therefore I like to acknowledge

- the Director of Mariteleradar Livorno for hosting the Livorno'96 trial,
- the organising and co-ordination team:
  - Col. de Palo (Mariteleradar Italy), RSG.21 member
  - Dr. A. Ricci (Mariteleradar Italy), the trial director and RSG.21 member
  - Capt. Francalacci and Capt de la Valle (Mariteleradar Italy), the trial co-ordinators ,
  - miss T. Westacott (DRA, UK) and
  - mr J. Bassett (DRA UK), assistant trial co-ordinators
- the RSG.21 members:
  - miss M. Renier (CTSN, France), dr. F. Talbot (DRA, UK), mr C. Flament (DCN, France),
  - mr R. Makaruschka (FGAN-FHP, Germany),
  - mr. J. Köhler (WTD71, Germany),
  - mr G. Lindqvist (DDRE, Denmark),
  - dr. R. Norland (NDRE, Norway),
  - Dr. Y. Hurtaud (CELAR, France),
  - mr K. Anderson (NRaD, USA),
  - mr D. Lohrman (NRL, USA)
- all members of the measurement teams from the participating institutes and Meteo France
- commanders of the Granatiere, Bradano and the small boat
- helicopter pilots
- all others who have contributed to the planning and execution of the Livorno'96 measurements.
- NATO Defence Research Section for the financial support of the measurements.

**Discussor's name:** G. BROWN

### Comment/Question:

Do you have any plans to reduce the rough surface scattering data?

### Author/Presenter's reply:

I will bring this point up in the RSG. We will consider the possibility of putting the data into a data base that can be used by other researchers.

(Addition: the forward scattering properties of the sea surface are part of the analysis and will be taken into account in the study on environmental effects).

**Discussor's name:** U. LAMMERS

**Comment/Question:**

In relation to your radar path length you are measuring meteorological parameters to great heights. Do you think these heights are involved in signal propagation?

**Author/Presenter's reply:**

For the ranges and the geometry for which we have made our measurements, great heights are not involved in the signal propagation. The reason for measuring the meteorological parameters was a comparison/validation of models that compute the vertical refractivity profile and to enable a correlation with the measurements by the Meteo-France aircraft.

**Discussor's name:** L.F. GALLE

**Comment/Question:**

The objectives of the "Livorno Trial 96" were, among others, to compare RCS simulations with measurements and to compare the individual national codes. In the ship infrared research world there is a policy to go to an international standard IR simulation code. Do you think this is the way for ship RCS?

**Author/Presenter's reply:**

The models used by the RSG are all based upon physical optics and geometrical optics/ray-tracing. Some include diffraction theory. So the outcome of the comparison of national codes could lead to a recommendation for a common/standard code. The availability of a standard code can be very valuable. Besides, a standard code can be used as a reference for new models for further improvements of existing codes. It is hard to say whether or not this can be realised. However, I will not exclude it.

## REPONSE IMPULSIONNELLE DE CIBLES MILITAIRES TRIDIMENSIONNELLES CONCEPTION, DEVELOPPEMENT ET VALIDATION D'UN BANC DE MESURE

Marc Piette

Ecole Royale Militaire/Chaire de Télécommunications  
30, Avenue de la Renaissance B-1000 Bruxelles  
Belgique

### 1. SOMMAIRE

Après un rappel du problème général de l'identification de cibles radar non-coopératives et un bref aperçu sur les techniques d'identification les plus prometteuses, la présente communication décrit le banc de mesure qui a été conçu et développé dans les laboratoires de l'Ecole Royale Militaire pour mesurer la réponse impulsionnelle de cibles tridimensionnelles. L'originalité de ce banc réside essentiellement dans le fait que la mesure s'effectue *directement dans le domaine temporel* et qu'elle ne nécessite pas de chambre anéchoïque comme la méthode fréquentielle classique à laquelle elle est comparée. Validé au moyen de cibles canoniques, le banc est maintenant utilisé à la détermination expérimentale de la réponse impulsionnelle de cibles tridimensionnelles quelconques.

### 2. INTRODUCTION

D'intenses programmes de recherche sont menés depuis plusieurs années tant en Europe qu'aux Etats-Unis pour tenter de mettre au point des techniques d'identification de cibles radar non-coopératives (Non Cooperative Target Radar Identification).

#### 2.1 Le problème de l'identification des cibles non-coopératives

Par *cible non-coopérative*, on entend une cible qui n'est pas équipée du système IFF (Identification Friend or Foe) ou une cible dont l'IFF est défectueux. Le système IFF fut inventé pendant la Seconde Guerre mondiale pour faire automatiquement la distinction entre un avion ami et un avion ennemi avant tout engagement. Il est toujours utilisé aujourd'hui tant par l'aviation civile que par l'aviation militaire. Il consiste en un transpondeur placé à bord de l'avion, transpondeur qui, dès qu'il est interrogé par le radar secondaire de l'aéroport civil ou de la base militaire, a pour fonction de lui répondre par un signal codé contenant toutes les informations nécessaires à l'identification de l'avion.

En temps de paix, l'identification correcte de chaque avion est primordiale pour une gestion efficace du trafic aérien, mais en temps de crise ou de guerre, elle est d'une importance vitale. On se rappellera à ce propos deux faits marquants.

En 1988, un avion de ligne iranien est abattu par erreur dans le Golfe persique par le croiseur américain VINCENNES. Cette tragédie coûta la vie aux 290 passagers. Plus récemment, en juin 1994, deux hélicoptères américains sont abattus par erreur dans la zone d'exclusion aérienne au nord de l'Irak par deux chasseurs F-15 américains qui les avaient confondus avec des hélicoptères Hind irakiens.

Sur le plan opérationnel, il est infiniment regrettable qu'un avion de combat ou de reconnaissance, après avoir accompli sa mission en territoire ennemi et échappé aux multiples dangers de la défense anti-aérienne et de l'aviation ennemies, soit abattu par les siens, par simple méprise. Ceci est malheureusement arrivé quelques fois dans plusieurs conflits régionaux de l'après-guerre, soit parce que l'avion avait eu son système IFF endommagé des suites d'un combat aérien, soit parce que le pilote, dans le feu de l'action, avait oublié de changer le code, comme il convient de le faire à intervalles réguliers.

Pour les forces terrestres, il n'existe actuellement, à notre connaissance, aucun moyen fiable d'identification automatique comparable à l'IFF, bien que le concept de BIFF (Battlefield Identification Friend or Foe) ait timidement fait son apparition dans certaines revues spécialisées. La nécessité d'un tel système pour les troupes au sol a pourtant été clairement démontrée par la Guerre du Golfe puisque dans les faibles pertes subies par les Alliés, plus de 30 % étaient dues à des tirs fratricides. Des chiffres qui rappellent ceux de la guerre du Yom Kippour où bon nombre d'hommes tombèrent sous les coups amis.

L'efficacité des armes intelligentes modernes, leur grande précision et le délai de réaction extrêmement bref qu'elles laissent désormais au combattant pris à partie, font que celui-ci, face à un ennemi supposé, est parfois enclin à tirer le plus tôt possible pour ne pas périr dans les instants qui suivent.

L'OTAN a pris conscience de ce problème et a créé en son sein un groupe spécial de recherche chargé d'étudier les solutions techniques d'avenir pour l'identification de cibles non-coopératives.

Il s'agit du groupe RSG 12 de la Commission X de l'AC/243.

## 2.2 Techniques prometteuses d'identification

Parmi les techniques d'identification radar émergentes, on peut citer d'une part des méthodes d'imagerie : la HRR (High Range Resolution), et la 2D-ISAR (2D-Inverse Synthetic Aperture Radar) et d'autre part des techniques d'identification traitant directement les signaux radar sans passer par la construction d'une image telles que la technique E-Pulse (Extinction Pulse) et la JEM (Jet Engine Modulation). L'objet principal du présent article n'étant pas d'examiner en détail chacune de ces techniques, on se limitera ici à en souligner les avantages essentiels et les limitations les plus importantes [1].

La méthode JEM consiste à analyser finement la modulation du signal radar résultant de sa rétrodiffusion par les aubes en rotation des réacteurs de l'avion. Cette technique offre une réelle possibilité d'identification. Cependant, elle nécessite un rapport signal-à-bruit relativement élevé et est limitée à certains angles d'aspect de la cible. En outre, elle ne peut être appliquée qu'à une classe restreinte de radars hôtes.

La méthode basée sur les profils HRR qui sont des images unidimensionnelles à haute résolution de la cible, peut être regardée comme une technique très prometteuse pour l'identification de cibles non-coopératives. Elle fonctionne bien pour tous les angles d'aspect avec, il est vrai, quelque dégradation des performances en incidence latérale. Le rapport signal-à-bruit nécessaire est modeste en comparaison de celui exigé par la technique JEM, une identification positive est possible à une distance qui approche la distance maximale de détection du radar et reste appréciable même lorsque le temps de passage du faisceau radar sur la cible est très court. On cite un taux d'identification de l'ordre de 80 à 90% suivant la nature de la cible et son angle d'aspect. Cette méthode sera applicable à un large éventail de radars de la nouvelle génération, tant terrestres que navals et aéroportés, pour autant bien sûr qu'une bibliothèque de signatures HRR puisse être constituée.

L'identification basée sur les images ISAR bidimensionnelles demande une grande puissance de calcul, en particulier pour les cibles manoeuvrantes qui imposent d'appliquer aux données des algorithmes d'imagerie assez sophistiqués. En outre, la méthode n'est pas insensible à l'angle d'aspect et pour les vols purement radiaux les images obtenues en vue frontale et en vue arrière dégènerent en profils en distance unidimensionnels. S'il est vrai qu'une image bidimensionnelle contient bien plus d'information qu'un simple profil en distance unidimensionnel, il faut quand même faire

remarquer que dans l'état actuel des techniques 2D-ISAR expérimentées, il n'est pas toujours possible de construire une image satisfaisante de la cible si celle-ci se met à manoeuvrer fortement pendant la durée d'observation. Les meilleures images de la cible sont obtenues en vue latérale (avec des taux d'identification proches de 80%), ce qui rend cette méthode complémentaire vis-à-vis des techniques HRR et JEM. Cette dernière remarque doit être soulignée car aucune des techniques susmentionnées ne permet seule de réaliser une identification avec un taux de réussite supérieur à 90% et pour tout angle d'aspect et toute cible.

Une autre conclusion de la Ref 1 est qu'il semble pour l'instant hors de portée de la plupart des grands laboratoires nationaux de la Défense de constituer des banques de signatures radar de taille et de variété suffisantes en employant uniquement des mesures de terrain avec cibles réelles. Les mesures sur modèles réduits et les codes de calcul de SER devraient donc apporter le complément d'information nécessaire, en particulier pour les cibles potentiellement hostiles qui se prêtent mal aux essais en vrai grandeur.

Enfin, on n'oubliera pas de citer la très récente méthode de l'impulsion d'extinction (E-Pulse en anglais pour Extinction Pulse), proposée par une équipe de chercheurs de l'Université d'Etat du Michigan. Cette nouvelle méthode, franchement novatrice, n'a pas été examinée par le groupe d'experts du RSG 12, car ceux-ci s'intéressaient surtout aux techniques d'identification utilisables avec les radars existants, qui sont pour la plupart des radars à bande étroite. La méthode E-Pulse nécessite en revanche un radar qui n'existe pas encore, si ce n'est à l'état de montage expérimental de laboratoire. Il s'agit du radar UWB (Ultra-Wide Band) dont la bande passante relative instantanée est par définition supérieure à 25%. L'intérêt croissant que suscite au sein de la communauté scientifique ce nouveau type de radar et la méthode d'identification qui en découlerait justifie qu'on lui consacre ici un paragraphe particulier.

## 2.3 Méthode de l'impulsion d'extinction

Cette méthode, proposée en 1985 par une équipe de l'Université d'Etat du Michigan [2][3] est basée sur la connaissance a priori des fréquences de résonance naturelle de la cible, lesquelles peuvent être extraites de sa réponse impulsionnelle. L'idée part de la constatation expérimentale suivante : alors que le début de la réponse impulsionnelle, dominé par les réflexions spéculaires associées aux hautes fréquences, dépend fortement de l'orientation de la cible, la seconde partie de la réponse, plus riche en basses fréquences, est quasiment indépendante de l'angle d'aspect. Ceci provient du fait que les oscillations qui caractérisent la fin

de la réponse impulsionnelle sont directement liées aux fréquences de résonance de l'objet, lesquelles dépendent de sa taille et de sa forme mais non de son orientation par rapport au radar. En fait, si l'on décompose la seconde partie de la réponse impulsionnelle en une somme pondérée de sinusoides amorties exponentiellement, on obtient un ensemble de pôles dans le plan complexe, dont la position s'avère indépendante de l'angle d'aspect. Seule l'amplitude des sinusoides amorties, c.-à-d. le résidu associé à chaque pôle change avec l'orientation de la cible. Les pôles les plus proches de l'origine correspondent aux oscillations les plus lentes.

La méthode d'identification consiste alors à synthétiser des signaux transitoires discriminants appelés "impulsions d'extinction" (Extinction-Pulses). Ces signaux sont construits de telle manière que leur transformée de Laplace présente dans le plan complexe un ou plusieurs zéros qui coïncident avec les pôles de la cible attendue qui sont les plus proches de l'origine. Ainsi, lorsqu'on convolue dans le récepteur radar ces signaux avec la réponse impulsionnelle de la cible attendue, on obtient une impulsion qui tend *rapidement* à s'annuler, tandis que si on convolue ces mêmes signaux avec la réponse impulsionnelle d'une autre cible que celle attendue, l'impulsion résultante ne tend que *lentement* à s'annuler.

Les signaux discriminants des différentes cibles à reconnaître sont synthétisés à partir de leurs fréquences de résonance naturelle, lesquelles peuvent être extraites directement à partir de leurs réponses impulsionnelles par diverses techniques, notamment par la méthode de Prony [4].

En constituant une bibliothèque des impulsions d'extinction des cibles susceptibles d'être rencontrées, on serait donc en mesure d'identifier celles-ci.

### 3. METHODE DE MESURE DE LA REPONSE IMPULSIONNELLE DES CIBLES

La réponse impulsionnelle d'une cible peut être déterminée expérimentalement de deux façons. La première, dite *méthode fréquentielle*, est la plus répandue et la plus ancienne. La seconde, appelée *méthode du régime transitoire*, est plus récente et encore fort méconnue.

#### 3.1. Méthode fréquentielle

La méthode fréquentielle consiste à relever la réponse de la cible en amplitude et en phase en fonction de la fréquence sur un très large spectre de fréquences et à effectuer sur celle-ci une transformation de Fourier discrète inverse. La réponse en fréquence est obtenue en illuminant la cible avec une onde sinusoïdale entretenue, de fréquence et de polarisation déterminées, et en

mesurant, pour diverses orientations de la cible, l'amplitude et la phase du signal qu'elle renvoie au moyen d'un analyseur de réseau. Cette méthode est aujourd'hui largement répandue car d'une part, elle repose sur des techniques de mesure éprouvées et d'autre part, elle permet par l'utilisation d'un signal à bande étroite et d'antennes directives aux hyperfréquences, d'obtenir des rapports signal-à-bruit élevés (et donc une excellente précision de mesure) malgré une puissance d'émission modeste.

Lors de la mise en oeuvre de la méthode, certaines précautions doivent cependant être prises, notamment pour se prémunir contre les réflexions parasites en provenance des objets avoisinant la cible. Pour ce faire, la mesure est effectuée soit à l'extérieur, en espace libre et dégagé (solution peu commode pour des mesures de laboratoire), soit dans une chambre anéchoïque de dimensions suffisantes. Les absorbants radio-électriques qui tapissent l'intérieur de la chambre atténuent en effet considérablement les réflexions parasites sur les parois et l'influence néfaste qu'elles exercent sur la qualité de la mesure. La chambre anéchoïque présente aussi l'avantage de permettre la mesure par tout temps et à n'importe quelle époque de l'année. Une telle installation est cependant fort coûteuse car pour rester dans la zone de champ lointain, l'antenne de réception doit être à une distance au moins égale à  $2D^2/\lambda$  (condition de Fraunhofer), où D représente la dimension caractéristique de la cible. A 8 GHz, et pour une cible ayant une dimension caractéristique de 40 cm seulement (la maquette d'un avion par exemple), cette distance est déjà de 8,50 m et elle croît encore à fréquence plus élevée.

D'autre part, comme bon nombre de radars militaires modernes sont capables de changer rapidement de fréquence (radars dits à *agilité de fréquence*) et qu'à moyen terme apparaîtra une nouvelle famille de radars à bande ultra-large (radar UWB), on est de plus en plus intéressé à connaître la variation de surface équivalente radar des cibles en fonction de la fréquence sur une bande déterminée, voire sur plusieurs bandes de fréquences. Pour obtenir cette information, il faut alors répéter la mesure en autant de fréquences nécessaires à une analyse plus fine de la SER, et cela pour chaque angle de vue et dans chaque polarisation. Or, lorsque la cible est un objet tridimensionnel de forme complexe, sa SER présente plusieurs pics de résonance en fonction de la fréquence. Ces pics n'apparaissent à la mesure que si celle-ci est répétée en un nombre suffisant de fréquences dans la bande considérée. La mesure fine de la SER d'une cible tridimensionnelle complexe requiert par conséquent un nombre élevé de points de mesure, qu'il faut en outre répéter pour chaque orientation de la cible et chaque polarisation. Cela prend dès lors un temps considérable si la chaîne de mesure n'est pas automatisée. Ainsi au David Florida Laboratory

de l'Agence Spatiale du Canada, les mesures de SER se font en chambre anéchoïque entre 2 et 18 GHz sur 801 fréquences, à raison d'une mesure tous les degrés et dans chacune des quatre polarisations (hh,vv,hv,vh), soit quelque 1.152.000 mesures par cible[5]. En Belgique il n'existe actuellement pas de site de mesure organisé de SER en espace libre et le seul site de mesure fermé est un petit tunnel anéchoïque de 2,5 m de long au laboratoire Radar et Micro-ondes des Services Techniques de l'Armée, qui est utilisé pour caractériser la réflectivité radar de petits échantillons (maximum 15 cm x 15 cm) de matériaux anti-radar minces.

### 3.2. Méthode du régime transitoire

La seconde méthode de mesure de la SER, dite méthode du régime transitoire, est basée sur la mesure directe de la réponse impulsionnelle de la cible dans le domaine temporel. Bien que son principe soit connu depuis plus d'une trentaine d'années - les premières publications théoriques à ce sujet remontent à 1958 [6] -, cette méthode est restée longtemps inapplicable par manque de composants électroniques et d'oscilloscopes à très large bande et l'absence de générateurs d'impulsions suffisamment brèves. La méthode consiste à illuminer la cible au moyen d'une onde électromagnétique transitoire extrêmement brève et à mesurer l'écho de la cible - en fait sa *réponse impulsionnelle* - directement dans le domaine temporel. L'impulsion d'excitation est rayonnée vers la cible par une antenne à large bande, alimentée par un générateur d'impulsions. L'écho transitoire de la cible est mesuré au moyen d'une antenne de réception (ou capteur de champ) et d'un oscilloscope, tous deux à large bande.

Comme la réponse impulsionnelle de la cible est directement liée à sa géométrie, elle est de ce fait un outil particulièrement adapté à l'étude de la contribution des différentes parties de la cible à son écho et permet d'identifier les points brillants de la cible. Etant donné en effet la vitesse de propagation finie des ondes, l'écho renvoyé par une partie située à l'arrière de la cible parvient au récepteur de mesure avec un certain retard sur l'écho renvoyé par une partie située à l'avant. La possibilité de distinguer les parties de la cible qui sont à l'origine des réflexions, c.-à-d. la résolution radiale sur la cible, est directement liée à la durée de l'impulsion d'excitation.

D'un point de vue expérimental, la méthode du régime transitoire présente également bien des attraits :

- la rapidité avec laquelle la réponse de la cible peut être mesurée (quelques secondes).

- la possibilité d'installer le banc de mesure dans un local banalisé. La coûteuse chambre

anéchoïque indispensable avec la méthode fréquentielle, n'est pas nécessaire avec la méthode du régime transitoire car on peut, par un choix judicieux de l'implantation du banc dans le local, tirer parti du délai de propagation entre la réponse de la cible et les échos parasites renvoyés par les murs.

- la détection immédiate d'un défaut de connexion dans le montage du banc de mesure ou d'une désadaptation locale d'impédance. Ces défauts, qui sont des sources d'erreurs insidieuses dans la méthode fréquentielle, se trahissent dans la méthode du régime transitoire par des réflexions parasites facilement observables sur le signal obtenu à l'oscilloscope.

A côté de ces nombreux avantages, la méthode du régime transitoire a bien sûr aussi quelques inconvénients. Le premier est que c'est une méthode encore fort méconnue. Ceci tient au fait que d'une part, pendant longtemps, on n'a pas disposé des composants électroniques nécessaires à sa mise en oeuvre (générateurs de signaux transitoires très rapides, oscilloscopes de mesure à bande ultra-large et instrumentation de grande bande passante) et que d'autre part, la grande majorité des ingénieurs électroniciens, habitués à travailler et à raisonner dans le domaine fréquentiel, n'ont pas toujours l'expérience du régime transitoire. Le second inconvénient de la méthode est qu'elle fait appel à des techniques de mesure spécifiques et délicates, inhérentes à l'emploi de signaux hyperfréquences.

## 4. DESCRIPTION DU BANC DE MESURE DEVELOPPE

Le banc de mesure conçu et développé dans les laboratoires de l'Ecole Royale Militaire comprend un générateur d'impulsions ultra-brèves (signal en échelon de temps de montée inférieur à la nanoseconde) alimentant une antenne monocone sur plan de masse. Cette antenne, qui jouit de plusieurs propriétés remarquables, notamment une bande passante ultra-large, a été développée spécialement pour les besoins du banc. La cible, qui est posée sur le plan de masse à quelque distance du cône est illuminée par l'impulsion électromagnétique rayonnée de manière omnidirectionnelle par le cône. L'onde rétrodiffusée par la cible est détectée au moyen d'un petit capteur de champ transitoire, placé entre le cône et la cible. La sortie du capteur est reliée à un oscilloscope à échantillonnage séquentiel de 20 GHz par l'intermédiaire d'amplificateurs à large bande. Un ordinateur contrôle le fonctionnement de l'oscilloscope et permet aussi d'effectuer les opérations de traitement de signal nécessaires et l'archivage des données (Fig.1).

Le choix du générateur d'impulsions à utiliser comme source du banc de mesure est essentielle

car les diverses qualités du signal électrique fourni par le générateur (pureté de la forme d'onde, stabilité de phase et d'amplitude, temps de montée, fréquence de répétition) sont déterminantes quant aux performances globales du banc (justesse, résolution, précision, dynamique, temps de mesure). Après étude comparative des différents types de générateurs de signaux transitoires existants sur le marché, le choix s'est porté sur deux générateurs à ligne de transmission externe commutés par transistor à avalanche : le premier fournit un échelon de 50 V/350 ps et le second un échelon plus raide de 10 V/45 ps, avec des taux de distorsion et des instabilités aussi faibles que 2%.

L'antenne d'émission à choisir pour le banc de mesure doit être apte à rayonner des impulsions très brèves avec un minimum de distorsions. En effet, le banc de mesure a pour but de mesurer le plus exactement possible la réponse impulsionnelle d'un objet en l'excitant avec un champ transitoire en forme d'échelon et en mesurant sa réponse au moyen d'un capteur différentiel. Il est dès lors essentiel, pour garantir la justesse de la mesure, que l'antenne rayonne l'échelon de tension appliqué à ses bornes avec un minimum de distorsions. Ceci implique qu'elle doit posséder à la fois une très large bande passante et une bonne linéarité de phase. De plus, l'onde rayonnée par l'antenne doit atteindre la cible à l'essai sous la forme d'une onde sphérique TEM de manière à approcher autant possible les conditions de propagation de l'onde radar sur une cible réelle.

Après avoir examiné diverses antennes candidates, le choix s'est finalement porté sur l'antenne monococone sur plan de masse alimentée par une ligne coaxiale TEM. Cette antenne, qui est la version asymétrique de l'antenne biconique, jouit en régime transitoire de propriétés remarquables. Si  $L$  est la longueur du cône et le rayon du plan de masse et  $c$  la vitesse de la lumière dans l'air, pendant les instants qui précèdent la réflexion du courant au sommet du cône et au bord du plan de masse ( $t < L/c$ ), tout se passe comme si l'onde progressive de courant se propageait le long d'une antenne monococone de longueur infinie. L'impédance d'entrée de l'antenne est alors purement réelle et indépendante de la fréquence. Elle dépend uniquement du demi-angle d'ouverture du cône et est donnée par la formule de Schelkunoff.

En outre, pendant cet intervalle de temps, l'antenne rayonne en tout point du demi-espace supérieur (au dessus du plan de masse) une onde sphérique TEM dont l'évolution temporelle est une *réplique exacte* de l'impulsion de tension appliquée à la base de l'antenne, du moins lorsque le demi-angle d'ouverture du cône est faible ( $< 5^\circ$ ) et que l'ouverture coaxiale à sa base

reste petite par rapport à la plus petite longueur d'onde présente dans le spectre de l'impulsion à rayonner. Dans ce cas en effet, les modes d'ordre supérieur engendrés à la jonction de la ligne d'alimentation cylindrique avec la pointe du cône restent négligeables devant le mode dominant TEM. Dans le plan équatorial de l'antenne (plan perpendiculaire à l'axe du cône, la polarisation est verticale.

Après une étude théorique du fonctionnement de cette antenne en régime transitoire, une antenne prototype d'impédance caractéristique égale à 200 Ohms et longue de 180 cm a été construite et testée (mesure de l'impédance par réflectométrie en régime transitoire et mesure des champs transitoires rayonnés. L'influence de la forme exacte du point d'alimentation de l'antenne sur son impédance d'entrée a été étudiée avec une attention particulière, d'abord théoriquement, puis expérimentalement avec des impulsions aussi courtes que 35 ps [7].

Grâce à la grande pureté de forme de l'échelon fourni par les générateurs d'impulsions et grâce au fait que l'antenne n'introduit aucune distorsion dans le signal, on obtient finalement une belle impulsion gaussienne de durée à mi-hauteur égale à 300 ps avec le premier générateur et à 94 ps avec le second (Fig.2). L'impulsion est suivie, il est vrai, d'un signal parasite, dû à la réflexion du courant en bout de cône, mais celui-ci n'atteint le capteur que 10 ns après le passage de l'impulsion principale, ce qui est un intervalle de temps suffisamment long pour pouvoir observer la réponse impulsionnelle des cibles envisagées.

Pour mesurer les diverses composantes du champ rayonné par l'antenne le long du plan de masse, on utilise deux types de capteur : un capteur électrique et un capteur magnétique.

Le capteur de champ électrique est un petit monopôle cylindrique mince de 1,39 cm de haut, monté perpendiculairement au plan de masse et disposé dans le prolongement du conducteur central de la ligne coaxiale qui le relie au récepteur de mesure (Fig.3). C'est un capteur de champ différentiel de grande bande passante : pour toutes les longueurs d'onde grandes par rapport à la hauteur du monopôle, le signal de sortie est proportionnel à la dérivée première du champ électrique incident ou, plus exactement, de la composante du champ électrique qui est parallèle au monopôle. La bande passante du capteur s'étend du continu à une fréquence de coupure qui dépend de sa hauteur  $h$ . Avec  $h=13,9$  mm, elle est de 2,56 GHz, ce qui est suffisant pour détecter un échelon ayant un temps de montée de 350 ps, c.-à-d. une fréquence de coupure à 3 dB correspondante de 1 GHz. Pour mesurer le champ obtenu avec l'échelon de 45 ps fourni par le second générateur, on utilise un capteur du même type, mais dont on réduit la hauteur en proportion de l'accroissement de bande passante

nécessaire. Le capteur de champ magnétique quant à lui est une petite boucle semi-circulaire mince de 0,6 cm de diamètre, disposée dans un plan vertical et raccordée d'un côté au plan de masse et de l'autre au conducteur central de la ligne coaxiale de 50 Ohms qui le relie au récepteur de mesure (Fig.4). C'est également un capteur différentiel de grande bande passante : pour toutes les longueurs d'onde qui sont grandes par rapport à la longueur de la boucle, le signal de sortie est proportionnel à la dérivée première du champ magnétique incident ou, plus exactement, de la composante qui est perpendiculaire au plan de la boucle. La bande passante du capteur s'étend du continu à une fréquence de coupure qui dépend du rayon de la boucle. Avec  $b' = 3,0$  mm la bande passante est de 2,56 GHz. Les capteurs sont reliés à l'oscilloscope par l'intermédiaire d'une série d'amplificateurs à bande ultra-large et à faible bruit. Etant donné que l'adaptation d'impédance aux accès de chaque amplificateur n'est pas parfaite sur toute l'étendue de leur bande passante, chaque amplificateur est relié au suivant par un câble coaxial suffisamment long pour que les réflexions éventuelles entre amplificateurs ne viennent pas contaminer le signal direct à mesurer.

Comme le récepteur de mesure doit permettre d'acquérir, de visualiser et de mesurer l'écho transitoire de la cible, ce doit être nécessairement un oscilloscope à mémoire de très grande bande passante. Il s'agit en l'occurrence d'un oscilloscope à échantillonnage séquentiel, très sensible et de bande passante ultra-large (20 GHz). Muni de quatre canaux, il est aussi équipé d'un générateur d'échelons intégré pour les mesures de réflectométrie en régime transitoire (échelon de 200 mV/35 ps). La résolution verticale de l'oscilloscope est de 12 bits en mode d'acquisition normal et de 14 bits en mode de moyennage. Ce dernier permet de moyennner jusqu'à 2048 fois le signal pour en augmenter le rapport signal-à-bruit. Avec un coefficient de balayage horizontal qui peut varier entre 1 s/div et 10 ps/div et un nombre d'échantillons prélevés égal à 501, la résolution horizontale varie de 20 ns à 0,2 ps. Quant à la précision, elle est de 0,4 % en amplitude et de 10 ps en intervalle de temps. Outre ces caractéristiques de base, l'oscilloscope offre de nombreuses possibilités d'analyse statistique et de traitement du signal : mesure automatique des paramètres du signal, calcul d'histogrammes pour mesurer la gigue de phase ou la fluctuation d'amplitude, opérations algébriques simples sur les signaux (+, -, x, inversion de signe).

## 5. VALIDATION DU BANC AU MOYEN DE CIBLES CANONIQUES

Avant de pouvoir utiliser le banc à la mesure des réponses impulsionnelles de cibles complexes, il est indispensable de le valider en tant que nouvel

instrument de mesure, c'est-à-dire de s'assurer qu'il fournit bien la réponse impulsionnelle exacte d'une cible connue. Pour ce faire, on a mesuré à l'aide du banc les réponses de cibles canoniques et on les a comparées à leurs réponses impulsionnelles théoriques. Par *cible canonique* on entend un objet pour lequel le calcul du champ rétrodiffusé admet une solution analytique rigoureuse ou, à tout le moins, une solution approchée de précision suffisante dans la bande de fréquences couverte par l'impulsion d'excitation. Parce que leur surface équivalente radar est bien connue en fonction de la fréquence et qu'il est relativement aisé de les fabriquer avec une bonne précision mécanique, on a choisi comme objets canoniques la sphère conductrice, la sphère diélectrique et la plaque plane conductrice. L'intérêt de ce choix est qu'il comporte à la fois une forme douce comme la sphère et une forme à arêtes vives comme la plaque et qu'on y traite aussi bien des corps conducteurs qu'un corps diélectrique.

Pour chacun de ces objets, on a calculé par transformation de Fourier inverse de la solution fréquentielle leurs réponses transitoires à grande distance à des impulsions gaussiennes de 100 ps et 300 ps. Ensuite, on a mesuré au banc leurs réponses à des impulsions de même durée.

Pour la sphère conductrice, la réponse mesurée correspond bien à la réponse calculée à partir des séries de MIE (Fig.5). On y distingue clairement les pics associés à la réflexion spéculaire et à l'onde rampante qui fait le tour de la sphère. Leurs amplitudes relatives et l'intervalle de temps qui les sépare sur la réponse mesurée sont pratiquement égaux aux valeurs théoriques, à l'imprécision de mesure près.

Pour la sphère diélectrique en Teflon, la correspondance entre la réponse théorique calculée par les séries de MIE et la réponse mesurée au banc à 300 ps est aussi bonne que pour la sphère conductrice (Fig.6). A 100 ps le signal obtenu est malheureusement trop faible et n'a pu être mesuré. Le générateur d'impulsions utilisé ne fournit en effet qu'un échelon de 10 V (soit cinq fois plus faible que le générateur de 50V/350 ps) et le capteur, dont on a dû diminuer la hauteur pour augmenter la bande passante, a vu aussi sa sensibilité réduite d'un facteur 16. A moyen terme, il sera possible d'améliorer le seuil de sensibilité et donc la dynamique du banc de mesure par l'emploi d'amplificateurs ayant un meilleur facteur de bruit.

Pour la plaque plane conductrice, la réponse transitoire en incidence normale a été mesurée tant à 300 ps qu'à 100 ps et correspond parfaitement à ce qui est prédit par la théorie géométrique de la diffraction. Lorsque la plaque est de dimensions suffisantes pour que sa taille

électrique soit grande pour les fréquences les plus élevés de l'impulsion d'excitation, le début de sa réponse est proportionnel à la dérivée de l'impulsion incidente (Fig.7).

## 6. CONCLUSION

L'objet de cette communication était de présenter le banc de mesure en régime transitoire qui a été conçu, développé et validé à l'Ecole Royale Militaire pour relever la réponse impulsionnelle de cibles tridimensionnelles. Celle-ci constitue en effet une signature électromagnétique de l'objet qui peut être utilisée pour tenter de l'identifier par la méthode de l'impulsion d'extinction.

Le principe du banc est d'illuminer la cible avec une impulsion électromagnétique ultra-brève et de mesurer l'écho de l'objet directement dans le domaine temporel. Dès lors, le banc comprend nécessairement un générateur d'impulsion puissant, une antenne d'émission à large bande apte à rayonner sans distorsion le signal impulsionnel du générateur, un capteur de champ transitoire, apte à détecter le champ transitoire rétrodiffusé par la cible, et un oscilloscope à mémoire pour l'acquisition, la visualisation et la mesure du signal impulsionnel obtenu.

Sur la base des caractéristiques nécessaires du signal transitoire à fournir par la source (forme, durée, fréquence de répétition, stabilité) pour obtenir les performances désirées pour le banc, deux générateurs ont été choisis parmi le large éventail de générateurs existant sur le marché. Il s'agit de générateurs à transistor à avalanche qui fonctionnent suivant le principe de la décharge d'une ligne de transmission par l'intermédiaire d'un commutateur rapide. Ils fournissent des échelons de 50 V/350 ps et de 10V/45 ps respectivement. La forme de l'échelon est d'une grande pureté (distorsions maximales de 1 %) et le signal est très stable en phase et en amplitude (gigue et fluctuation inférieures à 2 %).

Etant donné l'inaptitude des antennes usuelles à rayonner sans distorsion des signaux transitoires aussi brefs, on a entrepris le développement d'une antenne d'émission répondant à ces exigences. Il s'agit de l'antenne conique longue sur plan de masse, alimentée coaxialement par la base. L'idée de concevoir cette antenne très spéciale est venue de l'observation des propriétés remarquables dont jouit l'antenne biconique infinie (impédance d'entrée purement réelle et indépendante de la fréquence et champ rayonné suivant une onde sphérique TEM).

L'étude approfondie de l'antenne conique sur plan de masse en régime transitoire a montré qu'entre le moment où le signal fourni par le générateur d'impulsions est appliqué à la base du cône et l'instant où le courant lancé sur le cône atteint l'extrémité de ce dernier, l'antenne

rayonne sans distorsion et sous la forme d'une onde sphérique TEM, l'échelon appliqué à ses bornes. L'analyse des modes de propagation possibles de l'onde le long de l'antenne indique que, compte tenu de la façon dont elle est alimentée, des modes TM, excités à la jonction du cône avec la ligne d'alimentation, peuvent se superposer au mode TEM dominant. Cependant, en choisissant une ligne d'alimentation coaxiale de section transverse suffisamment petite et un faible demi-angle d'ouverture pour le cône ( $<5^\circ$ ), on limite fortement la contribution au champ de rayonnement de l'ouverture coaxiale et des modes TM qui y prennent naissance.

Fort de ces résultats, on a alors construit une antenne conique de 180 cm, avec un demi-angle d'ouverture de  $4^\circ$ , montée perpendiculairement à un plan de masse carré de 3 m de côté. L'antenne est alimentée à la base par une ligne coaxiale. La mesure de l'impédance d'entrée de l'antenne par réflectométrie en régime transitoire a montré qu'elle possède effectivement les propriétés attendues (impédance purement résistive de 201 Ohms indépendante de la fréquence). La mesure du champ transitoire rayonné dans le plan équatorial de l'antenne (le long du plan de masse) a montré que le champ transitoire initial est bien rayonné suivant une onde sphérique TEM et que son amplitude correspond à la valeur prédite par la théorie.

Grâce à la grande pureté de forme de l'échelon fourni par le générateur et grâce au fait que l'antenne n'introduit aucune distorsion dans le signal, on engendre finalement une belle impulsion de champ de durée à mi-hauteur égale à respectivement à 300 ps et 94 ps suivant le générateur utilisé, ce qui confère au banc de mesure une résolution radiale de 4,1cm et 1,4 cm respectivement. L'impulsion est suivie, il est vrai, d'un signal parasite dû à la réflexion du courant en bout de cône, mais celui-ci ne se fait sentir que 10 ns au moins après l'impulsion principale, un retard qui est suffisamment long pour permettre l'observation de la réponse impulsionnelle des cibles envisagées.

Ensuite, le banc de mesure a été validé en tant que nouveau moyen de mesure sur diverses cibles canoniques, telles que la sphère conductrice, la sphère diélectrique et la plaque plane. Les mesures effectuées sur ces objets ont montré que leur réponse impulsionnelle mesurée au banc correspond bien à leur réponse théorique.

## 7. REMERCIEMENTS

L'auteur tient à exprimer tout sa reconnaissance à Messieurs les Professeurs E.Schweicher et A. Vander Vorst pour leur appui, leurs suggestions et les nombreux conseils qu'ils lui ont prodigués tout au long de la thèse de doctorat dont la présente contribution est le fruit.

## 8. REFERENCES

1. AC/243 Panel 10/RSG 12 on Non-Cooperative Air Target Identification by Radar, June 1996 DS A/DR(96)364.
2. K.Chen, D. Nyquist, E. Rothwell, L.Webb, B. Drachman, "Radar Target Discrimination by Convolution of Radar Return with Extinction-Pulses and Single-Mode Extraction Signals" IEEE Trans. on Antennas and Propagation, Vol. 34 N°7, July 1986, pp 896-904.
3. K. Chen, D. Nyquist, E. Rothwell, "Radar Target Discrimination and Identification Using Extinction - Pulses and Single-Mode Extraction Pulses", Final Report of Contract 14-87-K-0336 prepared for Office of Naval Research, Jan 1991.
4. M.Van Blaricum, R. Mittra "A Technique for Extracting Poles and Residues of a System Directly from its Transient Response", IEEE Trans. Antenna & Propagation, AP 23, 1975, pp. 777-781.
5. C.Larose, S.Mishra, C.Trueman "Graphics for Visualizing RCS as a Function of Frequency and Angle", IEEE Antennas and Propagation Magazine, Vol. 36, N°3, June 1994, pp. 7-12.
6. E. Kennaugh and R. Cosgriff "The use of impulse response in the electromagnetic scattering problems", 1958 IRE Nat. Conv. Rec., Part 1, pp. 72-77.
7. M. Piette, E. Schweicher, A. Vander Vorst "High frequency effect of the junction between cone tip, coaxial feeder and ground plane on the input impedance of a long monocone antenna on ground plane". Ninth International Conference on Antennas and Propagation, Eindhoven University of Technology, 4-7 April 1995, Vol. 1, pp. 465-469.

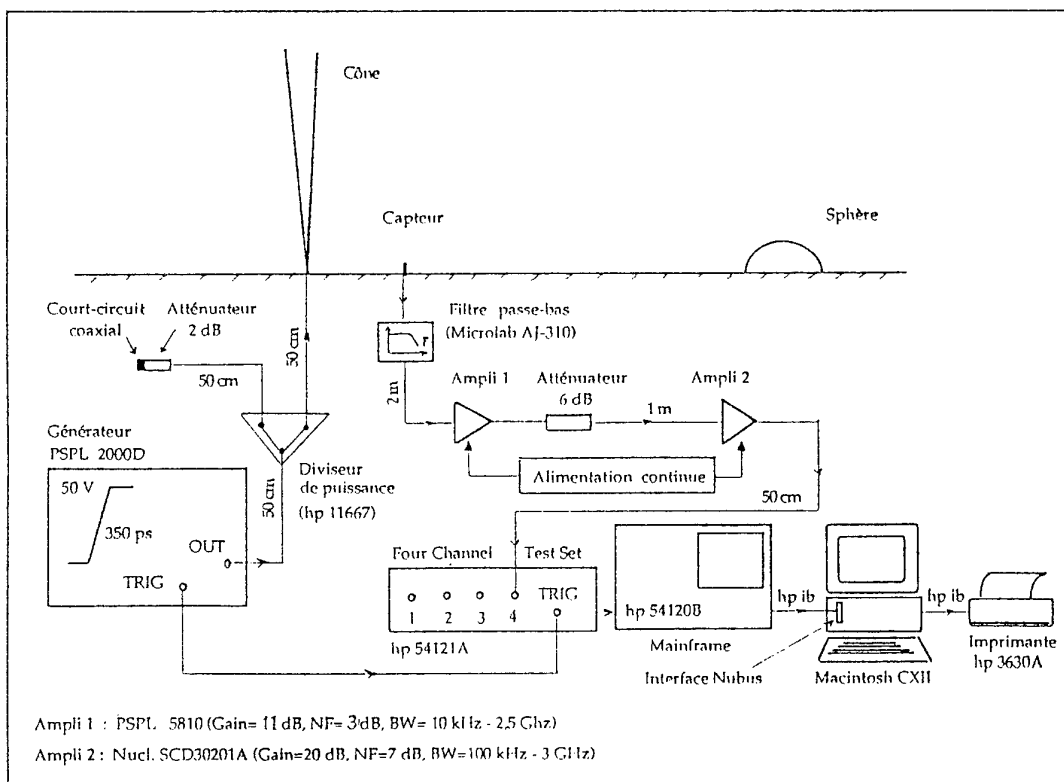


Fig. 1 Vue synoptique du banc de mesure en régime transitoire

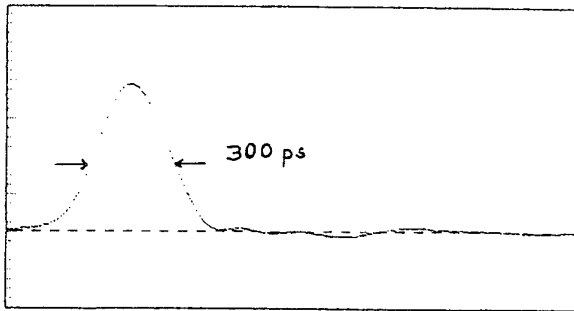


Fig. 2a Impulsion rayonnée de 350 ps

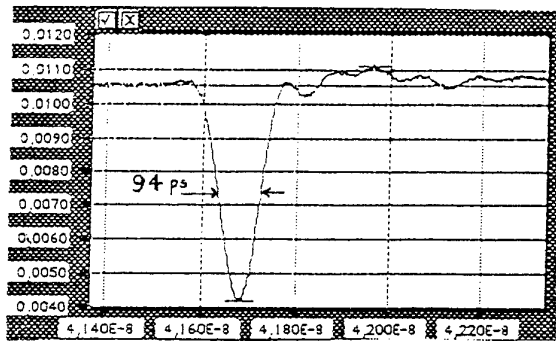


Fig. 2b Impulsion rayonnée de 94 ps

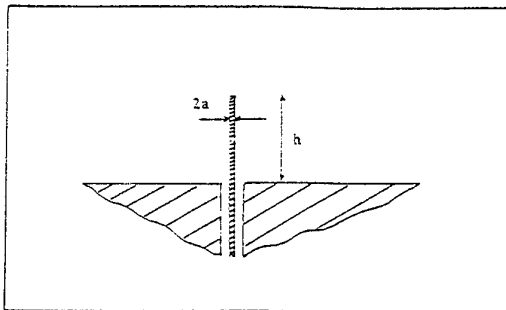


Fig. 3 Capteur de champ électrique

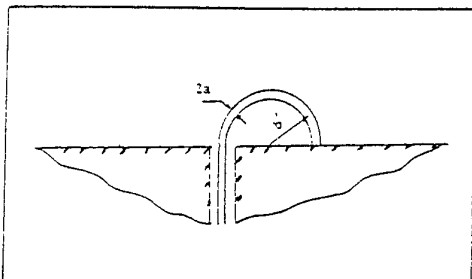


Fig. 4 Capteur de champ magnétique

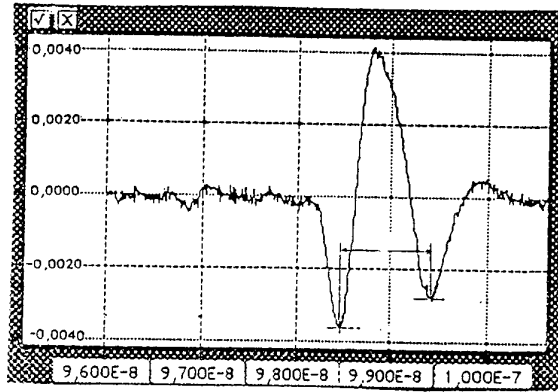


Fig. 5 Réponse impulsionnelle monostatique d'une sphère conductrice de 5 cm de rayon à l'impulsion de 350 ps

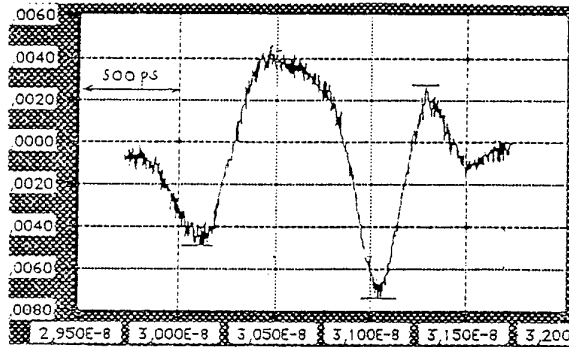


Fig. 6 Réponse impulsionnelle monostatique d'une sphère en Teflon de 5 cm de rayon à l'impulsion de 350 ps

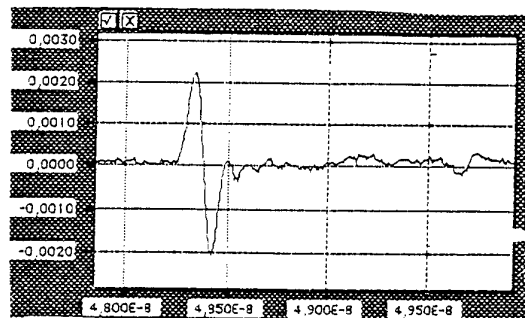


Fig. 7 Réponse impulsionnelle monostatique d'une plaque plane conductrice de 20 cm de côté à l'impulsion de 94 ps (incidence normale)

**Discussor's name:** A. PRIOU

**Comment/Question:**

Le banc de mesure génère des multiréflexions (cône, détection, cible et plan de masse). Utilisez-vous un traitement spécial pour tenir compte ou supprimer ces multi-réflexions ou envisagez-vous de surélever la cible? Ces multiréflexions prendront de l'importance pour l'étude et l'analyse de cibles complexes.

*Translation:*

*The measurement bench generates multi-reflections (cone, detection, target and horizontal plane). Do you use any special processing to allow for or eliminate these multi-reflections or are you thinking of elevating the target? These multi-reflections will take on a certain importance for the examination and analysis of complex targets.*

**Author/Presenter's reply:**

Les dimensions du banc de mesure (longueur du cône, surface du plan de masse, distance entre cible et cône) ont été choisies pour que les diverses réflexions qui se produisent inévitablement dans le système n'affectent pas la réponse impulsionnelle mesurée. Ceci conduit à définir une zone optimale sur le plan de masse à l'intérieur de laquelle la cible doit être placée pour que les conditions de planéité du front d'onde incident, les conditions de champ lointain et les conditions de non-contamination par les réflexions, soient réalisées.

*Translation:*

*The dimensions of the measurement bench (length of the cone, area of the horizontal plane, distance between the target and the cone) have been selected in such a way that the various reflections which inevitably occur in the system do not affect the pulsed response measured. The end result is the definition of an optimum area on the horizontal plane inside which the target has to be placed in order that the conditions of flatness of the incident wave front, the far field conditions and the conditions of non-contamination by reflections are met.*

**Discussor's name:** C. GOUTELARD

**Comment/Question:**

Votre système est très séduisant, très intéressant. Cependant:

1. Les antennes, et principalement l'antenne d'émission de par sa taille, apportent des limitations:
  - a) sur la bande de fréquence - notamment les bancs fréquences
  - b) sur la forme de l'impulsion au niveau de la cible compte tenu du rayonnement de l'antenne d'émission
2. Pourriez-vous préciser les limitations apportées par ces antennes?

*Translation:*

*Your system is very attractive, very interesting. However:*

1. *Antennas, and in particular transmission antennas, due to their size, introduce limitations.*
  - a) *on the frequency band - in particular at low frequencies.*
  - b) *on the shape of the pulse at target level given the radiation of the transmission antenna.*

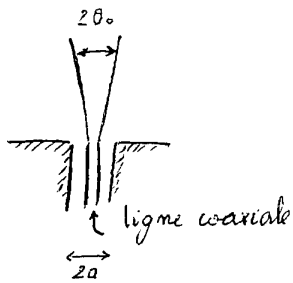
*Could you detail the limitations introduced by these antennas?*

**Author/Presenter's reply:**

1. a) Etant donné sa longueur (2 mètres), l'antenne monocône fonctionne en régime d'onde progressive pendant environ 6 nanosecondes (temps nécessaire à l'impulsion de courant lancée à sa base pour atteindre l'extrémité du cône). Pendant cet intervalle de temps, tout se passe comme si l'impulsion de courant, qui ne "voit" pas encore le bout du cône, se propageait sur un cône de longueur infinie. Or, l'antenne conique infinie présente une impédance d'entrée purement réelle et INDEPENDANTE de la fréquence dont la valeur dépend uniquement de l'angle d'ouverture  $2\theta_c$  du cône suivant la formule de Schelkunoff

$$Z_c = R_c + 0j \text{ avec } R_c = 60 \ln \cotg \frac{\theta_c}{2} \text{ (ohm).}$$

Pendant les six premières nanosecondes, la bande passante de l'antenne est donc virtuellement infinie, sans limitation vers les basses fréquences. Vers les hautes fréquences, il faut toutefois tenir compte du rayonnement de l'ouverture coaxiale par laquelle le cône est alimenté (Fig. 1).



Une étude approfondie de l'influence de cette ouverture coaxiale sur l'impédance d'entrée et sur le champ rayonné a montré que si le rayon de l'ouverture reste petit devant la plus petite longueur d'onde présente avec une énergie significative dans le spectre de l'impulsion (a «  $\lambda_{\min}$ ) et si l'angle d'ouverture du cône est faible ( $\theta_0 > 5^\circ$ ), cette influence est négligeable et les modes d'ordre supérieur excités à la jonction du cône avec la ligne d'alimentation coaxiale restent très négligeables, devant le mode dominant TEM rayonné par le cône.

1. b. L'impulsion rayonnée dans l'espace délimité par le plan de masse et la surface du cône est la réplique temporelle exacte de l'impulsion de tension appliquée à la base du cône, du moins pendant les 6 nanosecondes qui précèdent les premières réflexions (en bout de cône et au bord du plan de masse). Ceci résulte de la bande passante virtuellement infinie de l'antenne pendant cet intervalle du temps.

2. Trois limitations sont à considérer:

- la distance entre la cible et le cône ( $R_c$ ) doit être suffisante pour que l'onde sphérique incidente puisse être considérée comme localement plane au niveau de la cible de hauteur  $h$ . Le critère est

$$R_c > 5h^2 \text{ avec}$$

$$\text{---}$$

$$ctm$$

$t_m$  = temps de montée de l'impulsion incidente  
 $c$  = vitesse de la lumière dans l'air.

- le capteur doit être dans la zone de champ lointain de la cible

pour les hautes fréquences  $\Delta R > \frac{2h^2}{\lambda_{\min}}$  (condition de Fraunhofer)

pour les basses fréquences  $\left[ \begin{array}{l} \Delta R > 10h \quad (\text{source ponctuelle}) \\ \Delta R > 10 \frac{\lambda_{\max}}{2\pi} \quad (\text{composantes radiales du champ} \\ \quad \quad \quad \text{négligeables devant les composantes} \\ \quad \quad \quad \text{transverses}) \end{array} \right.$

- les réflexions terminales qui limitent la durée d'observation sans contamination à environ 10 nanosecondes.

Translation:

1. a. Given its length (2 metres) the monocone antenna operates in the travelling wave mode for approximately 6 nanoseconds (the time required for the current pulse generated at its base to reach the tip of the cone). During this time, the current pulse, which cannot yet "see" the tip of the cone, behaves as if it were being propagated over a cone of infinite length. But an infinite conical antenna has a purely effective input impedance which is INDEPENDENT of frequency, the value of which depends solely on the angle of aperture  $2\theta_0$  of the cone, in accordance with Schelkunoff's formula.

$$Z_c = R_c + j\omega L_c \text{ in which } R_c = 60 \ln \cotg \frac{\theta_0}{2} \text{ (ohms)}$$

The antenna bandwidth is therefore virtually infinite during the first six nanoseconds, without any limits down to the low frequencies. In the high frequency direction however, allowance must be made for radiation from the coaxial aperture through which the cone is fed. (Fig. 1).

An in-depth study of the influence of this coaxial aperture on input impedance and radiated field showed that if the aperture radius is small in comparison with the smallest available wavelength of significant power in the pulse spectrum ( $\lambda_{\min}$ ) and if the aperture angle of the cone is narrow ( $\theta_0 < 5^\circ$ ) then this influence is negligible and the upper order modes excited at the junction between the cone and the coaxial supply line remain negligible compared with the dominant TEM mode radiated by the cone.

1. b. The pulse radiated into the space defined by the horizontal plane and the surface area of the cone is the precise temporal replica of the voltage pulse applied to the base of the cone, for at least the 6 nanoseconds which precede the initial reflections (at the tip of the cone and at the edge of the horizontal plane). This is due to the virtually infinite antenna bandpass during this time slot.

2. There are three types of limitation:

- the distance between the target and the cone ( $R_c$ ) should be such that the incident spherical wave can be considered as locally plane for a target height  $h$ . The criterion is:

$$R_c > \frac{5h^2}{ct_{\text{rise}}} \text{ with } \begin{array}{l} t_{\text{rise}} = \text{rise time of the incident pulse} \\ c = \text{speed of light in air} \end{array}$$

- the sensor must be in the far field of the target

for high frequencies  $\Delta R > 2 \frac{h^2}{\lambda_{\min}}$  (Fraunhofer's condition)

for low frequencies  $\Delta R > 10h$  (point source)

field components)  $\Delta R > 10 \frac{\lambda_{\max}}{2\pi}$  (radial field components negligible compared to transverse

- the terminal reflections, which limit observation time without contamination to approximately 10 nanoseconds.

# Novel HF, RADAR, and IR Absorber Material

Günter Nimtz

II. Physikalisches Institut, Universität zu Köln, D-50937 Köln

## 1. ABSTRACT

A novel broadband absorber is introduced. Instead of the classical voluminous carbon loaded foam, the new absorbing element is a thin metal layer of only some 10 nm thickness. Measurements of the electromagnetic specifications of anechoic chambers built with absorbers made of the new material have revealed a better field homogeneity than known from those built with the classical foam absorbers. Other favourite properties are the light weight of the absorbers and they can be made from non-combustible material. The absorbing and low reflecting properties of the mesoscopic metal layers are effective up to infrared frequencies. There will be introduced some applications of the novel technology.

## 2. INTRODUCTION

Carbon loaded foam pyramids have been the classical broad band absorbers for high frequency radiation and microwaves over a period of nearly a century. Quite recently a novel absorber type has been introduced and its sovereign electromagnetic specifications and general properties have been already demonstrated [1,2]. The novel absorber is based on a thin metal layer with a thickness of the order of only one percent of a micrometer. Such thin layers belong to the class of mesoscopic systems, which in consequence of their geometric confinement do have electromagnetic and mechanical properties quite different from those we are used to from the corresponding bulk material. Mesoscopic systems have dimensions in between those of single atoms or molecules and those of bulk material, typically the size regime between 1 and 100 nm

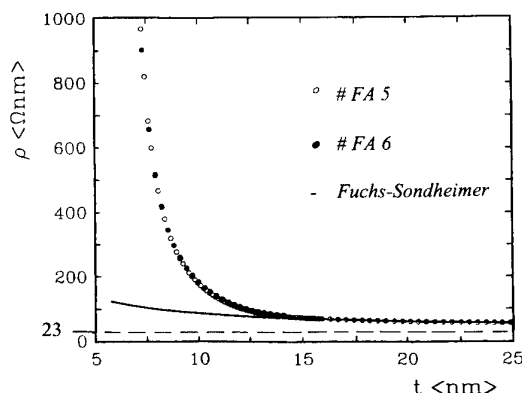


FIG. 1. Resistivity  $\rho$  of gold vs layer thickness  $d$ , the bulk value with  $2.3 \cdot 10^{-8} \Omega m$  is shown for comparison.

## 3. THE MATERIAL

Our specific interest has been focused on the electrical resistivity of various 1-, 2-, and 3-dimensional mesoscopic systems [3-5]. For instance in the case of two-dimensional metal layers it has been observed that for 10 nm layer thickness the resistivity increases by more than one order of magnitude compared with the bulk value. This is demonstrated in Fig. 1 for Au films [6]. A similar behaviour of the resistivity was also observed for other metals like Ag, Al, Cr, Cu, Ni or Pt [7]. Formerly it was thought, that the increased resistivity below 100 nm was caused by surface scattering of the free electrons in the metal film, becoming more and more impor-

tant with decreasing layer thickness [8]. However, the surface scattering, often called Fuchs-Sondheimer effect, is not strong enough to explain the observed rapid increase of resistivity. Several experimental and theoretical investigations have revealed, that the layers have a fractal structure and correspondingly the electron diffusion (electron mobility) becomes strongly hampered. Electron micrograph data of an Au layer support the interpretation as shown in Fig. 2 [6]. Obviously a Swiss-cheese model, in which insulating holes (white) are located randomly in a conducting background describes well the topology of thin metal layers [7].

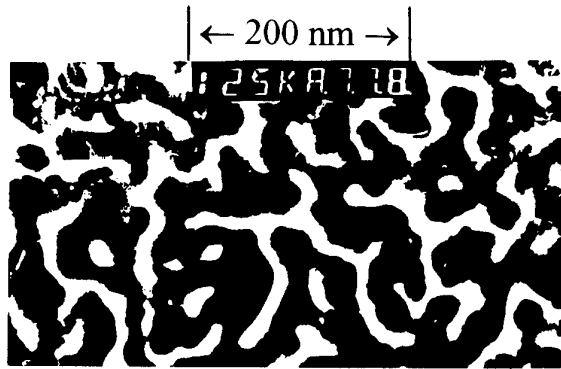


FIG. 2. Electron microscopic data of Gold

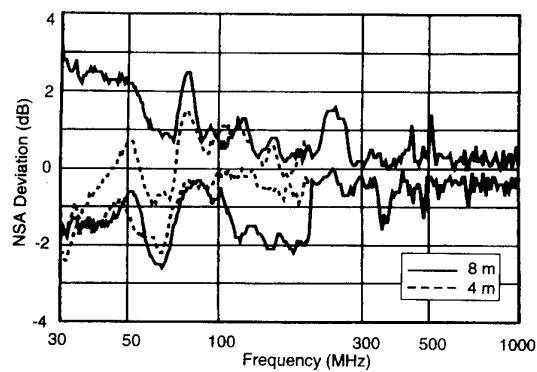
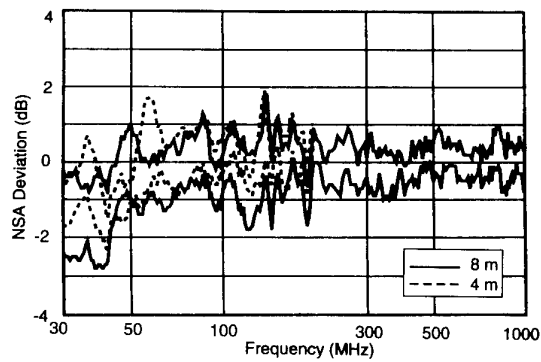
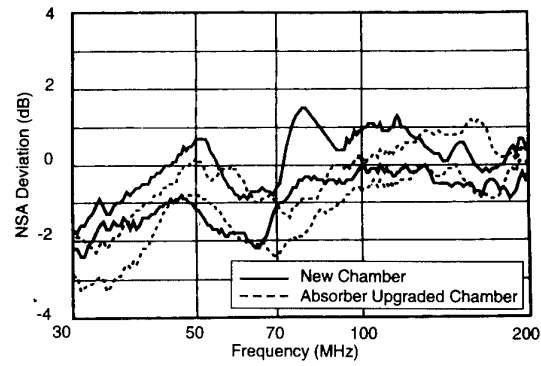
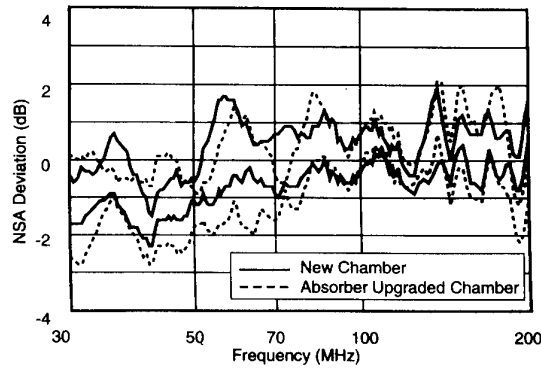
**a. Horizontal Polarization****b. Vertical Polarization**

FIG. 3. Ten-meter EMC anechoic chamber: min/max worst-case NSA deviations according to ANSI C63.4 (back-most position omitted); 8-m test volume diameter (solid lines); 4-m test volume (dotted lines, only 30 to 200 MHz).



**a. Horizontal Polarization**



**b. Vertical Polarization**

FIG. 4. Comparison of min/max worst-case NSA deviations according to ANSI C63.4 of two different 10-m EMC anechoic chambers in the critical range 30 to 200 MHz. New chamber with 4-m test volume diameter (solid lines); older chamber after absorber upgrade with 3-m test volume diameter (dotted lines).

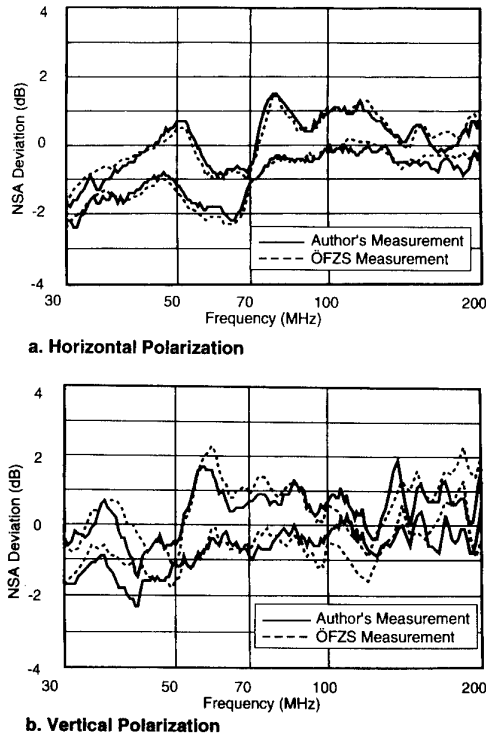


FIG. 5. Comparison of two independently performed ANSI C63.4 compliance tests (min/max worst-case NSA deviations) in 10-m EMC anechoic chamber with 4-m test volume diameter: measurements made by A.Enders (solid); measurements made by ÖFZS (dotted, by courtesy of Österreichisches Forschungszentrum).

#### 4. THE ABSORBER

The basic idea of the design of the novel absorber is explained in the following: The high resistivity of mesoscopic metal films allows to produce metal layers having a film resistance of  $377\Omega$  [2]. This value equals the impedance of air, i.e. of vacuum. If such metal layers are confronted with electromagnetic radiation they would absorb the waves without reflecting them. However, depending on the geometrical form of the absorber the film resistance has to be modified in order to obtain an optimum in broad band reflexion loss. The best value of film resistance has to be determined empirically.

For example Ti layers are deposited on a some  $10\ \mu\text{m}$  thick organic film of polyethylen by a PVD process. The organic film carrying the metallic layer is put on a hollow pyramid. The pyramid itself can be formed by suitable corrugated paper or by sheets of a non-combustible material depending on the specifications in question. Mayor advantages of the new technology are the lightweight, the possibility of using non-combustible material, the weatherproof quality, and the superior reproducibility of absorber performance. The technology is also ecologically favourable, since

toxic chemical additives are not necessary in order to make the foam material non-flaming. Also the transportation volume is rather small by stacking the hollow absorbers.

A really exciting point of the new technology is the fact, that a thin metal layer of only about 10 nm thickness can do a better absorption job, than the roughly 10 Million times thicker graphite-impregnated pyramidal shaped foam absorber.

#### 5. THE PERFORMANCE

The novel absorber has been already installed in more than a dozen of anechoic chambers. We shall present some data of a new EMC test center which includes a 10 m semi-anechoic chamber (semi-anechoic chamber including a ground-plane). The inner dimensions of this chamber are 25 m x 16 m x 9 m (shield) and a turn-table with an 8 m diameter. The chamber is equipped with the new absorbers in a non-combustible version. Test results on ANSI C63.4 performance are shown in Fig. 3 [1]. The values are summarized as two worst-case NSA deviation curves which result from all data taking the minimum and maximum values at each frequency point. Results

are displayed for an 8 m test volume diameter for horizontal and vertical polarization. Below 200 MHz, equivalent results for a 4 m test volume diameter are also displayed. This is a more common turn-table dimension. Even better performance results with 4 m with an overall worst-case value of 2.4 dB, while the corresponding value for 8 m is 3.2 dB.

Anechoic chambers which predate the new field homogeneity standards most often can not meet these requirements. The question arises whether an absorber-upgrade with the new absorbers can improve the chamber's performance. Such an upgrading has been successfully carried out with an anechoic chamber of inner dimensions 22 m x 20 m x 8.5 m. Originally it was equipped with classical pyramidal carbon loaded foam absorbers of 1.2 m height. The ANSI standard criterion  $\pm 4$  dB was met only far above 100 MHz. After installation of an absorber upgrade, the chamber was fully compliant according to the dotted curves in Fig. 4. It should be mentioned, that upgrade costs were minimized by retaining foam absorbers on less critical wall regions. In Fig. 5 we present the results of two independent ANSI C63.4 compliance tests for the same anechoic chamber. Both are based on the dual antenna factor calibration method [1]. The agreement between the measured data are good for the vertical polarization and nearly perfect for the horizontal polarization.

## 6. FREQUENCY DEPENDENCE

The dc conductivity of an electronic conductor is given by the following relation:

$$\sigma_0 = \frac{ne^2\tau}{m}$$

where  $n$  is the electron density,  $e$  the electron charge,  $\tau$  the momentum relaxation time, and  $m$  the effective electron mass.  $\sigma_0$  is the dc conductivity, the ac case is given by the relation:

$$\sigma(\nu) = \frac{\sigma_0}{1 + (2\pi\nu\tau)^2} - i \frac{\sigma_0 2\pi\nu\tau}{1 + (2\pi\nu\tau)^2}$$

where  $\nu$  is the ac frequency. For a bulk metal  $\tau \approx 10^{-14}$  s holds at room temperature. Neglecting the imaginary part of the relation, which is in charge of the dispersion, we obtain for the infrared frequency corresponding to a wavelength of  $14\mu\text{m}$  a  $\sigma(\nu) = \sigma_0/100$ . That means the film resistance should have increased by a factor of 100 at this infrared frequency and would not be useful for absorbing tasks. However, our infrared investigations have shown, that the momentum relaxation time  $\tau$  has decreased nearly by two orders of magnitude compared with  $\tau$  of bulk material. The mesoscopic metal layers of about  $10\mu\text{m}$  thickness have still the same film resistance value at the even shorter wavelength of  $4\mu\text{m}$ .

## 7. INFRARED APPLICATIONS

The strongly reduced momentum relaxation time in mesoscopic metal layers allows their application in electromagnetic absorbing devices from dc up to the infrared regime of  $4\mu\text{m}$ . The necessary film resistance of about  $377\omega$  is still effective in the infrared. Several investigations have proven, that the absorbing and low reflection is already obtained with one layer. For instance reflection losses of less than 10 dB have been measured with only one metal layer in front of a metallic mirror. Thus the mesoscopic metal layers seem to be very promising to solve infrared shielding problems.

## 8. SUMMARY

All the electromagnetic data have shown, that the novel absorber technology based on quasi two-dimensional metal resistance layers sets a new standard in the performance for EMC anechoic chambers. Such a field homogeneity has never been achieved by the classical absorbers using ferrites, graphite-impregnated foams or combinations of them. It has also been shown, that the film resistance is not significantly changed in the infrared regime. Accordingly the absorbing effect with low reflection of the layers have an unusually broad frequency band potential. In addition the novel technology offers ecological and economical advantages.

- 
- [1] A.Enders, ITEM (1996) pgs. 154-158 and 244-248  
A.Enders, IEEE-EMCS Symposium Santa Clara August 1996, in press
  - [2] G.Nimtz und A.Enders, Physik in unserer Zeit, **27/1** (1996) 38
  - [3] R.Pelster, P.Marquardt, G.Nimtz, A.Enders, F.Petzoldt, Phys.Rev. **B 45** (1992) 8929
  - [4] G.Nimtz, A.Enders and R.Pelster, Int. J. Electronics **73** (1992) 983
  - [5] R.Pelster, G.Nimtz, B.Wessling, Phys.Rev. **B 49** (1994) 12718
  - [6] G.Dumpich, Festkörperprobleme - Advances in Solid State Physics, **31** (1991) 59
  - [7] Y.Yagil et al., Phys.Rev.Letter **69** (1992) 1423  
C.S.Yoon and Sung.Ik Lee, Phys.Rev.**B 42** (1990) 4594  
Yi.Song et al., Phys.Rev. **B 46** (1992-I) 14  
Ritu Suri et al., J.Appl.Phys. **46** (1975) 2574  
M.Aprili, Solid State Communications **98** (1996) 221  
Gao-xiang Ye et al., Physics Letters **A 198** (1995) 251  
A.Enders and G.Nimtz, private communication
  - [8] Charles Kittel, Introduction to Solid State Physics, John Wiley and Sons, Inc. New York (1967)

## Experimental Evaluation of Material Parameters for RCS Prediction Codes

J. Preißner, V. Stein

Institute of Radio Frequency Technology  
German Aerospace Research Establishment (DLR), D-82230 Wessling, Germany

### ABSTRACT

The material parameters, permittivity  $\epsilon$  and permeability  $\mu$ , which are needed for the calculation of the mono- and bistatic radar cross section of complex structures, have been determined for a lot of samples in the frequency range from 8 GHz to 110 GHz. Three different methods, the measurement of the S-parameters in a waveguide, the measurement of the reflection or transmission factor under free space conditions, measurements of the reflection factor by a coaxial probe, have been applied and are described in detail. The quality of the results is dependent on the method chosen, as well as on the accuracy in the fabrication of the samples, which is in general more critical at higher frequencies. Some measurement results are presented and discussed in detail.

### 1. INTRODUCTION

The computer codes SIGMA and BISTRO are developed in our Institute to predict the radar cross-section (RCS) of objects with metallic and nonmetallic surfaces [1]. Both computer codes are based on high frequency methods. The first code is used for the prediction of the monostatic RCS characteristics of complex structures, the second for the bistatic analysis of simple shaped structures with work in progress to extend the code also to complicated shapes. A third code based on rigorous methods is under consideration to determine the RCS of electrically small objects. The first two codes were extensively tested in the past comparing predicted RCS data with experimental RCS data. A variety of canonical as well as complex structures served as test objects. The RCS test ranges used for experimental verification operate in the frequency bands 8 - 18 GHz (outdoor test range) and 92 - 96 GHz (indoor test range). A further test range in the frequency band 32 - 36 GHz is under design. Since the validation of the code SIGMA for metallic objects was very successful it is now applied increasingly for the RCS prediction of complicated realistic objects. With some time delay the code BISTRO is also extended to treat objects with noncanonical shapes.

The current work deals with the validation of both computer codes for canonical objects with nonmetallic surfaces or partially nonmetallic surfaces such as a coated flat plate or a coated cube. In a following phase also objects in their natural environment come under

consideration. For this purpose a precise knowledge of the constituent parameters and the thickness of the individual layers or the Fresnel reflection coefficients at the surface of the top layer for both polarization states is required. The latter are sufficient for approximation methods as used in SIGMA and BISTRO.

Since there is a great variety of materials (solid, flexible, liquid, amorph; homogeneous or inhomogeneous in depth and surface profile; lossy dielectric or/and ferromagnetic; smooth, weakly rough and rough surface; easily machined smooth contour or rough contour of brittle materials; etc.) one cannot favorize a single experimental setup. In view of the listed material properties we made the decision, to establish experimental setups based on the following two principles.

- Measurement of the S-parameters of the materials in a waveguide and direct analytic determination of the constituent parameters followed by the computation of the reflection coefficients.
- Measurement of the reflection and transmission coefficients for both polarization states and different incidence angles under free space conditions and numerical evaluation of the constituent parameters if the computer codes SIGMA and BISTRO use the latter values as input parameters.

Depending on the specific material under test the first or the second principle is preferred. If the material is suited to be measured on both experimental setups the results can be used for cross-checks which allow to estimate the accuracy of the experiments. Since the experiments have to be carried out in each of the mentioned frequency bands a high effort in the construction of the setups and considerable costs will arise in realizing the concept. A third method, based on reflection measurement by a coaxial probe, was used in some cases to determine the permittivity  $\epsilon$  for liquids and semisolid materials in the frequency range from 0.5 - 20 GHz. The following sections of the paper present the state of the measurement facilities, the used computer codes and experimental results for a great variety of materials.

## 2. MEASUREMENT FACILITIES

### 2.1 Classification of the materials

The materials which have been investigated are very different and can be classified in the following way. Regarding the electrical parameters only we distinguish between pure dielectric materials with the permittivity  $\epsilon$  and materials with dielectric and magnetic properties with the additional permeability  $\mu$ .

If we look at the mechanical parameters we can first consider the three aggregate states solid, liquid and gaseous. The materials can consist of one component only or can be mixtures of two or more components, f.i. carbon loaded plastic material or wet sand, which is a mixture of sand, water and air. The mixtures can be homogeneous or inhomogeneous, where homogeneous means that the inclusions in an host material are small compared to the wavelength of the electromagnetic wave. The surface of the material can be uniform or structured and can be additionally smooth or rough. The different classification parameters are shown in Fig. 1.

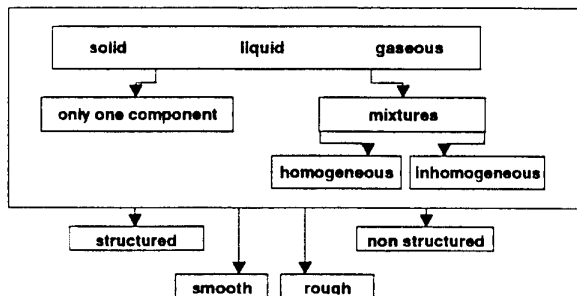


Fig. 1: Classification of the mechanical properties of materials.

### 2.2 Experimental setups

#### 2.2.1 General remarks

Our experimental setups are, as already mentioned, based on the two principles, namely measurement of reflection and transmission of samples in a waveguide, and measurement of these parameters under free space conditions. The facilities are prepared to cover the whole frequency range from 8 GHz upto 110 GHz. The actual state of the setups and the measurements which have been carried out till now are shown in Table 1.

Additional to these measurement facilities in some cases a coaxial probe from HP was used to get information on the complex permittivity  $\epsilon$  only by a quick and simple measurement procedure. Good results can be obtained for liquids (f.i. water) or semisolid materials (f.i. soil) in the frequency range from 0.5 to 20 GHz.

#### 2.2.2 Waveguide measurements

The measurement of the complex permittivity  $\epsilon$  and permeability  $\mu$  was done with a vector network analyzer from WILTRON. A detailed description is given in [2]. Additional to this analyzer a sweep generator and a S-parameter test set is needed (see Fig. 2).

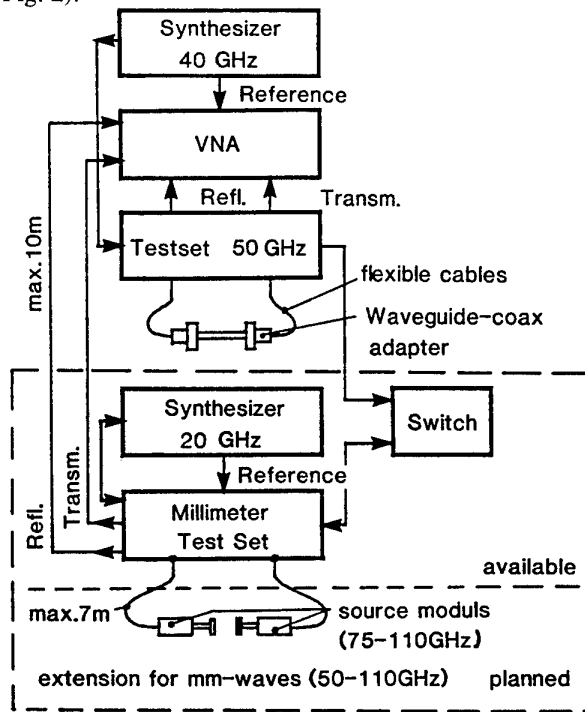
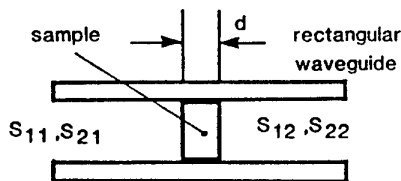


Fig. 2 Principle of S-parameter measurements.

The samples have been located in a rectangular waveguide transmission line. In principle also a coaxial transmission line can be used, but the fabrication is more difficult. The samples must be machined very carefully in order to avoid air gaps between the sample and the inner wall of the transmission line. The meaning of the S-parameters is explained in Fig. 3. Measurements have been carried out in the X-band (8.2 GHz to 12.4 GHz) and in the Ka-band (26.4 GHz to 40 GHz).



- $S_{11}$  = reflection factor at port 1
- $S_{21}$  = transmission factor at port 1
- $S_{12}$  = transmission factor at port 2
- $S_{22}$  = reflection factor at port 2

Fig. 3 Definition of the S-parameters.

Frequencies	X-Band 8.2-12.5 GHz	Ku-Band 12.4-18 GHz	K-Band 18-26.5 GHz	Ka-Band 26.5-40 GHz	Q-Band 33-50 GHz	V-Band 50-75 GHz	W-Band 75-110 GHz
Basic Equipment	Vector Network Analyzer 40 MHz - 50 GHz, Wiltron 360 B						
	First Synthesizer					Second Synthesizer	
	Testset (S-Parameter Measurements)					mm-Wave-Testset	
						Source Moduls no            yes	
	Calibration Kit, Wave Guide Adapters						
	yes	yes	yes	yes	yes	no	yes
S-Parameter Measure- ments of Samples in a wave-guide	yes	no	no	yes	no	no	no
Transmission Measure- ments (free space conditions)	first results	no	no	in construc- tion	no	no	yes, a new setup is planned
Reflection Measure- ments (free space conditions)	yes	no	no	in construc- tion	no	no	planned

Table 1 Actual state of the setups and the measurements

We have measured all four S-parameters, where two of them  $S_{11}, S_{21}$  or  $S_{22}, S_{12}$  are sufficient to calculate the values of  $\epsilon$  and  $\mu$ . For some samples we fabricated two or three different thicknesses and measured again the S-parameters and calculated once again the values of  $\epsilon$  and  $\mu$ . In most cases the results were nearly the same. The differences gave us a good information about the total accuracy which can be achieved by this measurement method.

### 2.2.3 Measurements under free space conditions

The principle of measurements of transmission and reflection under free space conditions is shown in Fig. 4 and Fig. 5. For the experimental setup two antennas are used, one for transmitting and one for receiving the signals. The distance between the two antennas must fulfill the far field condition and is in our case, dependent on the frequency, in the range of 50cm to 120cm. The sample can be positioned horizontally or vertically to the ground (see index a) or index b) in the Figures above).

For the measurement of the transmissivity we have built a transportable rack using the principle shown in Fig. 4a). The details of this method are described in [3] and [4]. The antennas and the sample can be moved on a precise fabricated rail. The sample can be turned either in the x-axis or the y-axis. So we can measure the transmissivity in dependence on the incidence angle for both orthogonal polarizations without changing the antenna position. Measurements at flat samples, size 15cm x 15cm, of glass

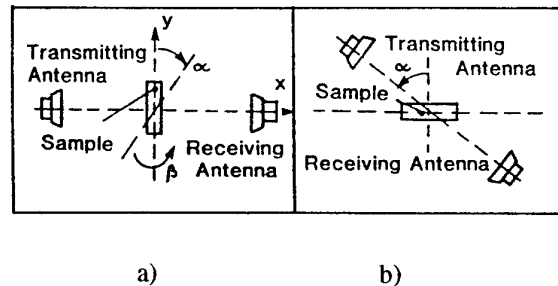


Fig. 4 Transmission measurements;  
a) Sample position vertical,  
b) Sample position horizontal.

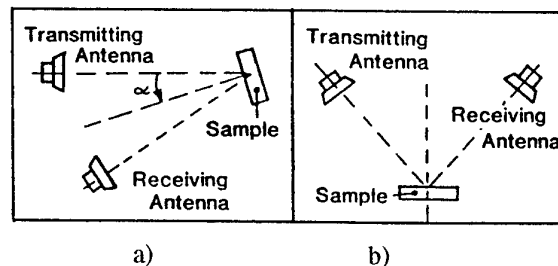


Fig. 5 Reflection measurements;  
a) Sample position vertical  
b) Sample position horizontal.

and plexiglass have been carried out in the W-band from 75 GHz to 96 GHz. Measurements in the Ka-band (26 GHz to 40 GHz) are in preparation. Measurements of the reflectivity, see Fig. 5a), will also be done in the future.

Each measurement at the sample itself must be preceded by a reference measurement. In the case of transmission this simply can be done by removing the sample under investigation. In the case of reflection measurements however the sample must be replaced by a metal plate (reflectivity 1). The spatial position of each sample must be exactly the same. We try to get position accuracies in the order of 1/100mm which can only be managed by distance measurements on the basis of a laser triangulation system.

Another measurement facility has been verified to obtain the reflectivity of samples at X-band (8.2 GHz - 12.5 GHz) where the sample is positioned horizontally (see Fig. 5b)). This facility has been built up in an anechoic chamber. The antennas can be moved separately according to the incidence angle wanted and the sample can be moved up and down in order to correct for different thicknesses. To get a definite background the sample is backed by a metal plate. For the reference measurement once again a metal plate is used. The configuration of this measurement facility allows not only to investigate solid materials but also liquid and semisolid materials, like water, sand, soil and so on. For this purpose we have built a box made of teflon into which the different materials can be filled. Measurements at different polarizations can be carried out by turning the antennas mechanically.

Transmission measurements according to Fig. 4b) have not been done till now because of difficulties in mechanical construction. In general one can say that with increasing frequency it is more and more difficult to meet the mechanical accuracies in the construction of the measurement setup as well as in the tolerances of the samples.

#### 2.2.4 Measurements with a coaxial probe

Additionally to our experimental measurement setups, mentioned above, we used in some cases a coaxial probe, developed by the company Hewlett Packard (HP). We carried out a lot of measurements of the permittivity  $\epsilon$  for liquid and semisolid materials. The covered frequency range was 0.2 GHz to 20 GHz. This measurement method gives good results for liquid, moderate results for semisolid materials, like soil, and poor results for solid materials. The reason is that there must be a direct contact of the probe to the sample, which is fulfilled only for liquids. At solid materials there are usually more or less big gaps of air between the probe and the sample. The advantage of this measurement method is to obtain results in a simple and quick way at a wide frequency range, the disadvantages are, as already mentioned, the poor results for solid materials and the limitation of the measurements to

dielectric materials. The permeability  $\mu$  can not be determined with this method.

### 3. COMPUTER CODES

#### 3.1 Computer code MYEPS

The computer code MYEPS calculates the complex material constants  $\epsilon$  and  $\mu$  from the measured S-parameters  $S_{11}, S_{21}$  or  $S_{22}, S_{12}$ . The formulas can be written in an analytically closed form. The derivation of the formulas and the description of the program can be found in [2]. Input parameters are the measured S-parameters, the frequency, the cutoff frequency of the rectangular waveguide and the thickness of the sample. If the sample is shorter than the sample holder a correction for the nonlinear phase shift must be carried out.

The computer program works very well for materials with relatively high loss ( $\tan \delta > 0.1$ ). For very low loss samples ( $\tan \delta < 0.01$ ) the results are not satisfactory and other measurement techniques, such as resonator methods must be used.

#### 3.2 Computer codes REFMEs and TRAMES

The computer code REFMEs calculates the complex material constants  $\epsilon$  and  $\mu$  from the measured complex reflection factor; the computer code TRAMES from the measured complex transmission factor. Details can be found in [4] and [5].

These codes are used if only reflection or only transmission measurements of samples are available. In this case a calculation of  $\epsilon$  and  $\mu$  in an analytically closed form is not possible. Therefore computer programs have been developed which can be characterized as a sophisticated „trial and error“ procedure. The input to the program is the measured complex reflection or transmission factor and an estimation of  $\epsilon$  and  $\mu$ . If the input consists only of one measurement value, one will get as result a lot of possible  $\epsilon$  and  $\mu$  parameters. In order to reduce the ambiguity it is necessary to introduce additional measurement values, for instance measurements at different incidence angles and polarisations. Then a curve fitting method can be applied and in most cases appropriate values for  $\epsilon$  and  $\mu$  will be found by the computer program. If the measurement accuracy is not sufficient it can occur that this procedure works only for nonmagnetic materials, that means only the value of  $\epsilon$  can be calculated.

#### 3.3 Computer code REFL

The computer code REFL calculates the complex reflection factor for single or multilayered media in dependence on incident angle, polarization, frequency and thickness of one of the layers for given values of  $\epsilon$  and  $\mu$ . It is described in detail in [6].

Some parts of this program are used in the computer code REFMES. Mainly the program is used for cross checks if the material parameters  $\epsilon$  and  $\mu$  and the reflection factors of a material have been measured or are given by the manufacturer of the material.

The reflection factors are also used as input parameters for the computer codes SIGMA and BISTRO which have been developed to predict the radar cross section of objects, what is already mentioned in the introduction of this paper.

## 4. RESULTS

### 4.1 Solid materials

The material parameter  $\epsilon$  has been determined for a lot of solid materials, like glass, plexiglass, plywood, pure plastic materials and composite plastic materials. Additionally some materials with magnetic properties, which consist of iron loaded polyurethan, have been investigated and the parameters  $\epsilon$  and  $\mu$  have been calculated.

#### 4.1.1 Glass

The determination of the material parameter  $\epsilon$  of glass at different frequencies will now be described in more detail and should be representative for other measurements carried out. For the X-band (8.2 GHz to 12.4 GHz) we used the method to measure the S-parameters of the sample in a rectangular waveguide (see 2.2.2). The fabrication of the samples with the size 22.86mm x 10.16mm was not too difficult. The thickness of the glass sample, we used, was 1.58mm. For the complex permittivity  $\epsilon = \epsilon' - j\epsilon''$  we got the frequency independent mean value of 6.83 - j0.095 with a standard deviation of 0.04 - j0.01.

The same measurement method we used in the Ka-band (26.4 GHz to 40 GHz). The dimension of the sample in this case was only 9.14mm x 5.59mm and the preparation, especially for glass, was very difficult. Actually the mechanical accuracy of the sample was not quite satisfactory because of lack of appropriate tools for the precise fabrication. Therefore we got moderate results only in the frequency range from 26.4 GHz to about 32 GHz. The mean value for the complex permittivity we calculated as  $\epsilon = 7.25 - j0.28$  with a relative high standard deviation of 0.20 - j0.06. We intend to repeat the measurements at glass with the method using free space conditions (see 2.2.3).

Because of the difficulties in manufacturing very small samples we used the free space method for our measurements in the W-band (75 GHz to 110 GHz). We determined the complex transmission factor of a glass plate, size 15cm x 15 cm, at four different incident angles, 10°, 20°, 30°, 40° and at six different frequencies. The results of the calculated material

parameters  $\epsilon'$  and  $\epsilon''$  are shown in Fig.6. For the mean value we got  $\epsilon = 6.74 - j0.22$  with a standard deviation of 0.12 - j0.02. From an earlier measurement of glass at 94 GHz we obtained  $\epsilon = 6.78 - j0.20$  which is in good agreement with our recent measurements. These results are better than we achieved at

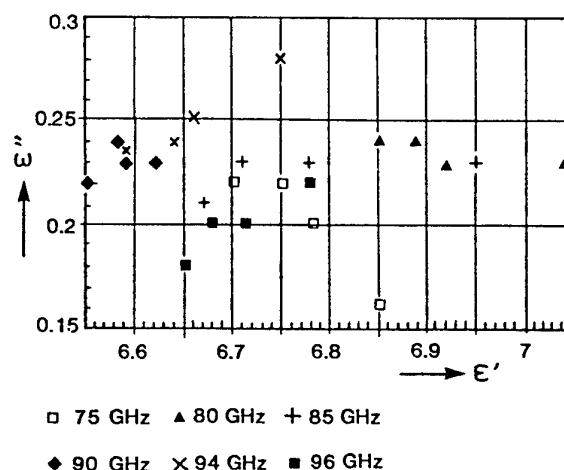


Fig. 6 Calculated material parameters  $\epsilon'$  and  $\epsilon''$  for glass obtained from measured transmission factors (W-band).

the Ka-band with the S-parameter measurement method. Evidently in this case the free space measurement method has some advantage at high frequencies.

#### 4.1.2 Absorber materials

The material parameters  $\epsilon$  and  $\mu$  have been determined for six different absorber materials with magnetic properties with the method of S-parameter measurements of samples in a waveguide. The measurements have been carried out in the X-band and in the Ka-band. The absorbing materials have been delivered by the company EMC as flat plates with the size 30cm x 30cm. From these plates we produced at our institute the appropriate samples with different thicknesses for insertion into the rectangular waveguides. The different materials MF 110, MF 112, MF 114, MF 116, MF 124, MF 190 consist of iron loaded polyurethan, where the iron content is higher with increasing MF-number. The calculated material constants  $\epsilon', \epsilon'', \mu', \mu''$  gained for the X-band are presented in Fig. 7 a), b), c), d). For the measurements in the Ka-band as an example only the parameters  $\epsilon'$  and  $\mu'$  are shown in Fig. 8 a), b). The results obtained in the Ka-band fit very well in opposite to the measurements of glass at the same frequency. The reason is that the fabrication of these samples, made of MF-material, could be done much more precisely, with the tools available, than the manufacturing of the sample made of glass.

A comparison of  $\epsilon'$  and  $\epsilon''$  parameters for the material MF 112, obtained by different measurement methods and partly carried out at different institutions, is shown in Table 2. The differences are in some cases very large. The reason is not quite clear and will be investigated. One possible reason may be that, according to the information of the manufacturer, the delivered samples are partly from different production charges, and therefore the iron content may vary slightly and can not be guaranteed.

Institution/ Method	$\epsilon$	$\mu$
DLR, 1994 (Waveguide)	5.52-j0.28	1.31-j0.37
DLR, 1996 (Waveguide)	5.75-j0.24	1.26-j0.33
DLR (Reflection)	4.78-j1.10	1.33-j0.13
MBB (Waveguide)	5.35-j0.13	1.25-j0.34
THD (Waveguide)	5.18-j0.03	1.29-j0.41
Manufacturer	4.86-j0.21	1.10-j0.25

Table 2: Comparison of the complex material parameters  $\epsilon$  and  $\mu$  of the absorber material MF 112 carried out at different institutions and obtained by different measurement methods.

4.1.3 Structured absorber

Finally we tried to determine the permittivity  $\epsilon$  of a structured absorber, as it is sketched in Fig. 9. The material was kindly send to us for measurement purposes by the development department Gerd Hugo in Schondorf, Germany. It is a waffle like plate, size 25cm x 25cm, with a thickness of about 3.3mm. The absorber is backed by a metal plate. The single elements have the size of 2.2 cm x 1.5cm. The material itself is a special plastic filled with irregular oriented carbon sticks and has no magnetic properties.

We measured the complex reflection factors at seven different incidence angles and at two orthogonal polarizations at a frequency of 9.6 GHz by the method indicated in Fig.5b). Then we calculated the resulting permittivity  $\epsilon$  by the computer code REFMES, described in 3.2. The result for  $\epsilon$  is not the true  $\epsilon$  of the material itself, but it is a composition of the electrical and geometrical properties of the material. That means , that a flat and smooth material with the same permittivity  $\epsilon$  would have nearly the same reflection factors at the different incidence angles. We call therefore this permittivity pseudo  $\epsilon$  and we got the value  $\epsilon(\text{pseudo}) = 4.40 - j1.22$ .

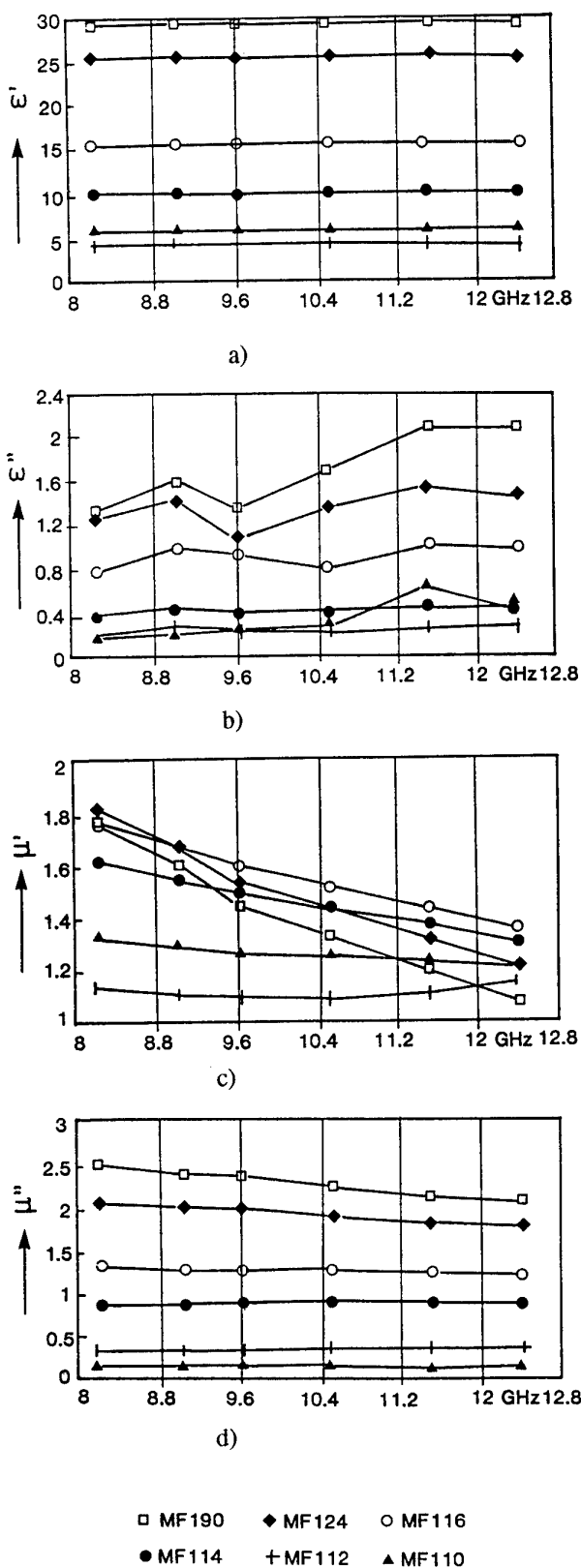
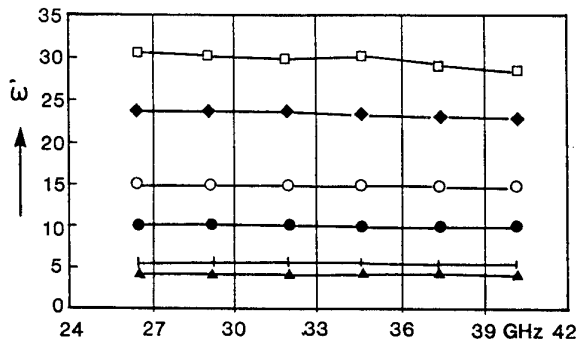
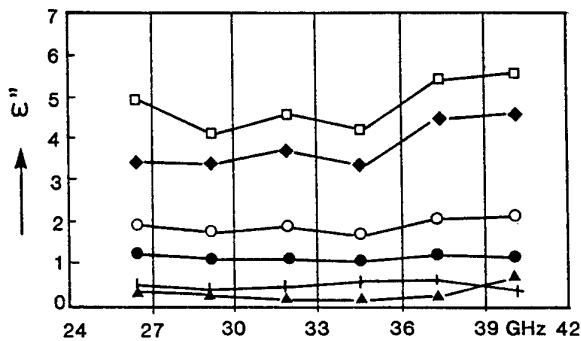


Fig. 7 Calculated material parameters  $\epsilon'$ ,  $\epsilon''$ ,  $\mu'$ ,  $\mu''$  for different absorber materials obtained from S-parameter measurements (X-band).



a)



b)

□ MF190    ◆ MF124    ○ MF116  
 ● MF114    + MF112    ▲ MF110

Fig. 8 Calculated material parameters  $\epsilon'$ ,  $\epsilon''$  for different absorber materials obtained from S-parameter measurements (Ka-band).

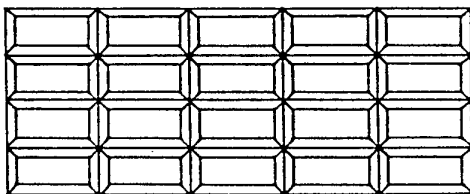


Fig. 9 Geometry of a structured absorber.

## 4.2 Liquids and semisolid materials

### 4.2.1 Water

With the aid of a coaxial probe, described in chapter 2.2.4, we first determined the permittivity  $\epsilon$  for a lot of special alcoholic liquids, which are used as calibration normals. Then distilled water was investigated in more detail. As an example the measurement results for the real part of the permittivity  $\epsilon'$  in dependence on the temperature in the range from 5°C to 95°C are shown in Fig. 10. The curves are

presented for a measurement frequency of 3 GHz. The first curve shows the result when the water was heated, the second when the water was cooled. The agreement between the two curves is in general quite good. A third curve is added as reference and shows the results obtained by A.v.Hippel [7]. The agreement to our measurements is only good to about 45°C, for higher temperatures it is not very well. The reason therefore is not clear.

### 4.2.2 Soil

The coaxial probe from HP was also used to measure the permittivity  $\epsilon$  of different soils, like fir wood or

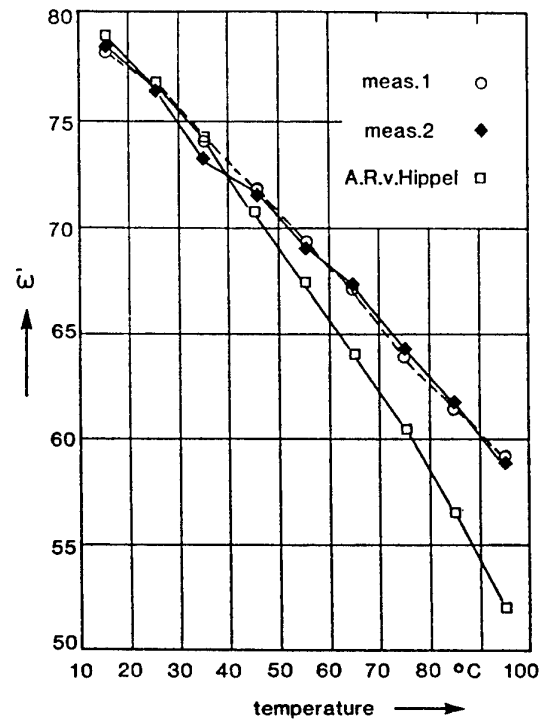


Fig. 10 Real part of the permittivity  $\epsilon'$  for distilled water in dependence on temperature at 3 GHz.

beech wood soil. These investigations have been in connection with the X-SAR mission, where extensive radar measurements have been carried out from the space shuttle. Fig.11 shows as an example the real part of the permittivity  $\epsilon'$  as a function of the frequency. The four different curves are the results from four different samples taken at different days before and after rainfall. Because of the nonuniform structure of the samples, in each case the mean value of ten independent measurements was used for presentation.

## 5. Summary

For the computer codes SIGMA and BISTRO, which are used to predict the mono- and bistatic cross sections of complex structures, the knowledge of the

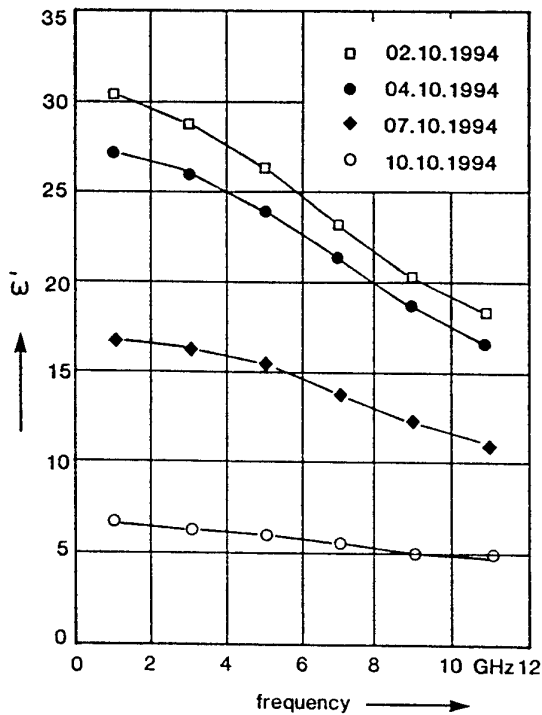


Fig. 11 Real part of the permittivity  $\epsilon'$  for earth from a fir wood measured at different days in dependence on frequency.

reflection factors or, in the more general case, the knowledge of the material parameters  $\epsilon$  and  $\mu$  in dependence on the frequency is necessary. Because of the variety of the materials, concerning their composition as well as their geometric surface, in many cases different measurement methods must be used to get the best possible result. Different measurement methods, applied to the same material, have been carried out for reliability tests. The measurement setups, we used to determine the complex material parameters, cover the frequency range from 8 GHz to 110 GHz. Three different methods can be distinguished.

The first is based on the measurement of the so called S-parameters (scattering parameters) of samples in a waveguide followed by the calculation of  $\epsilon$  and  $\mu$  by a special computer code. The samples must be produced with high accuracy in order to avoid air gaps between the sample and the inner wall of the sample holder. The results which have been obtained with this method depend strongly on the accuracy with which the samples can be fabricated. We got very good results for the material glass in the frequency range from 8 GHz to 12.4 GHz (standard deviation for  $\epsilon \pm (0.04 - j0.01)$ ) and good to moderate results in the frequency range from 26 GHz to 40 GHz (standard deviation for  $\epsilon \pm (0.20 - j0.06)$ ). Above 40 GHz it is more and more difficult to produce samples with sufficient accuracy.

The second method is based on the measurement of the reflection or transmission factor of relatively large samples under free space conditions. In this case two antennas, a transmitting and a receiving one, is used. Once again a special computer code must be applied, which can be described as a "trial and error" procedure to find by an iterative calculation the most appropriate values for the material parameters. The results, we achieved by this method, are good for nonmagnetic materials, like glass, where we got a standard deviation for  $\epsilon$  of  $\pm 0.12 - j0.02$ . For magnetic materials the accuracy cannot be specified clearly, because the exact composition of the materials was different from charge to charge and could not be guaranteed by the manufacturer.

The third method uses the measurement of the reflection factor of the sample by a special coaxial probe, developed by the company Hewlett Packard, and may be used preferably for liquids and semisolid materials in the frequency range from 0.2 GHz to 20 GHz. This method allows the determination of the permittivity  $\epsilon$  only. The results are quite good for liquids and sufficient accuracy will be obtained for mixtures of different materials, like soil, if the mean value of several measurements is used.

A priority of our future work will be the automation of our existing measurement facilities. A new setup will be installed to carry out reflection and transmission measurements under free space conditions in the frequency range from 26.4 GHz to 40 GHz. The material parameters of mixtures and the dependence on temperature are further items of investigation.

## 6. Acknowledgement

I want to thank all colleagues who have been engaged in this work. Especially Mr. Dreher, who was responsible for the construction of the measurement facilities, and the team of our mechanical workshop contributed very much to the success of these results.

## 7. References

- [1] D.Klement State of Development, Validation J. Preissner and Application of the Radar Signature Models SIGMA and M. Ruppel V. Stein BISTRO at DLR. Ground Target Modeling and Validation Conference Keweenaw Research Center, Michigan Technological University, Houghton, Michigan, 23-25 August, 1994.
- [2] K.-H.Dreher Bestimmung der Stoffparameter J. Preissner fester Materialien durch Messung M. Ruppel der Streuparameter im Hohlleiter. DLR, Institut für Hochfrequenztechnik, IB 551-3/94, 1994.

- [3] R.Nitsche Aufbau und Charakterisierung einer Meßeinrichtung zur Durchführung von Reflexions- und Transmissionsmessungen bei 94 GHz zur Bestimmung von Stoffkonstanten.  
Diplomarbeit TU München, Lehrstuhl für Hochfrequenztechnik, Aug. 1993.
- [4] R.Nitsche A Free Space Technique for Measuring the Complex Permittivity  
J. Preissner and Permeability in the Millimeter  
E.M. Biebl Wave Range.  
1994, IEEE MTT-S Digest,  
pp.1465-1468.
- [5] M.Ruppel Theoretische und experimentelle Untersuchungen zur Lösung bistatischer Streuprobleme mit der physikalisch-optischen Näherung.  
Dissertationsschrift an der Technischen Hochschule Darmstadt, 1994.
- [6] J.Preissner Reflexion an mehrschichtigen Medien unter besonderer Berücksichtigung des Mikrowellenbereichs.  
DFVLR-Mitt. 89-03, 1989.
- [7] A.R.v.Hippel Dielectric Materials and Applications.  
The M.I.T. Press, Massachusetts Institute of Technology,  
Cambridge, Massachusetts, 1966.

**Discussor's name:** A. PRIOU

**Comment/Question:**

Remarks: free-space microwave measurement techniques can go from 3 GHz to 100 GHz with various branch tests. In order to avoid the edge effects you have to use focused beam free-space techniques (either from a dielectric lens or elliptic reflector). I have published a paper on this technique in JEWA, 1992, Special Issue on Materials and Measurement Techniques, MIT Press or VSNU Press Editor.

**Author/presenter's reply:**

Thank you very much for this valuable hint.

**Discussor's name:** J. G. GALLAGHER

**Comment/Question:**

Have you quantified the error associated with the match of the transmitting and receiving horns?

**Author/Presenter's reply:**

We have not quantified the errors but we have minimized them by choosing a relatively large distance of 2 m between the two antennas. In this way, the unwanted reflections caused by mismatch of the antennas (VSWR 1 : 1.2) are attenuated on this long path.

In addition, we avoid for our free space transmission measurements a position of 0° to 5° of the sample, so that reflections at the sample cannot come directly into the transmitting antenna.

**Discussor's name:** I. ANDERSON

**Comment/Question:**

What is the contribution to your measurement errors by illumination of the edges of your samples in free-space reflection measurements?

**Author/Presenter's reply:**

Our X-band measurements antenna spot (3dB - beamwidth) is within the sample. Nevertheless, the remaining illumination of the edges of the sample causes errors, especially at shallow incidence angles. We have not quantified this effect which is different from material to material. But we have minimized it by placing irregularly cut strips of absorbing material at all four edges of the sample. There will still remain an error of approximately  $\pm 0.2$  dB.

For our free space measurements at 90 GHz the antenna beam (3dB - beamwidth) illuminates only about 20% of our sample.

## CAPTIVE-TARGET IMAGING AT SUB-MM THROUGH CM WAVELENGTHS

Richard A. Marr

Uve H. W. Lammers

Rome Laboratory, 31 Grenier Street  
Hanscom AFB, Massachusetts, 01731-3010

### 1. SUMMARY

We developed instrumentation radars in the sub-mm and mm wavelength range for two dimensional (2-D) imaging. Salient features of these systems are mechanical frequency shifting for a very high degree of phase stabilization and target precessional motion for crossrange/ crossrange imaging. We designed a cm wavelength radar which additionally uses a wideband waveform for ranging to permit three dimensional (3-D) imaging. The latter system is fully polarimetric. All radars use a form of moving target indicator (MTI) cancellation to suppress background clutter. The operation of these systems and examples of data measured on canonical bodies and model targets are discussed.

### 2. INTRODUCTION

Apart from computational methods, radar measurements on scale models at correspondingly scaled wavelengths provide a cost effective means to analyze the scattering behavior of full size targets. Image resolution commensurate with scaled size requires wideband and/ or highly coherent instrumentation radars. At Rome Laboratory, we built three such systems in the sub-mm, mm and cm wavelength ranges. The purpose of this work is to better understand scattering mechanisms, to verify analytical scattering algorithms and to precisely identify scattering centers on complex structures. The scattering from metallic and non-metallic bodies at microwaves and shorter wavelengths has both military and commercial importance. Applications range from radar cross section control and target identification to non-destructive testing and medical imaging. We are working toward an optimum utilization of the information contained in the radar signal.

### 3. PRESSION/ PHASE STABILIZATION

Radar imaging of targets in their operational environment is typically 2-D. It involves a wideband waveform to resolve detail along the range direction and phase shift due to target rotation to resolve detail in the crossrange direction. Observation is often limited to a narrow angular region. With a target captive on a radar range, observation is possible over a complete 360° revolution. In Figure 1a, this is indicated by a target T rotating about

the  $f_z$  axis in frequency space, and the radar probing along the  $f_y$  axis.

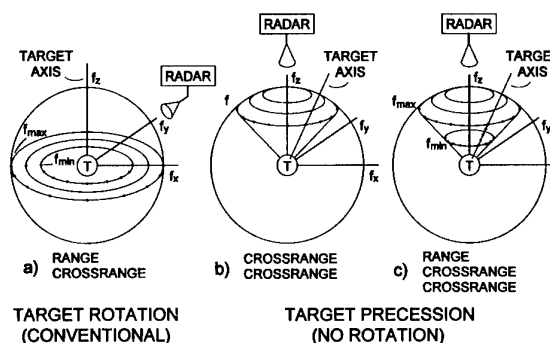


Fig.1 2-D and 3-D imaging regimes in frequency space

At mm wavelengths, and particularly at sub-mm wavelengths, wideband waveforms are difficult to produce. For 2-D imaging, we have therefore chosen the approach indicated in Figure 1b. The radar now observes from the  $f_z$  direction, while the target precesses around the same axis. That is, a target axis intersecting the origin describes the surface of a cone. In analogy with the well known failing motion of a mechanical top, this is called precession. Note, however, in contrast to the top, the precessing target does not rotate. A series of such cones provides data on a spherical cap in frequency space which is required for crossrange/ crossrange imaging. At cm wavelengths, where we have a wideband signal available, Figure 1c applies. Data, additionally generated along the frequency (radial) direction, fill the volume of a truncated cone in frequency space, a condition for 3-D (range/ crossrange/ crossrange) imaging. Compared with the wide angular observation range of a rotating target in Figure 1a, precession in Figures 1b and 1c has several advantages. Crossrange resolution is on the order of one wavelength even with the narrow observation interval of  $\pm 10^\circ$  as used in the measurements reported here. This reduces the variability of reradiation from directive and polarization sensitive scatterers. It also reduces mutual shielding of scatterers. In effect, the point spread function of scatterers is improved [1].

Targets with crossrange dimensions of many wavelengths lead to imaging times from minutes to hours. Since data must be coherent over the whole period, this requires extreme short and long term phase stability of the signal sources involved. In the mm and sub-mm systems we achieve phase stabilization through mechanical frequency shifting of a single, unstabilized source and dual frequency conversion in the receiver. Mechanical frequency shifting is power efficient, but limits intermediate frequencies (IF) to below 100 kHz or so. High mixer noise at such low IF is somewhat compensated for by the extremely narrow coherent bandwidth of the imaging process. The bandwidth is the inverse of the measurement time. Figure 2 explains the application of the frequency shifter in a block diagram.

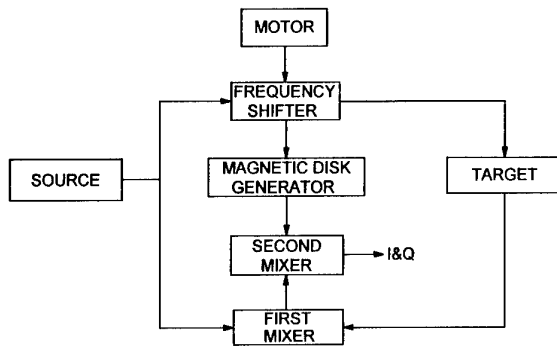


Fig 2. Phase stabilization of a single-source radar

The shifter is a rotating mechanical device for Gaussian wave propagation at sub-mm waves [2] or for waveguide propagation at mm waves. Co-rotating with the shifter is a disk of magnetic material. A stationary head writes to or reads from this magnetic disk. The source signal in Figure 2 is divided into two components. One is used as a first local oscillator (LO) signal, the other, after frequency shifting, as the transmit signal. With a short radar path, phase instabilities in both signals due to the source are essentially the same. They cancel in the first mixer. Phase instabilities of the transmit signal due to rotation rate changes or mechanical imprecision of the shifter do not cancel. We therefore write the first IF signal from a strong, stationary target to the magnetic disk and use this signal as the LO in a second mixer to generate the baseband I and Q signals for any precessing target to be imaged. Phase instabilities due to the frequency shifter are completely eliminated in the second mixer.

#### 4. SUB-MM AND MM SYSTEMS

The sub-mm radar in Figure 3 operates as outlined in Figure 2. It is a quasi-optical system with simulated Gaussian beam directions overlaid on the figure. The rotating central disk of the frequency shifter on the left shows the dark magnetic material attached to it. The beam entering centrally is deflected twice by two plane mirrors inside the disk before exiting tangentially. After reflection from one of four involute-shaped stationary reflectors, the frequency shifted beam returns to where it came from.

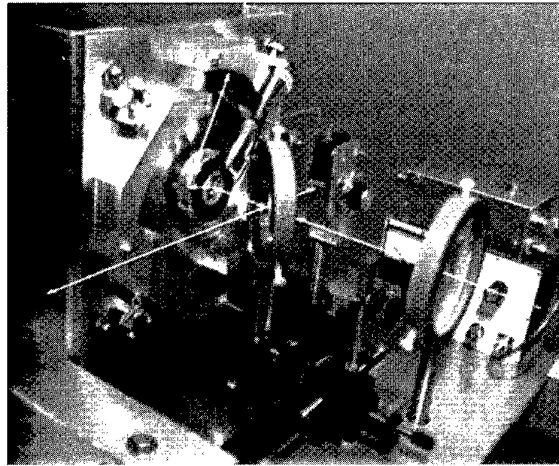


Fig. 3 Quasi-optical implementation of phase stabilization scheme

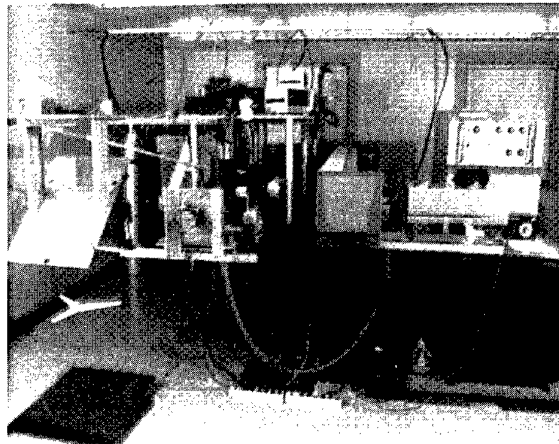


Fig. 4 Laser based sub-mm wave imaging radar

In the picture of the sub-mm radar, Figure 4, the right half is occupied by the CO<sub>2</sub> laser and its high voltage supply and cooling system. The lasing medium in the far infrared laser in the center is formic acid which is pumped to produce several mW of source power at 584 GHz. The transmit beam is shaped by a round focusing mirror in the left background to have a waist at the target after downward reflection by the flat 45° mirror. The target is suspended on a Styrofoam tripod. Computer controlled stepper motors change the length of the strings suspending the tripod to introduce target precessional motion. The string suspension facilitates two measurements of the target response at each aspect angle. Raising or lowering the target by a quarter wavelength between measurements and subtracting these from each other yields a target signal enhancement of 6 dB and a stationary clutter reduction of 40 dB or more. Here, as with the other two systems, we trade an increase in the measurement time for greatly reduced demands on the absorptive properties of the chamber. The radar, including target range and target, is attached to an optical table. For mechanical stability,

the latter features a vibration isolation system and automatic leveling. As an example, the 2-D image in Figure 5 taken with this system displays the relative magnitudes of a three-scatterer target. They are corner cubes of different size mounted in a plane normal to the radar direction.

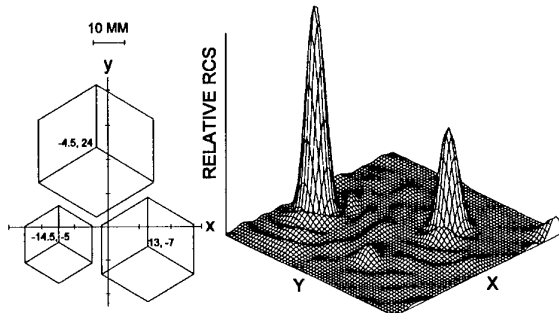


Fig. 5 2-D image of three corner cube target at 584 GHz

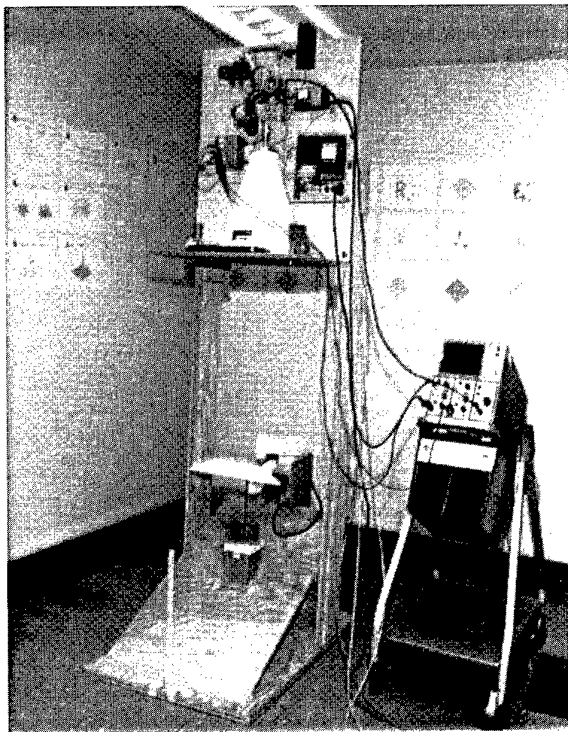


Fig. 6 MM-wave radar for 2-D monostatic and bistatic imaging

The mm radar in Figure 6 uses an unstabilized 94 GHz Gunn oscillator as a source. It is a waveguide system and has many similarities with the sub-mm radar. The transmit beam is collimated by a horn lens antenna permitting linear and circular polarizations as well as co- and cross-polarized measurements. Although primarily monostatic, Figure 6 shows the radar in a bistatic configuration, with a plane, precessing metal plate underneath the stationary target reflecting signals back into the horn lens antenna.

As obtained by this radar, a nose-on monostatic image of a metallic cone with  $60^\circ$  apex angle and seven wavelengths base diameter is seen in Figure 7.

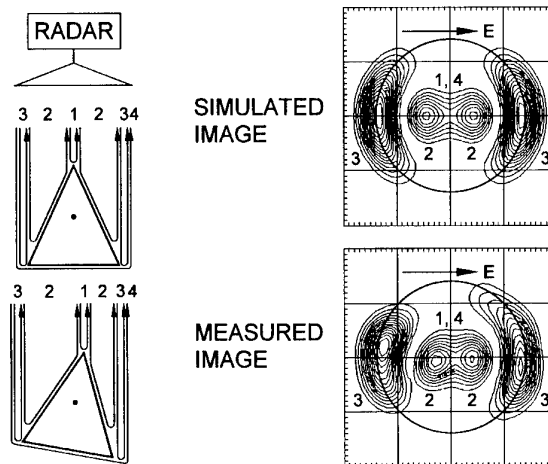


Fig. 7 2-D nose-on diffraction image of metallic cone at 94 GHz

During precession, no specularly reflected signal returns to the radar. First and second order diffraction account for the measured image. The sketches on the left show the cone in its non-precessed and precessed orientations. Minimal radial motion relative to the radar occurs at the cone's tip, maximal and opposite radial motion occurs at the edges. Tip diffraction (1) therefore images at the center, edge diffraction (3) images on the periphery of the disk which is a projection of the cone as seen by the radar. Tip and edge signals are singly diffracted. The tip-to-edge (2) signal is doubly diffracted. It undergoes only half the phase excursions of the edge diffracted signal and consequently images halfway between center and edge. The edge-to-edge signal (4) is also doubly diffracted and images at the center. This is due to canceling phase excursions at opposite edges. With properly chosen relative magnitudes and based on the same path geometry, a comparable image can be simulated. The direction of the E vector determines the image orientation.

## 5. CM SYSTEM

Of the three radars described here, the cm system measures the most complete set of scattering parameters. It images three dimensionally with a wideband signal (12.4-18.4 GHz) for ranging in addition to target precession. A commercial vector network analyzer provides the transmitter and two receivers. Four vertically stacked waveguide horn antennas are indicated in Figure 8 for transmission and reception. The target is attached to the azimuth-over-elevation positioner by way of a linear translation stage which carries out the target transposition for clutter cancellation. The target, attached to the positioner, is made to undergo a quasi-precessional motion. The aspect axis is still tilted by  $\theta$  but the target is rotated during data collection. To achieve equivalence with true precession, the polarization vector must be rotated in synchronism with the target. At tilt angles

$\theta = 10^\circ$  or less we consider the target rotation plane and the polarization vector plane to be parallel.

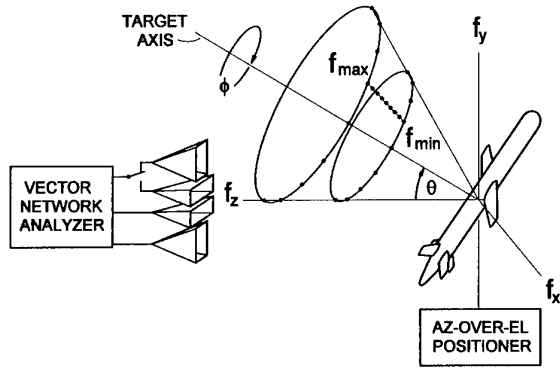


Fig. 8 Quasi-precessional target motion for 3-D imaging with cm-wave system

Horizontally and vertically polarized signals are transmitted in sequence by the upper two antennas in Figure 9. In either state, horizontally and vertically polarized signals are received by the lower two antennas and processed by the two receive channels of the network analyzer. This is repeated for both MTI positions at all  $\phi$  orientations of the target in such a fashion as to minimize the number of mechanical movements. Finally, the sequence is repeated at all  $\theta$  elevations. Measuring orthogonal polarization components allows one to synthesize any angle  $\phi_0$  between target direction and polarization vector. Equations to derive the co- and cross-polarized target response from the component measurements are given in the figure.

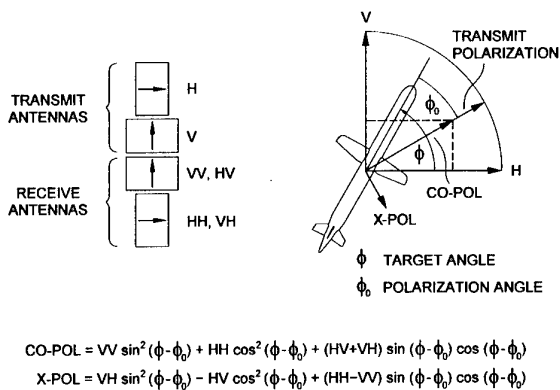


Fig. 9 Polarization rotation synthesized from vertical and horizontal component measurements

Signal processing is applied in stages. First, target data are calibrated against measurements from a 4-inch calibration sphere. At the same time, MTI subtraction is performed and the desired image polarization angle  $\phi_0$  is selected. Then the image is generated by either correlation processing or by fast Fourier transform (FFT). Correlation produces high quality images of relatively small targets whereas FFT processing is required for

larger targets where correlation processing time would be prohibitive. If FFT processing is selected, it is preceded by an interpolation routine (after Bucci [3]) to put polar acquired data onto a Cartesian raster. Sub-mm and mm data have so far been exclusively processed by the correlation algorithm.

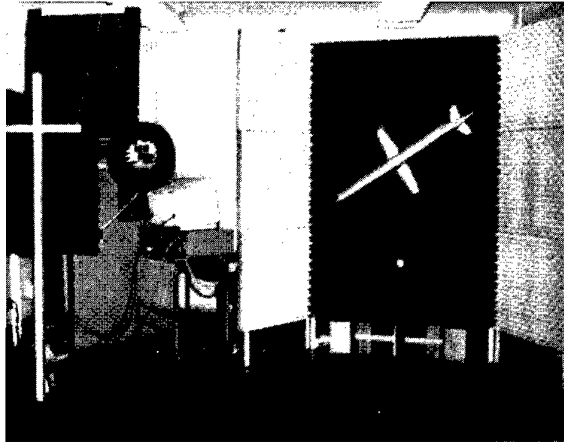


Fig. 10 Folded cm-system with radar and target side-by-side

As a folded system, the cm radar and target are located at one end of the chamber in Figure 10. Both face a plane reflector at the opposing wall. The one-way target range is 11 m, yielding a maximum target dimension of about 0.3 m (at 18.4 GHz) to be considered far field. This is a requirement to generate radar cross section (RCS) data. For imaging purposes, the same far field constraint applies to individual scattering centers only. Resolvable scattering centers on a larger target will image properly without regard for how they phase with each other. The sparing use of absorber material around the chamber attests to the effectiveness of range gating in the network analyzer and the clutter subtraction method. A vertical in-line arrangement of antennas has been found to be superior to the original cluster shown in the figure surrounded by the absorber ring.

A generic missile consisting of fuselage, wings and tail surfaces is imaged three-dimensionally in Figure 11. The three graphs are to be visualized as the top (x,y), side (x,z) and front/back (y,z) view of a 3-D image, while the radar looks at the target from the top. The radar does not move between looks. The front and side views show the z location of scatterers imaged in the top view. This is distinctly different from a set of graphs where the top, front and side of the target face the radar. Consider, for example, the limited response from the vertical tail surface. It would have imaged strongly, had the radar seen the missile broadside.

To illustrate the radar's ability to discriminate against co-polarized signals when generating a cross-polarized image, we mounted three metallic spheres in an equal sided triangle forming a plane orthogonal to the radar direction. The spheres image as three point scatterers

located at their centers when using the co-polarized returns.

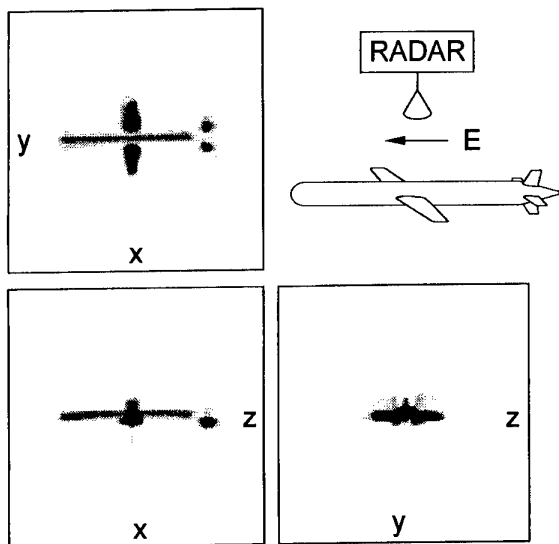


Fig. 11 Orthogonal views of 3-D generic missile image at 12.4-18.4 GHz

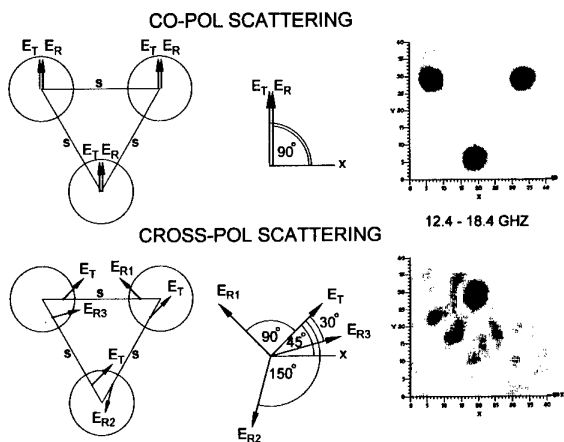


Fig. 12 Co- and cross-polarized 2-D images of three sphere target

The co-polarized receive vector  $E_R$  has the same orientation as the transmit vector  $E_T$  in Figure 12. This is true for  $\phi_0 = 90^\circ$  and for any other angle. Illuminating the target at  $\phi_0 = 45^\circ$  and imaging the cross-polarized returns shows a strong response from  $E_{R1}$ . The two tangential planes on adjacent spheres, from which the vectors extend, form  $90^\circ$  dihedrals. Upon  $\phi_0 = 45^\circ$  illumination, the signal  $E_{R1}$  doubly reflected by the upper two spheres is perfectly cross-polarized as seen in the vector diagram. The other two,  $E_{R2}$  and  $E_{R3}$  are weak because their associated dihedrals are illuminated unfavorably for cross-polarization. By appropriately rotating the transmit polarization comparable images are derived from  $E_{R2}$  and  $E_{R3}$ . The cross-polarized images are centered between the co-polarized ones. Because of the extra traverse

pathlength, they appear further removed from the radar (not shown). The ratio of co-polarized to cross-polarized power is 11 dB. The co-polarized responses are suppressed in the cross-polarized image.

According to Boerner [4], the optimal image of a target can be reconstructed by incoherently summing any two co-polarized images at orthogonal polarizations plus their corresponding cross-polarized images. In Figure 13, we have done this for the generic missile image. Quantities  $|S_{VV}|^2$  and  $|S_{VH}|^2$  refer to co-polarized and cross-polarized images at  $\phi_0 = 90^\circ$ . Correspondingly,  $|S_{HH}|^2$  and  $|S_{HV}|^2$  are the same images at  $\phi_0 = 0^\circ$ . Given the fact that the missile produces a cross-polarized image which is on the order of 20 dB weaker than the co-polarized one over the range of aspect angles employed here, we do not see much change in the composite image of this particular target. Still, valuable information may be retrieved about substructure of the target as the cross-polarized signal is observed over the full  $180^\circ$  angular range.

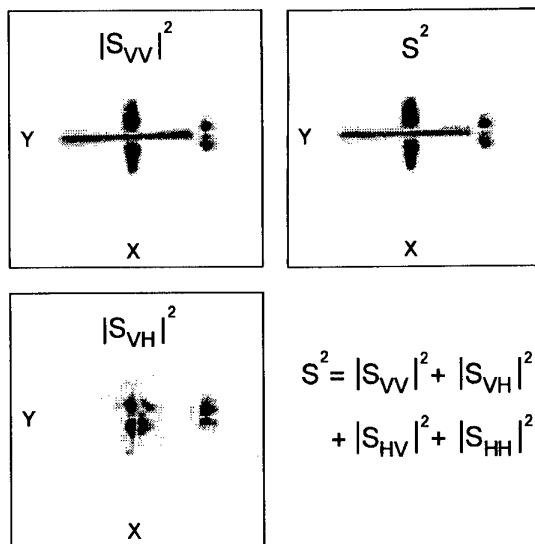


Fig. 13 Co-polarized, cross-polarized and composite top views of generic missile

As an example of a non-metallic target, we present the image of a dielectric cube in Figure 14. The material (TPX) with  $\epsilon_r = 2.13$  and very low loss is otherwise used for sub-mm wave lenses. For imaging, an axis of the cube passing through the centers of two opposing edges is being precessed. Again, in this range of orientations there is no specular reflection back to the radar. The side (x,z) view image appears outside of the borders of the target. This is due to the reduced propagation velocity and to the peculiar propagation inside the dielectric. The image consists of three separate zones, also evident in the top (x,y) view. One, smaller in extent but higher (not shown) in power is centered on the origin. The other two are equal to each other in size and symmetrically arranged around the centered one. The mechanisms responsible for the observed image have been tentatively identified as

higher order scattering and demonstrate the inability of an imaging algorithm assuming first order scattering such as ours to properly interpret the signals received.

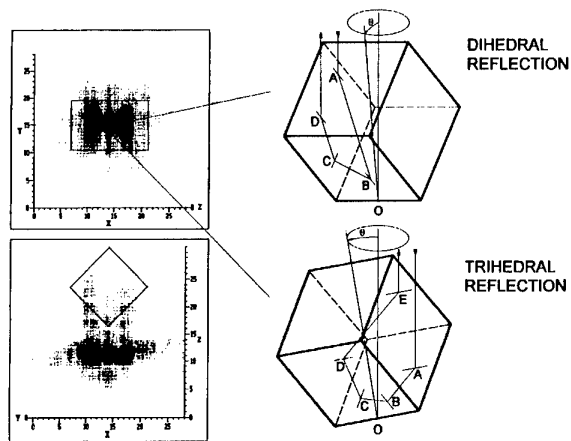


Fig. 14 3-D image of dielectric cube at 12.4-18.4 GHz due to higher order scattering

While in its precessional motion, the cube exposes two distinctive aspects to the radar. In the first one, with the cube's base edge normal to the radar direction, rays can only enter and exit through the sides forming the top edge of the cube. The upper sketch shows a ray entering at A and undergoing refraction inside the dielectric according to Snell's law. After reflection from two other sides at B and C, it leaves the dielectric at D, again after undergoing refraction. For the incoming and outgoing rays to be parallel, they have to be on the same side of the cube. The reversal at B and C is by dihedral reflection. Similar dihedral reflection occurs on the other side defining the top edge of the cube. This condition repeats twice during a precessional cycle. Rays that enter and exit on the same side exhibit a resultant phase shift. They make up the outer two zones of the image.

The second distinctive aspect of the cube, when its base edge is maximally tilted, exposes a trihedral to the radar as shown in the bottom sketch of Figure 14. Here, a ray entering at A is reflected at B, C and D after undergoing refraction. The refracted ray exiting at E is again parallel with the one entering at A. As is well known of trihedral reflection, rays enter and exit radially symmetric relative to the trihedral apex. Hence there is no phase shift from this signal which in turn images in the central zone. This condition also happens twice per precession cycle.

## 6. FUTURE WORK

Current system performance is satisfactory and measurements on a wide range of targets is in progress. Still, improvements in several areas are under consideration. These include true monostatic operation with a single radar antenna, beam collimation for a planer field and unfolding of the cm radar path. Polarimetric information in the radar signal deserves greater attention. Linear prediction techniques to enhance image resolution

have thus far been implemented in the frequency domain only. They will be extended to three dimensions within the constraints of available computational power. On one hand, the reradiation from many scatterers of interest is directive and polarization sensitive in nature. On the other hand, a wider range of precessional aspect angles increases image resolution and even allows 3-D imaging with a single frequency radar. We are therefore interested in generating scatter data over a wider range of aspect angles, also with the objective to better interpret higher order scattering phenomena.

## REFERENCES

1. Mensa, D. L., "High Resolution Radar Cross-Section Imaging", Artech House, Boston, 1991.
2. Lammers, U. H. W., Marr, R. A. and Morris, J. B., "A Coherent Mechanical Submillimeter Frequency Shifter", *Int. J. of IR and MM Waves*, 11, 3, 1990, pp 367-381.
3. Bucci, O. M., Genarelli, C. and Savarese, C., "Optimal Interpolation of Radiated Fields over a Sphere", *IEEE Trans. Antennas Propagation*, 39, 11, November 1991, pp 1633-1643.
4. Boerner, W.-M., El-Arini, M. B., Chan, C.-Y. and Matoris, P. M. "Polarization Dependence in Electromagnetic Inverse Problems", *IEEE Trans. Antennas Propagation*, 29, 2, March 1981, pp 262-270.

**Discussor's name:** R. KLEINMAN

**Comment/Question:**

How much data (in terms of aspect angle) was used in obtaining the images of the target?

**Author/Presenter's reply:**

A conical region with 20 degrees apex angle was generally used, however, for imaging strongly scattering targets we plan to use a much wider range in the future.

**Discussor's name:** J. SCHILLER

**Comment/Question:**

If I understood you correctly the targets are in a precession mode. That means, in your experiment the distances of the different scatterers on the target are changing nonlinearly in time, i.e. there must be a change in Doppler frequency. Doesn't this fact make computations rather complicated, i.e. don't you have to correct for this fact, at least for longer observation times (wider aspect range)?

**Author/Presenter's reply:**

Radar to scatterer distances do change non-linearly with time and our imaging algorithms account for this accurately, independent of aspect range. The computations are extensive, not necessarily complicated.

# Imaging 3D Structures from Limited-Angle Backscattered Data

D. A. Pommet, M. A. Fiddy, R.A. Marr<sup>\*</sup>, U. H. W. Lammers<sup>\*</sup> & J. B. Morris<sup>\*</sup>

Department of Electrical Engineering,  
University of Massachusetts-Lowell,  
Lowell, MA 01854

<sup>\*</sup> Rome Laboratory, Hanscom AFB, MA 01731

## 1. SUMMARY

We consider the problem of imaging strongly scattering, penetrable targets by inverting scattered field data. We describe a method to recover images of strongly scattering targets based on a modification of the well-known technique of diffraction tomography. It is a nonlinear (differential cepstral) filtering process. In order to overcome the problems associated with limited angular measurements of the scattered field, as described by Lammers and Marr in the preceding paper, we have to incorporate Fourier-based methods for spectral estimation. The advantages and difficulties associated with this new method are described.

## 2. INTRODUCTION

Imaging from scattered field data is traditionally referred to as diffraction tomography. This imaging method, which is Fourier inversion-based and yet mathematically rigorous, requires that the scattering objects be only weakly scattering, (e.g., based on the first-order Born or Rytov approximations). This severely limits their usefulness in practice.

Many advances have been made based on iterative techniques, for example, to extend the class of objects that can be imaged, with mixed success. We report on a new approach that can be applied when these weakly scattering approximations are not valid. The new technique is still a Fourier-based procedure, which incorporates a nonlinear filter. Most inversion techniques, including the one reported here, assume that scattered field data are available all around the object, for a set of incident field directions that circumscribe the object. Here we also consider the recovery of strongly scattering permittivity distributions from severely limited angular data, including backscattered data. This constraint occurs in many radar applications, both monostatic and bistatic, as well as in medical

imaging, remote sensing and non-destructive testing applications. Being Fourier-based, one can apply well known spectral estimation and noise handling algorithms when required.

One can compensate for limited angle and noisy data by incorporating some prior knowledge about the radar target, or the extent of the volume to which it is confined, into the inversion algorithm. The way in which this prior knowledge is incorporated is as a weighting function applied to a set of basis functions used to represent the restored image in a well-defined and optimal (i.e., minimum norm) sense. There is a trade-off that occurs between the number of available data points, the information content of the prior estimate used and the degree of regularization required to ensure a well-posed inversion algorithm. In the case of severely limited data, the approach lends itself to the estimation of a target signature, weighted to different prior estimates, in order to assign a classification to the target.

We consider these techniques for a radar system designed to study general scattering phenomena and to image scale model targets. Examples will be shown using simulated data from an exact model.

## 3. INVERSION METHOD

Diffraction tomography techniques can be formulated as straightforward Fourier inversion procedures [1]. The scattered field data under these conditions, based on the first-order Born and the Rytov approximations, are mapped onto the Ewald sphere in  $k$ -space and inverse Fourier transformed. This method of diffraction tomography is numerically attractive, but the approximations are rarely applicable in practice, thus limiting their usefulness.

Although more robust than the Born approximation, the Rytov approximation requires a nonlinear transformation of the data to be made prior to using an identical inversion step as that

performed when the Born approximation is valid. This nonlinear step requires that the logarithm of the scattered field measurements be taken. There are numerous problems in doing this when the magnitude of the scattered field is close to zero and when the phase of the scattered field has a range that exceeds  $2\pi$ . Phase unwrapping is exceedingly difficult, especially in two and higher dimensional problems, in which wavefront dislocations can naturally occur in large numbers, rendering the idea of a smoothly unwrapped phase meaningless. We return to this point later.

When the Born approximation is not valid, a Fourier-based method can still be exploited, and this is the key to the nonlinear filtering approach described here. The limitations of weak scattering and distorted wave inverse scattering methods can be overcome by recognizing that the image recovered using the Born approximation is distorted by the internal scattered field and can be filtered to recover the target structure. The method still expects multiple illumination directions to be employed with scattered field data being collected all around the target for each illumination direction. This is not the case in the imaging technique described in the previous paper.

#### 4. DIFFRACTION TOMOGRAPHY

We consider a scattering target having a permittivity  $\epsilon(\mathbf{r})$  which is embedded in a host or background medium of permittivity  $\epsilon_0$ , where  $\epsilon(\mathbf{r}) = \epsilon_0[1 + V(\mathbf{r})]$ . We assume that the target has a compact support  $D$  and that  $\epsilon_0$  is the free-space permittivity.  $V(\mathbf{r})$  is referred to as the target or object function, i.e., it represents  $\epsilon_r - 1$  and it is the quantity we wish to identify or image, if sufficient data are available. If the scattering target possesses cylindrical symmetry and the polarization of the incident time-harmonic electromagnetic wave is along the symmetric axis of the scattering object, the depolarization term in the vector wave equation can be neglected [1]. We assume the case of an incident plane wave  $\Psi_0(\mathbf{r}, k\hat{\mathbf{r}}_0) = e^{ik\hat{\mathbf{r}}_0 \cdot \mathbf{r}}$ , where  $k$  is the wavenumber, which can be variable if the illuminating frequency is swept. From the scalar Helmholtz

equation we can express the total field  $\Psi(\mathbf{r}, k\hat{\mathbf{r}}_0)$  in terms of an inhomogeneous Fredholm integral equation of the first kind, namely,

$$\begin{aligned} \Psi(\mathbf{r}, k\hat{\mathbf{r}}_0) &= \Psi_0(\mathbf{r}, k\hat{\mathbf{r}}_0) - \\ & k^2 \int_D d\mathbf{r}' G_0(\mathbf{r}, \mathbf{r}') V(\mathbf{r}') \Psi(\mathbf{r}', k\hat{\mathbf{r}}_0) \\ & = \Psi_0(\mathbf{r}, k\hat{\mathbf{r}}_0) + \Psi_s(\mathbf{r}, k\hat{\mathbf{r}}_0), \end{aligned} \quad (4.1)$$

where  $\Psi_s(\mathbf{r}, k\hat{\mathbf{r}}_0)$  is the scattered field resulting from the interaction of the incident wave  $\Psi_0(\mathbf{r}, k\hat{\mathbf{r}}_0)$  with the scattering target distribution  $V(\mathbf{r})$ ,  $G_0(\mathbf{r}, \mathbf{r}')$  is the free-space Green's function, and  $\hat{\mathbf{r}}_0$  denotes the direction of illumination.

The integration in eq. (4.1) is over the support of  $V(\mathbf{r})$  defined by  $D$ . Using the far-field approximation for the outgoing spherical wave  $G_0(\mathbf{r}, \mathbf{r}')$ , we obtain

$$\Psi_s(\mathbf{r}, k\hat{\mathbf{r}}_0) = k^2 \frac{e^{ikr}}{4\pi r} \int_D d\mathbf{r}' e^{-ik\hat{\mathbf{r}} \cdot \mathbf{r}'} V(\mathbf{r}') \Psi(\mathbf{r}', k\hat{\mathbf{r}}_0) \quad (4.2)$$

When adopting the first Born approximation, the total field (or internal field)  $\Psi(\mathbf{r}, k\hat{\mathbf{r}}_0)$  is replaced with the known incident field  $\Psi_0(\mathbf{r}, k\hat{\mathbf{r}}_0)$  in the above integral [2]. This approximation is valid when  $k|\epsilon_r - 1|a < \pi/2$ , which, as stated earlier, is not valid for most problems of interest. The parameter  $a$  is the characteristic dimension of the object, and as  $a$  increases or the magnitude of the permittivity fluctuations increases, the first Born approximation becomes increasingly poor. The Born approximation improves, however, by increasing the wavelength of the illumination, but this in turn degrades the resolution of the resulting image as will be evident below.

Equation (4.2) may be written

$$\Psi_s(\mathbf{r}, k\hat{\mathbf{r}}_0) = k^2 \frac{e^{ikr}}{4\pi r} f(k\hat{\mathbf{r}}, k\hat{\mathbf{r}}_0), \quad (4.3)$$

where  $f(k\hat{\mathbf{r}}, k\hat{\mathbf{r}}_0)$  is the scattering amplitude which is defined as

$$f(k\hat{\mathbf{r}}, k\hat{\mathbf{r}}_0) \equiv \int_D d\mathbf{r}' e^{-ik\hat{\mathbf{r}} \cdot \mathbf{r}'} V(\mathbf{r}') \Psi(\mathbf{r}', k\hat{\mathbf{r}}_0). \quad (4.4)$$

In the first Born approximation, the relationship between the (complex) scattering amplitude and the scattering function  $V(\mathbf{r})$  becomes a Fourier transformation, namely,

$$f^{BA}(k\hat{\mathbf{r}}, k\hat{\mathbf{r}}_0) = \int_D d\mathbf{r}' e^{-ik\hat{\mathbf{r}} \cdot \mathbf{r}'} V(\mathbf{r}') e^{ik\hat{\mathbf{r}}_0 \cdot \mathbf{r}'} \quad (4.5)$$

One can calculate and estimate  $V(\mathbf{r})$  by performing an inverse Fourier transformation on the measured far-field scattering amplitude data,  $f^{BA}(k\hat{\mathbf{r}}, k\hat{\mathbf{r}}_0)$ . These data are related to the object distribution by Fourier transformation when the scattering amplitude data are located on the Ewald sphere in  $k$ -space, a locus of points tangent to the  $k$ -space origin and of radius  $k$ . Inverse Fourier transforming these data is formally equivalent to backpropagating the scattered field into the object domain from the measurement space.

Since the scattered field data are mapped into  $k$ -space on circles of radius  $k$ ; forward scattered data maps close to the  $k$ -space origin

while backscattered data are located furthest from the origin giving high spatial frequency information about the target. As  $k$  increases, one can expect that higher spatial frequency information about the target can be recovered. Any inversion necessarily results from limited  $k$ -space coverage and it is to be expected that the image artifacts that result will depend on how uniformly the data cover  $k$ -space and the signal to noise ratio.

When the Born approximation is not valid, this Fourier relationship can still be exploited and this is the key to the novel nonlinear filtering approach we describe. One can readily see that inverting the scattering amplitude data determines not  $V(\mathbf{r})$ , but rather the function  $V_B(\mathbf{r}, k\hat{\mathbf{r}}_0)$  [3], given by

$$V_B(\mathbf{r}, k\hat{\mathbf{r}}_0) \approx V(\mathbf{r}) \frac{\Psi(\mathbf{r}, k\hat{\mathbf{r}}_0)}{\Psi_0(\mathbf{r}, k\hat{\mathbf{r}}_0)} \quad (4.6)$$

The symbol  $\approx$  in the above equation recognizes the fact that the reconstruction is approximate since the Fourier transformation can only be taken for each  $\hat{\mathbf{r}}_0 = \text{constant}$ , and limited  $k$ -space coverage will limit accuracy. The total field can be expressed by

$$\Psi(\mathbf{r}, k\hat{\mathbf{r}}_0) = \Psi_0(\mathbf{r}, k\hat{\mathbf{r}}_0) -$$

$$k^2 \int_D d\mathbf{r}' G_0(\mathbf{r}, \mathbf{r}') V(\mathbf{r}') \frac{\Psi(\mathbf{r}', k\hat{\mathbf{r}}_0)}{\Psi_0(\mathbf{r}', k\hat{\mathbf{r}}_0)} \Psi_0(\mathbf{r}', k\hat{\mathbf{r}}_0), \quad (4.7)$$

for the case of a general scattering object, and one can write the Fourier relation

$$f(k\hat{\beta}, k\hat{\alpha}) = \int_D d\mathbf{r}' e^{-ik(\hat{\beta}-\hat{\alpha})\cdot\mathbf{r}'} V(\mathbf{r}') \frac{\Psi(\mathbf{r}', k\hat{\alpha})}{\Psi_0(\mathbf{r}', k\hat{\alpha})} \quad (4.8)$$

Consequently, a first Born inversion of the

scattered field data for  $\hat{\mathbf{r}}_0 = \text{constant}$ , generates a filtered estimate of  $V(\mathbf{r}) \Psi(\mathbf{r}, k\hat{\mathbf{r}}_0) / \Psi_0(\mathbf{r}, k\hat{\mathbf{r}}_0)$  from which one can estimate  $V(\mathbf{r})$  directly, since it is assumed that

$$\Psi(\mathbf{r}, k\hat{\mathbf{r}}_0) \approx \Psi_0(\mathbf{r}, k\hat{\mathbf{r}}_0) \quad (4.9)$$

$\Psi(\mathbf{r}, k\hat{\mathbf{r}}_0)$  is the field within the scattering volume  $D$  and cannot be assumed to be equal to the incident field. It is explicitly dependent on the direction of the incident plane wave, which is known, and so for each illumination direction used, one obtains an "image" of the function  $V(\mathbf{r}) \Psi(\mathbf{r}, k\hat{\mathbf{r}}_0)$ . Given data from many illumination directions, a set of these "images" can be generated, one for each illumination direction, and in which  $V$  is common to each one of them but  $\Psi$  is different. The recovery of an image of  $V$  can therefore be formulated as a problem in which an ensemble of noisy images of  $V$  require processing, the "noise" being multiplicative in nature.

## 5. HOMOMORPHIC FILTERING

For each direction of the illuminating radiation, the product  $V(\mathbf{r}) \Psi(\mathbf{r}, k\hat{\mathbf{r}}_0)$  will change, and a set of these single-view backpropagated reconstructions can be generated. We regard the term  $\Psi(\mathbf{r}, k\hat{\mathbf{r}}_0)$  as an unwanted factor or multiplicative noise term, which contains a certain range of spatial frequencies determined by the distribution of energy in the radiation field and its effective wavelength within the object. With respect to the spatial frequency content of the scattering object, this *multiplicative* factor can be removed by homomorphic filtering techniques [4-6]. Band-pass filtering is not appropriate to separate multiplied functions of this kind since their spectra are convolutions.

One can speculate on the nature of this internal field. For a weakly scattering target, the internal field approximately equals the incident field and will have a characteristic spatial frequency in the direction of propagation since plane wave illumination is assumed. As the degree of scattering increases, the internal field will become increasingly complex in all directions, but will retain a characteristic correlation length or minimum scale determined by the wavelength of the radiation in the medium  $V(\mathbf{r})$ . As the mean permittivity of the penetrable target increases, the mean effective wavelength in the scatterer

decreases. Thus, there will be some characteristic set of spatial frequencies associated with  $\Psi(\mathbf{r}, k\hat{\mathbf{r}}_0)$  inside the target. The backpropagated scattered field can be filtered in the *cepstral* domain since the spatial frequency content of  $\Psi(\mathbf{r}, k\hat{\mathbf{r}}_0)$  will be concentrated around some limited range of spatial frequencies.

The cepstral filtering inversion approach is as follows: taking the logarithm of  $V(\mathbf{r})\Psi(\mathbf{r}, k\hat{\mathbf{r}}_0)$  changes the multiplicative relationship between  $V$  and  $\Psi$  into an additive one. This then permits linear filtering techniques to be applied to the spectrum of  $\log[V(\mathbf{r})\Psi(\mathbf{r}, k\hat{\mathbf{r}}_0)]$  to remove, or at least minimize, the effect of  $\Psi$ . The spectrum of  $\log[V(\mathbf{r})\Psi(\mathbf{r}, k\hat{\mathbf{r}}_0)]$  is referred to as the cepstrum of  $V(\mathbf{r})\Psi(\mathbf{r}, k\hat{\mathbf{r}}_0)$  [7]. This operation will modify the spatial frequency content of  $V$  over the same spectral region as that of the removed  $\Psi$ , but a second data set gathered from a different illumination wavelength will remedy this.

In practice there are difficulties associated with taking the logarithm of the product  $V(\mathbf{r})\Psi(\mathbf{r}, k\hat{\mathbf{r}}_0)$  because the phase of  $\log[V(\mathbf{r})\Psi(\mathbf{r}, k\hat{\mathbf{r}}_0)]$  can be highly discontinuous if the phase delay incurred on propagation through the object exceeds  $2\pi$  radians. The first Born approximation assumes that this phase delay is much less than  $\pi$ . The phase function will therefore be wrapped into  $[-\pi, \pi]$  and abrupt discontinuities in this phase function generate unwanted harmonics in the cepstrum, making it difficult to filter correctly. A solution to this problem that avoids phase wrapping difficulties, is to make use of the differential cepstrum [8].

After summing the partial derivatives of  $\log[V(\mathbf{r})\Psi(\mathbf{r}, k\hat{\mathbf{r}}_0)]$ , we obtain an expression defined by the quantity  $S$

$$S = \frac{1}{V\Psi} \left[ \frac{\partial(V\Psi)}{\partial x} + \frac{\partial(V\Psi)}{\partial y} \right] \quad (5.1)$$

where  $\mathbf{r} = (x, y)$  in two dimensional problems. Only derivatives of  $V(\mathbf{r})\Psi(\mathbf{r}, k\hat{\mathbf{r}}_0)$  need be calculated, which can be easily done using a property of the Fourier transform, and the phase wrapping problem is removed. A drawback in doing so is that the dc level of the function  $V(\mathbf{r})\Psi(\mathbf{r}, k\hat{\mathbf{r}}_0)$  is also lost. This can be estimated from forward and

backscattered data values however. One can define the differential cepstrum as the logarithmic derivative with respect to either  $x$  or  $y$  if one wishes to avoid only the phase ambiguity [4]; it is not necessary to form the derivative with respect to both spatial variables.

The sequence of steps required for this algorithm is shown in Figure 1

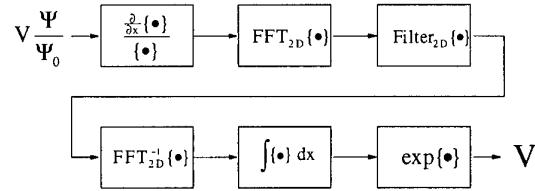


Figure 1: Differential cepstral filtering.

There is an ill-conditioning problem that arises when  $V(\mathbf{r})\Psi(\mathbf{r}, k\hat{\mathbf{r}}_0)$  takes on small values. This can be overcome by multiplying both the numerator and the denominator of  $S$  by  $[V(\mathbf{r})\Psi(\mathbf{r}, k\hat{\mathbf{r}}_0)]^*$  (where  $*$  represents complex conjugate) and then adding a small positive regularization parameter to  $|V(\mathbf{r})\Psi(\mathbf{r}, k\hat{\mathbf{r}}_0)|^2$ . The dominant contribution of  $\Psi(\mathbf{r}, k\hat{\mathbf{r}}_0)$  in the differential cepstrum is from the fundamental spatial frequency component present.

In Figure 2, we illustrate the reconstruction of a simple cylinder with the permittivities shown on the left, namely, an  $\epsilon$  of 4.0 in the central region and 2.0 in the outer annulus. The free space wavelength used was 3.0cm and the outer radius of the cylinder was 9.9cm. The exact expression for the field scattered from these concentric cylinders was calculated and used as data to check the inversion step. The differential cepstrum of the backpropagated field for one illumination direction was low-pass filtered. As can be seen the basic features of the original object are evident and the regions have amplitudes proportional to the original permittivity differences.

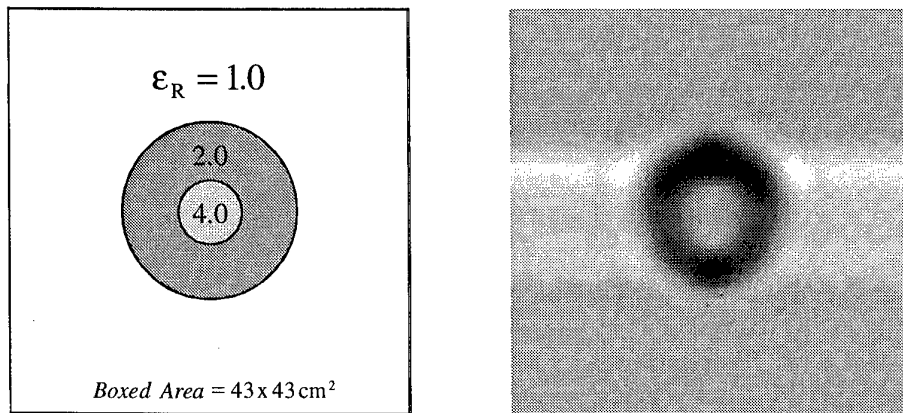


Figure 2: Differential cepstral filtering.

## 6. LIMITED K-SPACE DATA

Many important imaging techniques are based on measuring backscattered radiation. Several inverse synthetic aperture (ISAR) systems, for example, have been developed with the objective of extracting a maximum amount of information about complex targets, just from backscattered signals. Common to these methods is a stationary radar and a target whose radar aspect is varied in some specified way. In this case, an arbitrary target axis intersects the radar beam axis, making

an angle  $\theta$  with it. As the target axis precesses around the beam axis its motion is similar to a precessing top. Varying  $\theta$  between 0 and values on the order of 10 degrees yields k-space data on a spherical cap with nearly constant polarization illumination and nearly aspect-independent return levels from specular scatterers. Examples of the extent of data coverage in k-space is shown in Figure 3 below, for both the two and three dimensional cases.

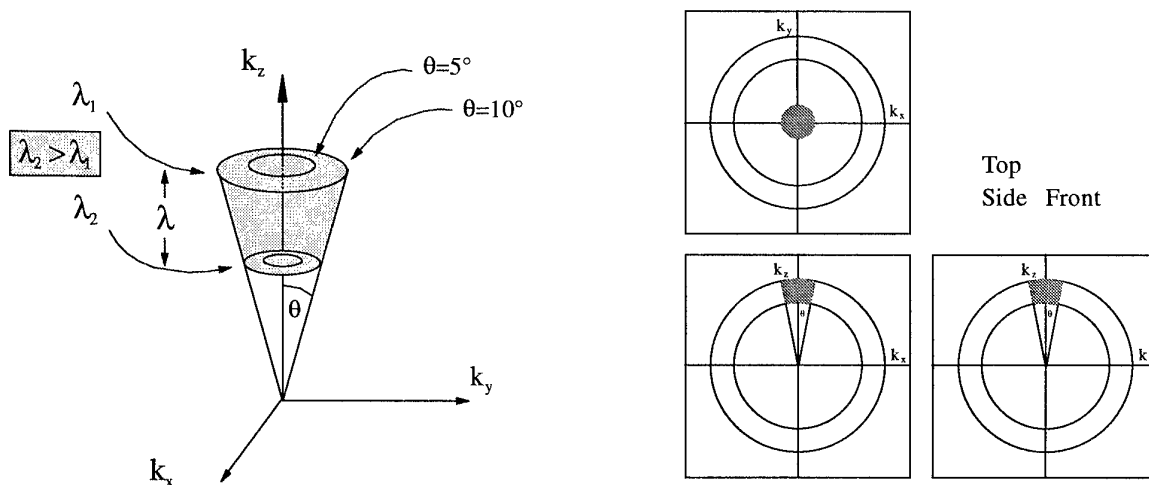
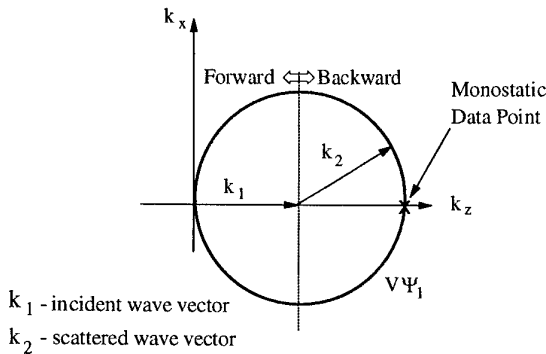


Figure 3: Limited data in 3-d k-space and corresponding 2-d projection coverage.

This imaging technique has proved to be very effective for metallic targets, as demonstrated in the previous paper by Lammers and Marr. The method provides uniform resolution in  $x, y$  and  $z$  by essentially correlating the  $k$ -space data with the anticipated scattering pattern from point targets within the target volume. For this reason, the method works very well with targets having strong point scattering centers and glints, as well as weakly scattering (i.e., first Born approximate) penetrable targets. From this perspective, one can see that removal of the incident field from the backscattered field data is equivalent to translating the  $k$ -space data to the  $k$ -origin, allowing a simple 3D Fourier inversion to also provide an image.

Once an image is formed, one cannot use this to represent the same  $V\Psi$  to which we refer above. The correlation method of forming the image makes this clear. Since the imaging facility is a monostatic radar, each data point measured upon illumination of the target, represents the value of  $V\Psi$  at a point farthest from the  $k$ -space origin, but on Ewald sphere whose radius is determined by the wavenumber and whose center is at a location determined by the angle of illumination, Figure 4. These are the raw data with which we must work.



**Figure 4: Monostatic data on the Ewald sphere.**  
Each monostatic data point corresponds to a different  $\Psi_n$ .

For strongly scattering penetrable targets, we need to work directly with the  $k$ -space data, which represents a small conical distribution of data in one quadrant of the  $k$  domain (Figure 3.). One could make use of the projection slice theorem and project this  $k$ -space data in  $k_x, k_y$  and  $k_z$  onto the  $k_x k_y$  plane and invert this. This corresponds to data on the 3D function  $V\Psi$  in just the  $x, y$  plane. In this way we may reduce the problem to effectively a 2D problem in order to simplify the

reconstruction step. This has some limitations, however, since strictly speaking the projection of  $k$ -space data onto the  $k_x k_y$  plane requires the  $k$  domain to be filled with data. If we assume that the data around the  $k$  origin are missing, as are the data in the opposite  $k$  half space (Figure 5),

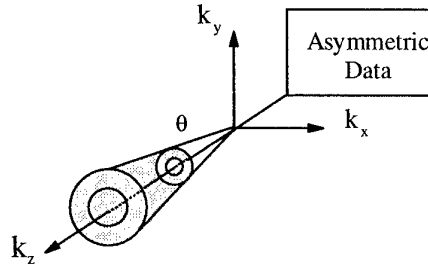


**Figure 5: Asymmetric k-space data.**

then the projection obtained on the  $k_x k_y$  plane is high-pass filtered and would lead to information in the  $x, y$  plane on  $V\Psi + i \text{HT}\{V\Psi\}$ , where  $\text{HT}$  denotes the Hilbert transformation. One must therefore be careful to apply the cepstral filter to the correct function in order to recover an estimate of  $V$ .

An alternative to this is to extrapolate the limited  $k$ -space data into the entire  $k$  domain. A method that can do this, based on a prior estimate of the target is described next.

### 7. PDFT FOR SPECTRAL EXTRAPOLATION

The reconstruction of an image from this limited  $k$ -space coverage results in considerable distortion of the image. The available data comprise a truncated conical region in  $k$ -space of angular extent  $2\theta$  with co- and cross-polarization information over the full angular range of  $2\pi$ .

Let us assume that there is a prior estimate of the target, for example, an image or signature of what it could possibly be, or of the domain in which it should be confined, i.e., a support estimate. The following spectral estimation procedure exploits this prior knowledge when only limited  $k$ -space data are acquired. It takes a prior estimate,  $P(\mathbf{r})$ , of the broad features of  $V(\mathbf{r})$ , e.g.,  $V_1(\mathbf{r})$ , and a set of equations of the form, expressed in 1D for convenience, [9-11]:

$$f(m) = \sum_{n=-N}^N a_n p(m-n) ; \quad m = -N, \dots, N \quad (7.1)$$

The values  $p(m)$  ( $m = -N, \dots, N$ ) are taken from the discretized Fourier transform of  $P(r)$ , and the scattering amplitude data are represented by  $f(m)$  ( $m = -N, \dots, N$ ). Inversion of a matrix with elements derived from  $p(m)$  allows one to solve for the coefficients  $a_n$  ( $n = -N, \dots, N$ ). In principle, the data,  $f(m)$ , need not be uniformly sampled, which means that this approach can be used to interpolate and extrapolate both nonuniformly sampled and incomplete data sets. Obtaining the coefficients,  $a_n$  allows one to define an estimator that minimizes the approximation error given by:

$$\int_{-\pi}^{\pi} dr \frac{1}{P(r)} \left| V(r) - P(r) \sum_{n=-N}^N a_n e^{inr} \right|^2 \quad (7.2)$$

The resulting estimator of  $V(r)$  is termed the PDFFT estimator because of its form, namely,  $\text{PDFFT}(r) = P(r)A(r)$ , where  $A(r)$  is the trigonometric polynomial with coefficients,  $a_n$ , i.e., we have

$$\text{PDFFT}(r) = P(r) \sum_{n=-N}^N a_n e^{inr} \quad (7.3)$$

If no prior knowledge is available,  $P(r)$  is a constant and the estimator reduces to the DFT of the available Fourier data. In other words, if the prior estimate,  $P(r)$ , is a constant for  $\pi r^2$ , then  $a_n = f(n)$  and the PDFFT reduces to the discrete Fourier transform (DFT) estimator. This PDFFT estimator is both continuous and data consistent, and the algorithm is easily extended to the two- or higher-dimensional case.

This estimation technique is easily regularized in the presence of noise. To do this one can either modify the prior estimate,  $P(r)$ , to take a small value outside the anticipated support of the scatterer,  $V(r)$ , or one can add a small positive constant to the diagonal of the matrix,  $p$ . These can be shown to be equivalent to a Miller-Tikhonov regularization process. The algorithm is computationally intensive because it requires the solution of a large set of linear equations. For  $2M$  by  $2M$  uniformly sampled scattered field data, one must invert a  $2M$  by  $2M$  matrix if the prior estimate,  $P(r)$ , can be expressed as a separable function; otherwise, a  $(2M)^2$  by  $(2M)^2$  matrix must

be inverted. For many targets, a simple 2D or 3D prior estimate that is separable is also quite ineffective if the target is only loosely confined by the prior. The *tighter* the prior estimate and the more oversampled the  $k$ -space data, the more effective the PDFFT is.

## 8. CONCLUSIONS

We have described a method of processing backpropagated scattered field data collected from either monostatic or bistatic systems. Two problems are addressed. The first is to provide a method for the interpretation of these scattering data when the target is penetrable and strongly scattering. The differential cepstral filtering approach allows direct inversion of scattered field data to recover an estimate of the target structure. It does not rely on linearizing methods based on the Born, Rytov, or their associated distorted-wave approximations.

The filtering step has not yet been optimized, but in all cases studied to date, the spatial frequency content of  $\Psi$  has been higher than that of the scattering object, and a simple low-pass filter employed [12]. This filter will necessarily result in some loss of information about the target at these frequencies. On-going work involves processing more data, especially that obtained from experiments using non-symmetric targets. Computational difficulties have been encountered using this method, and work continues to try to resolve them. On occasions the filtering step is unsuccessful and indications are that this occurs when the estimates of  $V\Psi$  are not adequately sampled. Also, for penetrable targets with a high permittivity, it is better to first estimate the scattered field at the boundary of  $V$  and then compute *new* far field data, assuming the intervening medium is no longer free space but is a homogeneous medium having the same mean permittivity as expected of  $V$ . This provides a better estimate of  $V\Psi$  to filter.

The second problem was that of having only a portion of  $k$ -space containing measured data. One can reduce the 3D problem to a 2D one by employing the projection slice theorem to provide a function of  $V\Psi$  on which to operate the differential cepstral filter. An alternative to this is to extrapolate the data in  $k$ -space, to provide more uniform coverage, by employing the PDFFT

algorithm. This requires some *a priori* knowledge of the target to be effective. An estimate of the approximate size and/or shape of the target will normally suffice. However, if the PDFT is increasingly ineffective the poorer this prior estimate is to the actual target. If one has a set of possible targets that the data could have been generated from, use of this set provides a mechanism for determining which prior estimate is most consistent with the data, thereby providing a target recognition capability, even if the associated image is poor [9,13].

The inversion method described can also be used as a powerful technique for the *design* of low cross section targets. Inverse scattering algorithms can be used both for imaging when scattered field data are measured and for target synthesis when scattered field behavior is specified. Also, for multiply scattering targets situated in a random background or buried beneath penetrable layers, the PDFT method, combined with the DCF, provides a good target discriminator.

## 9. ACKNOWLEDGEMENTS

MAF and DAP acknowledge the support of ONR Grant N00014-89-J-1158 and Department of the Air Force contract F19628-95-C-0035.

## 10. REFERENCES

- [1] F. C. Lin and M. A. Fiddy, "Image estimation from scattered field data," *Int. J. Imaging Systems and Technology*, 2, 76-95, 1990.
- [2] E. Wolf, "Three-dimensional structure determination of semi-transparent objects from holographic data," *Optics Comm.*, 1, 153, 1969.
- [3] M. Slaney, A.C. Kak and L.E. Larsen, "Limitations of imaging with first-order diffraction tomography," *IEEE Trans Microwave Theory and Techniques MTT-32*, 860, 1984.
- [4] D. Raghuramireddy and R. Unbehauen, "The two-dimensional differential cepstrum," *IEEE Trans. Acoustics, Speech and signal Processing, ASSP-33*, 1335, 1985.
- [5] W. K. Pratt, *Digital Image Processing*, John Wiley & Sons, New York, 1978.
- [6] R. C. Gonzalez and P. Wintz, *Digital Image Processing*, Addison-Wesley Publishing Co., Reading, Massachusetts, 1977.
- [7] A. V. Oppenheim and R. W. Schaffer, *Digital Signal Processing*, Prentice Hall, Englewood Cliffs, New Jersey, 1975.
- [8] H. Rossmannith and R. Unbehauen, "Formulas for computation of 2-D logarithmic and 2-D differential cepstrum," *Signal Processing*, 16, 209-217, 1989.
- [9] C.L. Byrne and M. A. Fiddy, "Estimation of Continuous Object Distribution from Limited Fourier Magnitude Data." *Journal of the Optical Society of America*, A4, pp. 112-117, 1987.
- [10] C. L. Byrne, R. L. Fitzgerald, M. A. Fiddy, T. J. Hall, and A. M. Darling, "Image restoration and resolution enhancement," *J. Opt. Soc. Am.* 73, 1481-1487, 1983.
- [11] C. L. Byrne and M. A. Fiddy, "Images as power spectra; reconstruction as a Wiener filter approximation," *Inverse Problems*, 4, 399-409, 1988.
- [12] Morris, J.B., M. A. Fiddy and D. A. Pommert, "Nonlinear filtering applied to single-view backpropagated images of strong scatterers," *Opt. Soc. of Amer. A*, 13, July 1996.
- [13] Chen, P-T, M. A. Fiddy, C-W. Liao and D. A. Pommert, "Blind deconvolution and phase retrieval using point zeros," *Opt. Soc. of Amer. A*, 13, July 1996.

**Discussor's name:** A. BICCI

**Comment/Question:**

Could you let me have details concerning the operations performed to pass from backpropagated images to the final images and is this step just an addition?

**Author/Presenter's reply:**

For the case of weakly scattering targets, it is usual to backpropagate the scattered field produced for each incident illumination direction, into the image domain. These field patterns are then coherently summed in the image domain, each backpropagated image being correctly oriented with respect to the incident field directions. Since the backpropagated field represents the scattering potential,  $V(r)$  multiplied by the quotient of the field within  $V(r)$  and the incident field, the backpropagated field provides a good rendition of  $V(r)$ , provided the internal field is well approximated by the incident field. The latter is only the case when the first Born approximation is valid, which corresponds to the case of very weak scattering. For stronger scattering, our proposed differential cepstral filtering technique is applied to each backpropagated field, in order to acquire an estimate of  $V(r)$  from this product. Once an estimate of  $V(r)$  is found for each incident field direction, all of the estimates are then coherently summed to provide the final estimate for  $V(r)$ .

## Reconnaissance Automatique des Cibles Détectées par le Radar de Surveillance SCB2130A

M.C. Pirlot

Major Ingénieur du Matériel Militaire  
Ecole Royale Militaire  
Chaire Armement et Balistique  
Avenue de la Renaissance, 30  
B-1000 Bruxelles  
Belgique

### 1. SOMMAIRE

Cet article décrit les phases essentielles de l'étude de faisabilité relative à la reconnaissance automatique des cibles détectées par le radar de surveillance du champ de bataille SCB2130A.

Cet appareillage de haute technologie équipe l'escadron de reconnaissance le 2 Ch Ch (Deuxième Chasseurs à Cheval). La mission de cette unité est bien évidemment la surveillance du champ de bataille.

En effet, le radar permet de détecter des cibles en mouvement. Les opérateurs du 2 Ch Ch peuvent, avec leur matériel, repérer et localiser des véhicules divers (chars, véhicules blindés transporteurs de troupes, véhicules à roues, etc. ...) mais aussi des cibles plus petites comme un homme isolé.

Cette information est bien utile; cependant, il serait souhaitable de pouvoir reconnaître les cibles détectées. A cette fin la signature Doppler des cibles est rendue audible. L'utilisateur devrait, en écoutant "attentivement" ce son, différencier par exemple, le char de combat du véhicule à roues.

Le but de la reconnaissance automatique d'objectifs (RAO) est la réalisation d'une interface intelligente entre le radar SCB 2130A et l'utilisateur.

La solution proposée, en phase de faisabilité, s'appuie sur la théorie générale de la classification et l'emploi de réseaux neuromimétiques.

### 2. CLASSIFICATION

#### 2.1. Modèle de classification

Il s'agit d'un problème de classification. La classification d'objets peut être représentée à l'aide du schéma fonctionnel repris à la figure 1 [Réf.1]:

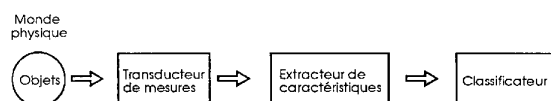


Figure 1 : Schéma fonctionnel de la classification

L'action de classification d'objets est décomposable en trois phases. La perception des objets à l'aide d'un transducteur de mesures précède l'extraction de caractéristiques qui est suivie de la classification proprement dite.

La séparation des phases d'extraction de caractéristiques et de classification proprement dite n'est pas toujours indispensable.

Il faut d'ailleurs remarquer que le schéma fonctionnel proposé (figure 1) est une modélisation qui propose une segmentation arbitraire des actions aboutissant à la classification.

Il serait tout à fait déplacé de réduire le comportement humain au schéma fonctionnel présenté. La solution naturelle est beaucoup plus complexe et notre méconnaissance actuelle tient autant à la fusion des trois phases qu'à l'aspect "inconscient" de l'exécution naturelle. Mais le modèle décrit peut aider lors de la résolution de certains problèmes de classification.

Dans sa version actuelle, le radar SCB remplit la fonction de transducteur de mesures. Il permet à son utilisateur de percevoir son environnement d'une manière particulière.

#### 2.2. Reconnaissance automatique d'objectifs (RAO)

Le but de la RAO est de prolonger la fonction transducteur de mesures par l'extraction des caractéristiques qui doivent permettre la classification des cibles détectées.

La confrontation des points de vue des utilisateurs aux possibilités a permis de dresser les caractéristiques principales de la RAO (en phase faisabilité):

- la RAO doit assister l'opérateur dans la reconnaissance (classification) des objectifs détectés. Le but ultime est la prise en charge totale de la classification par le système. Une assistance moins poussée qui consisterait à aider l'opérateur dans le processus de prise de décision serait déjà "acceptable".

- le temps de réponse du classificateur ne devrait pas dépasser quelques secondes.

- dans un premier temps, il sera fait usage de la signature Doppler des cibles à l'exclusion de tout autre source d'information. Cette limitation intentionnelle écarte actuellement les renseignements provenant de l'écran comme les positions relatives des cibles, l'itinéraire suivi etc. La situation tactique particulière connue par l'opérateur ne sera pas exploitée. Il en va de même pour les limitations physiques telle que la vitesse maximale possible pour un type de cible.

L'emploi d'un système expert n'est donc pas envisagé, du moins dans un premier temps.

#### 2.3. Méthode de travail

La méthode de travail retenue pour l'étude de faisabilité découle directement du fonctionnement du classificateur, exposé au préalable. Trois opérations successives doivent aboutir à la classification visée.

La première phase est celle de l'acquisition des signatures Doppler, de cibles connues, dans des circonstances expérimentales bien définies. La deuxième opération consiste à

extraire les caractéristiques de ces signatures. Finalement, la classification doit avoir lieu en utilisant ces caractéristiques.

Le rythme dicté par les contraintes pratiques pendant l'acquisition (cfr. infra) impose une séparation temporelle nette entre les campagnes de mesures et le dépouillement de celles-ci.

L'ampleur des préparatifs et le coût élevé des campagnes de mesures interdisent une démarche caractérisée par une alternance rapide des périodes d'essais et des exploitations.

### 3. MESURES

#### 3.1. Signal audio

Les caractéristiques du signal audio (signature Doppler) déterminent les exigences de la chaîne de mesures.

Les spécifications précises et la nomenclature de l'appareillage ne seront pas détaillées. Seules les grandes lignes sont reprises ici.

La bande passante du signal audio est comprise entre 0-2000 Hertz. Un filtre de garde (passe-bas) est placé entre la sortie du radar et l'enregistreur pour éviter tout dépassement en fréquence ou interférence avec d'autres signaux.

Les essais de validation du SCB ont montré qu'il faut acquérir le signal audio à la sortie de l'émetteur-récepteur et non au niveau du haut-parleur. Cette précaution supprime l'effet de l'amplificateur placé en aval du haut-parleur.

L'expérience montre que l'opérateur, libre de choisir le niveau d'amplification, a tendance à exagérer au point que le signal utile du haut-parleur est souvent saturé.

L'enregistrement analogique des signatures Doppler a été effectué à l'aide d'un enregistreur à bande magnétique. Il a été fait usage d'un modulateur de fréquence afin de garantir la qualité et la fidélité des enregistrements aux basses fréquences.

Un second canal de mesures, banalisé celui-là, a été utilisé pour commenter oralement et en parallèle les prises de mesures.

#### 3.2. Contraintes pratiques

A côté des contraintes précitées des limitations d'ordre pratique existent.

Il faut en effet avoir à sa disposition :

- un transducteur de mesures, c'est-à-dire un exemplaire du radar SCB 2130A accompagné d'opérateurs du 2 Ch Ch.
- des cibles (objectifs) réalistes : idéalement des véhicules militaires faisant partie de la menace potentielle. Pour des raisons évidentes, nous nous sommes limités aux véhicules militaires belges.
- un terrain de manoeuvre militaire permettant la mise en oeuvre de véhicules chenillés et l'interdiction de passage dans la zone de mesures.

Ces trois exigences déterminent le rythme de l'étude. Il a été nécessaire de grouper les essais d'enregistrement des signatures Doppler en campagnes.

Ces périodes réservées exclusivement à l'acquisition sont suivies d'une phase de dépouillement. Les résultats de cette exploitation permettent d'établir les spécifications pour la prochaine campagne de mesures.

#### 3.3. Enseignements

Les principaux enseignements sont repris ci-après. Ils ont été relevés dans le cadre des projets de la RAO mais certains sont valables pour l'emploi opérationnel du système.

#### a. Mise en batterie

La mise en batterie n'est pas toujours rapide. Par mauvaise visibilité et lorsque la distance de détection s'accroît, les difficultés apparaissent. Elles sont comparables à celles rencontrées par les artilleurs : détermination du point de station et d'une direction de référence.

#### b. Conditions météorologiques

Par temps de pluie les performances du radar sont réduites. L'opérateur peut monter un polariseur sur le cornet d'émission de l'antenne pour diminuer l'effet néfaste des précipitations. Cette parade, qui consiste à changer la polarisation du rayonnement est bien connue des radaristes [Réf.2].

Le vent peut aussi perturber le bon fonctionnement du radar. Une cible isolée et la même cible entourée d'une végétation agitée par le vent ne présentent pas du tout les mêmes signatures Doppler. Plus le vent est fort, plus le fouillis correspondant est important et il n'y a pas de remède direct pour annihiler ce phénomène.

#### c. Nature du sol

Un véhicule chenillé en progression dans un terrain lourd peut, par la projection de boue, augmenter considérablement le bruit de sa signature Doppler. Chaque motte de terre en mouvement fournit sa contribution, aussi modeste soit elle, à l'élaboration de l'écho cible.

#### d. Suivi manuel

Il incombe à l'opérateur de poursuivre la cible en mouvement. La précision et la continuité de cette opération manuelle influent aussi sur la signature d'une cible. Un opérateur nerveux qui balaye constamment son objectif en le perdant régulièrement fournira un signal beaucoup plus accidenté qu'un opérateur calme et expérimenté qui parvient à anticiper les mouvements de la cible.

#### e. Coût des essais

Le coût élevé des séances doit nous inciter à réduire au strict minimum les essais dévolus exclusivement au projet RAO. Dès que possible il faut tenter de profiter des manoeuvres militaires en utilisant des observateurs avancés pour fournir les informations indispensables à l'identification correcte des enregistrements.

#### f. Paramètres

La signature Doppler d'un véhicule dans un environnement bien déterminé varie en fonction des paramètres de fonctionnement du radar. Il est hors de propos de reprendre ici toutes les possibilités offertes à l'opérateur et nous nous bornerons à signaler qu'il faut rester attentif et veiller à assurer la continuité d'une campagne à l'autre.

#### g. Validation des signatures Doppler

Plutôt que d'enregistrer en continu le signal provenant du radar, nous avons sélectionné les passages utiles. Les critères de sélection sont au nombre de trois.

Le premier est tout naturellement l'avis de l'opérateur radar. Un utilisateur entraîné peut distinguer la signature Doppler d'une cible du bruit de fond.

Un deuxième moyen de validation est l'emploi d'un oscilloscope classique. Il permet de visualiser les signaux candidats à l'enregistrement.

Enfin, nous avons utilisé un analyseur de spectre qui fournit la représentation spectrale du signal candidat.

## 4. ANALYSE

### 4.1. Caractère fréquentiel

Avant d'aborder la classification proprement dite, il peut être intéressant d'analyser les signaux. En effet, l'étude approfondie des signatures Doppler peut grandement faciliter la compréhension des phénomènes observés.

Plusieurs arguments justifient le choix de l'analyse spectrale au détriment de la représentation temporelle des signatures.

- L'effet Doppler, à l'origine du signal audio, est un phénomène essentiellement fréquentiel. Il s'agit de la variation apparente de la fréquence perçue par un observateur en mouvement par rapport à une source d'ondes entretenues.

- La déclaration du constructeur de l'antenne du radar selon laquelle un opérateur bien entraîné parvient à classer les cibles détectées uniquement à l'écoute du signal audio. L'oreille humaine contient, en effet, un analyseur spectral très particulier et très performant.

- Il apparaît en outre que les caractéristiques temporelles des signaux, principalement leur amplitude, sont plus sensibles aux perturbations extérieures que les caractéristiques spectrales [Réf.2].

- Et enfin, le suivi manuel pendant la phase de classification a une influence considérable sur les variations d'amplitude du signal.

La figure 2 illustre les variations de l'amplitude du signal Doppler. Les ordonnées correspondent aux valeurs numériques obtenues par conversion analogique-numérique du signal Doppler.

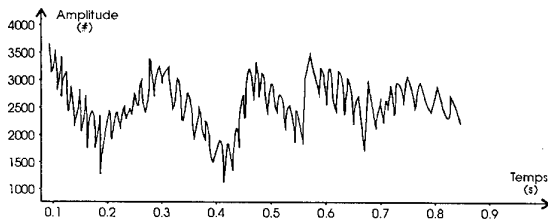


Figure 2 : Signal Doppler, représentation temporelle

### 4.2. Analyse spectrale

Les qualités intrinsèques de l'analyse spectrale comme outil mathématique sont bien connues par les spécialistes du traitement des signaux.

Le calcul de la convolution, de la corrélation est de loin plus facile en transformant les signaux temporels en équivalent fréquentiel.

Mais l'analyse spectrale permet souvent aussi une interprétation plus directe et plus aisée d'un signal temporel d'apparence chaotique. Ce type d'analyse est très répandu. On peut citer, à titre d'exemples, les techniques radar et sonar, le traitement de la parole, le dépouillement des électrocardiogrammes et électroencéphalogrammes en médecine, l'analyse des signaux mécaniques et sismiques, l'étude spectrale des séries chronologiques en économie.

Les signaux étudiés étant aléatoires et non-stationnaires, il s'agit donc d'estimer la densité spectrale du signal en fonction de la fréquence et du temps.

Il existe actuellement à cet effet énormément de méthodes d'estimation disponibles. Le choix de l'une d'elles se fait en fonction de leur applicabilité et des performances souhaitées. Pour analyser les signatures Doppler nous avons choisi l'estimateur spectral modifié de Welch.

### 4.3. Mouvement radial

Les premiers enregistrements ont fourni les signatures Doppler de cinq véhicules évoluant à vitesse constante et pratiquement dans la direction d'observation du radar SCB (figure 3). Ce type de mouvement est appelé mouvement radial.

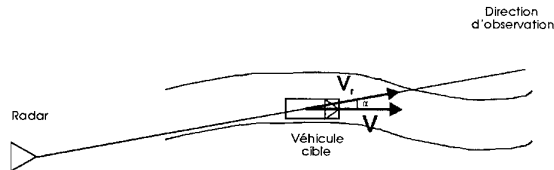


Figure 3 : Mouvement radial

Les spectres de fréquence de la figure 4 sont représentatifs des résultats de cette campagne de mesures et de tous les véhicules testés. Hormis la vitesse radiale (vitesse projetée sur la direction d'observation radar-cible) du véhicule observé, la signature Doppler ne contient apparemment pas d'autres informations.

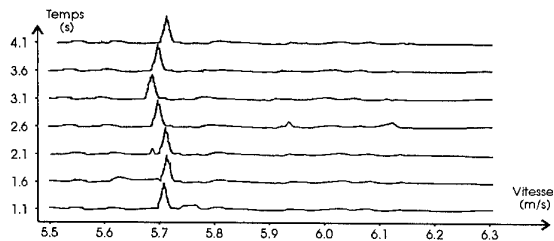


Figure 4 : Spectres d'un véhicule en mouvement radial

L'abscisse du maximum de chaque spectre de la figure 4 fournit la vitesse du véhicule à l'instant déterminé par l'ordonnée du spectre. On peut donc représenter l'évolution de la vitesse radiale en fonction du temps (figure 5).

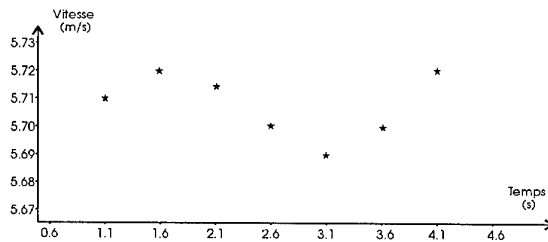


Figure 5 : Evolution de la vitesse radiale

Les variations mesurées de cette vitesse radiale proviennent des variations réelles de la vitesse du véhicule éclairé ainsi que des variations de l'angle d'observation.

### 4.4. Mouvement latéral

Les premiers résultats, peu encourageants, ont permis de fixer les modalités de la deuxième série d'essais: les cibles doivent évoluer latéralement à vitesse variable sur un terrain accidenté.

Des rampes à section trapézoïdale ont permis d'obtenir le profil désiré pour le parcours. Afin de tester les mêmes cibles sur un parcours plat, il était aussi possible d'emprunter la section d'essais sans passer sur les rampes. Dans le cas de l'observation latérale, les spectres obtenus présentent une particularité illustrée à la figure 6.

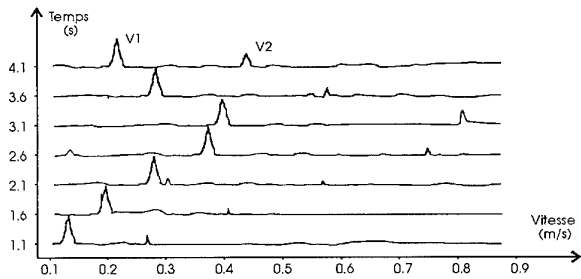


Figure 6 : Spectres d'un véhicule en mouvement latéral

Le pic principal (V1) est représentatif de la vitesse d'ensemble du véhicule éclairé. Le deuxième pic (V2), lorsqu'il est présent, se situe aux environs de 2V1. L'existence de cette harmonique, ou plus précisément de ce pic secondaire, peut s'expliquer aisément. En effet, si le véhicule possède une vitesse d'ensemble V1 (vitesse d'entraînement) par rapport à un observateur fixe, le radar en l'occurrence, certaines parties mobiles de ce véhicule ont une vitesse absolue supérieure. Pour un véhicule chenillé, la partie supérieure de la chenille se déplace deux fois plus vite par rapport au sol et donc au radar, que le véhicule lui-même en vertu de la superposition des vitesses (figure 7-a). Il en va de même pour les véhicules à roues, en ne considérant que la couche la plus excentrée du pneumatique au droit du moyeu (figure 7-b).

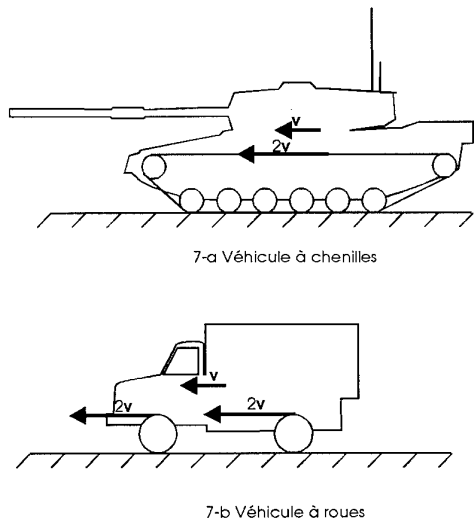


Figure 7 : Superposition des vitesses

La présence de pics secondaires est donc une caractéristique de l'observation latérale. La valeur maximale du rapport des vitesses (V2/V1) est en principe égale à deux.

**4.5. Rapport des vitesses d'un véhicule chenillé**

La figure 8 reprend l'évolution, en fonction du temps, du rapport des deux vitesses V2/V1 obtenu à partir d'un enregistrement d'un véhicule à chenilles. Il est remarquable de constater que la variation du rapport V2/V1 est continue. Elle fluctue autour de la valeur théorique de deux.

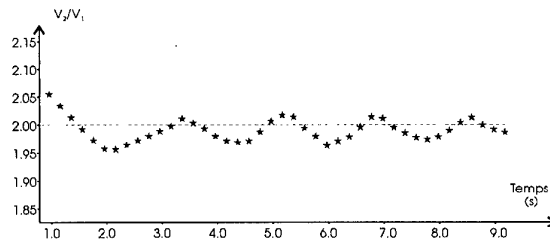


Figure 8 : Rapport des vitesses V2/V1 (véhicule chenillé)

**4.6. Rapport des vitesses d'un véhicule à roues**

Les opérations décrites au paragraphe précédent sont maintenant appliquées à une signature Doppler provenant d'un véhicule à roues observé latéralement. La figure 9 reprend le rapport des vitesses (V2/V1), en fonction du temps.

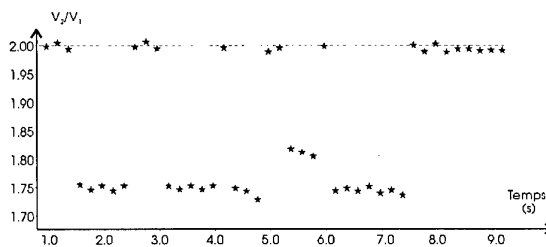
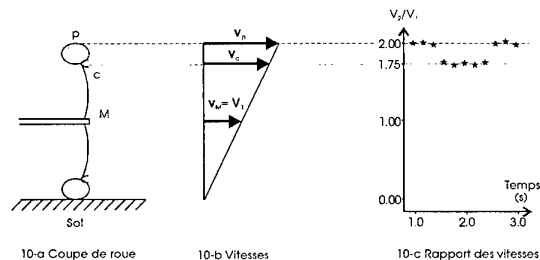


Figure 9 : Rapport des vitesses V2/V1 (véhicule à roues)

Le rapport des vitesses V2/V1 n'est pas toujours approximativement égal à la valeur théorique. D'après la figure 9 il semblerait qu'une deuxième valeur de V2/V1 apparaisse systématiquement. Ces résultats sont déroutants a priori. En seconde analyse et sur base d'une coupe des roues du véhicule utilisé, il est possible d'avancer une explication.

La figure 10 reprend : une coupe transversale des éléments d'une roue (figure 10-a), les vitesses absolues correspondantes de ces éléments (figure 10-b), l'évolution schématisée du rapport des vitesses correspondant (figure 10-c). Cette interprétation plaide pour l'existence de deux zones de réflexion préférentielles des ondes radar: la première est la couche la plus excentrée du pneumatique (p), la seconde se situe à la jonction entre le pneumatique et la jante (c). Cette dernière présente à cet endroit un profil particulier propice à la réflexion des ondes électromagnétiques [Réf.2].



Légende:

- p : Pneumatique
- c : Cornière
- M : Moyeu
- V<sub>x</sub> : Vitesse de l'élément x

Figure 10: Coupe transversale d'une roue

## 5. EXTRACTION DES CARACTERISTIQUES

### 5.1. Ingrédient de base

Le paragraphe précédent annonce l'aspect fréquentiel des caractéristiques du signal. Les interprétations des signatures Doppler corroborent ce choix.

L'extraction des caractéristiques est comparable au prétraitement, terme qui englobe toutes les actions préliminaires à l'opération principale : la classification. Cette phase préparatoire est importante et conditionne le bon déroulement de l'application.

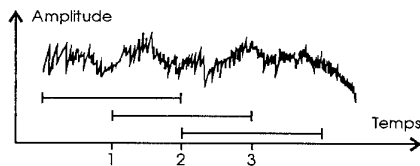
Conformément au choix posé, il a été fait usage de la transformée de Fourier discrète (TFD) pour effectuer l'analyse spectrale des signaux temporels. Cet outil classique a fourni l'ingrédient de base à partir duquel les caractéristiques ont été construites.

Les exemples concrets du paragraphe 4 sont autant d'illustrations de la matière première. Il est possible d'imaginer un grand nombre de caractéristiques à partir des analyses spectrales; l'empirisme de la démarche peut cependant paraître gênant.

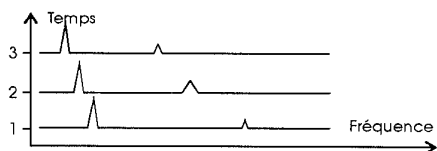
La suite de ce paragraphe est consacrée à la description de l'une d'entre elles: la caractéristique "Welch". Une "justification" de ce choix permet de diminuer l'aspect empirique incongru.

### 5.2. Caractéristique "Welch"

Comme son nom l'indique la construction se base sur l'estimateur de Welch : estimateur spectral utilisé en traitement des signaux.



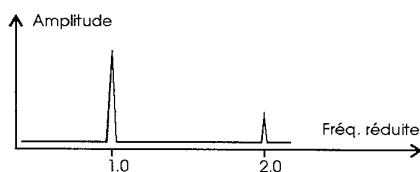
11-a Découpe du signal temporel



11-b TFD des sections temporelles



11-c TFD réduites (adimensionnelles)



11-d Somme des TFD réduites

Figure 11 : Construction de la caractéristique "Welch"

Il a été adapté, pour cette application, afin de mieux répondre aux besoins de la classification. Cette modification revient à rendre les spectres fréquentiels adimensionnels en normant les fréquences par rapport à la fréquence correspondant à la vitesse radiale instantanée.

La figure 11 reprend schématiquement les étapes qui transforment le signal temporel en caractéristique "Welch".

Le signal temporel est sectionné avec recouvrement partiel (figure 11-a). Le spectre de chaque section est ensuite évalué par TFD (figure 11-b). Les spectres des sections sont alignés en normant les fréquences par rapport à la fréquence instantanée correspondant à la vitesse d'ensemble du véhicule (figure 11-c). Finalement les spectres réduits sont additionnés (figure 11-d).

### 5.3. Justification

La technique de l'estimation spectrale par le biais d'un calcul de moyenne est tout à fait licite. Elle permet d'éviter l'évaluation de la fonction d'autocorrélation, prémices habituelles de l'estimation spectrale.

La réduction de l'axe des fréquences présente un double avantage. Elle permet d'éliminer des non-stationnarités du signal: les variations inévitables de la vitesse d'ensemble du véhicule sont gommées en alignant les analyses spectrales successives.

En outre, cette opération enlève des spectres l'information "vitesse d'ensemble", ce qui est indispensable au bon fonctionnement de certaines classifications.

La classification des véhicules ne peut pas se baser sur la grandeur de la vitesse. En effet, si deux véhicules A et B sont contraints, pour des raisons expérimentales, d'évoluer aux vitesses différentes  $V_a$  et  $V_b$ , la classification basée sur la grandeur des vitesses est triviale mais irréaliste.

## 6. CLASSIFICATION

Après l'acquisition des signatures Doppler et l'extraction des caractéristiques, il reste à effectuer la classification proprement dite.

Cette phase ultime doit établir la correspondance entre les différents types de cibles et leurs signatures Doppler, ou plus précisément, leurs caractéristiques extraites des signatures.

### 6.1. Théorie de Bayes

La question fondamentale, à laquelle la RAO devrait répondre, peut être énoncée comme suit : pour quelle caractéristique faut-il décider que la cible détectée est d'un tel type ?

La théorie de Bayes peut résoudre ce type de problèmes en calculant la probabilité - dite a posteriori - qu'une signature déterminée soit imputable à un type de véhicule.

### 6.2. Techniques neuromimétiques

A côté des théories classiques, comme celle de Bayes, il existe une approche basée sur l'emploi de réseaux de neurones (RN). Diverses raisons nous ont orientés vers ces techniques.

L'une d'elles est sans aucun doute l'attrait du nouveau, couplé à l'engouement généralisé. Il existe des justifications plus objectives comme le nombre croissant d'applications réussies, l'apparition de théories cohérentes et l'élaboration de liens avec des procédés classiques [Réf.3].

Dans le cas particulier de la classification, les auteurs de [Réf.3] ont établi un lien formel entre la théorie bayésienne et un type particulier de réseaux de neurones.

L'interprétation du fonctionnement des RN dépend essentiellement de l'application envisagée. Dans le cas de la classification on parle de mémoire associative [Réf.4;Réf.5].

La caractéristique d'une signature Doppler est présentée en entrée du RN. En sortie, on désire obtenir le type de véhicule qui a engendré la signature Doppler.

Une vérification de cohérence de la base de données d'apprentissage consiste à présenter ces données et de vérifier les sorties. Normalement le résultat du test doit avoisiner les 100 % [Réf.6]. Après cette première phase, il faut tester le RN avec d'autres données que celles déjà utilisées.

Certains auteurs [Réf.6] n'hésitent pas à invoquer un parallélisme entre le fonctionnement d'un RN et celui d'un écolier.

Dans un premier temps les problèmes sont proposés avec leurs solutions; après cet apprentissage le pédagogue peut poser les mêmes problèmes sans proposer les solutions et, en cas de succès, passer à des problèmes "jamais vus au cours".

Cette comparaison peut aider à la compréhension de la séparation des données (apprentissage et test) et de la valeur des vérifications, mais le rapprochement s'arrête là.

### 6.3. Exploitation

Une exploitation est définie par :

#### a. La sélection d'une base de données

Le choix d'une base de données : un certain nombre d'enregistrements issus des campagnes de mesures.

#### b. La partition de la base de données

Une subdivision de cette base de données en deux parties: un groupe de mesures destiné à l'apprentissage du RN, un second sous-ensemble dédié au test du RN.

#### c. L'attribution de deux notes

##### 1. Cohérence de la base d'apprentissage

La première note chiffre la cohérence de la base d'apprentissage: cette note doit approcher 100%.

##### 2. Test du RN

La seconde note reflète les performances du RN testé par des nouvelles signatures.

### 6.4. Meilleurs résultats

Le meilleur taux de classification est obtenu, en phase de faisabilité, pour l'exploitation définie par:

#### a. La sélection d'une base de données

189 signatures sont extraites des enregistrements issus de deux campagnes de mesure. Six types de véhicules ont servi de cible pour ces enregistrements : 3 véhicules chenillés (LEOPARD, CVRT et M109) et 3 véhicules à roues (MAN, VOLVO et JEEP).

#### b. La partition de la base de données

Les 189 signatures sont réparties entre bases d'apprentissage (127 signatures) et de test (62 signatures).

#### c. L'attribution de deux notes

##### 1. Cohérence de la base d'apprentissage

Après apprentissage les caractéristiques sont à nouveau présentées au RN. Les résultats de cette classification sont repris dans la matrice supérieure du tableau 1.

##### 2. Test du RN

Huit signatures des 62 présentées n'ont pas été classifiées correctement, ce qui

correspond à un pourcentage de classification correcte de 87.1 %. Les résultats sont repris dans la matrice inférieure du tableau 1.

Sortie RN	Chenillé % n	Roues % n	Jeep % n
Entree RN			
Chenillé (73)	98.6 (72)	(-)	(-)
Roues (28)	(-)	96.4 (27)	(-)
Jeep (26)	(-)	(-)	92.9 (24)

Matrice de classification - cohérence de la base d'apprentissage

Sortie RN	Chenillé % n	Roues % n	Jeep % n
Entree RN			
Chenillé (29)	82.8 (24)	(-)	(-)
Roues (19)	(-)	89.5 (17)	(-)
Jeep (14)	(-)	(-)	92.9 (13)

Matrice de classification - test du RN

Légende:            n            : nombre de signatures  
                      %            : pourcentage correspondant  
                      (-)        : valeur non disponible

Tableau 1 : Matrices de classification apprentissage et test

Les RN sont, sans doute, bien adaptés au problème de la RAO. Mais l'empirisme des techniques utilisées implique une exploitation systématique du champ d'investigation. Les exemples présentés ne sont que deux échantillons d'une longue série. Le taux de classification en mode "test" est le critère de comparaison et de classement des exploitations entre elles.

### 7. CONCLUSION

Notre contribution originale, au projet de la RAO, comprend:  
- la mise au point d'une méthode expérimentale pour l'acquisition des signatures Doppler dans des circonstances bien définies.

- l'interprétation fouillée de ces signatures dans divers cas: véhicules à roues et à chenilles en mouvement radial et latéral.

- l'illustration des performances potentielles importantes du radar SCB 2130A.
- l'extraction d'une caractéristique des signatures Doppler, indépendante de la vitesse d'ensemble du véhicule.
- l'utilisation de réseaux de neurones artificiels pour la classification de ces caractéristiques.

Les premiers résultats (87.1 % de taux de réussite) ont été considérés comme encourageants et ont justifié la poursuite de l'étude.

A côté des résultats partiels mais prometteurs exposés dans le présent article, d'autres arguments ont plaidé pour la continuation du projet:

- le suivi automatique des cibles détectées a été réalisé. Cette option présente un intérêt opérationnel indiscutable et améliore la qualité des signatures Doppler.
- la première réalisation (prototype) de la carte RAO comprend un filtre numérique qui permet le filtrage adaptatif des signatures Doppler. Cette opération de filtrage améliore la qualité des signatures Doppler par l'élimination du fouillis du radar.

#### Références

- [1] R.O. DUDA, P.E. HART  
"Pattern Classification and Scene Analysis"  
John Wiley and Sons, New York, 1973.
- [2] M. SKOLNIK  
"Introduction to Radar Systems"  
International Student Edition, Auckland, 1981.
- [3] D. RUCK and al  
"The Multi Layer Perceptron as an Approximation to  
a Bayes Optimal Discriminant Function"  
IEEE Transactions on Neural Networks,  
December 1990.
- [4] R.P. LIPPMANN  
"An Introduction to Computing with Neural Nets"  
IEEE ASSP Magazines,  
April 1987.
- [5] T. KOHONEN  
"Self Organisation and Associative Memory"  
Series in Information Sciences, Volume 8,  
Springer Verlag, Berlin, 1989.
- [6] D.E. RUMELHART J.L. Mac CLELLAND  
"Parallel Distributed Processing : Exploration in the  
Microstructure of Cognition"  
The MIT Press, Massachusetts, 1987.
- [7] J.J. HOPFIELD  
"Artificial Neural Networks"  
IEEE Circuits and Devices Magazines,  
September 1988.

**Discussor's name:** P. GINS

**Comment/Question:**

Que ce passe-t-il en cas de patinage des chenilles?

Comment réagit le réseau de neurones?

*Translation:*

*What happens if the tracks slip?*

*How does the neurone network react?*

**Author/Presenter's reply:**

Lors de cette étude de faisabilité nous n'avons pas envisagé un éventuel patinage des chenilles. Nous avons validé les résultats (deuxième pic de vitesse " $V_2$ ") par emploi de panneaux atténuateurs (pour les chars) ou en isolant le mouvement des roues (véhicules à roues) en les faisant tourner dans le vide.

Le réseau de neurones n'a pas été testé vis-à-vis du patinage éventuel.

*Translation:*

*We didn't allow for the tracks slipping in the original feasibility study. We validated the results (second velocity peak " $V_2$ ") using attenuator panels (for tanks) or by isolating wheel movement (for road vehicles) by leaving the wheels to spin.*

*The neurone network was not tested for track slippage.*

## Modeling of ISAR Imagery for Ships

K.Emir  
 Netas Northern Electric Communications Inc.  
 System Planning Dept.  
 81244 Umraniye, Istanbul Turkey

E.Topuz  
 Technical University of Istanbul  
 Electronics and Communications Dept.  
 80626 Maslak, Istanbul Turkey

### 1. SUMMARY

An alternative approach is proposed for the modeling of ISAR imagery for ships, which can effectively be used to generate images in sufficient accuracy as to correctly represent the dominant scattering phenomena. This approach relies on doing some preprocessing on the data for each particular problem, so as to simplify the modeling of the ships surface. Our preliminary numerical results demonstrate that the proposed technique is computationally very efficient. Moreover, the generated data is sufficiently accurate and can be fed into the recently developed automatic classification algorithms which are based on localization of dominant scattering centers on the target.

### 2. INTRODUCTION

High resolution radars provide resolution cell sizes which in range and cross range are 2-3 orders of magnitude lower than the corresponding dimensions of surface ships. With appropriate shaping and processing the radar signal can then be used to effectively discriminate field constituents scattered from different spatial domains of the target. Imaging radars display the distribution of the strength of the signal to the corresponding radar resolution cells, thereby providing a low resolution snapshot image of the target. The resulting image has a very rapidly scintillating character due to the random variations in the various parameters which specify a particular snapshot. When target classification is the prime interest one will have to stabilize this data via identification and extraction of certain features.

In this work we consider the modeling of surface ships from the point of view of high resolution radars capable of target classification via ISAR mode of operation. Although, ISAR capable sea surveillance radars have become operational more than a decade ago, automatic ship classification via ISAR images is still in its infancy. The classification algorithms in the open literature reduce the immense amount of available data to a bare

minimum, to extract only 2-3 features [1]. More recently, there is an increased interest in developing ISAR classification algorithms which will make use of substantially more features and exploit the available data in more sophisticated ways. The most promising approach, along this direction seems to be the point of view of trying to localize the dominant scattering centers on the target. This can in principle be achieved by trying to establish a "best fit" between the measured data and the synthetic data generated via model calculations and utilizing a few judiciously chosen hypotheses as to the number and spatial positions of these dominant scatterers [2].

The main objective of this study is to focus only on the dominant scattering phenomena and to investigate the feasibility of utilizing the resulting rather crude models in generating the synthetic data to be fed to these second generation automatic classification algorithms. Placing the emphasis on computational efficiency, rather than on improving accuracy we have tried to simplify both the modeling of the ships surface and also the ISAR processing schemes. Giving careful consideration to the range of possible motions of the ship in a particular imaging problem, we do some preprocessing and try to simplify the modelling of the ships surface, so that the required number of surface patches is reduced to the order of  $10^4 - 10^5$ . Our aim is to have a code which will, under short pulse type illumination, generate an ISAR image in no more than few hours run time on a state of the art PC. To achieve this goal we totally neglect diffraction effects, and furthermore, assuming that sufficient signal power will be intercepted we disregard clutter and noise considerations. At its present stage our code suffers from a number of shortcomings, i.e.,

- \* Idealized surface reflectivities are assumed.
- \* Convex surfaces and multiple interactions are accounted for in an approximate way.
- \* Multipath is not incorporated.

Work is going on to improve the model by addressing the above items, which we believe to be of comparatively more importance for our intended areas of application.

### 3. METHOD

#### 3.1 Modelling the surface of the target

The targets of interest are surface ships for which the characteristic dimensions are typically 2 to 4 orders of magnitude larger than the wavelength of the illuminating microwave signal. Assuming an X band illumination and a moderate size ship, one will have to use  $10^8 - 10^9$  surface patches if the characteristic patch dimensions are required to be in the order of one wavelength. If the surface patch sizes are increased or reduced, the required number of surface patches decreases or increases in a cubic fashion.

We have chosen to model the surface of the vessel via triangular, planar patches. The main advantages of this approach are the ability to economically represent different surface shapes of large radii of curvature and the possibility of yielding closed form analytical expressions for the scattered field under physical optics approximation. The modeling of the hull presents no major problem, and we have noticed that, with the exception of regions which give specular returns, one can use patch sizes at least an order of magnitude larger than the wavelength. For a particular problem a careful investigation reveals the regions responsible for specular or near specular returns, wherein we define our patches on a finer grid. For certain ships, like tankers, the complexity of the superstructure is not excessive and similar considerations may apply to the major part of the superstructure. For an accurate description of the remaining parts of the superstructure in terms of triangular patches, the required amount of data grows rather rapidly with a corresponding increase in the CPU time. In order to keep the computation time small we have assumed that the problematic parts of the superstructure can be approximated by inclusion of a small number of additional scattering centers. These scattering centers are modelled in form of idealized scatterers for which the scattered field can be approximately described by closed form expressions [3-4].

#### 3.2 Modelling the motions of the target

Hypotheses for cross-range scaling of ISAR images greatly benefit from the presence of some a priori knowledge or estimate on the motions of the ship. The ship motion is basically governed by a set of second-order linear differential equations of the form

$$\left[ A \frac{\partial^2}{\partial t^2} + B \frac{\partial}{\partial t} + C \right] q(t) = f(t) \quad (1a)$$

where  $q(t)$  represents a vector of surge, sway and heave motions and the variations of roll, pitch and yaw orientations, while  $f(t)$  corresponds to the vector of wave excitation input. The matrix coefficients A, B and C

represent virtual mass, damping and the restoring stiffness, respectively. These coefficients can be assumed to be constant and determined by the dimensions and shape of the ship [5]. The main problem here is in the estimation of the driving forces. The wave excitation can be approximated by a superposition of sinusoidal components, as

$$f(t) = \sum_{v=1}^N a_v \sin(\xi_v t + \psi_v) \quad (1b)$$

where  $a_v$ ,  $\xi_v$  are the amplitudes and spectral frequencies which remain essentially constant over the measurement periods, and  $\psi$  represents the phase of each different wave.

For a ship travelling with a constant forward speed  $u$  and in the direction which makes an angle  $\gamma$  with regard to the propagation direction of the sinusoidal waves, the frequencies  $\xi_v$  in (1b) have to be replaced by the actual encountered frequency,  $\bar{\xi}_v$ ,

$$\bar{\xi}_v = \xi_v - \frac{\xi_v^2}{g} u \cos \gamma \quad (1c)$$

where  $g$  is the gravitational acceleration [6].

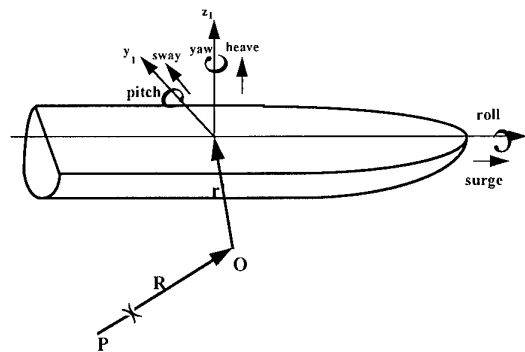


Figure 1 Motions of a ship

In general, the phase angles in (1b) are taken as random variables, and amplitude and frequencies are estimated via the standard Pierson-Moskowitz (I.T.T.C.) spectral density function for given characteristic wave height and period [7]. The problem of estimating ships motion is further complicated since the forces acting on the ship are determined locally by the interaction between the vessel and the sea [8,9].

#### 3.3 Modelling the scattered field

In order to conveniently introduce the basic formulation of the problem we consider the backscattered field from a perfectly conducting closed surface  $S$  at an observation point  $S$  which is assumed to be quite far away from the scattering surface. We choose a coordinate origin  $O$  in the immediate vicinity of  $S$ , as depicted in Fig.1, and denote the position vectors of the

observation point P and of a typical scattering center T by,  $\vec{r} = R \vec{u}_R$  and  $\vec{r}'$ , respectively. The position vector from T to P can be written as  $\vec{r} - \vec{r}' = R' \vec{u}_s$ , where  $\vec{u}_R$  and  $\vec{u}_s$  denote unit vectors.

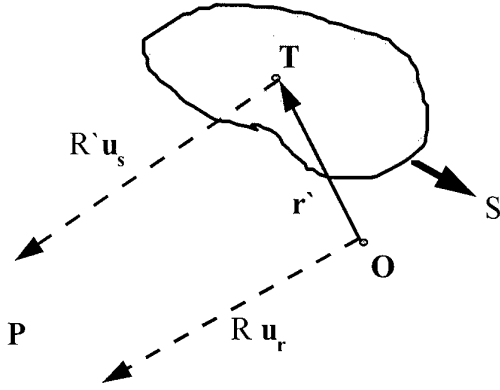


Figure 1 Notation

Let the induced surface current density be  $\vec{J}_s$  then the Hertzian vector of the electric type at P is obtained as,

$$\vec{\Pi}(\vec{r}) = \frac{1}{j\omega\epsilon} \oint_S G(\vec{r}, \vec{r}') \vec{J}_s dS \quad (2a)$$

where the integral is over the source region S and G is the free space Green's function,

$$G = \frac{\exp[-jk(R\vec{u}_s \cdot \vec{u}_R - \vec{u}_s \cdot \vec{r}')] }{4\pi R'} \quad (2b)$$

Once the Hertzian vector is known, the scattered electric field at P can be obtained as,

$$\vec{E}_S = \nabla \times \nabla \times \vec{\Pi} \quad (2c)$$

Recalling that  $\nabla$  above, operates on observation point coordinates one obtains [10],

$$\vec{E}_S = \frac{jk\eta_0}{4\pi R} \oint_S [\vec{u}_R(\vec{u}_R \cdot \vec{J}_s) - \vec{J}_s] \exp(-jkR(\vec{u}_s \cdot \vec{u}_R)) \exp(jk\vec{u}_s \cdot \vec{r}') dS \quad (3)$$

where  $\eta_0$  is the free space wave impedance.

Up to now, care has been exercised to keep phase terms intact and, far field approximations are introduced only in the amplitude terms. The above expression can therefore be considered exact, provided that R, R' are much larger than the characteristic dimensions of the scatterer, implying  $\vec{u}_S \cong \vec{u}_R$ . Whenever the receiver can be considered to be in the far zone of the target one can approximate  $\vec{u}_S$  by  $\vec{u}_R$  also in the phase terms, in which case the first exponential in (2a) can be taken out simply as  $\exp(-jkR)$ .

The main difficulty in obtaining  $\vec{E}_S$  resides, of course, in estimating the surface current density  $\vec{J}_s$ . Lowest order Physical Optics (PO) approximation provides a very convenient and fairly accurate solution to this problem. One then assumes that the induced surface current density can be expressed as,

$$\vec{J}_S = 2 \vec{u}_n \times \vec{H}_i \quad (4a)$$

on the illuminated portion of S and vanishes elsewhere. Here  $\vec{H}_i$  is the magnetic field component of the incident wave and  $\vec{u}_n$  is the outward directed unit normal of S.

Both the limitations of the PO assertion and also ways of improving this approximation by the introduction of corrective (Ufimtsev) currents are well known [11,12]. For our purposes we note that (3a) becomes insufficient or inaccurate on the edges of the surface and also in parts where the radii of curvature are smaller than about 10 wavelengths.

Considering plane wave incidence the electric field can be expressed as,

$$\vec{E}_i = \vec{u}_i E_i \frac{\exp(-jkR')}{4\pi R'} \quad (4b)$$

where  $\vec{u}_i$  is a unit vector in the direction of the incident E field. Then, since

$$\vec{H}_i = \eta_0 \vec{u}_s \times \vec{E}_i \quad (4c)$$

one obtains the scattered PO field as

$$\vec{E}_S = \frac{jk}{2\pi R} \vec{u}_i E_i \oint_S \vec{u}_n \cdot \vec{u}_s \exp[-j2kR(\vec{u}_s \cdot \vec{u}_R)] \exp(j2k\vec{u}_s \cdot \vec{r}') dS \quad (5)$$

When the scattering surface S is expressed as a collection of patches with surfaces denoted by  $\Delta S_\nu$ ,

$$S = \sum_{\nu=1}^N \Delta S_\nu \quad (6a)$$

then the total scattered field can be synthesized via its constituents which are defined over the corresponding patches, as,

$$\vec{E}_S = \sum_{\nu=1}^N \vec{E}_{S\nu} \quad (6b)$$

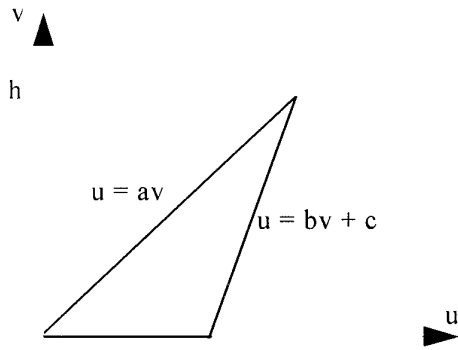


Figure 2 A Triangular Patch

We have chosen to use triangular patches. With this choice the backscattered field from the patches can be evaluated in closed form. Considering a general surface element as depicted in Fig.2, and adopting spherical coordinates with  $\theta$  measured from the surface normal of the patch and  $\phi$  from the  $u$  axis, one obtains,

$$\bar{E}_s = \bar{u}, E, \frac{j h \cot \theta}{8 \pi R \cos \phi} \left\{ \exp(-j k c \sin \theta \cos \phi) \right.$$

$$\exp[-j k h \sin \theta (\sin \phi + b \cos \phi)]$$

$$\sin c[k h \sin \theta (\sin \phi + b \cos \phi)]$$

$$- \exp[-j k h \sin \theta (\sin \phi + a \cos \phi)]$$

$$\left. \sin c[k h \sin \theta (\sin \phi + a \cos \phi)] \right\} \quad (5)$$

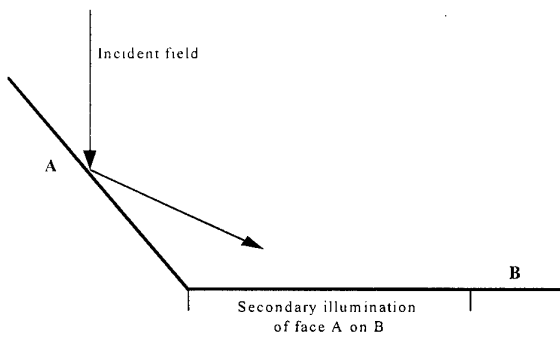


Figure 3 Second order illumination via GO

Although, the calculation of the scattered primary field generally provides satisfactory approximation over convex parts of the surface  $S$ , multiple scattering has to be taken into account on concave sections of  $S$ . Within the realm of the PO this can be achieved by taking the higher order illuminations resulting from multiple scattering properly into account. In general, it suffices to account only for the second order illumination, calculated via geometrical optics (GO) as schemetized in Fig.3 [ 13 ].

#### 4. Numerical Results and Conclusions

In order to investigate the applicability of the simplifications introduced in this report we have performed a number numerical calculations. In the test runs to be described below we have used the data of a tanker, whith a length 105 meters and cross range dimensions of approximately 15 meters. The hull data was available with a precision of about one wavelength, and was generated utilizing TRIBON, a commercial CAD / CAM package used in ship design. This data was reduced to about 5000 points which described the hull with a precision of about 1 meter everywhere except regions of near specular return for aspect angles close to  $45^\circ$  looking astern. The mesh sizes utilized in these regions were 3-10 times smaller.

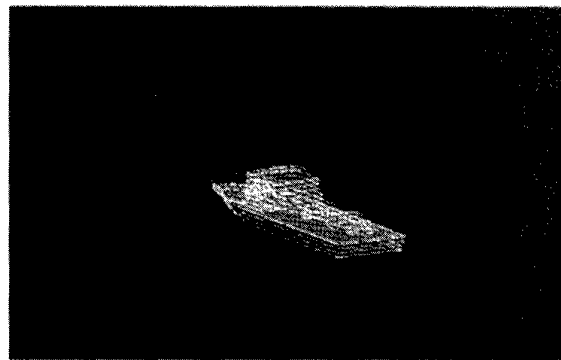


Figure 4 View of the target used in calculations.

The superstructure was defined with about the same number of patches and in a rather crude way as depicted in Figs 4 and 5a. The total number of scatterers used was slightly less than  $10^4$ .

Visibility calculations were considerably simplified by considering only the cases of near grazing angle incidence.

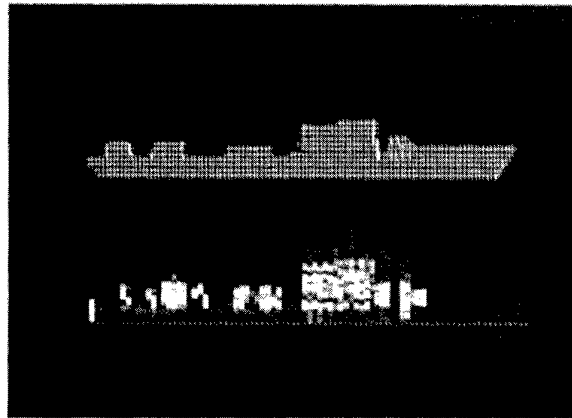
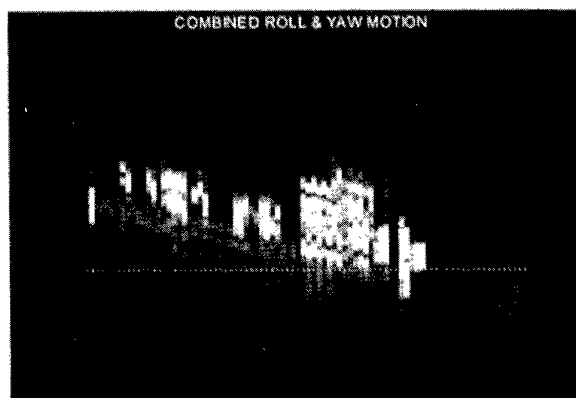
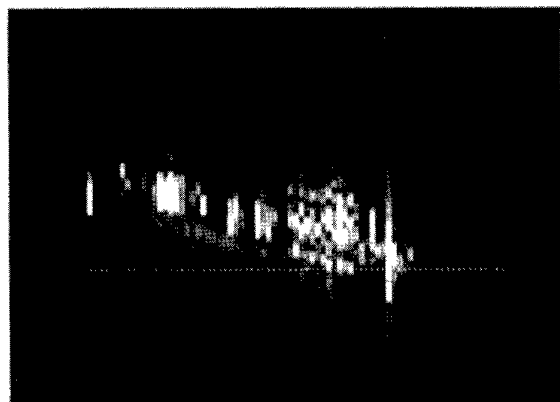


Figure 5a Target in pure roll motion. Aspect angle  $45^\circ$  astern.



**Figure 5b** Target in combined roll and yaw motion. Aspect angle  $44^\circ$  astern.



**Figure 5c** Target in combined roll, yaw and pitch motion. Aspect angle  $40^\circ$  astern.

For the examples given here the calculation times were about 45 minutes on a PC with a pentium processor and a clock frequency of 166 MHz.

It has to be noted that, certain features of the ISAR images depicted in Figs. 4 and 5 are preserved although they correspond to reasonably different measurement conditions.

The presented examples demonstrate that for this overly simplified case we have been able to correctly identify most of the dominant scatterers.

Although there remains much to be done we can conclude that our approach has the potential of correctly representing the dominant phenomena governing the backscattering of high resolution radar signals from electrically large targets, and that it will result in computer codes which run fairly fast and require only very modest computational resources.

## REFERENCES

1. M.M.Menon, E.R.Boudreau, P.Kolodzy, "An Automatic Ship Classification System for ISAR Imagery", *The Lincoln Lab. Journ.*, Vol.6, No.2, pp.289 - 308, 1993.
2. Z.D.Zhu, Z.R.Ye, X.Q.Wu, J.Lin,Z.S.She,"Super Resolution Range - Doppler Imaging, *IEE Proc. Radar,Sonar,Nav.*, Vol.142, pp.25- 32, 1995.
3. J.J.Bowman, T.B.Senior, P.E.Ushlengi, "*Electromagnetic and Acoustic Scattering by Simple Shapes*", North Holland, 1969.
4. E.F.Knott, J.F.Shaefer,M.T.Tuley, " *Radar Cross Section*" Artech House, 1985.
5. M.S.Triantafyllou,M.Bodson,M.Athans,"Real Time Estimation of Ship Motion Using Kalman Filtering Techniques",*IEEE Journ.Ocean Eng.*, Vol.OE 8,pp.9-20, 1983.
6. J.C.Chung, Z.Bien, Y.S.Kim, "A Note on Ship-Motion Prediction Based on Wave Excitation Input Estimation", *IEEE Journ.Ocean Eng.*, Vol. OE 15, pp.244 - 250.
7. Y. Goda, "*Random Sea and Design of Maritime Structures*" Univ.Tokyo Press, 1985.
8. H.P.Kröger, "Rollsimulation von Schiffen im Seegang", *Schiffstechnik*, Vol.33, pp.187-207, 1986.
9. D.Kring, P.D.Sclavounos, "Numerical Stability Analysis for Time-Domain Ship Motion Simulations", *Journ. of Ship Research*, Vol.39,pp.313-320.
10. A.Ishimaru, "*Electromagnetic Wave Propagation,Radiation and Scattering*" Prentice Hall, 1991.
11. Special Issue on Radar Cross Section, *Annals of Telecommunications*, Vol.50, No.4-5, 1995.
12. M.A.Plonus,R.Williams,S.C.H.Wang,"Radar Cross Section of Curved Plates Using Geometrical and Physical Diffraction Techniques",*IEEE Trans.AP*, Vol.AP-26, pp.488-493,1988.
13. T.Griesser,C.A.Balanis,"Backscatter Analysis of Dihedral Corner Reflectors Using Physical Optics and the Physical Theory of Diffraction",*IEEE Trans.AP*, Vol.AP-25, pp.1137-1147, 1987.

## Acknowledment

We gratefully acknowledge ITUV/SAM for hardware support, TDI Pendik Shipyards for the provision of hull data, E.E.Tepeli and A.Tanju for writing and testing some of the programs.

**Discussor's name:** G. WYMAN

**Comment/Question:**

How does your model and the inherent assumptions treat the temporal effects in high sea states? (For example, the hull and other sources of scattering will be obscured for some periods).

**Author/presenter's reply:**

These problems are not addressed in the present state of the code. Work is, however, continuing to incorporate both the masking and the multipath effects due to the presence of the sea surface into our model.

**Discussor's name:** C. SILLENCÉ

**Comment/Question:**

Real ships are covered with a mass of detail at all length scales, and in addition, their surfaces are significantly deformed from the geometrical ideal up to several wavelengths at 10 GHz. In the light of this, how relevant do you think images based on a large (100 L) flat facet representation will be?

**Author/Presenter's reply:**

The main advantage of our approach is flexibility, in that different mesh sizes are used in the same model. For the examples presented, the maximum and minimum mesh sizes used were about 30L and 3L, respectively. We believe that this level of precision should suffice to represent the dominant scattering characteristics of ships.

# An Approach to Physical Level Chaff Simulation

SHW Simpson and PER Galloway  
Roke Manor Research Ltd,  
Romsey, Hampshire,  
SO51 0ZN, UK.

## Abstract

This paper describes the construction and calibration of a signal generator for representing the distributed phasor vector radar signature of a chaff round. The fundamental approach together with some alternative methods of calibration are discussed, and some results are presented. The paper is written assuming that the reader is familiar with chaff, its terminology and its methods of deployment. The body of the paper concentrates on producing a model of chaff that is sufficiently accurate and adaptable to represent a given chaff round at a physical level. In particular, the possibility of using physical level Computer Aided Engineering (CAE) to calibrate the model is addressed.

## INTRODUCTION

Physical level modelling of a chaff round from a radar point of view presents a very difficult problem. This stems from the fact that it is a coupled fluid dynamics and electromagnetics problem. The paper addresses the full life cycle of the chaff cloud, but concentrates on the bloomed phase as this is the most significant from a radar view point. Both the fluid dynamics and the electromagnetic aspects of simulation are discussed and the relative merits of different approaches to calibration are considered.

The paper is written assuming that the reader is familiar with what chaff is and how it is used and concentrates on the problem of modelling the radar signature.

### *Fluid Dynamics Aspects*

The evolution of a chaff cloud is a fluid dynamics problem from the point of view that it starts its life cycle as a large collection of

small light particles densely packed around a charge. Then, shortly after the time of launching, the charge explodes. The gas from the charge disperses the particles over a large volume in a short space of time. The particles quickly lose their momentum and largely adopt the velocity and direction of the ambient air flow. From this time on gravity plays a significant part and gradually draws the particles to ground level. Their motion however, although random, is affected by the shape and stiffness of the particles and this tends to introduce a characteristic polarisation response or preference.

### *Electromagnetic Aspects*

From a simplistic point of view the chaff cloud is a non-rigid body with a random diffraction pattern. Whilst this is true, the fundamental laws of electromagnetism hold at all times and any physical level simulation must reflect these. This requirement suggests that a rigorous solution to the field equations must be sought throughout the life cycle of the chaff cloud. The sheer electrical size of the cloud precludes this however, and some approximation must be introduced.

### *Signal Processing Aspects*

Within a given polarisation plane the radar signature takes on the form of a random signal. Once the initial bloom phase has taken place and the particles adopt a relatively slow motion, the signal takes on a correlated nature when sampled at typical radar rates. If the autocorrelation function of the signal can be measured then the Doppler power spectrum which will represent the random signal can be calculated directly. Application of the central limit theorem explains why the signal distribution should be Gaussian, with its attendant Rayleigh envelope and uniform phase distributions.

## CONSTRUCTION OF A CHAFF SIMULATOR

The global problem facing the designer of a chaff model is that of maintaining sufficient physical level reality without incurring a compute load which prohibits its inclusion within the event loop of a simulator. In this section the approach chosen is introduced and the rationale behind it is explained.

### The Basic Signal Source

The statistical properties and time dependencies required of the signal source can be summarised as follows:

- It must have a Gaussian distribution with the attendant Rayleigh envelope and uniform phase.
- Its power spectrum and thus autocorrelation characteristic must be controllable, to match the Doppler power spectrum of the real chaff signature, without affecting the statistical distribution.

The latter requirement precludes the use of uncorrelated random number generators, as when these are filtered to introduce correlation the statistical distribution is adversely affected. An alternative approach which can meet both requirements is to synthesise the signal from a set of independent deterministic basis functions. This provides the required statistical distribution through the central limit theorem. The natural choice for these are complex sinusoids, as the power spectrum is then straightforward to control. The only issue is what power spectral density can be afforded by the compute budget. The power spectral density is proportionally related to the period of the signal if the basis functions are uniformly spaced. Using a random tone spacing avoids the exact repetition over the same period and is a useful technique when the compute budget is limited.

### The Microcloud concept

The Microcloud concept has two aspects to it. It originally evolved from the practical restriction of the number of chaff particles that could be rigorously modelled electromagnetically using codes such as NEC [1] and ZETA [2]. When such modelling is compared to measured data for investigation of the statistical distribution and frequency characteristic, extremely encouraging validation is seen. Furthermore, if a collection of microclouds, having various dipole cuts in the same ratio as an actual chaff round is

modelled, and the scattered field scaled in proportion, then good agreement is still maintained, Figure 1.

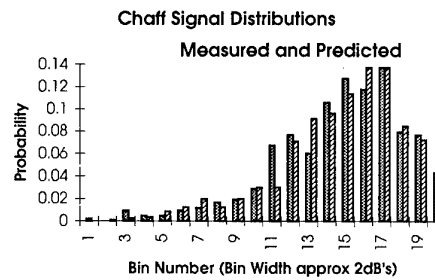


Figure 1. Simulated and Measured RCS Distributions

The second and useful aspect to the Microcloud concept is that spatial spreading, or physical bloom, of the chaff cloud can be readily modelled.

The actual nature of the Microcloud in the simulator is a single random signal source as described above, but the key factor is that the frequency characteristic, as opposed to the power spectrum, of a complex composite chaff round can be investigated using computational electromagnetics and thus programmed into the model. This is a great advantage when this parameter would be otherwise unknown. For example, a cut specification taken from Butters [4] has been modelled in just such a way and is shown in Figure 2.

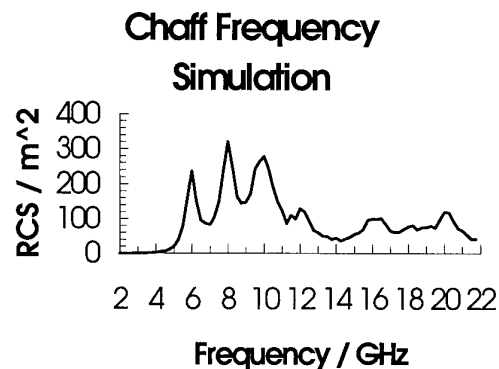


Figure 2. NEC Simulated Frequency Response

## CALIBRATION

As has been discussed above, the electromagnetic behaviour of a chaff round is coupled to its spatial evolution with time. So effectively, almost every parameter of a chaff cloud will vary with time. To characterise a given chaff round, the following parameters have been found to be necessary:

- Physical bloom with time

- RCS bloom with time
- VV, HH and cross-polar differences
- Signal autocorrelation function
- RCS with frequency characteristic
- Statistical distribution

Therefore, without a fluid dynamics model, the characteristics of the time dependent variables need to be provided from data gathered by an RCS measurement radar during chaff proofing trials.

Frequency and polarisation characteristics, whilst obtainable from proofing trials, can also be obtained from computational electromagnetics.

### **Calibration by measurement**

Essentially, with a sufficiently featured measurement radar, all of the above parameters can, in principle, be measured. The physical bloom is possibly the most difficult, as the method of range profiling by measuring the frequency transfer function fails because the measured phase change is increased, or polluted, by the Doppler spectrum. This manifests as a measured cloud extent which is greater than the physical extent. In effect, it is only possible to measure the physical bloom by examining the returned pulse shape and deconvolving this with the transmitted pulse. In this way it is possible to get reasonable estimates of the cloud extent, but higher order effects such as localised bunching, leading to variations in cloud density probably cannot be identified with a radar.

Figure 3 shows the cloud growth by recording the simulated received pulse length resulting from the convolution of a transmitted pulse with a blooming set of microclouds.

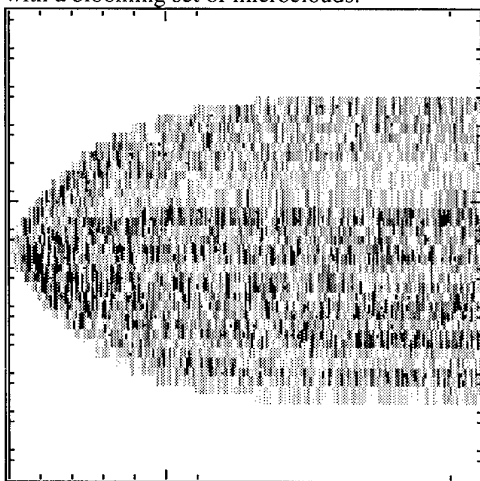


Figure 3. Pulse Recorder Time History

### **Calibration by modelling**

What is being referred to here is the task of calibrating the simulation of a chaff cloud by modelling the particles, or collections of particles, at a physical level.

Extraction of all the parameters is extremely difficult, but computer aided engineering (CAE) and modern computers are bringing this goal closer to reality. Currently, it is possible to characterise the electromagnetic parameters of microclouds using CAE provided data such as particle orientation bias, which determines the polarisation characteristic, can be reverse engineered from measurements. A fully couples fluid dynamics and electromagnetic analysis is still some way off.

## **CONCLUSIONS**

A philosophy for achieving a physical level model of a chaff cloud has been described. This has been implemented in a simulator and found to give accurate reproduction of known parameters whilst consuming only modest compute power. Physical level electromagnetic modelling has been found to be both useful and reliable for supplementing the data available from measurements for calibrating the model.

## **Acknowledgement**

This work has been carried out for the Defence Evaluation and Research Agency, an agency of the UK Ministry of Defence, and is supported by HMG.

## **REFERENCES**

- [1] Burke GJ, Poggio AJ, 'Numerical Electromagnetic Code (NEC)', Technical Document 116, Part III, July 1977, Lawrence Livermore Labs, California, USA.
- [2] Olley CA, Simpson SHW, ZETA - a computational electrodynamic code, Roke Manor Research Internal Document, July 1996.
- [3] Wickliff RG, Garbacz RJ, 'The Average Backscattering Cross-Section of Clouds of Randomised Resonant Dipoles' IEEE Trans AP-22 PP503-505, 1974.
- [4] Butters, BCF, 'Chaff' Proc IEE, Vol 129, Pt F, No3, June 1982.

**Discussor's name:** I. ANDERSON

**Comment/Question:**

1. Were the effects of mutual coupling between chaff elements modelled in your predicted results?
2. What was the polarisation dependency of your measured results?

**Author/Presenter's reply:**

1. Mutual coupling is only material for a very short time after the charge explodes. As the particles are pushed apart from each other by the gases from the explosion the mutual coupling is rapidly reduced. This effect is modelled, but only for a very limited duration, and a form of bulk approximation is used.
2. The predominating polarisation response was (I believe) horizontal, that is, the plot reflects the resonances of a bloom measured using HH polarised radiation. However, the reference to the "Butters" paper would clarify this point.

**Discussor's name:** G. WYMAN

**Comment/Question:**

You indicate that the decorrelation interval for the physical entities is very short. Could you comment on the macroscopic properties which might yield more stable parameters?

**Author/Presenter's reply:**

The autocorrelation function is the Fourier transform of the power spectrum, and both are bell shaped. The decorrelation interval actually depends on the chosen intersection threshold with the autocorrelation bell shaped curve. The parameters quoted are derived from measured values of Doppler power spectrum from trials data. There is nothing unstable about this. The parameters are relatively invariant through the bloom phase. The macroscopic parameters that are likely to govern this feature are the dynamic properties of the chaff particles under the influence of gravity and airflow.

## Analysis of experimental data for NCTR target modelling

Michel MORUZZIS, Jean-Claude GUILLEROT, Christian LESTRADE  
Thomson-CSF/ AIRSYS  
7 rue des Mathurins, BP 10, Bagneux, France

### ABSTRACT

Non Cooperative Target Recognition (NCTR) can be performed through different techniques of radar elementary signal analysis such as Doppler spectrum analysis (like Jet Engine Modulation -JEM- or Helicopter Rotor Modulation -HERM-), High Range Resolution (-HRR- providing a "down range" profile of the target), Inverse Synthetic Aperture Radar (-ISAR-, providing a "cross range" profile), and combinations of the above techniques as for instance HRR with ISAR to produce a two dimensional image of the target.

Performance robustness is one of the key issues in designing a target recognition system; such a system must use a set of reference features (database) more or less directly derived from actual measurements.

When interpreting actual radar measurements it is important to take in account a number of environmental conditions such as the target aspect angle, clutter surroundings and radar characteristics (parameters, waveform and processing). Obviously one must take the same precaution when building the reference database and also when it is used for the recognition of an unknown target.

In this paper one presents some experimental results obtained for different radar bands and different NCTR techniques. These results are then analysed in terms of robustness and one draws some trends regarding the kind of features which can be used for NCTR. Finally one suggests a method for designing NCTR systems based on both target and measurement conditions modelling.

## 1 INTRODUCTION

### 1.1 NCTR requirements

Recent events have highlighted increasing needs for better situation assessment, especially when fast military decision must be taken. More precisely, it is necessary to get:

- more detailed threat assessment,
- less risks of fratricide actions,
- shorter reaction delays,
- optimised riposte (weapon assignment, ECCM selection)
- optimised surveillance (matching of waveforms and processing to the target in order to improve the detection, localisation, identification, resistance to

interception -by ESM-, and aggression -by ECM and ARM-)

NCTR concept arose from the possible lack of information normally provided by cooperative means (such as transponders) when such means are not used for operational reasons (risk of interception by adverse IFF or ESM) or when they do not work properly (malfunction, destruction).

Thus non cooperative sensors are requested to participate to target recognition with the maximum efficiency.

### 1.2 The role of radar in NCTR

Radars have a prime role in this challenge because they are able to detect and identify targets at long range and in all weather conditions. Furthermore they can supply several complementary data sources regarding the target identity; one can split the NCTR sources in two broad categories: signal based sources and data based sources;

#### 1.2.1 Signal based NCTR sources

By "signal based" sources it is meant any information which can be supplied by a specific signal processing function, the result of which being finally expressed as a part of the plot created by the plot extractor. Among signal based NCTR techniques, one can distinguish Doppler and Imagery techniques.

- Doppler techniques:

They are used to get informations relative to the spectrum of mobile parts (power plant) of the target (engines, rotor, ...).

Most known methods are JEM (Jet Engine Modulation) and HERM (Helicopter Rotor Modulation) analysis; these methods are applied for targets such as aircraft (turbofan, propellers,...) and helicopters (main and/or tail rotor).

Depending on the available analysis time, on the waveform characteristics (RF, PRF) and on the spectral analysis method used (Fourier, High Resolution, Time-Frequency,...) one may extract either simple informations such as the principal frequency (related to the engine rate time its number of blades) or more refined ones such as elementary blade or hub spectrum which may inform on the number and type of blades and the type of hub.

- Imagery techniques:

They are also often called "High Resolution" techniques because they aim at giving a more detailed "image" of the target than often done by conventional radars (or radar processing).

Contrary to optical sensors, a radar image can be 1D, 2D or 3D, depending on which axis (or combination of axis) are used.

Imagery techniques aim at producing some level of target resolution where one separates as much as possible the elementary target components (or "scatterers"). Elementary radar imagery axis are slant and crosses (azimuth and elevation) ranges.

Basic methods used on slant range axis or often called High Range Resolution (HRR) techniques and produce some target range profile based on either coherent or non coherent processing. HRR is based on wideband signals, which can be produced by different methods such as Short pulses, Wide instantaneous spectrum or Synthetic Bandwidth.

Cross range analysis can be made through Inverse Synthetic Aperture Radar (ISAR) or high resolution Direction Finding. ISAR is a kind of long term Doppler analysis based on the fact that different scatterers of the same target can have different radial velocity depending on the overall target velocity and heading with respect to the radar.

Above methods can be applied together with polarimetric radar which means that instead of analysing the scalar target RCS one uses its backscattering complex matrix. Available radar polarimetric techniques are based on single polarisation transmission and dual reception, with some transmission polarisation agility. Polarisation analysis can also be used alone for improving clutter rejection.

### 1.2.2 Data based NCTR sources

"Data based" sources refer mainly to the tracking processing which can compute target kinematics such as height, velocity, rate of turn,...; used alone or in conjunction with external reference (digital terrain map, airways,...) and compared with an a priori data base describing the normal behaviour of known targets (or classes of targets) they may supply useful information for target classification.

### 1.2.3 NCTR processing

An operational NCTR processing will contain several subfunction such as:

- Data fusion:

As long as the NCTR sources can be different (see above) and can change from scan to scan (due to the

sensor management), it is necessary to merge all available data at the current time (updating time).

The simplest example which can be given deals with merging NCTR informations coming from the signal processing (for example a range profile based NCTR information) and put in the last plot associated to the track with some target class assessment evaluated from the track state vector (location, speed and acceleration).

- Time integration:

This function, which can be seen as a part of the tracking update function, is dedicated to producing the best estimate of the target class by integrating every NCTR data assigned to the track since its initiation; this function is preferably implemented in a recursive structure.

- Waveform management:

Signal based NCTR sources are potentially powerful means but may need some time spent to analyse the target, at a given scan. This time is in general greater than the time just required by a simple detection and location waveform, it is therefore necessary to manage, for each track, the best waveform to use for the next scan. This management must rely on an analysis of the current target recognition level, on the required level and on the potential of each possible waveform regarding the current target status (location, speed, aspect angle, heading,...).

## 1.3 Radar NCTR processing challenges

When more and more refined target recognition level is needed, requirements regarding the reference target data base becomes more critical. A simple illustration is given when considering JEM processing, for which a number of parameters must be known for as many targets as possible (for instance the number of engines, the possible rotation rates and the number of blades). More difficult technical problems arise when considering imagery techniques for which no relevant information can be drawn if no real measurement is made.

Establishing and updating a precise target signature data base is then somehow challenging, especially if one wants to consider the strong variations which can arise with target aspect angle, radar frequency, clutter and/or jamming environment.

For signal based NCTR, and when some accuracy is needed (high resolution for Doppler, Range, or ISAR processing), target motion compensation methods become critical. If no attention is paid to this problem, it will soon give the practical resolution predominant factor. Available compensation techniques rely on both target motion assessment (using tracking data) and signal likelihood evaluation (autofocus based methods).

For the overall NCTR function, great attention must be paid to data quality (or accuracy) handling and processing robustness.

## 2 EXPERIMENTAL RESULTS

In order to illustrate some data which can be obtained with existing long range operational systems, one shows hereafter one example taken from a VHF Surveillance Radar (RIAS) and from an S-Band Multifunction Radar (SMR).

### 2.1 RIAS

#### 2.1.1 Radar characteristics

RIAS stands for "Radar à Impulsion et Antenne Synthétique", which can be translated in English by "Synthetic Pulse and Antenna Radar".

It is developed in cooperation between ONERA ("Office National des Etudes et des Recherches Aérospatiales") and Thomson-CSF for fulfilling the objectives of a long range air defence radar.

It uses two sets of omnidirectional VHF antenna elements, arranged into two horizontal concentric circles (one for the transmission and the other for the reception).

The use of orthogonal codes (the choice made here was to use different frequencies) on each antenna element allows, by digital processing of received signal, to focus the energy in space (Range, Azimuth, Elevation). This process can be seen as a simultaneous 2D Digital Beamforming (Azimuth, Elevation) and pulse compression (Range).

4D (Range, Azimuth, Elevation, Doppler) processing is performed in order to produce the detection and localisation of any targets within the radar coverage.

#### 2.1.2 Experimental data

Left side of Figure 1 shows the flight path followed by a small jet aircraft, flying at a constant height and velocity, about 100 km away from the radar; the arrow indicates a part of the trajectory where the aircraft made two times the same manoeuvre (left turn); the right plot of Figure 1 is a zoom of these passes. It can be seen that the two trajectories are almost the same, with some differences due to the test conditions; there is about half an hour between the two passes.

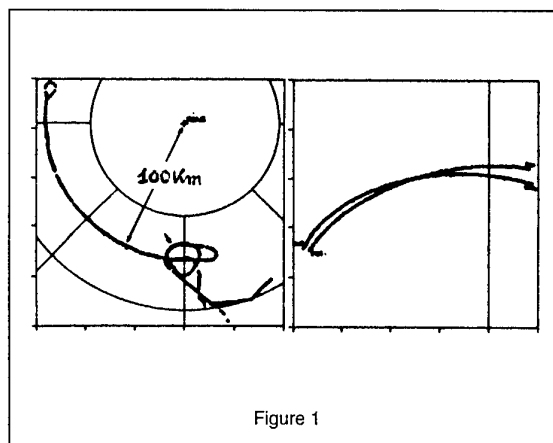


Figure 1

Figure 2 shows two plots of the signal amplitude as a function of the Doppler velocity. Because the conditions are identical in both cases, amplitude plots can be considered as proportional to the RCS, with the same scale factor.

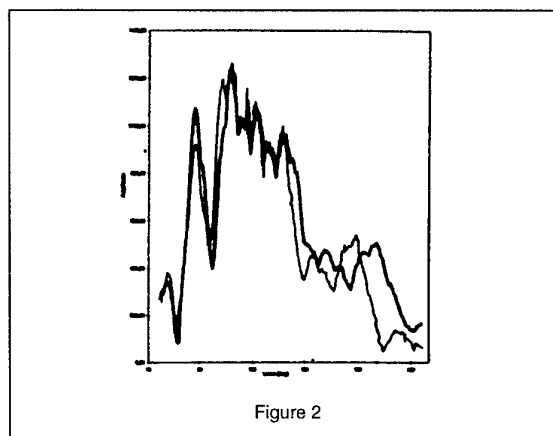


Figure 2

Figure 3 is a plot of an airliner trajectory flying at a constant height and velocity; during this trajectory, the aspect angle (mainly the yaw angle) nearly varied from 0 to 180°.

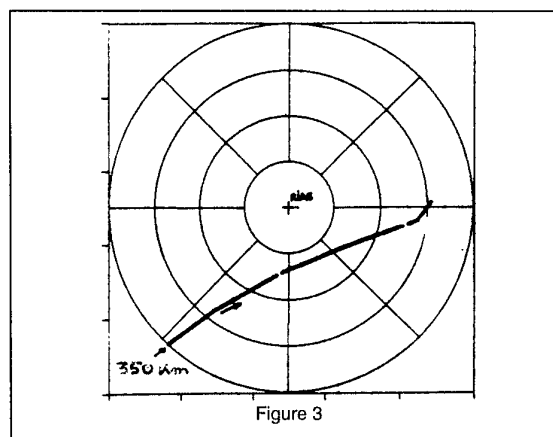


Figure 3

Figure 4 contains, on the left side, a plot of the measured RCS as a function of the aspect angle (reconstructed from the trajectory) and on the right side the same plot for a simulated airliner.

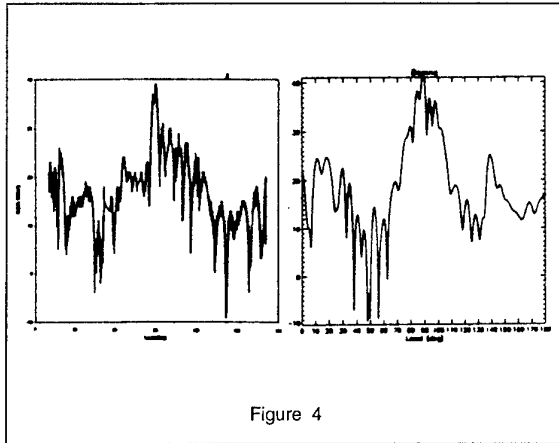


Figure 4

The RCS was reconstructed from the signal amplitude recorded after processing (tracking) corrected by the propagation (range, ground effects) and measurement (T/R and processing gains and losses) factors.

The simulation model used for this comparison is based on a simple decomposition of the target into elementary components, each component being located on the target and being described by its RCS radiation pattern; the resulting target RCS for a given aspect angle and a given frequency is computed as the complex combination of these elementary scatterers.

### 2.1.3 Analysis

Results shown on Figure 2 illustrate the very good reproducibility of the amplitude value for the same target when it is seen in the same conditions (range, azimuth, elevation, velocity, aspect angle, frequency, propagation and processing conditions,...). It would be noticed that an even better match can be obtained with a more precise reconstruction of the aspect angle (the results are plotted as a function of Doppler velocity which is not exactly proportional to the aspect angle).

As long as the amplitudes are obtained in the same conditions for both passes, it can be derived that the RCS plot is also a very reproducible parameter.

This RCS variation could be used by ISAR processing in order to generate a cross-range profile; ISAR performances are driven by the following relationships:

resolution:

$$\delta r_T = \alpha \cdot \lambda / (2 \cdot \Delta\theta) = \alpha \cdot \lambda \cdot R / (2 \cdot V_T \cdot T_{mes}) \quad (1)$$

ambiguity:

$$\Delta r_T = \lambda / (2 \cdot \delta\theta) = \lambda \cdot R / (2 \cdot V_T \cdot T_s) \quad (2)$$

In equation (1) and (2)  $\Delta\theta$  and  $\delta\theta$  represent, respectively, the angular target aspect angle variation during the analysis time and the sampling period.  $\lambda$  is the wavelength,  $R$  the target slant range,  $V_T$  is the target tangential velocity,  $T_{mes}$  is the analysis time and  $T_s$  is the sampling time.

The term  $\alpha$  in equation (1) is an efficiency coefficient whose value depends on the kind of processing used ( $\alpha$  is close to 1 for a conventional Fourier analysis, it may be close to 0.2 for a High Resolution method).

One of the most important issues in designing an ISAR system is related to the required analysis time. It can be seen, from equation (1), that this analysis time must verify the following relationship:

$$T_{mes} = \alpha \cdot \lambda \cdot R / (2 \cdot V_T \cdot \delta r_T)$$

ISAR is operationally feasible only for specific conditions in which the target aspect angle varies with time (for instance this is not applicable to target flying towards the radar).

When ISAR constraints (aspect angle variations) are not fulfilled, it would be necessary to extract another parameter such as the instantaneous RCS. This can be done by applying to the output signal amplitude a scaling coefficient taking in account every measurement gains and losses (see above).

The comparison of experimental and simulated results (respectively left and right sides of Figure 4), shows some similitudes, although the exact type of the airliner is not known for the experimental case.

In particular, the order of magnitude of the RCS is similar for both "nose-on" and side aspects, and the angular correlation is also comparable. Then it can be expected that after having modelled the exact target, one could have obtained a level of comparison compatible with at least a coarse classification (for instance airliner vs. fighter).

## 2.2 SMR

### 2.2.1 Radar Characteristics

A 3D S-Band Long Range Electronic Scanning Multifunction Radar was modified in order to generate High Range Resolution (HRR) waveforms. The basic HRR waveform is a set of  $N$  consecutive bursts, each burst containing  $P$  pulses transmitted at a constant PRF and RF; the RF is modified from burst to burst.

The signals (I,Q components) were recorded after A/D converters, within a fixed size window whose centre was controlled by a cooperative tracking radar locked onto the target(s).

The processing chain applied to the recorded signal contains the following sub-processing:

- MTI (Moving Target Indicator) to reject non moving clutter,
- tracking module to isolate the range bins containing the target signal,
- Doppler processing to separate the target airframe echo from other spectral components (e.g. JEM spectral lines),
- phase correction to compensate the phase variation due to target motion (this correction is necessary for the coherent range processing),
- coherent (and non coherent) HRR processing which produce respectively the target range profile and range profile autocorrelation.

### 2.2.2 Experimental data

The results presented below correspond to range profiles of a jet aircraft flying toward the radar at a constant speed and height; its slant range is approximately 50 km.

The X axis represents the normalised range, the full scale is 60m.

The Y axis represents the range profile level in dB, referenced to the maximum (the full scale is 30dB).

In order to evaluate both range profiles stability and target recognition attributes, one shows on Figure 5 the results obtained on different consecutive antenna scans.

Figure 5 represents 300 MHz profiles corresponding to consecutive scans and Figure 6 represents the envelope of all profiles.

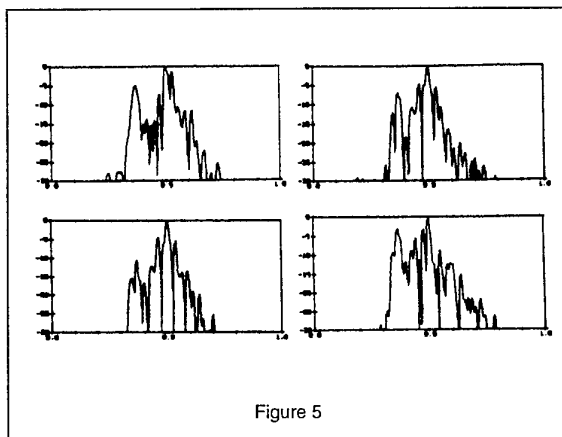


Figure 5

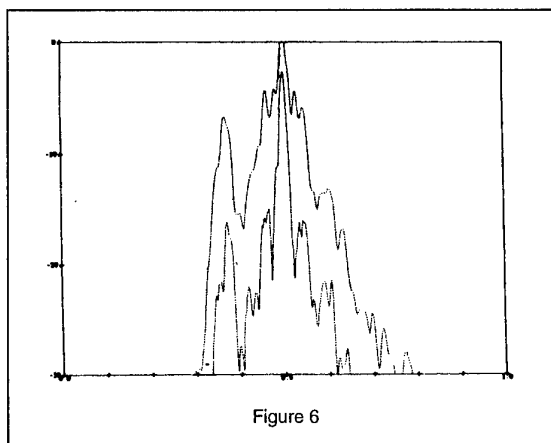


Figure 6

### 2.2.3 Analysis

It can be seen on Figure 5 that range profiles change from scan to scan; it is well known that range profiles can vary with the target aspect angle; a first order of the angular variation is given by considering the target as an antenna having an extension equal to its cross length. The equivalent target "3dB beamwidth" is then given by the following relationship:

$$\theta = \lambda / 2 L$$

( $\theta$  in radians,  $\lambda$  -wavelength- and  $L$  -target cross length- in meters)

Range profiles obtained on the same target seen under two aspect angles separated by more than  $\theta$  can become different due to the different scatterers amplitude and phase combinations.

An application to S-Band and a 10m target leads to a value of  $\theta$  of about  $0.3^\circ$ , which explains the variations which can be observed on actual profiles because such an angular variation may be due to the target flight path variations from scan to scan.

However, a general "shape" remains constant from scan to scan; a way to represent this shape is to plot the profile "envelope" (see Figure 6); it can be seen that three broad areas (nose, centre and tail) have different average cross section; such "envelope" could be used for labelling the target with respect to a "model". Another parameter which remains stable is the profile "length" which can be computed by comparing the signal to a threshold.

## 3 THE REFERENCE DATABASE CHALLENGE

Radars already allow the generation of high resolution signal which should be used for NCTR purpose.

However the degree of complexity of the problem is such that no operational NCTR already exists and that even not any performance can be guaranteed in that area.

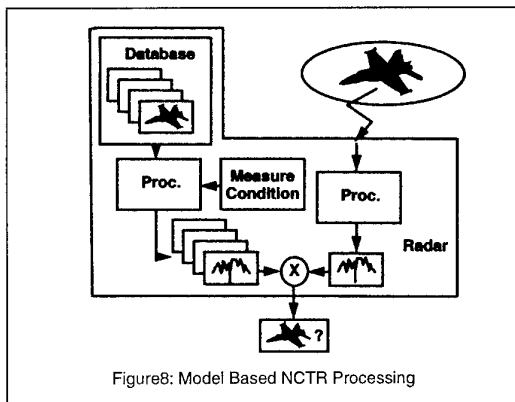
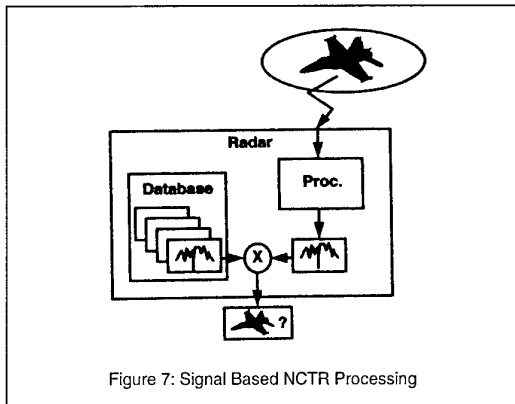
The present chapter tries to highlight some aspects of this problem and suggests some possible ways to overcome this challenge.

One will consider the most difficult case were it is aimed to identify the target itself (which means for instance that one wants to know if the unknown target is either a "Mirage F1" or a "Mirage 2000").

One will often use the following terms: "Signal Based Processing" -SBP-, and "model Based Processing" -MBP-:

- SBP is a class of processing in which the radar signal (Doppler Spectrum, Range Profile,...) is compared to a reference signal data base,
- MBP refers to another class of processing in which one uses some target models and a set of methods allowing to dynamically generate the corresponding reference signal which can then be used for comparison with the signal to identify.

Figures 7 and 8 gives a schematic representation of these two generic classes of processing.



### 3.1 SBP Combinatorial explosion

There are about 1000 different flying objects when one considers aircraft, helicopters, missiles,...

If one takes the simple example of range profiling, it was shown that range profiles can change with target

aspect angle. For a given wavelength  $\lambda$  and a target "size"  $L$ , it was shown that one should have different reference profiles as soon as the aspect angle is changed by  $\lambda/2L$ .

Consider an "average" target size of 10m ( $L=10m$ ), and let us consider the "average" case of an S-band radar ( $\lambda=0.1m$ ); then the aspect angle resolution is approximately  $0.3^\circ$ .

For all possible aspect angles (pitch, yaw) and one polarisation, that leads to about  $5 \cdot 10^5$  different range profiles.

If one assumes some left/right symmetry (for aerodynamic reasons) one gets the order of magnitude of about  $2.5 \cdot 10^5$  profiles.

It is assumed that a range resolution of 0.5m will be necessary for identifying the targets. Thus a range profile would contain at least 20 points for a 10m long target. Assuming that one byte is required for describing one range bin, one finds that 20 bytes are necessary for representing one range profile.

Multiplying the number of targets ( $10^3$ ), the number of profiles per target ( $2.5 \cdot 10^5$ ) and the number of bytes per profile (20) leads to a 5 Gb database.

Such a database, whose generation and management becomes questionable, must be set up again for another radar in the same band if it uses another bandwidth or polarisation, and again for other radar bands.

Furthermore it was assumed so far that one could directly correlate the unknown profile with a number of reference profiles. In that case both profiles must have been produced with the same process and in the same conditions.

If one considers what can happen onto a real radar signal (thermal noise, clutter effects, hardware limitations -such as stability-, motion compensation errors, ..) and thus what should have been taken in account for generating databases for such SBP systems clearly shows that this approach is almost impossible.

The same conclusion could have been drawn for Doppler Spectrum analysis (keeping in mind for instance that the target spectrum foldover will depend on the target speed and on the radar waveform, and that the output spectrum may be polluted by clutter signal).

In conclusion it appears that such Signal Based Processing approach has severe drawbacks, because the number of objects is large, but mainly because the conditions in which it can be obtained are incredibly numerous.

### 3.2 The MBP approach

In the MBP approach one uses target models designed in order to be, as much as possible, independent of the radar; the same model will be used for any kind of NCTR level (from simple narrowband RCS or Doppler template analysis up to 3D polarised high resolution imagery).

The main advantage is that one needs only one model for one target and for a given radar band (for instance some models can be used from L-band up to X-band signal). In our 1000 targets situation that means that one would have to set up 1000 models.

A (very) simple example of such a model is the "hot spot" model where the target is described by a number of scatterers, each one being described by its coordinates with respect to the target centre of mass, and by its reradiating pattern (giving its RCS -or its scattering matrix- as a function of pitch and yaw angles).

More sophisticated models exist, up to very detailed representation of the target surface currents and EM computations using 3D Integrals.

Let us analyse the amount of data required for solving our 1000 targets problem.

Evaluating the necessary data for representing one "average" target with such a model can be made only when the model is known. The choice of a "good" model is one of the key topics which must be addressed for the MBP approach.

Heuristically, when one tries to model a target by defining a number of elementary representative components (such as the fuselage sides, the air intakes, the wing leading and trailing edges,...), one needs no more than 10 to 100 elements.

Let us assume that 50 is a reasonable average.

For each element, one needs to define its coordinates (3 values), its orientation (3 values), the type of canonical RCS model to be used and its parameters.

Again the quantity of data will depend on the type of canonical model. Let us assume that an "average" canonical model requires 10 parameters. If one adds the coordinates, orientations, etc.,..., one finds about 20 parameters per "average" canonical model.

Assuming that each parameter can be represented with one byte, we find that about 1000 bytes (50 elements \* 20 bytes/ element) are necessary to model an "average" target.

For such a MBP approach, the total model database will then require no more than about 1 Mb (1000 objects \* 1000 bytes/object).

This rather small database can be easily managed in an operational radar system. However there remains three key issues:

- this database must be produced; there is of course a production and updating problem, but the most difficult point to solve is the choice of a "good" model able to represent the reality. This choice can not be made independently of the NCTR objectives; it must be made by a comparative approach on a number of "representative" targets for which real data are available,
- the database must be used in real time to simulate the signal in the same conditions as the unknown signal; this point can be solved by using parallel architecture (the same process must be applied to several target models), and preprocessing in order to reduce the number of models to be run,
- it must be used in the same conditions as the unknown signal; leaving apart the radar parameters (for instance the waveform) which are easily known once the measurement is made, that implies the use of specific processing designed to provide the instantaneous environmental conditions (target aspect angles, clutter and jamming properties, ...) and its uncertainties.

The choice of a "good" model would be made in relation with the NCTR objectives. The following approach can be used as a general guideline:

Let  $A_i$  and  $M_i$  be the signal corresponding respectively to the actual target (i) and its model (the signal can be a range profile, a Doppler spectrum or any other NCTR signal); if  $L_{ij}$  represents the "distance" between  $M_i$  and  $A_j$ , the model  $M_i$  will be sufficient as soon as:

$$L_{ii} < L_{ij} \quad \forall i \neq j$$

### 4 CONCLUSIONS

In order to provide more efficient informations during crisis times, it is necessary to improve the level of knowledge data that NCTR sensors can produce. Among these sensors, radars have a crucial role because they can provide detection, localisation and target recognition data at long range and in all weather conditions.

Existing radar systems can be improved in order to provide useful informations such as cinematic derived target recognition data and RCS data; however, In order to be robust these informations must contain a quality factor; estimating this quality factor in real time is certainly the key issue in the design of a reliable NCTR operational processing based on radar retrofitting.

Furthermore, existing radar technology allows the generation of high resolution target signatures (Doppler, Down-range and Cross-Range), providing 1D, 2D or even 3D electromagnetic "images" of the target.

Experiments in real conditions have undoubtedly proven that these signatures are representative of the measured targets. However the multitude of measurement conditions in which they can be obtained is a severe drawback for the design of an operational NCTR system based on a direct signature database correlation procedure.

In order to overcome this challenge, this paper suggests a "model based processing -MBP-" approach.

This approach relies on the use of target physical models which are independent of the measurement conditions (aspect angle, radar, waveform, environment,...). The amount of data required by a MBP database is shown to be easily tractable for operational systems.

This paper also highlights the key developments related to the MBP approach:

- choice of the representative target physical model,
- production and updating of the target model database,
- estimation of measurement conditions in real time,
- real time reference signal and quality computation using parallel processing architectures,

#### **Acknowledgements**

We gratefully acknowledge the French "Délégation Générale à l'Armenent" (DGA) who participated to the funding of the radar developments presented in this paper.

## **Banc à Haute Résolution (BHR) pour l'analyse de cibles marines**

### **High Resolution Bench (HRB) for the Analysis of Ship Signatures**

Christian DELHOTE, Frédéric PERRET, Jean ISNARD  
THOMSON-CSF Applications Radar  
6, rue Nieuport - BP 86  
78143 Vélizy-Villacoublay Cedex  
France

#### **1. SOMMAIRE**

La maîtrise de la signature radar de bâtiment de surface est un élément clef pour leur survivabilité. Après avoir fait un bref rappel des motivations pour la connaissance et le contrôle de cette signature, trois principales méthodes d'analyse sont exposées avec leurs avantages et inconvénients. Puis dans les paragraphes suivants est décrit en détail le BHR (Banc à Haute Résolution), moyen de mesure polarimétrique large bande, développé par THOMSON-CSF Applications Radar, mis en oeuvre par les services techniques de la Marine Nationale Française, et qui permet l'analyse fine des signatures des bâtiments y compris dans des environnements de leurres électromagnétiques d'auto-protection. Après une description physique du moyen de mesure et de ces modes d'utilisation, les caractéristiques des mesures accessibles par le BHR sont exposées ainsi que les logiciels d'analyse fine de ces signatures. Puis les données techniques des composants principaux du radar sont détaillées et enfin est rappelé succinctement le problème de calibration que pose ce type de moyen de mesure polarimétrique large bande.

#### **1. SUMMARY**

The control of the radar signature for surface vessels is a key factor to their survivability. After a short reminder about the motivations for the knowledge and control of this signature, three main analysis methods are presented along with their advantages and drawbacks. Next, the HRB (High Resolution Bench) is described in detail as a large bandwidth polarimetric measurement equipment, developed by THOMSON-CSF Applications Radar, operated by the French Navy technical services, and which enables a refined analysis of the vessels signature, even in an environment comprising self-screening electromagnetic decoys. After a description of the measurement instrument and its operating modes, the characteristics of the measurements which the HRB can provide are presented as well as the refined analysis software for these signatures. Next the technical characteristics for the main components of the radar are detailed. Finally, the calibration problem posed by this type of large bandwidth polarimetric measurement equipment is briefly discussed.

## 2. INTRODUCTION

### 2.1 Maîtrise des signatures

La connaissance et le contrôle de la signature radar de bâtiment de surface est un élément clef pour leur survivabilité.

En effet, la connaissance de la SER d'un bâtiment permet de dimensionner de manière plus efficace ses systèmes d'armes et plus particulièrement ses moyens de leurrage électromagnétique d'autoprotection. L'analyse fine et la compréhension physique de la signature radar permet, quant à elle, de mettre en oeuvre des moyens de réduction de signature soit en installant des matériaux absorbants sur les zones localisées à haut pouvoir réfléchissant, soit en agissant sur les formes même du bâtiment lors de sa conception.

### 2.2 Méthodes d'analyse de signatures

Trois grandes méthodes sont classiquement utilisées pour obtenir cette connaissance de la signature, chaque méthode ayant ses avantages et inconvénients ; la première est l'analyse théorique et la modélisation électromagnétique, la deuxième est la mesure en laboratoire sur des maquettes à échelle réduite à des longueurs d'onde ayant subi la même grandeur réelle, enfin la troisième est la mesure grandeur réelle.

#### 2.2.1 Modélisation électromagnétique

Le calcul de la S.E.R. d'une cible radar comporte une étape d'analyse géométrique de la cible et une étape de calcul des interactions. Ces étapes ne sont pas indépendantes dans le sens où le traitement géométrique doit prélever dans le modèle de la cible les informations nécessaires aux calculs d'interaction (les phénomènes de diffraction dépendent étroitement du type de discontinuité).

Le logiciel ALBEDO qui est utilisé à THOMSON-CSF Applications Radar a été originellement conçu pour modéliser des objets volants et calculer des S.E.R. pour les bandes de fréquences radar (bandes L, S, C, X...).

La modélisation géométrique de la surface de la cible est effectuée à l'aide de polynômes quadratiques rationnels paramétriques en coordonnées homogènes.

La description d'une surface composite est effectuée par le raccordement de zones différentes, les conditions de raccordement entre deux zones étant spécifiées dans les données. Un exemple de modèle géométrique d'un bâtiment est donné figure 1. Cette représentation permet d'aboutir à des modèles très précis dans le détail.

Les phénomènes de diffraction à prendre en compte dans les calculs d'interactions dépendent du type de singularité

que présente la cible. Il est donc particulièrement important de faire une analyse géométrique de la cible qui mette en évidence le type de singularité que présente cette cible.

L'ensemble du traitement est basé sur la notion de périmètre de visibilité : ce périmètre, défini pour chaque zone, sépare ce qui est vu de ce qui est caché. L'analyse de la raison de disparition d'une partie du modèle permet ensuite de reconnaître le type de singularité à prendre en compte dans les calculs d'interactions.

Les parties régulières et vues de surfaces sont discrétisées en triangles plans sur lesquels on effectue les calculs d'interactions précisés ci-dessous. Les arêtes sont de la même façon approchées par des segments de droites.

Le nombre d'éléments plans nécessaires à un bon calcul des interactions est généré automatiquement par ALBEDO, compte tenu de la fréquence et des courbures de surfaces.

Les calculs d'interactions sont effectués à partir des développements asymptotiques haute fréquence de l'électromagnétisme, c'est-à-dire essentiellement, la Théorie Physique de la Diffraction (T.P.D.) mais également la Théorie Géométrique de la Diffraction (T.G.D.) dans certains cas particuliers, ces théories étant étendues au cas des matériaux pénétrables que sont les absorbants.

Dans le cadre de la T.P.D., les contributions dominantes, dues à la réflexion, sont calculées par l'Optique Physique (O.P.).

Les effets de diffraction d'arêtes sont calculés par la Méthode des Courants Equivalents (M.C.E.), qui consiste à définir sur l'arête un courant fictif représentant les modifications du courant induit dues à cette arête.

Les phénomènes pris en compte dans les calculs d'interactions sont les suivants :

- réflexion (au sens de l'OP) de surfaces quelconques,
- diffraction d'arêtes vives de formes quelconques,
- réflexions doubles (dièdres rentrants),
- réflexions de surfaces recouvertes d'absorbant,
- diffractions d'arêtes vives recouvertes d'absorbant.

La modélisation des navires à flot exige d'inclure la réflexion sur la mer si l'on veut estimer correctement les niveaux de S.E.R. Cela consiste à sommer la réponse monostatique de l'incidence directe et la réponse bistatique de l'incidence réfléchi par la surface de la mer considérée comme parfaitement conductrice.

La modélisation électromagnétique appliquée à des bâtiments de surface pour des fréquences radar assez hautes se heurte à un certain nombre de difficultés :

- le degré de précision imparfait du modèle géométrique ainsi que des calculs électromagnétiques car les dimensions de l'objet sont très importantes par rapport à la longueur d'onde ;
- la modélisation en général approximative de l'environnement du bâtiment : la mer ou les leurres ;
- la modélisation toujours difficile des absorbants.

### 2.2.2 Les mesures à échelle réduite

Des maquettes à échelle réduite des bâtiments sont réalisées et des mesures en général en laboratoire sont faites à des longueurs d'onde ayant subi le même facteur d'échelle. Ce type de mesure se heurte également à un certain nombre de problèmes somme toute très voisins de ceux de la modélisation électromagnétique :

- le degré de précision imparfait de la maquette ;
- l'environnement du bâtiment mal pris en compte (mer, leurres,...) ;
- l'influence des absorbants mal évaluée, ceux-ci ayant des effets fondamentalement non linéaires, le facteur linéaire d'échelle n'est plus valable.

### 2.2.3 Les mesures à échelle réelle

Les mesures à échelle réelle permettent de résoudre les problèmes mentionnés précédemment, par contre leurs inconvénients principaux sont, une certaine lourdeur de mise en oeuvre (disponibilité des bâtiments, disponibilité des moyens d'essais, campagne d'expérimentation longue...) et un échantillonnage souvent incomplet de l'ensemble des paramètres à prendre en compte (fréquence, polarisation, attitude du bâtiment,...). Il est donc très important que le moyen de mesure radar soit d'un emploi quasi tactique (facilement déplaçable et installable avec une infrastructure réduite) et soit capable d'acquiescer le plus rapidement possible des mesures avec différents paramètres électromagnétiques (fréquence, polarisation, résolution...).

La suite de cet article concerne la description du moyen de mesure BHR (Banc à Haute Résolution) développé par THOMSON-CSF Applications Radar pour le compte des services techniques de la Marine Nationale Française et actuellement en service opérationnel.

## 3. PERFORMANCES DU BHR

### 3.1 Modes d'utilisation

Le BHR est un moyen d'analyse de signatures de bâtiment y compris dans des environnements de leurre électromagnétique d'autoprotection. Il doit permettre :

- d'accéder à une meilleure connaissance des SER des bâtiments actuels afin entre autre de mieux dimensionner les leurres électromagnétiques ;
- d'accéder à une analyse fine des zones réfléchissantes des bâtiments actuels permettant de mettre en oeuvre des absorbants pour réduire la signature (exemple figure 2) ;
- d'accéder à une meilleure compréhension sur l'origine physique des zones à haut pouvoir réfléchissant afin d'optimiser la conception des futurs bâtiments notamment en agissant sur leurs formes (par exemple frégate La Fayette) ;
- d'analyser le comportement et mesurer l'efficacité du déploiement de leurres électromagnétiques ;
- de mesurer in fine l'efficacité des actions de discrétion mis en oeuvre sur les bâtiments.

Pour ce faire, le radar est conçu pour un emploi soit en extérieur, soit en intérieur. Trois grands types de configuration de mesure sont possibles :

- *Mesures en chambre anéchoïde*

Les mesures en chambre consistent à mesurer avec une très haute résolution la S.E.R de contributeurs présents sur le bâtiment (échelle, feux de navigation...) et à tester l'efficacité de différents absorbants, ces contributeurs étant à très courte distance.

- *Mesures à quai*

Les mesures à quai consistent à évaluer puis éventuellement à réduire la contribution à la S.E.R. globale de certaines zones spécifiques du bâtiment (celui-ci étant à courte distance).

- *Mesures en mer*

Les mesures en mer consistent à évaluer la signature d'un bâtiment à la mer et à analyser sur cette signature l'influence de la fréquence et l'attitude de la cible (présentation et roulis / tangage). Ces mesures sont complétées par des situations opérationnelles associant des cibles et des contre-mesures électromagnétiques.

### 3.2 Description physique

Le BHR est constitué de trois ensembles principaux (notés A, B, C) et d'une cabine d'exploitation climatisée faisant de BHR une station totalement autonome d'analyse (figures 3 et 4). Chaque ensemble est aisément décomposable en éléments constitutifs portables par une ou deux personnes afin de faciliter la manutention pour l'installation et les déplacements.

- ▶ Le premier ensemble principal (noté A, figure 5) est constitué :

- d'un aérien comportant les antennes d'émission réception radar, une caméra vidéo et un coffret contenant la partie émission réception hyperfréquence ;
  - d'un positionneur ;
  - d'un trépied support.
- Le deuxième ensemble principal (noté B, figures 3 et 4) est constitué :
- de la chaîne pilotée,
  - du récepteur bande de base et des codeurs.
- Le troisième ensemble principal (noté C, vue partielle, figure 6) est constitué :
- du séquenceur radar,
  - d'un pupitre de commande radar et d'une visualisation de contrôle (figure 6),
  - d'un moyen d'enregistrement,
  - d'un calculateur d'exploitation avec ses logiciels d'analyse de signature (figure 6).
- La cabine d'exploitation est équipée de coins de conteneurs normalisés pour l'arrimage et l'élingage. Ses dimensions sont largeur et hauteur 2,4 m (gabarit ISO), longueur 4 m.

Pour le transport l'ensemble du radar (A, B, C) se loge dans la cabine, le poids total du radar avec sa cabine est inférieur à 3 tonnes. Pour des mesures en extérieur seul l'ensemble C est à l'intérieur de la cabine ce qui laisse une plus grande liberté d'installation pour l'aérien radar (A) et le coffret, non liés rigidement à la cabine, la distance possible entre l'aérien et la cabine pourrait aller jusqu'à 100 m.

Les ensembles A et B sont donc conçus pour être étanches et fonctionner dans la gamme de température  $-20^{\circ}$ ,  $+40^{\circ}$ . L'énergie nécessaire au fonctionnement du radar est inférieure à 10 kVA, 380 V / 50 Hz triphasé. Enfin, pour des mesures en chambre la cabine n'est plus nécessairement utilisée, les ensembles A, B, C étant installés directement dans la chambre.

### 3.3 Caractéristique des mesures

Les caractéristiques principales des mesures obtenues par le BHR sont les suivantes :

- Gamme de fréquence : 8 - 18 GHz
- Pas en fréquence : réglable de 10 MHz à 10 GHz
- Temps de commutation de fréquence : 50 ms
- Résolution distance :  $\left\{ \begin{array}{l} 1 \text{ m, } 6 \text{ m, } 20 \text{ m} \\ 10 \text{ cm en chambre} \end{array} \right.$
- SER mesurée : matrice de polarisation HH, HV, VH, VV
- Cadence de renouvellement : 200 Hz
- Précision :  $\pm 2$  dB (sur une SER de  $10 \text{ m}^2$  à  $10 \text{ km}$ )
- Sensibilité :  $S/B = 22$  dB sur une SER de  $10 \text{ m}^2$  à  $10 \text{ km}$

- Datation : interne ou synchronisation externe (IRIGB).
- Poursuite distance : automatique par D.O. externe ou manuelle par opérateur.

Aérien :

- ouvertures site gisement :  $\left\{ \begin{array}{l} 2,5^{\circ} \text{ à } 18 \text{ GHz} \\ 5^{\circ} \text{ à } 8 \text{ GHz} \end{array} \right.$
- couverture :  $\left\{ \begin{array}{l} \pm 110^{\circ} \text{ en gisement} \\ - 30^{\circ} \text{ à } +19^{\circ} \text{ site} \end{array} \right.$
- mode :  $\left\{ \begin{array}{l} \text{Balayage sectoriel réglable} \\ \text{Poursuite, automatique par D.O.} \\ \text{externe ou manuelle par opérateur.} \end{array} \right.$

### 3.4 Logiciels d'analyse

Les logiciels d'analyse fonctionnent en temps différé sur des stations de travail HP série 9000 avec le système d'exploitation UNIX, ils permettent l'analyse fine des signatures de bâtiment à partir de fichiers contenant les mesures BHR et les paramètres bord du bâtiment mesuré. Ce logiciels sont de quatre types :

- . représentation de l'environnement de la cible,
- . tracés des SER en fonction de différents paramètres physiques et électromagnétiques,
- . analyse des fluctuations temporelles de la SER,
- . analyse et identification des points brillants.

#### 3.4.1 Représentation de l'environnement

Ce logiciel permet une représentation spatiale 2D (gisement, distance) de la SER de l'environnement, le BHR fonctionnant en balayage sectoriel. Un exemple est donné figure 7. Ce type de présentation permet notamment d'analyser le déploiement de leurres électromagnétiques.

#### 3.4.2 Tracé des SER

Différentes présentations des SER en fonction de différents paramètres sont possibles.

- . Présentation en fonction de 2 paramètres (2D), la SER étant représentée par des niveaux de couleur, par exemple :
  - SER en fonction de la présentation de la cible et de sa profondeur (figure 8),
  - SER en fonction de la présentation de la cible et de son roulis (ou de son tangage).
- . Présentation en fonction d'un seul paramètre (1D), par exemple :
  - SER en fonction de la présentation de la cible la représentation est en général en diagramme polaire (figure 9),
  - SER en fonction de la profondeur de la cible (figure 10),

- SER en fonction de la fréquence d'émission.

### 3.4.3 Analyse des fluctuations temporelles de la SER

Deux logiciels permettent cette analyse, le premier représente une analyse spectrale de la SER dans une bande totale de 100 Hz et avec une résolution spectrale réglable, le deuxième réalise une analyse statistique temporelle, estime la fonction de répartition et la compare à des lois connues (SWERLING, RAYLEIGH,...).

La figure 11 présente un exemple d'analyse spectrale obtenue sur des mesures.

La figure 12 présente la fonction de répartition estimée sur des mesures et la compare à celle d'une loi de Rayleigh.

### 3.4.4 Identification physique des points brillants sur la cible

Ce logiciel permet avec l'aide d'un opérateur, d'identifier des points brillants de les associer à des éléments physiques du bâtiment, de les isoler et d'évaluer le comportement de leur SER séparément, par exemple en fonction de la présentation.

Plus précisément à partir de représentation du type figure 8, l'opérateur est capable de reconnaître certaines traces de points brillants, il peut alors grâce à un utilitaire graphique les isoler puis représenter leur SER en fonction par exemple du gisement.

Pour l'identification physique des points brillants sur le bateau, l'opérateur utilise des représentations graphiques du type figure 10 auxquelles est superposée une image numérisée d'un schéma de la cible à la même échelle et vue selon le même angle. Ensuite à l'aide d'un utilitaire graphique, ces deux images peuvent glisser l'une par rapport à l'autre jusqu'à ce qu'apparaisse une "bonne" correspondance entre les différents pics de la mesure et des points physiques sur le bâtiment. La figure 13 donne un exemple de cette superposition.

## 3.5 Evolutions

Les deux principales évolutions envisageables sont :

- l'implantation d'un mode imagerie spatiale 2D à haute résolution :
  - . holographie radar en chambre (10 cm × 10 cm),
  - . SAR sur des bâtiments à quai (1 m × 1 m),
  - . ISAR sur des bâtiments en mer (1 m × 1 m) ;
- l'installation sur un porteur type hélicoptère afin d'accéder à des mesures de bâtiment sous des angles d'incidence élevés représentatifs de ce que percevraient certains autodirecteurs.

## 4. DONNEES TECHNIQUES DU BHR

Outre la description physique faite au § 3.2., la figure 14 donne le schéma fonctionnel du radar. En plus, des caractéristiques décrites au § 3.3, les données techniques des composants principaux sont les suivantes :

Fonctionnement 8 - 18 GHz.

Aérien

2 réflecteurs paraboliques double polarisation linéaire  
diamètre 60 cm.

Ouverture site gisement : 5° à 2,5° dans la bande 8 - 18 GHz.

Positionneur

Débattement ± 110° gisement  
-30° à +19° site

Mode { balayage sectoriel  
{ D.O. externe ou manuelle

Emission

2 W crête

Forme onde FMCW { Bande réglable 10 MHz  
à 2 GHz.  
{ Durée rampe 2,5 ms.

Polarisation horizontale et verticale séquentiellement.

Réception

Facteur de bruit ≤ 4 dB

2 voies de réception simultanées polarisation H et V

Démodulation homodyne

Numérisation : 12 bits, 625 kHz

Débit crête de sortie ≤ 20 Mbits/sec.

Pupitre et visualisation

Station HP 425 sous UNIX

Logiciels BASIC

La figure 15 donne un exemple de la visualisation du BHR. Cet ensemble permet entre autre de :

- rentrer les paramètres généraux de l'essai : date, nom du bateau, météo,...
- rentrer la configuration de mesure du radar : en chambre, à quai, en mer, phase de mesure ou de calibration,
- rentrer les paramètres radar : résolution, agilité de fréquence,...
- rentrer certains paramètres des composants principaux du radar : puissance, gain, émission on/off, enregistrement on/off,...
- afficher sur écran l'ensemble de ses données,
- afficher l'état du radar avec ses dispositifs de tests intégrés,
- afficher à cadence réduite (typiquement toutes les secondes) la mesure de SER faite en fonction de la distance.

Moyen d'enregistrement  
Numérique

Station d'analyse

Station HP série 9000 sous UNIX  
Logiciels d'analyse PV WAVE, C  
Imprimante couleur.

## 5. CALIBRATION

La calibration des moyens de mesure de SER polarimétrique très large bande ayant des précisions de la classe du "dB" est un problème difficile. En effet, deux grands types de calibration existent : la calibration externe et la calibration interne.

La calibration externe consiste à mesurer une cible étalon de SER parfaitement connue, la mesure obtenue traduit alors directement la fonction de transfert de l'ensemble du radar. Malheureusement, deux difficultés existent :

- la propagation radar-cible étalon peut différer de celle en espace libre à cause de l'environnement et notamment des multitrajets sur le sol, et donc peut fausser la calibration ;
- les cibles étalons en crosspolarisation rectiligne n'existent pas à notre connaissance en large bande.

La calibration interne consiste à mesurer en usine l'ensemble de la fonction de transfert du radar en fonction de tous les paramètres pouvant jouer sur cette fonction de transfert (fréquence, polarisation, résolution distance, température,...).

Ces mesures sont assez lourdes et ne peuvent pas être, en pratique, renouvelées très souvent contrairement à la calibration externe. Le défaut de la calibration interne est donc essentiellement une dérive due au vieillissement entre la fonction de transfert réelle et celle mesurée initialement.

Pour BHR est proposée une calibration mixte :

- calibration externe des mesures copolarisation linéaires HH et VV sur un trièdre étalon dont l'environnement est suffisamment maîtrisé pour être sûr de la valeur de la propagation à mieux que le "dB" ;
- calibration interne pour les mesures copolarisation linéaire car il n'y a pas de cibles étalons. On peut alors montrer que compte tenu des calibrations externes crosspolarisation, la dérive due au vieillissement des mesures crosspolarisation n'est plus qu'une dérive différentielle entre les deux voies d'émission au lieu d'être une dérive absolue sur l'ensemble des constituants.

Figure 1

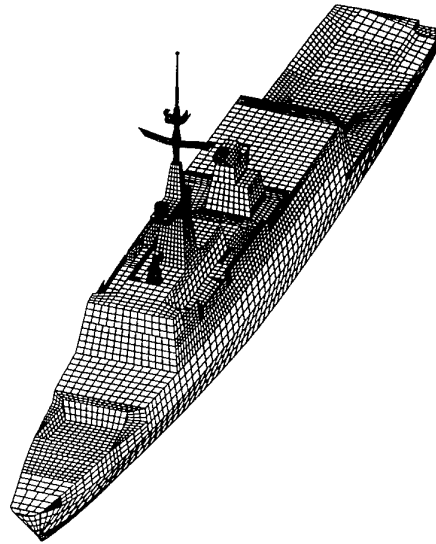


Figure 2

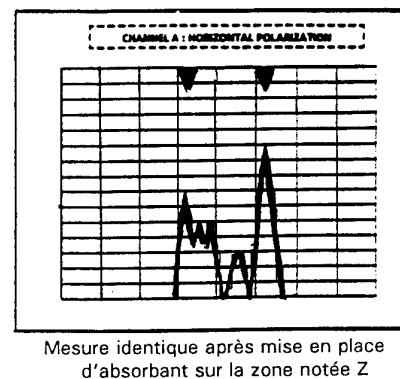
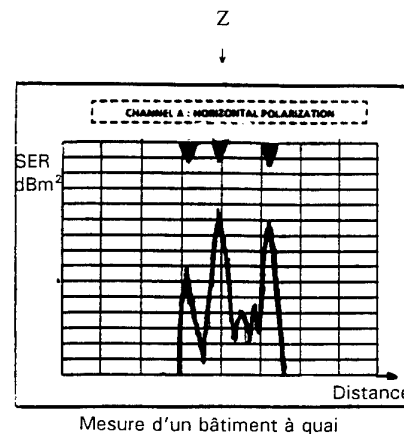


Figure 3

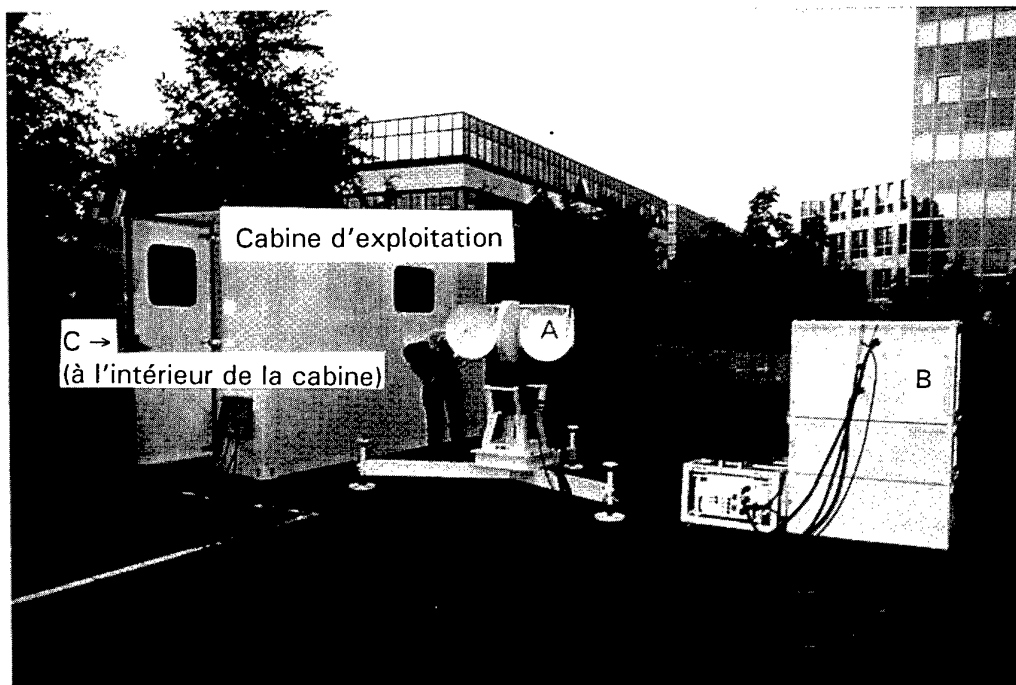


Figure 4

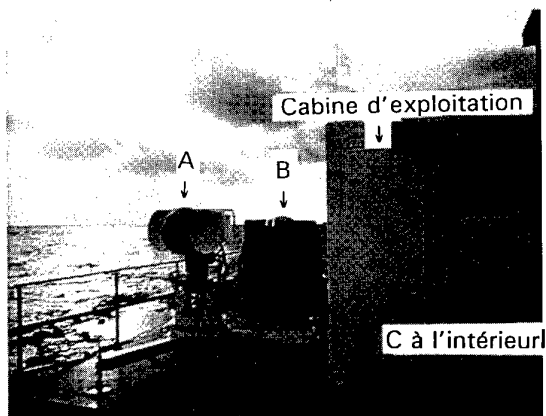


Figure 5

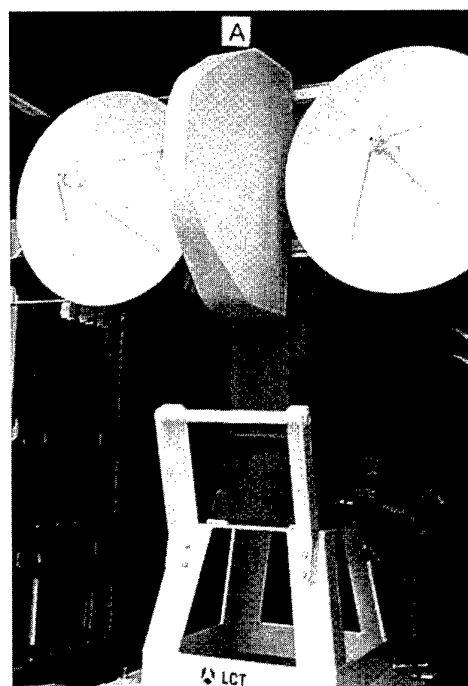


Figure 6  
Photographie partielle de C à l'intérieur  
de la cabine



Figure 7

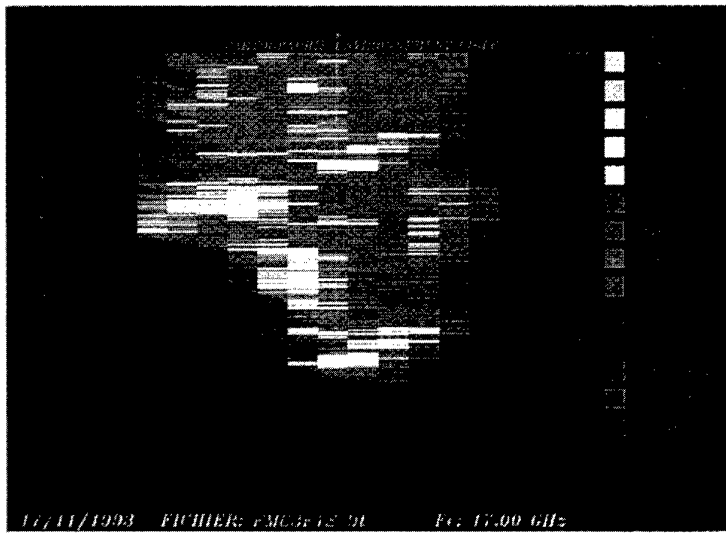


Figure 8

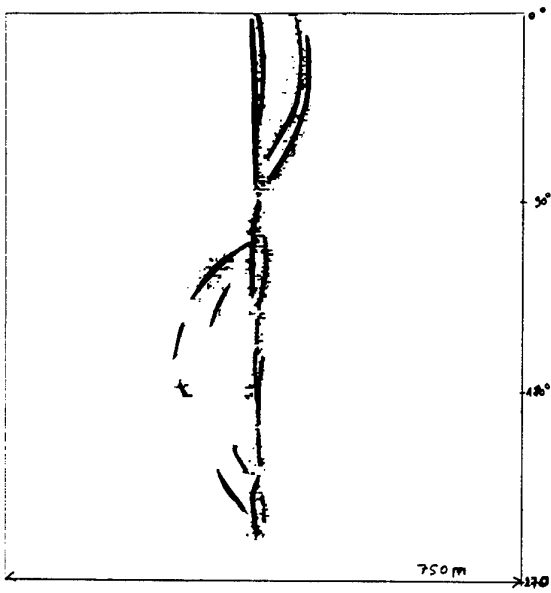


Figure 9

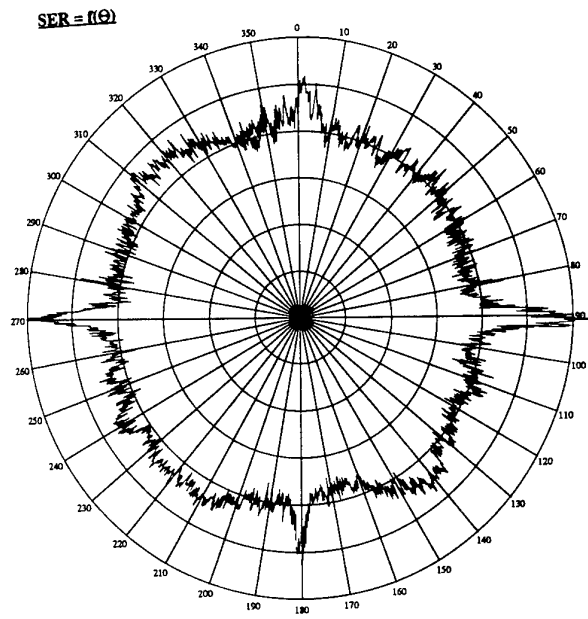


Figure 10

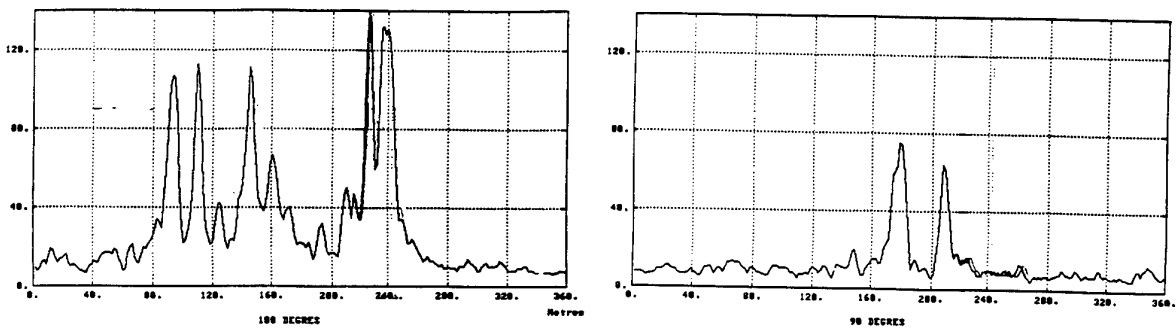


Figure 11  
Analyse spectrale

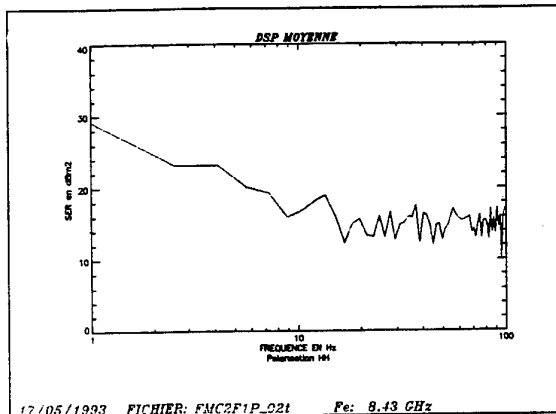


Figure 12  
Distribution statistique

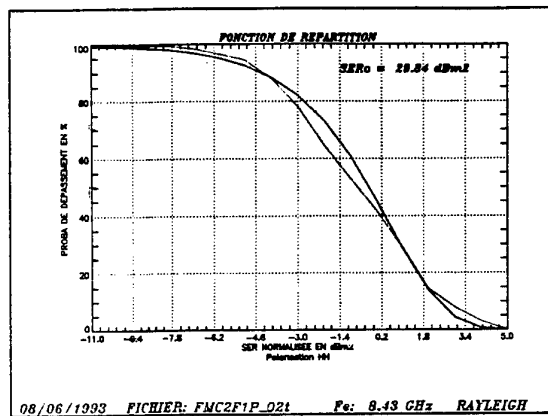


Figure 13

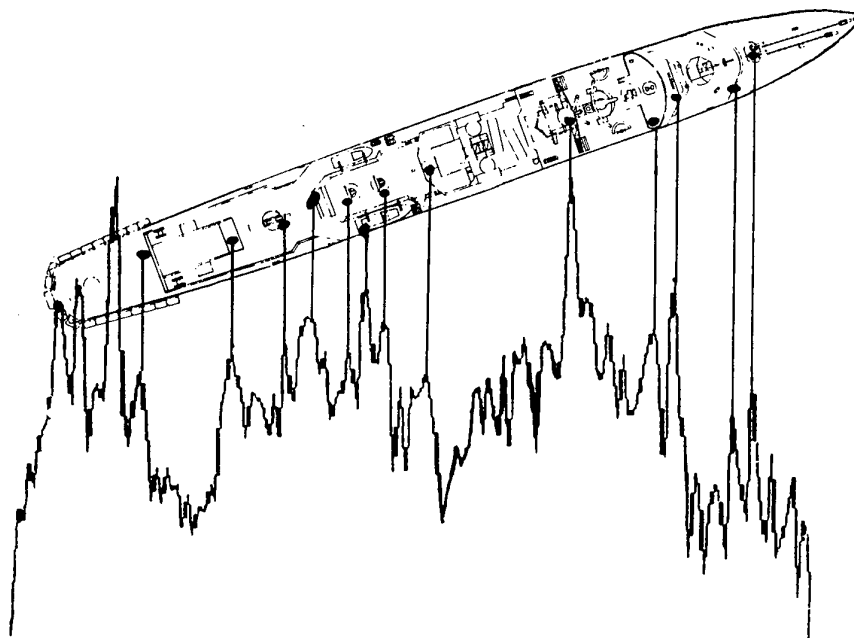


Figure 14  
Schéma fonctionnel

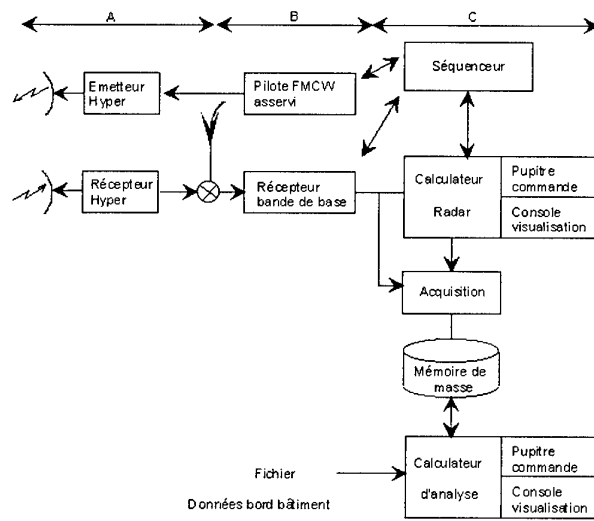
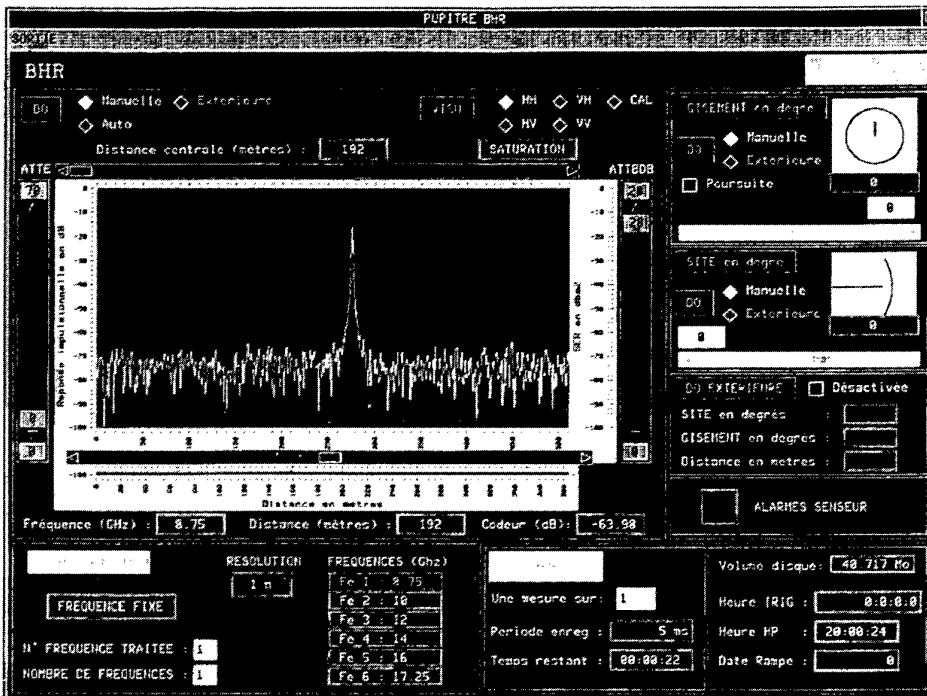


Figure 15





Aucun stock de publications n'a existé à AGARD. A partir de 1993, AGARD détiendra un stock limité des publications associées aux cycles de conférences et cours spéciaux ainsi que les AGARDographies et les rapports des groupes de travail, organisés et publiés à partir de 1993 inclus. Les demandes de renseignements doivent être adressées à AGARD par lettre ou par fax à l'adresse indiquée ci-dessus. *Veillez ne pas téléphoner.* La diffusion initiale de toutes les publications de l'AGARD est effectuée auprès des pays membres de l'OTAN par l'intermédiaire des centres de distribution nationaux indiqués ci-dessous. Des exemplaires supplémentaires peuvent parfois être obtenus auprès de ces centres (à l'exception des Etats-Unis). Si vous souhaitez recevoir toutes les publications de l'AGARD, ou simplement celles qui concernent certains Panels, vous pouvez demander à être inclus sur la liste d'envoi de l'un de ces centres. Les publications de l'AGARD sont en vente auprès des agences indiquées ci-dessous, sous forme de photocopie ou de microfiche.

CENTRES DE DIFFUSION NATIONAUX

## ALLEMAGNE

Fachinformationszentrum Karlsruhe  
D-76344 Eggenstein-Leopoldshafen 2

## BELGIQUE

Coordonnateur AGARD-VSL  
Etat-major de la Force aérienne  
Quartier Reine Elisabeth  
Rue d'Evere, 1140 Bruxelles

## CANADA

Directeur - Gestion de l'information  
(Recherche et développement) - DRDGI 3  
Ministère de la Défense nationale  
Ottawa, Ontario K1A 0K2

## DANEMARK

Danish Defence Research Establishment  
Ryvangs Allé 1  
P.O. Box 2715  
DK-2100 Copenhagen Ø

## ESPAGNE

INTA (AGARD Publications)  
Carretera de Torrejón a Ajalvir, Pk.4  
28850 Torrejón de Ardoz - Madrid

## ETATS-UNIS

NASA Goddard Space Flight Center  
Code 230  
Greenbelt, Maryland 20771

## FRANCE

O.N.E.R.A. (Direction)  
29, Avenue de la Division Leclerc  
92322 Châtillon Cedex

## GRECE

Hellenic Air Force  
Air War College  
Scientific and Technical Library  
Dekelia Air Force Base  
Dekelia, Athens TGA 1010

## ISLANDE

Director of Aviation  
c/o Flugrad  
Reykjavik

## ITALIE

Aeronautica Militare  
Ufficio del Delegato Nazionale all'AGARD  
Aeroporto Pratica di Mare  
00040 Pomezia (Roma)

## LUXEMBOURG

Voir Belgique

## NORVEGE

Norwegian Defence Research Establishment  
Attn: Biblioteket  
P.O. Box 25  
N-2007 Kjeller

## PAYS-BAS

Netherlands Delegation to AGARD  
National Aerospace Laboratory NLR  
P.O. Box 90502  
1006 BM Amsterdam

## PORTUGAL

Estado Maior da Força Aérea  
SDFA - Centro de Documentação  
Alfragide  
2700 Amadora

## ROYAUME-UNI

Defence Research Information Centre  
Kentigern House  
65 Brown Street  
Glasgow G2 8EX

## TURQUIE

Millî Savunma Başkanlığı (MSB)  
ARGE Dairesi Başkanlığı (MSB)  
06650 Bakanlıklar-Ankara

**Le centre de distribution national des Etats-Unis ne détient PAS de stocks des publications de l'AGARD.**

D'éventuelles demandes de photocopies doivent être formulées directement auprès du NASA Center for AeroSpace Information (CASI) à l'adresse ci-dessous. Toute notification de changement d'adresse doit être fait également auprès de CASI.

AGENCES DE VENTE

NASA Center for AeroSpace Information  
(CASI)  
800 Elkridge Landing Road  
Linthicum Heights, MD 21090-2934  
Etats-Unis

The British Library  
Document Supply Division  
Boston Spa, Wetherby  
West Yorkshire LS23 7BQ  
Royaume-Uni

Les demandes de microfiches ou de photocopies de documents AGARD (y compris les demandes faites auprès du CASI) doivent comporter la dénomination AGARD, ainsi que le numéro de série d'AGARD (par exemple AGARD-AG-315). Des informations analogues, telles que le titre et la date de publication sont souhaitables. Veuillez noter qu'il y a lieu de spécifier AGARD-R-nnn et AGARD-AR-nnn lors de la commande des rapports AGARD et des rapports consultatifs AGARD respectivement. Des références bibliographiques complètes ainsi que des résumés des publications AGARD figurent dans les journaux suivants:

Scientific and Technical Aerospace Reports (STAR)  
publié par la NASA Scientific and Technical  
Information Division  
NASA Langley Research Center  
Hampton, Virginia 23681-0001  
Etats-Unis

Government Reports Announcements and Index (GRA&I)  
publié par le National Technical Information Service  
Springfield  
Virginia 22161  
Etats-Unis  
(accessible également en mode interactif dans la base de  
données bibliographiques en ligne du NTIS, et sur CD-ROM)



AGARD holds limited quantities of the publications that accompanied Lecture Series and Special Courses held in 1993 or later, and of AGARDographs and Working Group reports published from 1993 onward. For details, write or send a telefax to the address given above. *Please do not telephone.*

AGARD does not hold stocks of publications that accompanied earlier Lecture Series or Courses or of any other publications. Initial distribution of all AGARD publications is made to NATO nations through the National Distribution Centres listed below. Further copies are sometimes available from these centres (except in the United States). If you have a need to receive all AGARD publications, or just those relating to one or more specific AGARD Panels, they may be willing to include you (or your organisation) on their distribution list. AGARD publications may be purchased from the Sales Agencies listed below, in photocopy or microfiche form.

NATIONAL DISTRIBUTION CENTRES

## BELGIUM

Coordonnateur AGARD — VSL  
Etat-major de la Force aérienne  
Quartier Reine Elisabeth  
Rue d'Evere, 1140 Bruxelles

## LUXEMBOURG

See Belgium

## CANADA

Director Research & Development  
Information Management - DRDIM 3  
Dept of National Defence  
Ottawa, Ontario K1A 0K2

## NETHERLANDS

Netherlands Delegation to AGARD  
National Aerospace Laboratory, NLR  
P.O. Box 90502  
1006 BM Amsterdam

## DENMARK

Danish Defence Research Establishment  
Ryvangs Allé 1  
P.O. Box 2715  
DK-2100 Copenhagen Ø

## NORWAY

Norwegian Defence Research Establishment  
Attn: Biblioteket  
P.O. Box 25  
N-2007 Kjeller

## FRANCE

O.N.E.R.A. (Direction)  
29 Avenue de la Division Leclerc  
92322 Châtillon Cedex

## PORTUGAL

Estado Maior da Força Aérea  
SDFA - Centro de Documentação  
Alfragide  
2700 Amadora

## GERMANY

Fachinformationszentrum Karlsruhe  
D-76344 Eggenstein-Leopoldshafen 2

## SPAIN

INTA (AGARD Publications)  
Carretera de Torrejón a Ajalvir, Pk.4  
28850 Torrejón de Ardoz - Madrid

## GREECE

Hellenic Air Force  
Air War College  
Scientific and Technical Library  
Dekelia Air Force Base  
Dekelia, Athens TGA 1010

## TURKEY

Millî Savunma Başkanlığı (MSB)  
ARGE Dairesi Başkanlığı (MSB)  
06650 Bakanlıklar-Ankara

## ICELAND

Director of Aviation  
c/o Flugrad  
Reykjavik

## UNITED KINGDOM

Defence Research Information Centre  
Kentigern House  
65 Brown Street  
Glasgow G2 8EX

## ITALY

Aeronautica Militare  
Ufficio del Delegato Nazionale all'AGARD  
Aeroporto Pratica di Mare  
00040 Pomezia (Roma)

## UNITED STATES

NASA Goddard Space Flight Center  
Code 230  
Greenbelt, Maryland 20771

**The United States National Distribution Centre does NOT hold stocks of AGARD publications.**

Applications for copies should be made direct to the NASA Center for AeroSpace Information (CASI) at the address below.

Change of address requests should also go to CASI.

SALES AGENCIES

NASA Center for AeroSpace Information  
(CASI)  
800 Elkridge Landing Road  
Linthicum Heights, MD 21090-2934  
United States

The British Library  
Document Supply Centre  
Boston Spa, Wetherby  
West Yorkshire LS23 7BQ  
United Kingdom

Requests for microfiches or photocopies of AGARD documents (including requests to CASI) should include the word 'AGARD' and the AGARD serial number (for example AGARD-AG-315). Collateral information such as title and publication date is desirable. Note that AGARD Reports and Advisory Reports should be specified as AGARD-R-nnn and AGARD-AR-nnn, respectively. Full bibliographical references and abstracts of AGARD publications are given in the following journals:

Scientific and Technical Aerospace Reports (STAR)  
published by NASA Scientific and Technical  
Information Division  
NASA Langley Research Center  
Hampton, Virginia 23681-0001  
United States

Government Reports Announcements and Index (GRA&I)  
published by the National Technical Information Service  
Springfield  
Virginia 22161  
United States  
(also available online in the NTIS Bibliographic  
Database or on CD-ROM)

